BERGISCHE
UNIVERSITÄT
WUPPERTAL

JÜLICH
Forschungszentrum

Development of an optical instrument for the observation of neutral winds in Earth's upper atmosphere

Dissertation

zur Erlangung des Grades
Doktor der Naturwissenschaften (Dr. rer. nat.)

vorgelegt der

Bergischen Universität Wuppertal
Fakultät für Mathematik und Naturwissenschaften

von

Daikang Wei

Wuppertal, 2020

The PhD thesis can be quoted as follows:

urn:nbn:de:hbz:468-20210531-102322-2
[http://nbn-resolving.de/urn/resolver.pl?urn=urn%3Anbn%3Ade%3Ahbz%3A468-20210531-102322-2]

DOI: 10.25926/b8qh-e462
[https://doi.org/10.25926/b8qh-e462]

Abstract

Neutral winds in Earth's upper atmosphere play an important role in atmospheric dynamics and energetics. As a candidate for the origin of ionospheric variability, the neutral winds prompt the interaction between neutral molecules and plasmas by blowing the ionospheric plasma across the Earth's magnetic field. Moreover, the behavior of upward propagating gravity waves between the planetary atmosphere and the near space environment is being studied, which leads to an increasing demand for the wind data in the upper atmosphere. Global network observation of thermospheric winds is an effective method to obtain the thermospheric wind data.

As a potential candidate to observe the neutral winds in Earth's upper atmosphere from the ground, an optical instrument based on a Doppler asymmetric spatial heterodyne (DASH) interferometer is developed in this dissertation. A DASH instrument, developed from a spatial heterodyne interferometer (SHI), records stationary interference fringes in an array detector, and its fringe phase is sensitive to Doppler shifts of emission lines owing to the introduction of an additional optical path on one arm. Based on the optical interference theory, a mathematical formula is deduced to describe the fringe pattern produced from a field-widening DASH interferometer, which provides the fundamental basis to derive the wind velocity. As a carrier of wind information, Doppler shifts of emission lines can be retrieved by a Fourier transform algorithm. A window function is generally used to isolate the targeted spectrum, and the choice of window function employed in a retrieval routine is also analyzed.

The first part of this dissertation examines the feasibility of wind measurements. A signal acquisition is always accompanied by instrument noises, which are critical factors to affect the measurement accuracy. With the knowledge of spectral radiance of the airglow emission and parameters of the instrument, the detected signal in a DASH instrument is estimated. A series of experimental tests have been performed for the detector, which quantifies the noise level including the dark current, read out noise and

signal offset. Using the estimated signal level and the performance of the detector, interferograms observed at different atmospheric conditions are simulated, and the corresponding signal-to-noise ratios are also discussed.

In the second part, a DASH instrument including a monolithic interferometer and a double-telecentric imaging system is designed. Since the fringe contrast decreases with the increase of optical path difference (OPD), an optimum OPD offset is found using numerical studies. In order to achieve field widening and thermal compensation, the Littrow angle, dimensions of each component as well as the material of each component are also optimized. A double-telecentic system is determined to relay the fringe pattern from the localization plane to the detector. With the support of ray-tracing software, interferograms in a designed DASH instrument are simulated and the corresponding visibilities are also discussed. Using the results of tolerance analysis, an instrument performance model is established and measurement uncertainties during different seasons are also investigated.

Finally, a thermally stable monolithic DASH interferometer with field-widening prisms is built and tested in the laboratory as part of this dissertation. A setup, monitoring the fringe contrast and the spatial frequency in real time, is built to assemble the DASH interferometer. The fringe visibility and the Littrow angle of the built interferometer are determined using a series of experimental tests. Before the wind velocity retrieval, the raw interferograms must be processed to produce corrected interferograms, and the general corrections include the spike and defect removal, dark current and signal offset correction, flat-field correction and phase-distortion correction. To evaluate the thermal performance, sensitivities of the spatial frequency and the optical phase are characterized based on experimental measurements and a model study. In laboratory Doppler measurements, Doppler velocities could be reproduced with a mean deviation of 1.82 m/s. Instrument field tests confirm that the interferogram produced from the oxygen red-line nightglow can be recorded and the corresponding phase information can be derived.

Contents

Chapter 1

Introduction

1.1 Background

Earth's atmosphere, a set of layers of gases surrounding the planet due to its gravity, provides us an environment suitable for life. According to temperature variation at different heights, the atmosphere is classified into four different layers, which are the troposphere, stratosphere, mesosphere and thermosphere from the lowest to the highest. Another useful classification refers to the ionized particles. The atmosphere lower than the height of about 80 km is called neutral atmosphere, because its main components are neutral molecules. At the higher altitudes, ionization processes become more significant, so it is named ionosphere in this region (*Koppmann*, 2017). With the differences of electron density, the ionosphere is further divided into the F region at heights above 150 km, E region from about 90-150 km and D region about 60 km to 90 km (*Hedlund*, 2010). The stratification of the atmosphere using the both methods is given in Figure 1.1, and the data of temperature and plasma density are taken from *Kelley* (2009).

The neutral and ionized compositions in Earth's upper atmosphere are relevant to the magnetosphere-ionosphere coupling, input solar wind and solar radiation at extreme ultraviolet (EUV) wavelengths (*Kelley*, 2009). Except for the external influences, a number of recent studies emphasize the interaction between the planetary atmosphere and near space environment, which highlights the propagation of waves generated in the troposphere and stratosphere (*Immel et al.*, 2009; *England et al.*, 2018; *Rider et al.*, 2015; *Immel et al.*, 2006; *England et al.*, 2006; *Sagawa et al.*, 2005). The transfer of energy and momentum from the lower atmosphere into the upper atmosphere is realized by atmospheric tides, planetary waves and gravity waves (*Immel et al.*, 2006; *Hagan et al.*, 2007; *Titheridge*, 1995). As a driver of ionospheric variability, the effect of upward propagating gravity waves is still not quantified and its mechanism is still not well

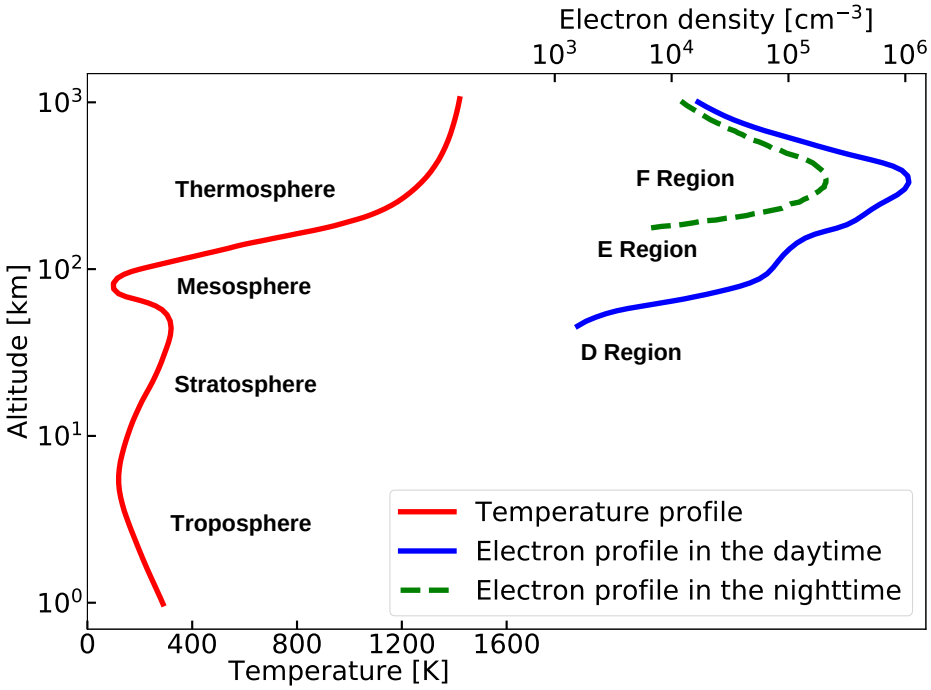

Figure 1.1: Stratification of Earth's atmosphere based on the vertical temperature profile and electron density.

understood (*Hines et al.*, 1993; *Killeen et al.*, 2006).

The neutral wind in the atmosphere, driven by pressure gradients resulting from the EUV solar radiation, auroral heating, large-scale convection of magnetic field lines and upward propagation energy (*Titheridge*, 1995), plays an important role in electrodynamics and neutral-plasma interactions. The neutral wind blows the ionospheric plasma across the magnetic field, which creates dynamo electric fields. Then the generating electric field interacts with the magnetic field to drive the F-region ion drifts (*Armstrong*, 2008). Therefore, the neutral wind can be the source of ionospheric variability, which requires observations of the wind profiles at different altitudes to verify (*Immel*, 2018). To understand these coupled neutral-ion processes, the knowledge of neutral winds is critical in the thermosphere and ionosphere.

The wind data in the lower atmosphere are routinely available based on the active Doppler-shift measurements (*Souprayen et al.*, 1999; *Gentry et al.*, 2000; *Reitebuch et al.*, 2009) , but there are still some challenges for the measurements of thermospheric winds. The main methods to obtain neutral winds in this region include rocket measurements, meteor radars measuring the drift of ionized trails, incoherent scatter radars and Doppler airglow observations (*Titheridge*, 1995). The Doppler airglow observation

is the strongest candidate to obtain precise wind information on a global scale in this region, which has been widely carried out in the past few decades (*Hays and HRDI Science Team*, 1992; *Oberheide et al.*, 2006; *Englert et al.*, 2017a).

1.2 Horizontal Wind Model

At low-latitudes and midlatitudes, the EUV absorption is the main source to drive the thermospheric winds, which was validated by early observations (*Salah and Holt*, 1974; *Burnside and Tepley*, 1989; *Hedin et al.*, 1988). At high latitudes, influences from the auroral heating and the ion-neutral coupling are also significant. Though the predominant processes of the circulation are almost understood, the wave coupling from below is not, which was considered as a primary driver of the day-to-day variability of the ionosphere (*Roble*, 2000; *Fang et al.*, 2013). With the increasing desire to understand the physics in the upper atmosphere, accurate specifications of the wind fields are expected.

Based on the data from satellite, rocket and ground-based wind measurements, an empirical model, Horizontal Wind Model (HWM), was derived to describe the complex dynamics of the atmosphere (*Hedin et al.*, 1994, 1996; *Drob et al.*, 2008, 2015). This model calculates horizontal wind fields from the ground to the exosphere with the specified latitude, longitude, time, and magnetic activity index (Ap index). The empirical specifications of wind fields can be used to check physical models as well as new measurements. HWM provides a reasonable start point and boundary conditions, which simplifies the complex computation during model calculations and retrieval algorithms (*Doornbos et al.*, 2010; *Kelly et al.*, 2014).

Hedin et al. (1988) released the first version of HWM in 1987 (HWM87), which only works in the altitude range from 220 km to 400 km. The new updated HWM model is HWM14, and all of analyses are based on this version in the following discussion. The global horizontal wind fields at 250 km on September 21, 2014 are presented in Figure 1.2, which is the calculation result from HWM14. The Ap index is 10 in the simulation according to the British Geological Survey (*Survey*, 2014). A purpose of this dissertation is to develop an instrument operating in Wuppertal, so that zonal and meridional winds are simulated for the location of Wuppertal as shown in Figure 1.3. The horizontal winds change with the local time, altitude and magnetic activity, and their speeds (magnitude) are mostly in the range from 0 to 150 m/s.

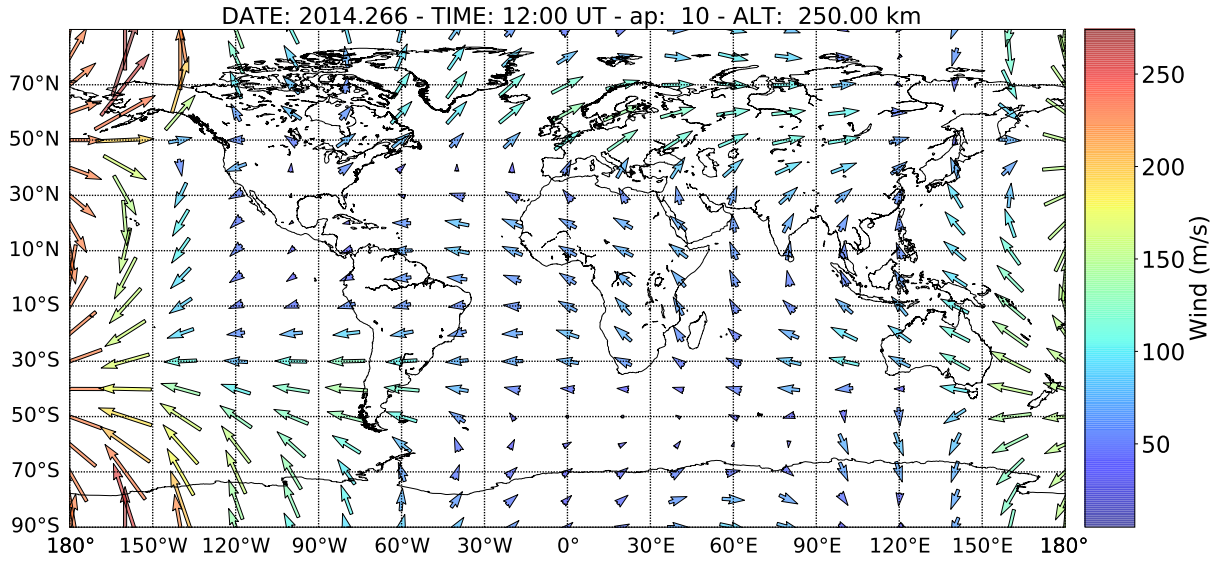

Figure 1.2: Daily averaged horizontal wind vectors at 250 km on September 21, 2014, as a function of latitude and longitude.

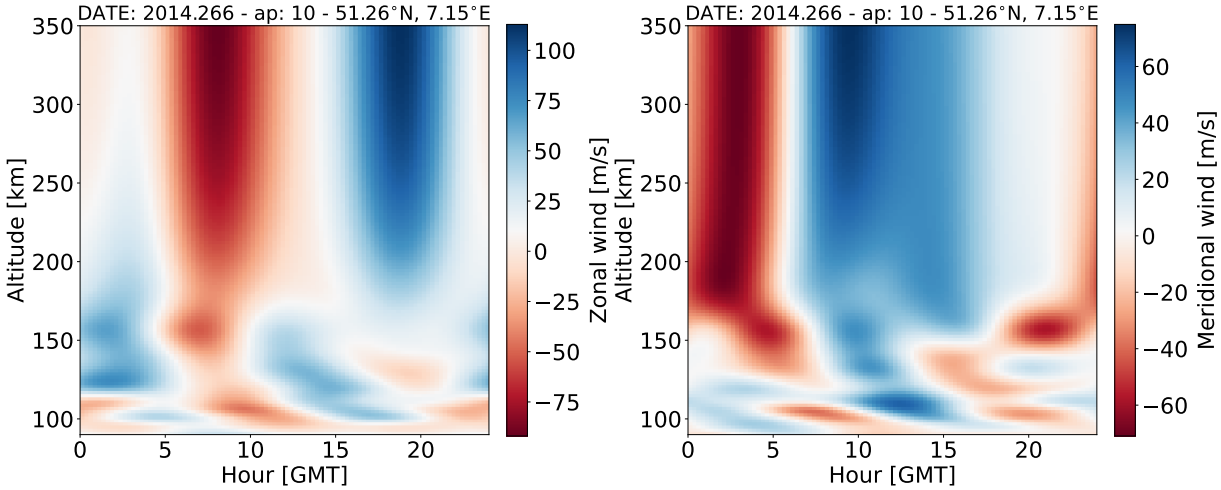

Figure 1.3: Zonal wind profiles and meridional wind profiles at Wuppertal (51.26°N, 7.15°E) on September 21, 2014, as functions of altitude and local time. Positive values represent eastward zonal winds (left) and northward meridional winds (right).

1.3 Atomic Oxygen Red Line Emission

In the Earth's atmosphere from 150 km to 300 km, atomic oxygen in metastable state emits light of 630.0 nm arising from the O(^{1}D-^{3}P) transition. Due to the long radiative lifetime (110 seconds), atomic oxygen experiences a sufficient number of collisions with its surrounding molecules, so that a thermodynamic equilibrium between atomic oxygen and its ambient atmosphere is established (*Shepherd et al.*, 1985, 1993; *Thuillier and Hersé*, 1991). Therefore, the Doppler shift of the emitted light contains the movement information of atomic oxygen, which is equivalent to the atmospheric neutral wind in this region.

Table 1.1: Chemistry of the 630.0 nm nightglow

No.	Reaction	Rate coefficient
R1	$O^+ + O_2 \rightarrow O_2^+ + O$	$k_1 = 3.23 \times 10^{-12} e^{3.72/(T_i/300) - 1.87/(T_i/300)^2}$ cm^3/s
R2	$O_2^+ + e \rightarrow 2O(^3P, ^1D, ^1S)$	$\alpha_1 = 1.95 \times 10^{-7} (T_e/300)^{-0.7}$cm^3/s, $\beta_{1_D} = 1.1$
R3	$O(^1D) + N_2 \rightarrow O(^3P) + N_2$	$k_3 = 2.0 \times 10^{-11} e^{111.8/T_n}$ cm^3/s
R4	$O(^1D) + O_2 \rightarrow O(^3P) + O_2$	$k_4 = 2.9 \times 10^{-11} e^{67.5/T_n}$ cm^3/s
R5	$O(^1D) + e \rightarrow O(^3P) + e$	$k_5 = 1.6 \times 10^{-12} T_e^{0.91}$ cm^3/s
	Transition	Einstein transition probability (s^{-1})
T1	$O(^1D_2 - ^3P_2)$	$A_{6300} = 5.15 \times 10^{-3}$
T2	$O(^1D_2 - ^3P_1)$	$A_{6364} = 1.66 \times 10^{-3}$

Based on the Atmosphere Explorer (AE) satellite measurements, atomic oxygen photochemistry in the nightglow was analyzed (*Cogger et al.*, 1980; *Link and Cogger*, 1988). The chemistry of the 630.0 nm nightglow is described in Table 1.1 (*Cogger et al.*, 1980; *Link and Cogger*, 1988; *Yiyi*, 2012). At night, the dissociative recombination of O_2^+ occurs with a rate coefficient of α_1 in the upper atmosphere, which produces $O(^1D_2)$ (R2 in Table 1.1). Then the metastable $O(^1D_2)$ emits a photon at the wavelength of 630.0 nm ($^1D_2 - ^3P_2$) or 636.4 nm ($^1D_2 - ^3P_1$). The molecular oxygen ion O_2^+ is the result of a reaction between O^+ and O_2 (R1 in Table 1.1), and its rate coefficient is k_1. Except the photon radiation, the $O(^1D_2)$ are also quenched by the N_2, O_2 and e with the corresponding rate coefficients of k_3, k_4 and k_5, respectively (R3 to R5 in Table 1.1). Accordingly, the volume emission rate (VER) of oxygen red line V_{6300} is given by

$$V_{6300} = \frac{0.76\beta_{^1D}k_1\left[O^+\right]\left[O_2\right]}{1+\left(k_3\left[N_2\right]+k_4\left[O_2\right]+k_5\left[e\right]\right)/A_{^1D}}, \tag{1.1}$$

where $[O^+]$, $[O_2]$, $[N_2]$ and $[e]$ represent the densities of these particles, $\beta_{^1D}$ is the production efficiency of $O(^1D)$ in the reaction, $A_{^1D}$ is the transition coefficient, which is the sum of A_{6300} and A_{6364} (*Link and Cogger*, 1988). These parameters are presented in Table 1.1, where T_e, T_i and T_n are the temperatures of electron, ion and neutral, respectively.

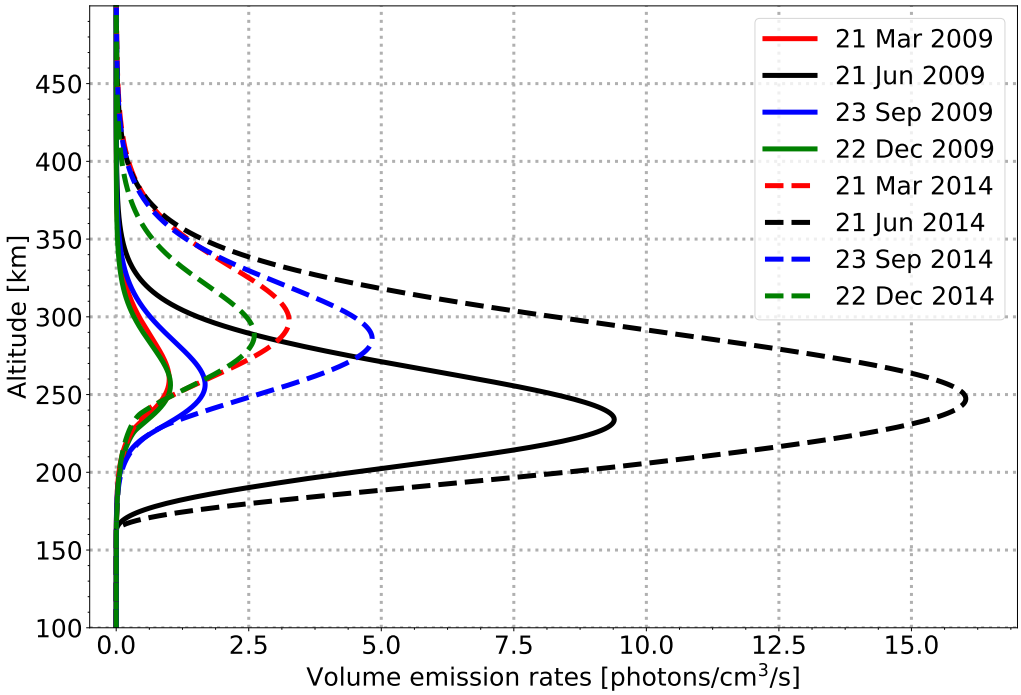

Figure 1.4: Volume emission rates of oxygen red line emissions at Wuppertal (51.26°N, 7.15°E) in the different seasons of 2009 (solar minimum) and 2014 (solar maximum) with the local solar time at midnight.

The densities and temperatures of particles in the atmosphere are available using empirical models. Naval Research Laboratory Mass Spectrometer Incoherent Scatter Radar 2000 (NRLMSISE-00) model can provide the $[O_2]$ and $[N_2]$ (*Picone et al.*, 2002). And the $[O^+]$, $[e]$, T_e, T_i and T_n can be modeled from International Reference Ionosphere 2012 (IRI2012) model (*Bilitza et al.*, 2014). The VER profile of oxygen red line emission can be therefore estimated. For example, VER profiles at Wuppertal (51.26°N, 7.15°E) in different seasons of 2009 and 2014 with the local solar time at midnight are shown in Figure 1.4. In a recent solar cycle, 2009 and 2014 are the years with the lowest

solar activity and strongest solar activity, respectively. The VER varies with the altitude, season and solar activity, and it achieves the peak at the altitude about 250 km. Apparently, the VER becomes higher when more solar energy is possible to be absorbed in the atmosphere such as in summer or on the year with stronger solar activities.

During daytime, the photoionization caused by the injected solar flux enhances the density of $O(^1D_2)$, which causes more red-line transitions to occur. On the other hand, the dissociative recombination still exists. The photochemical process becomes more complicated, which involves the electron impact, dissociative recombination, photodissociation, cascade O^1S, chemistry, collisional deactivation and radiative transition (*Witasse et al.*, 1999).

1.4 Optical Passive Detection Technique in the Atmosphere

Remote sensing is a general technique to study the atmospheric composition, thermal structure and dynamics. Based on different radiation sources, the remote sensing technique can be classified into active detection using radars or lidars and optical passive detection. A passive wind detection is generally implemented by observing the Doppler shift of natural emission lines. In the region of the thermosphere, the airglow lines emitted by atomic oxygen and molecular oxygen can be used as targets to measure thermospheric winds.

1.4.1 Fabry-Perot Interferometer

A Fabry-Perot interferometer (FPI) consists of two parallel reflecting plates (etalon), and it was firstly discussed in 1897 by Fabry and Perot (*Hernandez*, 1988). When a light beam goes through an FPI, multiple-beam reflections occur in the etalon and the multiple-beam interference produces a fringe pattern on the focal plane. Owing to the high spectral resolution, the Doppler shift can be determined from the fringe pattern change.

FPI instruments have been widely used to measure thermospheric winds due to their high sensitivity and simple configuration. In the 1950s, *Armstrong* (1955, 1959) firstly used an FPI to study atmospheric properties such as temperatures in the middle and upper atmosphere. With the development of the image plane detector and coupled charge device (CCD), an FPI technique without scanning process was developed and it was applied in ground-based observations and satellite observations (*Sivjee et al.*, 1980; *Killeen et al.*, 1983; *Hays and HRDI Science Team*, 1992). Most instruments observing ther-

mospheric winds from the ground are based on FPI, and this type of instruments was also utilized in space missions such as the High-Resolution Doppler Imager (HRDI) on NASA's Upper Atmospheric Research Satellite (UARS) and the TIMED Doppler Interferometer (TIDI) on NASA's Thermosphere-Ionosphere-Mesosphere Energetics and Dynamics (TIMED) mission (*Hays et al.*, 1993; *Killeen et al.*, 2006). The HRDI is a two-axis-gimbal system with three etalons, which was designed for the wind observations from 10 km to 120 km with an accuracy of 5 m/s (*Hays et al.*, 1993). The TIDI was developed for globally measuring the wind and temperature profiles in the mesosphere and lower thermosphere (MLT). With the applications of a circle-to-line imaging optic (CLIO) technique and a high quantum efficiency and low noise CCD, the circle fringes were transformed into line fringes and multiplexing observations were available (*Killeen et al.*, 1999). The TIDI inteferometer measured horizontal vector wind from an altitude of 60 to 300 km with a vertical resolution of $\sim$2 km and an accuracy about 3 m/s (*Killeen et al.*, 1999, 2006).

Extreme manufacturing tolerance (smaller than $\lambda/20$) of the etalon is required for an FPI, which results in its high costs. In order to achieve good optical throughput, the large and heavy volume is inevitable because of its limited field of view. But the FPI is still the most common instrument for thermpspheric wind observations.

1.4.2 Michelson Interferometer

The Michelson interferometer, also known as Fourier transform spectrometer (FTS), is another typical instrument for atmospheric wind detection. This interferometer monitors the phase shift of interferograms to trace the Doppler shift. For an isolated atmospheric emission line, a small number of phase points around a large optical path difference (OPD) are sampled during a scanning process. Detecting Doppler shifts requires high spectral resolution, which corresponds to large OPD values. A field-widening technique can be employed in a Michelson interferometer, which allows large-solid-angle illumination and highly improves the measurement responsivity. In addition, the system stability and accuracy are further improved due to the application of thermal compensation.

Owing to the particular advantages, field-widening Michelson interferometers were widely employed in atmospheric studies. A field-widening Michelson interferometer was firstly presented by *Bouchareine and Connes* (1963). Based on this concept, Hilliard and Shepherd developed an instrument to observe atmospheric temperatures, which are related to the fringe modulation depths (*Hilliard and Shepherd*, 1966). In 1985, *Thuillier and Shepherd* (1985) described a technique to thermally compensate a fixed-path Michelson interferometer, and this technique was adapted in the WINd and TemperaturE by Remote Sensing (WINTERS) instrument and its ground-based

version Michelson interferometer for coordinated auroral Doppler observations (MICADO) (*Thuillier and Shepherd*, 1985; *Thuillier and Hersé*, 1991). An achromatic field-widening Michelson interferometer with good thermal stability was developed to acquire images of winds and temperatures in the upper atmosphere (*Shepherd et al.*, 1985), and its name is wide-angle Michelson Doppler imaging interferometer (WAMDII). WAMDII is a Spacelab instrument which employs four quarterwave phase-stepped images to derive line-of-sight velocities from the line shifts with an error of 10 m/s (*Shepherd et al.*, 1985). The wind imaging interferometer (WINDII), a combination of WINTERS and WAMDII, was also launched on the UARS and achieved wind observations with an accuracy of 5 m/s from the satellite (*Gault et al.*, 1994; *Hersom and Shepherd*, 1995; *Shepherd*, 1996). Its targeted emission lines include OH (8-3) bands, O_2 atm (0-0) band, O^1S green line and O^1D red line in the altitude range from 80 km to 300 km. The WINDII interferometer recorded four (or eight) interferograms positions using the moving mirror which was controlled by piezoelectric pillars (*Shepherd et al.*, 1993).

In order to improve the system stability in a Michelson interferometer, large efforts were made to avoid moving parts. *Gault et al.* (1996) described a divided-mirror scanning technique that one of the mirrors is divided into four quadrants with a path difference of $\lambda/4$ from one quadrant to another using different coatings in the quadrants. In 2011, *Gao et al.* (2011) reported a modified super-wide-angle Sagnac imaging interferometer based on liquid crystals on silicon for atmospheric wind measurements, which can measure phase changes in multi-band emissions without moving mirror. A concept of novel static polarization wind imaging interferometer (NSPWII) was proposed for atmospheric wind and temperature measurements (*Zhang et al.*, 2011). In the NSPWII, a pyramid prism and a polarization array were adapted, so that four optical beams with different phases were recorded on a CCD simultaneously (*Zhang et al.*, 2011).

A challenge of a Michelson interferometer is the ultra-narrow prefilter, which is employed in isolating the single airglow emission line. When there are other emissions close to the targeted line, an additional Fabry-Perot etalon prefilter is necessary (*Ward et al.*, 2001, 2003), which further increases the system volume and reduces the system throughput. For each measurement, only one emission line is allowed to pass through the system, so that the instrument thermal drift can not be monitored using an artificial emission line. In addtion, stringent scanning stability and accuracy are also required for a Michelson interferometer.

1.4.3 Spatial Heterodyne Interferometer

The Spatial heterodyne interferometer (SHI) is an effective methodology to achieve a high-resolution spectrum using stationary interference fringes. It is similar to the

Michelson interferomter system with two diffraction gratings replacing the reflection mirrors. The principle of SHI is that two crossed wavefronts produced by a beamsplitter and gratings on two arms are imaged onto an array detector. Then a Fizeau fringe pattern,whose spatial frequency is determined by the input wavelength, Littrow wavelength and Littrow angle of the gratings, is recorded on the detector. The input spectrum can be recovered by a Fourier transform, and the resolution power of the dispersive elements (gratings) is maintained in this device. Field widening can also be employed in an SHI, which significantly increases its system throughput by four orders of magnitude compared to conventional grating spectrometers with similar spectral resolution (*Harlander et al.*, 1992). Its features of high throughput and no moving parts mean that a rugged compact SHI can be built, which is particularly suited for observations of weak diffuse emissions such as atmospheric airglow from space (*Harlander et al.*, 2002; *Kaufmann et al.*, 2018). A two-dimensional detector is utilized to record fringe images in a satellite instrument, which realizes limb observation for different altitudes simultaneously without limb scanning. In addition, SHI can be developed in all-reflection configurations, which provides additional advantage for UV and EUV applications.

The SHI concept was conceived by Pierre Connes in a configuration of Spectromètre interférentiel à sélection par l'amplitude de modulation (SISAM) (*Connes*, 1958). In order to search for an alternative to conventional FPI and FTS techniques, this concept was developed by Harlander and Roesler (*Harlander and Roesler*, 1990; *Roesler and Harlander*, 1990). Harlander discussed the concept of SHI, two-dimensional SHI technique, field widening and all-reflection SHI configuration (*Harlander*, 1991), which provides the basic theory of SHI. Based on this concept, a sounding payload was developed to investigate the hot component of the diffuse interstellar medium (*Harlander et al.*, 1993, 1994, 1995). In 1999, an infrared imaging spatial heterodyne spectrometer (IRISHI) for imaging spectroscopy at ultraspectral resolution (1 cm^{-1}) was reported (*Smith and Harlander*, 1999; *Smith et al.*, 1999; *Milligan et al.*, 1999). A monolithic SHI, shown in Figure 1.5, was firstly produced using optical contact bonding, which was a crucial part of the Spatial Heterodyne Imager for Mesospheric Radicals (SHIMMER) (*Harlander et al.*, 2003). The SHIMMER on the Space Test Program Satellite-1 (STPSat-1) observed the OH solar resonance fluorescence spectrum in the global scale, which successfully demonstrated the capability and advantages of SHI in a long-duration space mission (*Harlander et al.*, 2002; *Englert et al.*, 2010a). A method using SHI to vertically resolve the water vapor profile in the upper troposphere and lower stratosphere was presented (*Lin et al.*, 2005; *Langille et al.*, 2017). The Spatial Heterodyne Observations of Water (SHOW) on balloon and aircraft were successfully carried out (*Dupont et al.*, 2015; *Langille et al.*, 2018). Recently, a highly miniaturized satellite instrument based on a SHI was proposed to measure atmospheric temperatures by observing the O_2 A-band in limb viewing mode in the MLT (*Kaufmann et al.*, 2018).

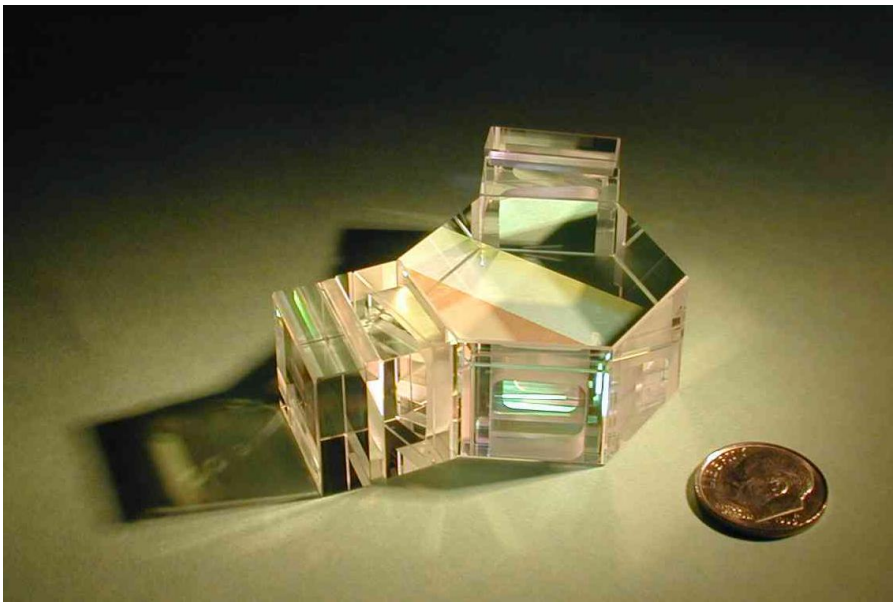

Figure 1.5: Monolithic SHI for the SHIMMER (*Englert et al.*, 2006).

1.4.4 Doppler Asymmetric Spatial Heterodyne Interferometer

The Doppler asymmetric spatial heterodyne (DASH) interferometer, developed from the Michelson interferometer and SHI, is a novel technique to probe atmospheric winds by observing the airglow emissions. The principle of a DASH interferometer, similar to Michelson interferometer, is that the Doppler shift can be resolved by comparing the phase change around a large OPD. Lengthening the optical path on one arm transforms an SHI into a DASH interferometer. This simple modification makes it possible to sample hundreds of phase points around a large OPD without moving components, which strengthens its immunity to ghost fringes and background noise. Owing to the fact that a DASH interferometer can resolve multiple emission lines simultaneously, it is possible to use a reference line to track instrument drifts. The thermal compensation and field widening can also be employed in a DASH interferometer. Compared with the conventional FPI and Michelson interferometer, the DASH instrument can not only achieve similar responsivity and accuracy but can also be built into a compact and robust system with looser manufacturing and alignment tolerances, which is expected for a space flight instrument.

Englert et al. (2006) extended the SHI concept to an innovative method to observe the winds in planetary atmospheres. Then the experimental demonstration was reported by the same group (*Englert et al.*, 2007), which proves that a DASH interferometer is capable of measuring atmospheric winds with an accuracy of 1.6 m/s. *Harlander et al.* (2010) designed a monolithic DASH interferometer based on a Köster's double-

reflection prism, where the two splitting beams go through different areas of a single field-widening prism and diffraction grating. The Redline DASH Demonstration Instrument (REDDI) was developed using this monolithic interferometer, which enables the thermal drift tracking with a calibration lamp (*Englert et al.*, 2010b). The ground-based REDDI measurements were successfully conducted, which was validated by the simultaneous FPI observations (*Englert et al.*, 2012). The Michelson Interferometer for Global High-Resolution Imaging of the Thermosphere and Ionosphere (MIGHTI), an instrument on NASA's Ionospheric Connection (ICON) Explorer satellite using the DASH technique, was developed to measure thermospheric winds and temperatures on a global basis (*Harlander et al.*, 2017; *Englert et al.*, 2017a). The limb image superimposing fringe pattern at altitudes from 90 km to 300 km is separately recorded by two MIGHTI interferometers from two perpendicular fields of view during day and night. Then the thermospheric horizontal wind profiles can be retrieved by observing Doppler shifts of the atomic oxygen red line (630.0 nm) and green line (557.7 nm) with an uncertainty ranging from 1.2 to 4.7 m/s (*Harding et al.*, 2017). Lower order Echelle diffraction gratings and a mosaic filter were employed in the MIGHTI instrument, so that red-line and green-line images can be detected simultaneously using one interferometer and one detector (*Englert et al.*, 2017b; *Harlander et al.*, 2017).

1.5 Research Objective and Instrument Requirements

The research objective of this dissertation is to develop a ground-based remote sensing instrument to observe thermospheric winds at altitudes of 250±50 km. A miniaturized and rigid DASH interferometer is selected for this instrument, which measures the Doppler shift of the atomic oxygen red line emission at 630.0 nm. This instrument is characterized by its high throughput at a small form factor, allowing scientific remote sensing measurements from the ground.

Since this instrument is developed to measure horizontal wind velocities including magnitude and direction, measurements pointing in two perpendicular directions are necessary, which requires a precise and stable skyscanner in the system. Another important measurement requirement is to achieve ±3 m/s accuracy in harsh environments of remote observatories. The instrument requirements driven by the measurement requirements include:

- wavelength shifts smaller than 8 orders of magnitude of the emission wavelength can be detected,
- high optical efficiency including all optics and detector quantum efficiency (larger than 25%),

- high throughput, full field of view $\geq 9^{\circ}$,
- low thermal drift sensitivity (1 rad/°C),
- low fringe distortion ($\leq 1.0\%$),
- high visibilities for the interferograms produced from atomic oxygen red line and calibration line ($\geq 60\%$),
- high resolving power (the interferograms produced from observed line and calibration line can be separated),
- stable temperature control ($\pm$ 0.1 °C for interferometer and $\pm$ 5 °C for camera optics),
- narrow bandpass optical filter ($\leq$ 5 nm),
- low detector dark current (≤ 0.6 e^{-1}/s/pixel) and readout noise (≤ 2 e^{-1}/s/pixel).

1.6 Motivation

Atmospheric winds play an important role in atmospheric dynamics and energetics. Thermospheric neutral winds impact on the interaction between neutral molecules and plasmas, which is relevant for space weather forecasts and modern satellite communications (*Hargreaves*, 1992; *Rees and Rees*, 1989; *Makela et al.*, 2009; *Sultan*, 1996). There is evidence from the wind observations that a link between the lower and upper atmosphere exists, which can be achieved by the propagation of atmospheric tides, planetary waves and gravity waves (*Hays and HRDI Science Team*, 1992; *Shepherd et al.*, 1993; *Killeen et al.*, 2006). The role of upward propagating gravity waves in the upper atmosphere is currently being studied, which requires more data to validate.

In order to study the evolution of mesospheric or thermospheric phenomena, global network observations of thermospheric winds are routinely carried out (*Meriwether*, 2006; *Emmert et al.*, 2006; *Jiang et al.*, 2012). The satellite measurements were performed as well, but the wind data in the upper atmosphere still remain sparse. With the increasing need, a more inexpensive and precise instrument has to developed, so that it can be widely employed in network observations. A thermally compensated DASH instrument is one of the potential candidates. In addition, another motivation behind this study is to explore the possibility to apply a DASH instrument in the future space mission.

1.7 Outline

This dissertation focuses on the development of a DASH instrument capable of measuring velocities of thermospheric winds. Firstly, Chapter 2 provides a theoretical framework of a DASH instrument. Using this theoretical framework, the fringe pattern obtained from a DASH interferomter is modeled and an algorithm to retrieve Doppler wind velocities is described. In Chapter 3, the instrument response is investigated taking into account realistic airglow emssions and the detection characteristics of the instrument. Combining the estimated signal level and detector performance, the signal-to-noise ratio of system is evaluated. In Chapter 4, a DASH interferomter design including the Littrow wavelength, OPD offset, thermal compensation and field widening is discussed. An imaging system to relay the fringe pattern to the detector is also designed using ray-tracing software. With the optimized configuration, an instrument performance model is established and uncertainties of the instrument are also analyzed in this chapter. Chapter 5 describes the construction and laboratory test of a demonstrated instrument built in an optical breadboard. In this chapter, properties of the instrument, interferogram corrections, the thermal performance, Doppler measurements and field tests are investigated experimentally, which confirms that this built instrument is a promising sensor for thermospheric winds. Finally, a summary concerning current work and an outlook for future work are presented in Chapter 6.

Chapter 2

Instrument Principle

The DASH interferometer, a modification of an SHI, is a passive detection technique to acquire neutral winds and temperatures by observing Doppler shifts and thermal broadening of an airglow emission in the thermosphere. In this chapter, the principle of the DASH interferometer is discussed from the aspects of the DASH instrument concept, derivation of wind velocity, derivation of Doppler temperature and associated algorithms. The interferogram produced from a DASH instrument is modeled, which helps to understand the instrument principle. A DASH instrument, similar to an SHI instrument, records stationary interference fringes on an array detector, where the spatial frequency of the interferogram is related to the Littrow angle of the grating, the Littrow wavenumber and the wavenumber of the incident radiation. The asymmetric optical path makes the interferometer sensitive to the phase change, which can be deduced by a fast-Fourier-transform algorithm. The fringe contrast, decreasing with the increment of the sampled OPD, contains the temperature information, which is the basis to retrieve the Doppler temperature. Algorithms for phase-change determination and thermal-drift calibration are also discussed here. A suitable window function implemented in spectral domain can retrieve more precise phase information from the obtained interferograms.

2.1 DASH Instrument Concept

The DASH instrument concept is developed from the SHI instrument and Michelson interferometer technique. Lengthening the optical path on one arm transforms an SHI into a DASH interferometer. This simple modification makes it possible to measure tiny wavenumber changes arising from Doppler shifts. In addition, the field-widening design highly increases the optical throughput, which allows the system to receive radiation from a relatively large solid angle with high fringe contrasts.

As illustrated in Figure 2.1, a conventional field-widening DASH interferometer consists of fore optics L1, a beamsplitter, two field-widening prisms, diffraction gratings and exit optics (L2 and L3). Incoming radiation is divided into two coherent wavefronts by the beamsplitter. After reflection from the gratings, these two wavefronts with an intersection angle of 2γ recombine on the detector producing a Fizeau fringe pattern, where the zero OPD point shifts from the center to some place on one side due to the additional length Δd on one arm. The fringe localization plane is located in a position close to the grating and this plane is a virtual image of the grating. The role of the exit optics (L2 and L3) is to image the fringes from the localization plane onto the detector.

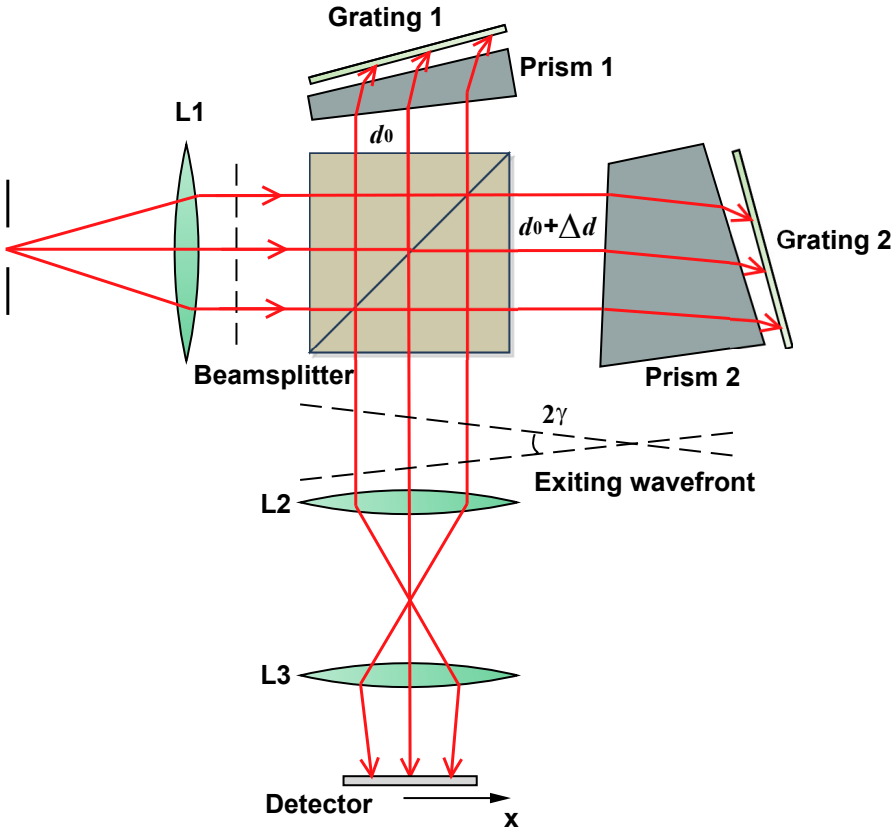

Figure 2.1: Schematic of a field-widening DASH interferometer. The quantities d_0 and $d_0 + \Delta d$ represent the optical paths from the beamsplitter to the gratings on the arm one and arm two, respectively.

The fringe pattern obtained in a DASH interferometer is modeled in Appendix A including the on-axis analysis and off-axis analysis. Assuming the intensity of the input radiation is I_0, the intensity of the interferogram $I(x)$ at position x can be expressed as

$$I(x) = \frac{I_0}{2}\left\{1 + V_I(\sigma_0, x)\cos\left[2\pi\left(fx + 2\sigma_0\Delta d_0\right)\right]\exp\left(-2\pi^2 P_D^2 L^2\right)\right\}, \tag{2.1}$$

where $V_I(\sigma_0, x)$ is the instrument visibility function, σ_0 is the central wavenumber of the emission line, f is the spatial frequency, and Δd_0 is the extended distance at the central wavelength of the emission line. P_D is a Doppler-broadening parameter defined in Equation A.11, which is related to the emission line wavenumber and the temperature. The spatial frequency f can be calculated by

$$f = 4\tan\theta\left(\sigma_0 - \sigma_L\right), \tag{2.2}$$

which is related to the Littrow angle of the grating θ and its corresponding Littrow wavenumber σ_L. When the incident wavelength is equal to the Littrow wavelength, a zero-spatial-frequency pattern is produced on the detector. In Equation 2.1, $L = D + 4\tan\theta x$, which is defined to describe a decrease of the fringe contrast. Note that D is defined to replace the fixed OPD offset ($2\Delta d$) when the optical dispersion is considered, and it is defined as

$$D = 2\Delta d_0 - \lambda_0\left[2\frac{\partial(\Delta d)}{\partial\lambda}\right], \tag{2.3}$$

where λ denotes the wavelength and λ_0 denotes the central wavelength of emission line. Using Equation 2.1, interferograms without and with Doppler shift can be simulated and the corresponding intensity difference between the two interferograms can be calculated. Comparing the two simulated interferograms, the interferogram without Doppler shift and the intensity difference between the two interferograms are presented in Figure 2.2. The fringe contrast of the interferogram declines with the increase of L, which is the result of the temperature broadening. The envelope of the intensity difference first increases with the increment of L, but then its rate of change becomes negative when L is larger than a certain value. Hence, there is an optimum OPD offset (D value), which makes the interferometer most sensitive to the change of the interferogram.

As for the SHI, the resolving power of DASH interferometer is determined by gratings, and the resolving power R can be calculated by

$$R = 4W\sigma\sin\theta, \tag{2.4}$$

with the illuminated width of grating W and the wavenumber of emission line σ. The derivation of the resolving power is discussed in Appendix A.4. With a good resolving power, aliasing interferograms with different spatial frequencies can be separated in the spectral domain. Accordingly, it is possible to select an artificial line to simultaneously tack thermal drifts during measurements.

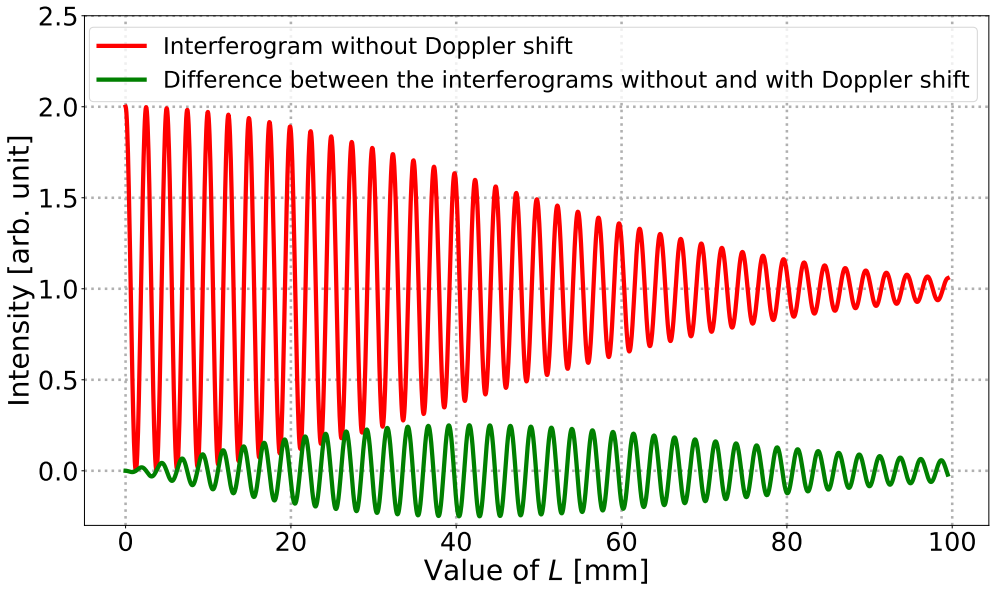

Figure 2.2: Interferogram without Doppler shift and intensity difference between interferograms without and with Doppler shift as functions of L. The temperature broadening of 1000 K and Doppler velocity of 300 m/s are applied here to simulate the interferograms.

2.2 Derivation of Wind Velocity

2.2.1 Field-measurement Strategy

In order to determine the wind velocity including the magnitude and the direction, a scientific observation strategy should be implemented, which is discussed in this section. The vector of wind velocity can be obtained by the sum of two velocities retrieved from two-orthogonal-direction measurements. Thus, it is necessary to perform at least two-direction measurements in field measurements. Figure 2.3 illustrates the field-measurement strategy of a ground-based DASH instrument. In order to detect the horizontal wind velocity, sequential measurements viewing zenith, eastward and northward are performed. The zenith measurements are used for zero-wind calibration, which assumes that the average vertical wind throughout the night is zero. It is a reasonable assumption because the vertical winds are mostly less than 7 m/s (*Widdel*, 1987; *Sipler et al.*, 1995; *Smith*, 1998). For each direction measurement, the horizontal wind is calculated by dividing the line-of-sight velocity by the cosine of the elevation angle. Finally, the wind velocity $\vec{v}$ can be expressed as

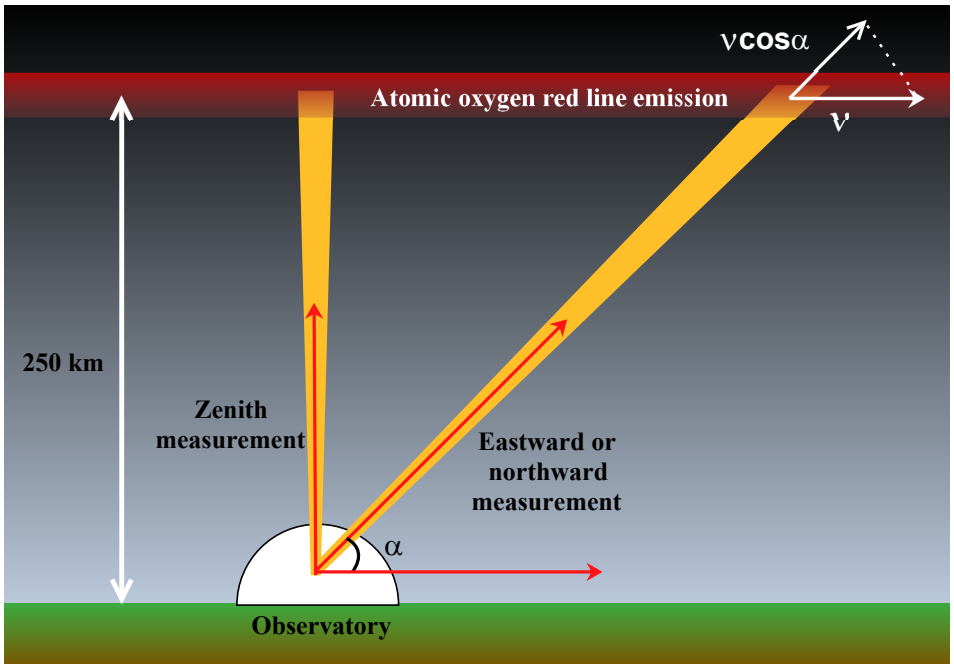

Figure 2.3: Measurement strategy of a ground-based DASH instrument. Note that α represents the elevation angle and v represents the horizontal wind velocity.

$$\vec{v} = \vec{v}_{east} + \vec{v}_{north}, \tag{2.5}$$

where $\vec{v}_{east}$ and $\vec{v}_{north}$ represent the horizontal wind velocities in the east and north directions.

2.2.2 Determination of Doppler Velocity

The thermospheric wind causes a Doppler shift of the airglow emission, which is generally smaller than 7 orders of magnitude of the emission wavelength. This small shift results in a small phase change in the interferogram recorded in a DASH system. The determination of line-of-sight velocity based on the phase change is presented in this section. Given a non-Doppler shifted wavenumber σ_0, the corresponding wavenumber σ_v with Doppler shift can be calculated by

$$\sigma_v = \sigma_0 \left(1 + \frac{v}{c}\right), \tag{2.6}$$

where v is the observed velocity of the emission source and c is the speed of light. According to Equation 2.1 and Equation 2.2, the obtained interferograms without and

with Doppler shifts can be generally written as

$$\begin{aligned} I_0(x) &\propto 1 + V_I(x)\cos\{2\pi[4\tan\theta(\sigma_0-\sigma_L)x + 2\sigma_0\Delta d_0]\}\exp\left(-2\pi^2 P_D^2 L^2\right) \\ I_v(x) &\propto 1 + V_I(x)\cos\{2\pi[4\tan\theta(\sigma_v-\sigma_L)x + 2\sigma_v\Delta d_v]\}\exp\left(-2\pi^2 P_D^2 L^2\right). \end{aligned} \tag{2.7}$$

The Doppler shift of the wavenumber results in a phase shift in the interferogram. Comparing these two interferograms, the phase change $\Delta\varphi(x)$ is obtained by

$$\Delta\varphi(x) = 8\pi\tan\theta(\sigma_v-\sigma_0)x + 4\pi(\sigma_v\Delta d_v - \sigma_0\Delta d_0). \tag{2.8}$$

Considering the optical dispersion, the extended value Δd varies with the wavenumber shift caused by the Doppler effect. An effective OPD D', similar to Equation 2.3, is defined. Consequently, a relationship holds for $2\Delta d_v\sigma_v$

$$2\Delta d_v\sigma_v = D'(\sigma_v-\sigma_0) + 2\Delta d_0\sigma_0. \tag{2.9}$$

Note that the D' is in reference to the emission line without Doppler shift, while the D in Equation 2.3 is in reference to the emission central line. Although their definitions are different, the numerical difference is negligible. Therefore, a unified effective optical path difference D is utilized in the following discussion. Substituting Equation 2.9 and Equation 2.6 into Equation 2.8 deduces a relation between phase change and wind velocity

$$\Delta\varphi(x) = 8\pi\tan\theta x\sigma_0\frac{v}{c} + 2\pi D\sigma_0\frac{v}{c}. \tag{2.10}$$

The first term of this equation presents the phase change across the detector, and the second term represents the contribution from the OPD offset. The phase change can be determined by the algorithm of Fourier transform or Hilbert transform, which will be discussed in Section 2.4. Combining the phase change information and the relation in Equation 2.10, the Doppler velocity is retrieved accordingly.

2.3 Derivation of Doppler Temperature

As shown in Equation 2.1, the interferogram visibility $V(\sigma,x)$ can be expressed as

$$V(\sigma,x) = V_I(\sigma,x)\exp\left(-2\pi^2 P_D^2 L^2\right). \tag{2.11}$$

Apparently, the fringe pattern contrast consists of two different terms including the instrument visibility function $V_I(\sigma,x)$ and the exponential term $\exp\left(-2\pi^2 P_D^2 L^2\right)$. $V_I(\sigma,x)$ is used to describe the instrument property, which is determined by its optics and system design. Another term is the product of the thermal broadening of emission line, which introduces a damping factor in the amplitude. This factor is related to its emission temperature, and its amplitude attenuation becomes more serious when the OPD gets larger. The function $V_I(\sigma,x)$ is an inner property of an instrument, which can be characterized by viewing a homogeneous source from a narrow-line laser or other calibration light with a known line profile.

After the Fourier transform, the modulated part of the interferogram can be obtained by implementing a window function in the spectral domain, which will be discussed in Section 2.4. The modulus of this modulated interferogram gives the interferogram amplitude, and the normalization of the amplitude is the corresponding interferogram visibility described in Equation 2.11. After dividing by the term $V_I(\sigma,x)$ obtained from the calibration, the temperature information can be retrieved from the exponential term based on Equation A.11. The exponential term is related to the effective OPD D, so the calibration for D is also significant.

The fringe contrast is affected by the background noise and stray light, which must be subtracted before the retrieval routine. For the dayglow, the oxygen red line is emitted by both hot atoms and non-thermal atoms (*Shepherd et al.*, 1993), which results in an underestimation of the temperature. Although there still are some problems to measure the temperature during the daytime using the fringe contrast, this methodology is suited to the temperature measurement during the nighttime. Doppler temperature measurements based on Michelson interferometers using the fringe contrasts have already succeeded (*Hilliard and Shepherd*, 1966; *Lathuillère et al.*, 2002).

2.4 Determination of Phase Change

Fourier transform decomposes a signal into its constituent frequencies, which is a general method to obtain the phase information of a signal. The Fourier transform of an interference pattern is a complex-value function of spatial frequency, whose argument provides the phase-offset information of the signal. But the inevitable spectral leakage, noise and spectral broadening bring in additional deviations of the phase estimation in the spectral domain. The more elegant strategy is to calculate the phase distribution in the spatial domain, which was presented by *Englert et al.* (2004, 2007). The targeted signal can be extracted in the spectral domain using a suitable window function, and then the backward transformation for the isolated spectrum yields the modulated part of the interferogram, which can be expressed as

$$I_f(x) = A(f,x)\{\cos[2\pi fx + \Phi(f,x)] + i\sin[2\pi fx + \Phi(f,x)]\}, \tag{2.12}$$

where f denotes the spatial frequency and $\Phi(f,x)$ denotes the phase offset. Consequently, the phase $\varphi(f,x)$ can be estimated by

$$\varphi(f,x) = 2\pi fx + \Phi(f,x) = \arctan\left\{\frac{\Im\left[I_f(x)\right]}{\Re\left[I_f(x)\right]}\right\}, \tag{2.13}$$

where $\Im\left[I_f(x)\right]$ and $\Re\left[I_f(x)\right]$ represent the imaginary and real parts of the modulated part of the interferogram, respectively. For each interferogram, the phase distribution can be obtained by Equation 2.13. The unwrapping process, making the phase continuous, is necessary before comparing the phase difference, which may cause additional computational efforts. Adopting trigonometric identities, bypassing the unwrapping to calculate the phase difference directly is possible. For interferograms with and without Doppler shift as shown in Equation 2.7, the modulated parts after isolating the corresponding spectrum can be expressed as

$$\begin{aligned} I'_0(x) &= A(f,x)\left[\cos(\varphi_0) + i\sin(\varphi_0)\right] \\ I'_v(x) &= A(f,x)\left[\cos(\varphi_v) + i\sin(\varphi_v)\right] \end{aligned}, \tag{2.14}$$

where $A(f,x) \propto V_I(\sigma,x)\exp\left(-2\pi^2 P_D^2 L^2\right)$ and $\varphi_{0,v} = 2\pi\left[4\tan\theta\left(\sigma_{0,v} - \sigma_L\right)x + 2\sigma_{0,v}\Delta d_{0,v}\right]$. Then according to the relation between their imaginary and real parts, the phase difference can be derived

$$\begin{aligned} \Delta\varphi(x) &= \arctan\left[\frac{\sin(\varphi_v - \varphi_0)}{\cos(\varphi_v - \varphi_0)}\right] \\ &= \arctan\left\{\frac{\Im\left[I'_v(x)\right]\Re\left[I'_0(x)\right] - \Re\left[I'_v(x)\right]\Im\left[I'_0(x)\right]}{\Re\left[I'_v(x)\right]\Re\left[I'_0(x)\right] + \Im\left[I'_v(x)\right]\Im\left[I'_0(x)\right]}\right\}, \end{aligned} \tag{2.15}$$

where $\Im\left[I'_{0,v}(x)\right]$ and $\Re\left[I'_{0,v}(x)\right]$ represent the imaginary and real parts of the corresponding modulated parts of the interferograms, respectively. It is not necessary to separately estimate the phase information for each interferogram. The phase change is determined directly using the Fourier transform results, which bypasses the phase unwrapping process. In addition, Hilbert transform can be considered as a phase shift of -$\pi/2$ to every Fourier component of a function in the frequency domain, which also can be used to retrieve the phase change. The similar method using a Hilbert transform to retrieve the phase difference was discussed by Liu et al. (*Liu et al.*, 2018).

Therefore, the process of phase-change determination is illustrated in Figure 2.4. Fourier transforms are performed for two interferograms, then the targeted spectra are isolated in the spectral domain by multiplying window functions. The complex interferograms are obtained after the inverse Fourier transforms for the targeted spectra. Using Euler's formula and trigonometric identities (Equation 2.15), the phase change is finally determined.

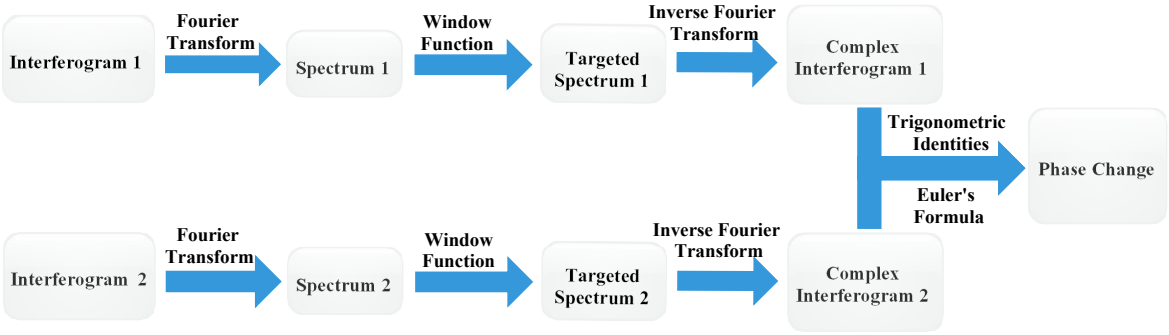

Figure 2.4: Process of the phase-change determination. Interferogram 1 and intefero-gram 2 are the obtained interferograms without and with Doppler shift.

2.5 Choice of Window Function

As a mathematical function that is zero-valued outside of some chosen interval, a window function is general used in Fourier transform analysis to reduce the amplitude of the discontinuities at the boundaries of a finite signal. As discussed previously, a window function also can be used to extract the targeted spectrum in the phase-change determination. Similar to the spectral leakage effect, the introduction of a window function results in an additional error in the phase determination. In this section, the choice of the window function is studied by comparing the errors using different window functions, and the width of the window is also investigated.

Based on Equation 2.1, an interferogram obtained from a DASH interferometer can be expressed as

$$\begin{aligned} I(x) &= \frac{I_0}{2}\{1 + A(f,x)\cos[2\pi(fx + 2\sigma_0\Delta d_0)]\} \\ &= \frac{I_0}{2} + \frac{I_0}{2}A(f,x)\exp[-2\pi i(fx + 2\sigma_0\Delta d_0)] \\ &\quad + \frac{I_0}{2}A(f,x)\exp[2\pi i(fx + 2\sigma_0\Delta d_0)], \end{aligned} \tag{2.16}$$

with $A(f,x) = V_I(\sigma,x)\exp\left(-2\pi^2 P_D^2 L^2\right)$. A window function $t(f)$ is implemented to isolate the positive component, so that the isolated modulated portion $I'(x)$ is yielded after inverse Fourier transform

$$I'(x) = T(x) \circledast \frac{I_0}{2} A(f,x)\exp\left[2\pi i\left(fx + 2\sigma_0 \Delta d_0\right)\right], \tag{2.17}$$

where $T(x)$ is the inverse Fourier transform of $t(f)$ and $\circledast$ denotes the convolution operator. The algorithm to determine the phase difference is based on the imaginary part and real part of $I'(x)$. In order to analyze the effect from the convolution term, a restored interferogram $I_r(x)$ is defined and it can be calculated by the relation below

$$I_r(x) = 2I'(x) + 1. \tag{2.18}$$

The convolution term of $T(x)$ causes a distortion of the restored interferogram compared with the original interferogram, which brings in an additional error in the retrieval routine. The difference between restored interferogram $I_r(x)$ and the initial interferogram $I(x)$, including intensity and phase differences, can be used to evaluate the deviation arising from the term of $T(x)$. The small difference means that the error resulted from $T(x)$ is also small. In order to choose the best window type, interferogram differences using different window functions are calculated, and the corresponding intensity differences and phase differences are presented in Figure 2.5(a), Figure 2.5(b) and Figure 2.5(c). The initial interferogram is produced based on Equation 2.1 with a temperature broadening of 1000 K and the phases of the interferograms are determined using Equation 2.13. Apparently, the interferogram differences in the middle region are pretty small, but the values on the both sides increase dramatically. The utilization of a rectangle window function results in the largest difference especially in the middle. For the other five window types, the interference difference attenuates quickly in the middle, and the minimum intensity difference and phase difference are achieved when a Hanning or Hamming window is selected. Therefore, it is suggested to use a Hanning or Hamming window to isolate the modulated signal, and the edge region needs to be excluded when computing the phase change.

The window width is another important parameter to consider. A narrow window function may lead to a loss of the spectral component, which further distorts the restored interferogram and produces retrieval error. On the other hand, the implementation of a wide window increases the risk to contain unwanted spectrum parts and noise, and then errors are produced accordingly. The simulated interferogram and the restored interferograms using Hamming windows with different widths are compared, and the corresponding intensity differences and phase differences are also plotted in Figure 2.6(a) and Figure 2.6(b), respectively. With the broadening of the window function, the interferogram difference attenuates. When the width is larger than 6 times of the spectral

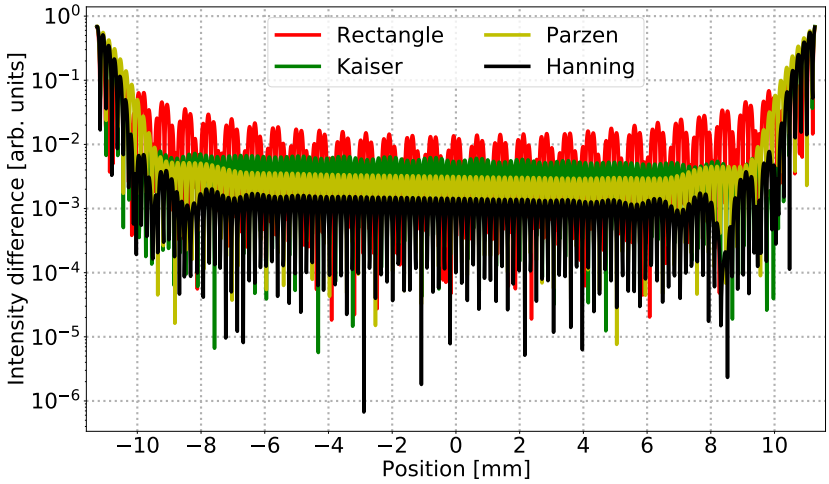

(a) Intensity differences using rectangle, Hanning, Kaiser and Parzen windows

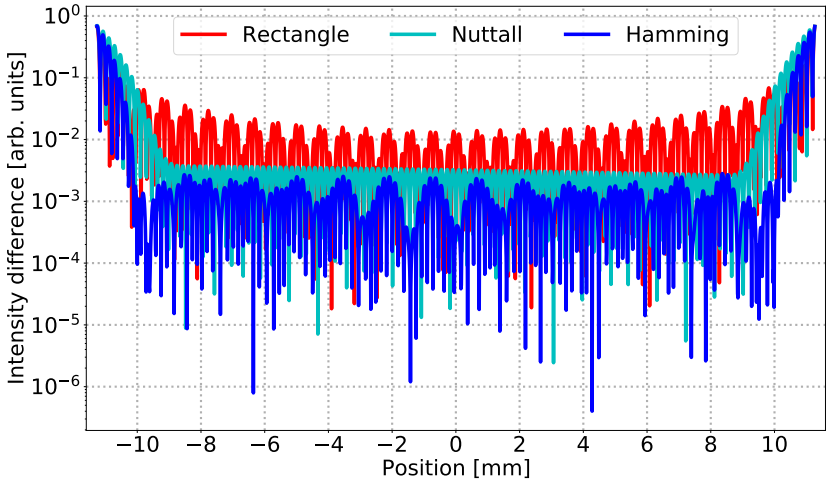

(b) Intensity differences using rectangle, Hanning and Nuttal windows

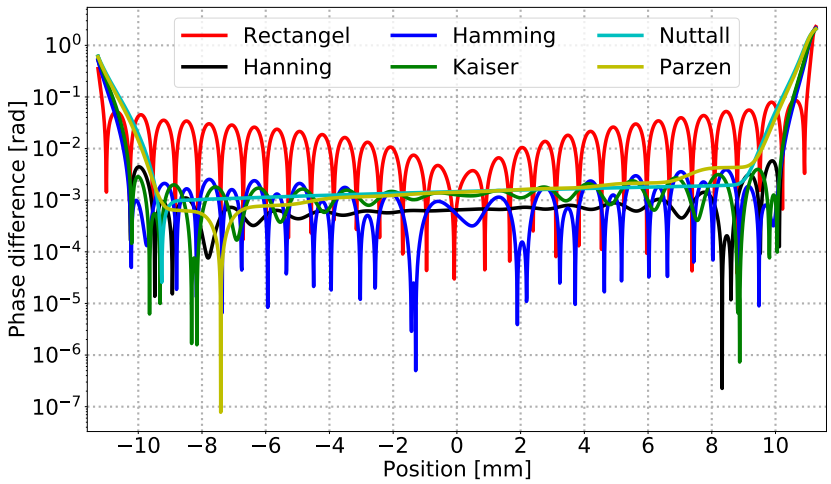

(c) Phase differences using different window functions

Figure 2.5: (a, b) Intensity and (c) phase differences between the restored interferograms and initial interferogram using different window functions. Note that the y axes are logarithmic coordinate and the window widths of 8 times of the spectral full width at half maximum (FWHM) are applied for all window functions.

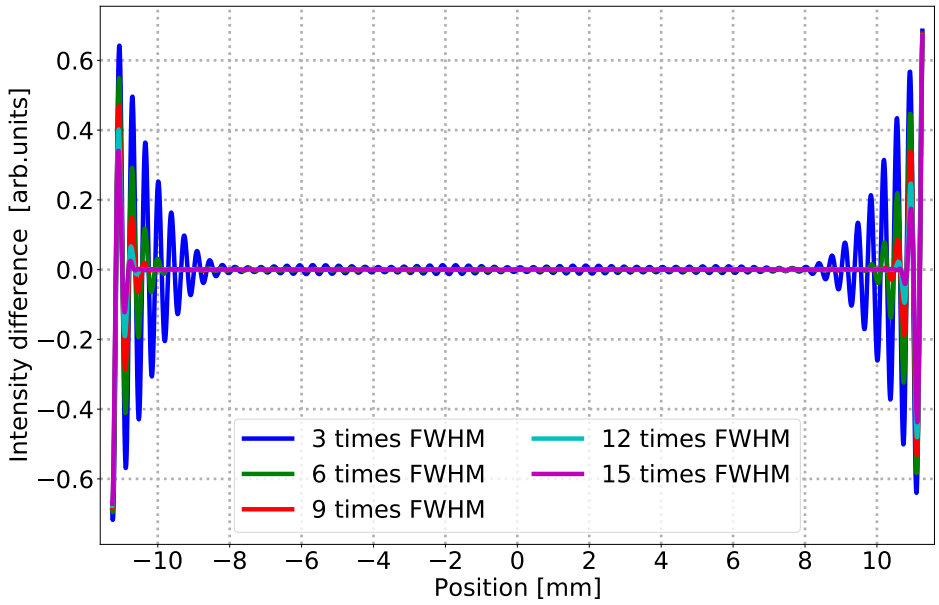

(a) Interferogram differences using different window widths

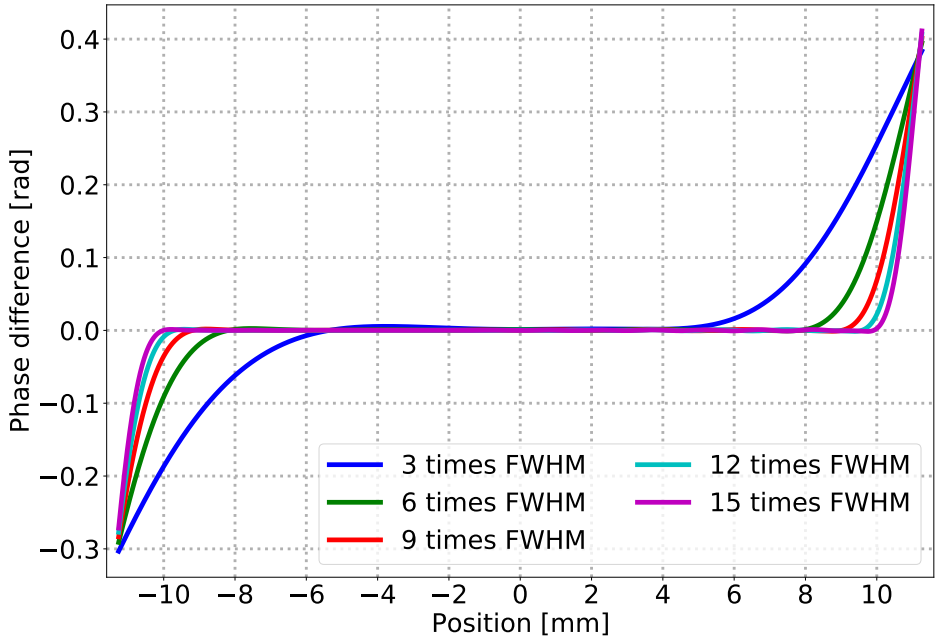

(b) Phase differences using different window widths

Figure 2.6: Top panel: (a) Intensity differences when Hamming window functions with different widths are applied. Bottom panel: (b) Phase differences when Hamming window functions with different widths are applied.

FWHM, the phase and intensity differences in the middle are almost equal to zero. Although the minimum difference obtained in the width of 15 times FWHM, it does not mean that the width of the window being as large as possible can perform better. The existence of adjacent spectrum and noise limit the width of window function. A Hanning or Hamming window with a suitable width is suggested to extract the targeted spectrum, which brings in the minimum error in the retrieval procedure.

2.6 Thermal-drift Calibration

The Doppler wind is measured by comparing phase differences, which are highly sensitive to ambient temperature around the instrument. For the 32 mm OPD offset, a thermal-induced phase shift of less than 3.2 mrad is required to achieve 3 m/s accuracy. Owing to the fact that a DASH interferometer can resolve multiple emission lines simultaneously, it is possible to use a reference line to track thermal changes to the instrument. In this section, the thermal-drift calibration is studied.

Based on Equation 2.1 and Equation 2.2, the phases of the red line emission φ_E and calibration line φ_{cal} in the zero-wind measurement (the zenith observation in the field measurement) can be expressed as

$$\begin{aligned} \varphi_E &= 2\pi \left[4\tan\theta \left(\sigma_E - \sigma_L\right) x + 2\Delta d_E \sigma_E\right] \\ \varphi_{cal} &= 2\pi \left[4\tan\theta \left(\sigma_{cal} - \sigma_L\right) x + 2\Delta d_{cal} \sigma_{cal}\right], \end{aligned} \tag{2.19}$$

where $\sigma_{E,cal}$ represent the wavenumbers of red line emission and calibration line, and $\Delta d_{E,cal}$ represent the extended values at the wavelengths of red line emission and calibration line. Assuming the ambient temperature changes in the second measurement, the corresponding phases φ'_E and φ'_{cal} are modified by

$$\begin{aligned} \varphi'_E &= 2\pi \left[4\tan\theta' \left(\sigma'_E - \sigma'_L\right) (x + \Delta x) + 2\Delta d'_E \sigma'_E + \delta d'_E \sigma'_E\right] \\ \varphi'_{cal} &= 2\pi \left[4\tan\theta' \left(\sigma_{cal} - \sigma'_L\right) (x + \Delta x) + 2\Delta d_{cal} \sigma_{cal} + \delta d_{cal} \sigma_{cal}\right]. \end{aligned} \tag{2.20}$$

Due to the Doppler shift, the wavenumber σ_E is changed to σ'_E. The thermal expansion of the grating and the thermal change of the refractive index in the field widening prism affect the Littrow angle and Littrow wavelength, so that the new Littrow angle and Littrow wavelength are denoted by θ' and σ'_L. The thermally induced OPD-offset variations are represented by $\delta d'_E$ and δd_{cal} at the wavenumbers of σ'_E and σ_{cal}, respectively. Though the interferometer is temperature controlled to minimize the phase shift, other components of the instrument are not, which may cause an image shift on the detector. This thermally induced image shift can be considered as a slight OPD

change for each pixel, which is described by the introduction of Δx in Equation 2.20. In general, the change rate of the Littrow angle is smaller than 10^{-6} radians/°C. With the precise temperature control for the interferometer, the difference between $\tan\theta$ and $\tan\theta'$ is negligible and one parameter of $\tan\theta$ is used to replace the both in the following discussion. The phase difference caused by the Doppler shift can be calculated by

$$\begin{aligned}\Delta\varphi \ =&\varphi'_E-\varphi_E-\left(\varphi'_{cal}-\varphi_{cal}\right)\\ =&2\pi\left[4\tan\theta\left(\sigma'_E-\sigma_E\right)x+2\Delta d'_E\sigma'_E-2\Delta d_E\sigma_E\right.\\ &\left.+4\tan\theta\left(\sigma'_E-\sigma_{cal}\right)\Delta x+\delta d'_E\sigma'_E-\delta d_{cal}\sigma_{cal}\right].\end{aligned} \tag{2.21}$$

Compared with Equation 2.8, the error $4\tan\theta\left(\sigma'_E-\sigma_{cal}\right)\Delta x+\delta d'_E\sigma'_E-\delta d_{cal}\sigma_{cal}$ remains. If there are ±2 °C temperature control for the optical bench and ±0.1 °C temperature control for the interferometer, the error resulting from image shift is less than 1m/s (*Englert et al.*, 2017a). In addition, the difference of σ'_E and σ_{cal} is only 11.3 cm^{-1} and the typical variation of optical offset ($\delta d'_E$ or δd_{cal}) is less than 10^{-5} cm/°C. With the thermal compensation design and the temperature control, the term of $4\tan\theta\left(\sigma'_E-\sigma_{cal}\right)\Delta x+\delta d'_E\sigma'_E-\delta d_{cal}\sigma_{cal}$ can be neglected. Accordingly, the obtained phase difference can be used to retrieve the wind velocity using Equation 2.10.

The thermally induced image shift is possible to be tracked by periodic notches on the top of grating (*Englert et al.*, 2010b, 2017a). The notch pattern is imaged on the detector along with the produced interferogram, so that the image shift can be obtained by monitoring the position change of the notch pattern. Using the quantification of the image shift, Δx in Equation 2.20 can be corrected and it will change to

$$\begin{aligned}\varphi'_E&=2\pi\left[4\tan\theta'\left(\sigma'_E-\sigma'_L\right)x+2\Delta d'_E\sigma'_E+\delta d'_E\sigma'_E\right]\\ \varphi'_{cal}&=2\pi\left[4\tan\theta'\left(\sigma_{cal}-\sigma'_L\right)x+2\Delta d_{cal}\sigma_{cal}+\delta d_{cal}\sigma_{cal}\right].\end{aligned} \tag{2.22}$$

Using the intercepts of φ_{cal} and φ'_{cal}, the phase shift $\delta d_{cal}\sigma_{cal}$ can be determined. Neglecting the dispersion effect, the phase shift $\delta d'_E\sigma'_E$ can be obtained by

$$\delta d'_E\sigma'_E=\frac{\delta d_{cal}\sigma_{cal}}{\sigma_{cal}}\sigma_E. \tag{2.23}$$

Combining the results of Equation 2.19, Equation 2.22 and Equation 2.23, the calibrated phase difference can be expressed as

$$\Delta\varphi \ =\varphi'_E-\varphi_E-\left(\varphi'_{cal}-\varphi_{cal}\right)+\delta d_{cal}\sigma_{cal}-\delta d'_E\sigma'_E. \tag{2.24}$$

Accordingly, the wind velocity can be determined by the relation of Equation 2.10.

Chapter 3

Instrument Response

The signal propagation is accompanied by uncertainties, which may impact on the measurement accuracy of a DASH instrument. In this chapter, the systemic input-output-response is investigated including the estimation of the detected signal, noise propagation, characterization of detector and analysis of signal-to-noise ratio. Spectral radiance of airglow emission can be modeled for a specific solar activity and solar local time. With the knowledge of the field of view, aperture and transmittance of instrument, the signal detected in a DASH instrument can be estimated. The noise propagation is described in the detection of airglow emission, and its main compositions are the photon-limit noise and detector readout noise. The performance of the selected image sensor is characterized by a series of tests involving dark current measurements and photon transfer measurements. To evaluate the instrument responsivity and noise effect, the detected interferograms are simulated based on the results of the characterization of detector, and the corresponding signal-to-noise ratios are also analyzed.

3.1 Estimation of Detected Signal

The low intensity of the atomic oxygen red line emission requires a high responsivity of the instrument. The detected signal is a crucial factor to determine the instrument responsivity, and the estimation of the received signal provides a baseline to determine the system aperture and field of view. As discussed in Section 1.3, the atomic oxygen red line emission is modeled given the date and solar activity. Based on the knowledge of airglow VER and instrument characteristics, the incoming photons can be estimated, which is significant to evaluate an instrument signal-to-noise ratio (SNR). For an isotropic source, the emission rate from an unit column along the line of sight is equal to $4\pi L_\gamma$ (*Hunten et al.*, 1956), where L_γ is the spectral radiance. Therefore, the spectral

radiance L_γ of the airglow can be calculated from the integration along the line of sight s

$$L_\gamma = \frac{\int_s \varepsilon(l)\, dl}{4\pi}, \tag{3.1}$$

where $\varepsilon(l)$ is the VER at position l. Assuming the radiation within the field of view is uniform, the photon flux Φ_γ on the aperture S can be expressed as

$$\Phi_\gamma = T_a L_\gamma \iint dS \cos\zeta\, d\Omega = T_a L_\gamma E, \tag{3.2}$$

where T_a represents the transmittance of the atmosphere, ζ is the inclined angle with respect to dS and E is the etendue of the instrument, which is defined to evaluate the flux gathering capability of an optical system. The etendue with a crossing area S can be calculated by $E = \iint dS\cos\zeta\, d\Omega = \pi S NA^2$, where NA is the numerical aperture of system. In an optical system, the etendue is a conserved parameter, so that the received photoelectrons n_{e_γ} on the detector is estimated

$$n_{e_\gamma} = Q_E t_{int} T_a T_f T_o L_\gamma E. \tag{3.3}$$

Here Q_E is the quantum efficiency of the detector, t_{int} is the exposure time, T_f and T_o are the transmittance of the filter and optics, respectively. Combining Equation 2.1 and Equation 3.3, the signal recorded on the detector yields

$$I(n_x) = \frac{n_{e_\gamma}}{2N}\left\{r_b + 1 + V_I(\sigma_0, n_x s_p)\cos\left[2\pi\left(f n_x s_p + 2\sigma_0 \Delta d_0\right)\right]\exp -2\pi^2 P_D^2 L^2\right\}, \tag{3.4}$$

with $L = D + 4\tan\theta n_x s_p$. Here N denotes the pixel number of the detector, $V_I(\sigma_0, n_x s_p)$ denotes the instrument visibility function, n_x denotes the pixel index in x direction, s_p denotes the pixel size, f denotes the spatial frequency of the interferogram, σ_0 denotes the wavenumber of the emission line, Δd_0 denotes the extended distance, D denotes the effective OPD, P_D denotes a Doppler-broadening parameter and θ denotes the Littrow angle of the grating. Within the transmission curve of the filter, spectra except the targeted emission line decrease the visibility of the fringe pattern, and this effect is described by r_b, which is a ratio of background spectra to the targeted emission line. Note that r_b is determined by the characteristic of the filter and atmospheric spectra.

3.2 Noise Propagation

Noise plays an important role in the detection of airglow emission, which is a photon-limited signal. The noise propagation based on a complementary metal-oxide-semiconductor (CMOS) detector is discussed in the following.

Shot noise occurs when photons arrive due to the uncertainty principle, and this process follows a Poisson distribution. In addition, another contribution to shot noise comes from the electrons spontaneously generated within the silicon chip even when no photons reach the detector, which is called detector dark current. Therefore, the variance of the shot noise σ_s^2 is equal to the mean signal, which consists of the photoelectons $\bar{n}_{e_\gamma}$ and dark current $\bar{n}_{e_d}$. Accordingly,

$$\sigma_s^2 = \bar{n}_{e_\gamma} + \bar{n}_{e_d}. \tag{3.5}$$

Except for the shot noise, the readout noise and the fixed pattern noise (FPN) are also noticeable, and they are Gaussian noise. The FPN describes the pixel-to-pixel variation under uniform illumination, which consists of signal offset and gain components. For CMOS sensors, the FPN usually can be corrected by adjusting the pixel gain on the whole detector. For the low-signal application, the FPN can be neglected. Therefore, the variance of the detector noise σ_{noise}^2 can be expressed as

$$\sigma_{noise}^2 = G^2\sigma_s^2 + \sigma_r^2, \tag{3.6}$$

where G is the system gain describing the conversion ratio from an electron number into a digital number (counts) and σ_r^2 represents the variance of the readout noise. Consequently, the SNR in the detector can be calculated by

$$SNR = \frac{G\bar{n}_{e_\gamma}}{\sqrt{G^2\sigma_s^2 + \sigma_r^2}}. \tag{3.7}$$

If background spectra with the ratio of r_b are considered, the SNR needs to be modified to

$$SNR = \frac{G\bar{n}_{e_\gamma}}{\sqrt{G^2\sigma_s^2 + \sigma_r^2 + Gr_b\bar{n}_{e_\gamma}}}. \tag{3.8}$$

3.3 Characterization of Detector

3.3.1 Overview of Image sensor

The performance of the detector affects the SNR of the signal obtained, which is an important factor to affect the measurement accuracy. A scientific CMOS image sensor, GSENS400BSI, is selected to record the fringe pattern owing to its relatively low noise levels and high quantum efficiency. This CMOS sensor can operate in both rolling shutter HDR (high dynamic range) and rolling shutter STD (standard dynamic range) modes, and a high-pixel gain and a low-pixel gain are available in STD mode, which are named STD-HG mode and STD-LG mode (*Gpixel Inc.*, 2017). According to our application requirement, the detector operates in STD-HG mode, which is optimized for low readout noise. The specification of the detector running in STD-HG mode is shown in Table 3.1, which is provided from the manufacturer (*Gpixel Inc.*, 2017). The pixel number of the detector is 2048 $\times$ 2048 with a pixel size of 11 μm, and the maximum active image size achieves 22.528 mm $\times$ 22.528 mm. The sensor operates in electronic rolling shutter and features extremely low temporal dark noise and readout noise. The quantum efficiency of the sensor is higher than 90% at the wavelength of 630.0 nm.

Table 3.1: Specification of GSENSE400BSI sensor running in STD-HG

Item	Description
Resolution	2048 horizontal $\times$ 2048 vertical pixels
Pixel size	11 μm $\times$ 11 μm
Active area	22.528 mm $\times$ 22.528 mm
Readout noise	1.6 e^-
Dark current	0.52 e^-/s/pixel at -16 °C
Gain	1.938 counts/e^-
Quantum efficiency	> 90% @ 630 nm
Shutter type	Electronic rolling shutter

3.3.2 Dark Current Measurements

The dark current measurements were performed in a dark room with the temperature control for the GSENSE400BSI device. Owing to the fact that the dark current is linearly related to the exposure time, the dark current was recorded during different exposure times. The tests were taken at exposure times from 0.25 seconds to 4 seconds with an

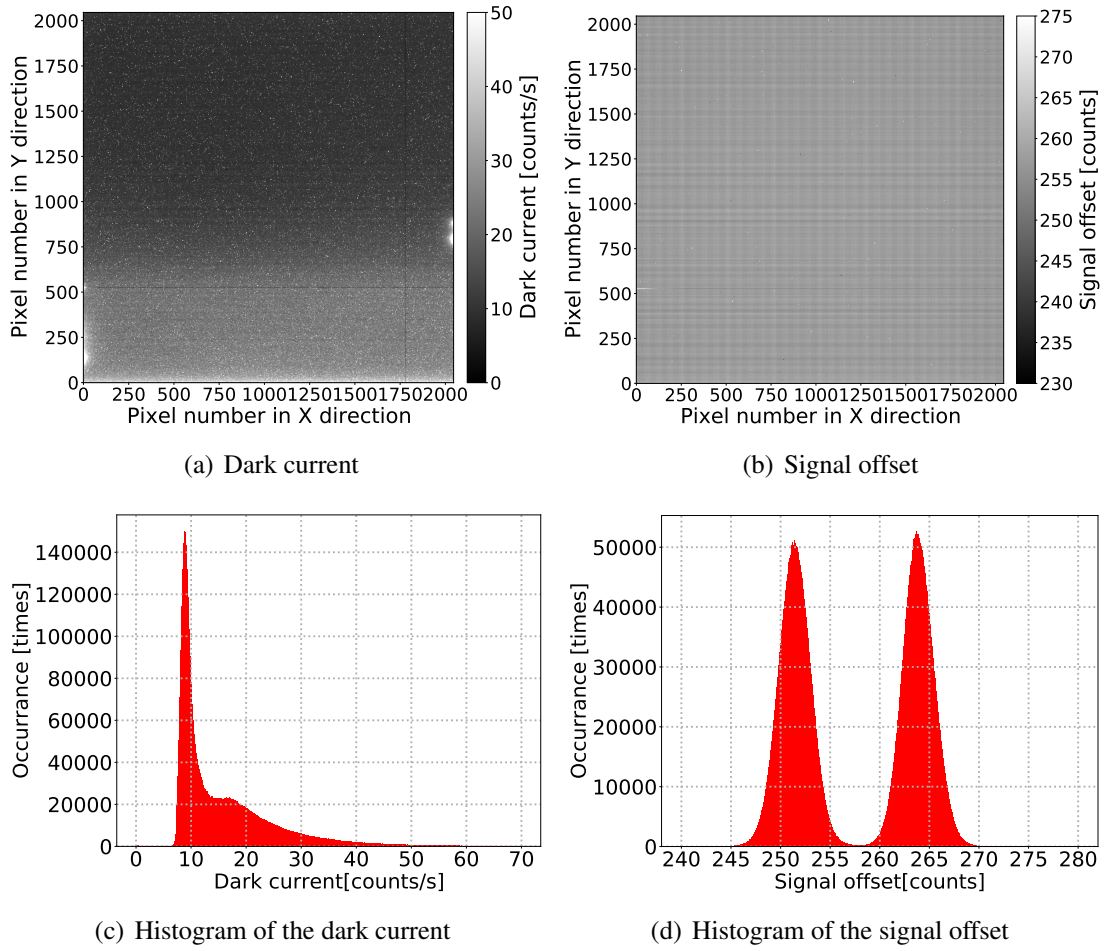

(a) Dark current

(b) Signal offset

(c) Histogram of the dark current

(d) Histogram of the signal offset

Figure 3.1: Upper plots: (a) Measured dark current and (b) signal offset at a temperature of 19.5 °C. Lower plots: (c) Histograms of the dark current and (d) signal offset at a temperature of 19.5 °C.

interval of 0.5 seconds. For each exposure time, 20 frames images were sampled, which can be used to calculate the mean value and standard deviation. Although the signal offset is always accompanied by the acquisition of the dark current, a linear regression of the obtained signal against the exposure time gives the signal offset (intercept). The temperature dependencies of the dark current and signal offset were also characterized by repeating the previous processes during different temperatures.

The mean value of the samples for each pixel as a function of the exposure time was calculated, then fitting a linear line to the mean values yields the dark current (slope) and signal offset (intercept). Taking an example at the temperature of 19.5 °C, the dark current and signal offset are displayed in Figure 3.1. The dark current and digital

offset vary with the position. The enhanced dark current is probably caused by the mechanical stress or the higher temperature of the read out circuit. Two peaks appear on the histogram of signal offset, which is the result of two separate programmable-gain amplifiers for odd lines and even lines. In order to remove the effects from hot pixels and defect pixels, a median dark current of all pixels is used to represent the dark current of whole detector. The detector dark current at temperatures of 13.5 °C, 16.5 °C and 19.5 °C were measured, and the results are plotted in Figure 3.2. Accordingly, the detector dark current at temperatures of 13.5 °C, 16.5 °C and 19.5 °C are 7 counts per second, 8 counts per second and 11 counts per second, respectively. The signal offsets for the three temperatures are almost same and the value is 261 counts. With the increase of the temperature, the detector dark current increases. Therefore, it is necessary to cool down the detector to further suppress the effect from dark current during instrument measurement.

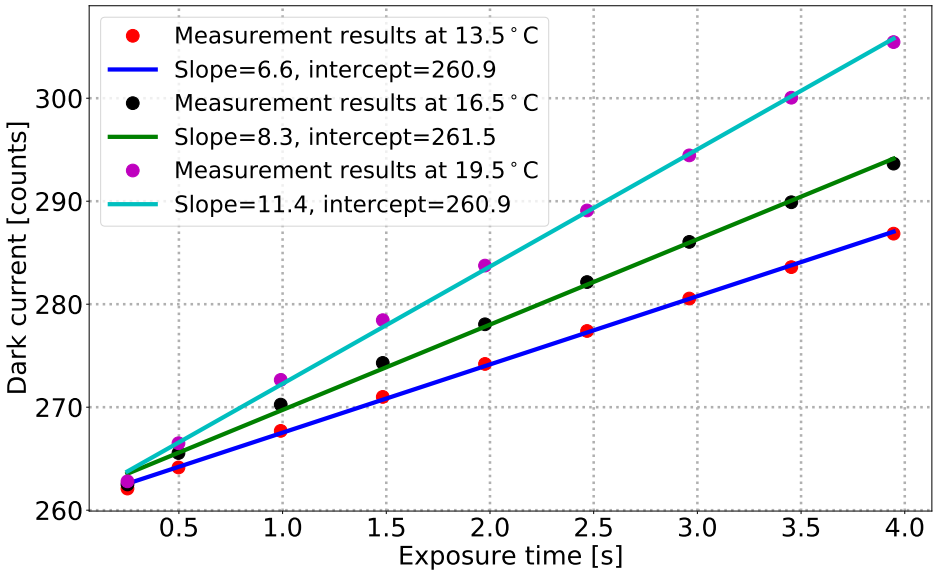

Figure 3.2: Comparison of dark current at the temperatures of 13.5 °C, 16.5 °C and 19.5 °C.

Similarly, the standard deviation of the samples for each pixel as a function of the exposure time was calculated, and the value of the standard deviation can be used to describe the noise. The readout noise can be estimated by fitting a linear function to the standard deviations. During the dark current measurements, the contribution of the noise only includes dark current noise and readout noise, so that the intercept of fitting results can be considered as the readout noise. Based on the measurements at temperatures of 13.5 °C, 16.5 °C and 19.5 °C, the dark current standard deviations were calculated and the results are shown in Figure 3.3(a). Note that a median standard deviation is used to

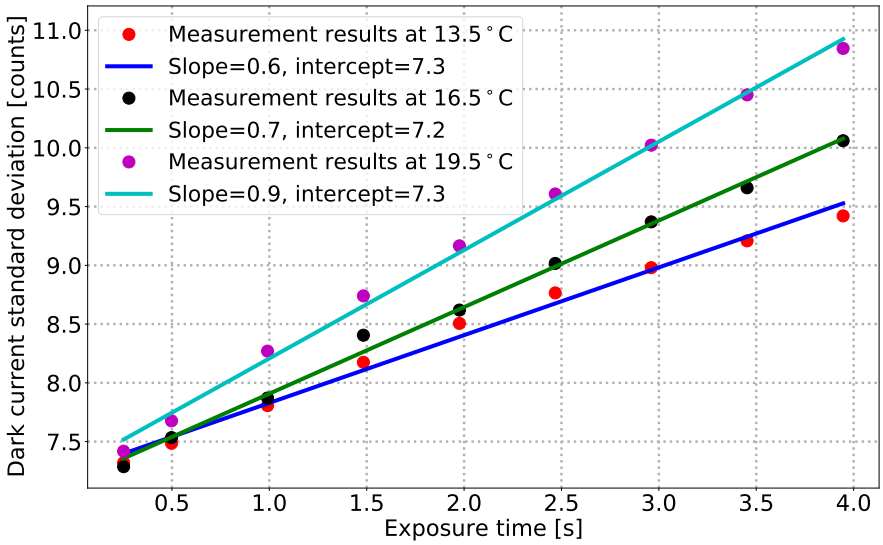

(a) Estimated dark current standard deviations

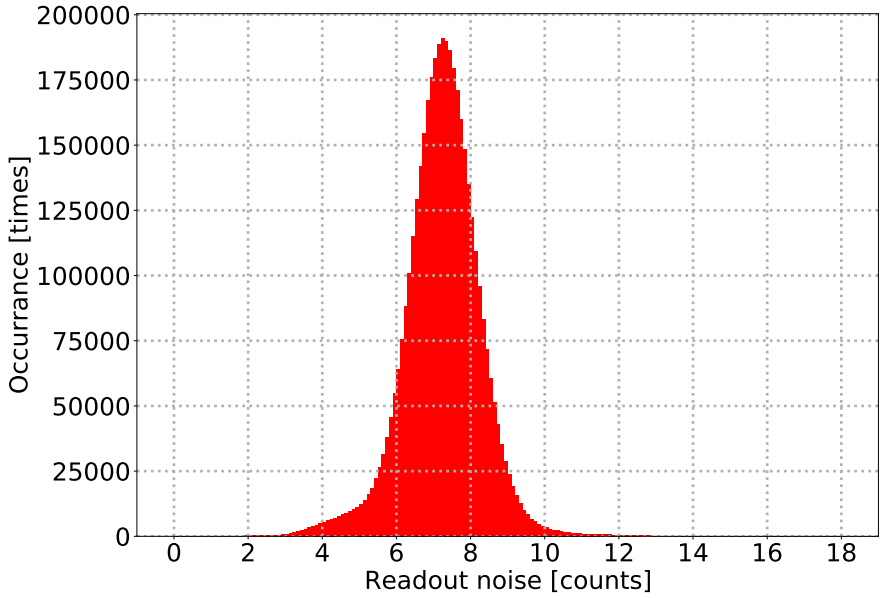

(b) Histogram of the readout noise

Figure 3.3: (a) Estimated dark current standard deviations during different temperatures and (b) distribution of the readout noise. In the upper plot, each measured point is the median dark current standard deviation of all pixels.

represent the standard deviation of whole detector here. Accordingly, the readout noise was estimated and the corresponding value is about 7 counts. The readout distribution is also presented in Figure 3.3(b), which indicates that the spatial variation of the readout noise is small.

3.3.3 Photon-Transfer Curve

Tho photon-transfer curve (PTC) described by Janesick (*Janesick et al.*, 1987) is a general method to determine the detector readout noise and system gain. The detector system gain is a parameter to describe the conversion rate between electron (e^-) and digital number. PTC method is based on the property of shot noise, which can be modeled by a Poisson distribution. As discussed in Section 3.2, the variance of the shot noise is equivalent to the mean value of signal. Therefore, the variance of the signal noise $\sigma^2_{noise,DN}$ in units of counts^2 can be expressed as

$$\sigma^2_{noise,DN} = G^2\sigma^2_{s,e^-} + \sigma^2_{r,DN} = G\left(\bar{S}_{DN} - \bar{S}_{SO}\right) + \sigma^2_{r,DN}, \tag{3.9}$$

where G denotes the system gain in units of counts/e^-, σ_{s,e^-} denotes the shot noise in units of e^-, $\sigma_{r,DN}$ denotes the readout noise in units of counts, $\bar{S}_{DN}$ denotes the mean signal in units of counts and the $\bar{S}_{SO}$ denotes the signal offset in units of counts. Consequently, a linear regression of $\sigma^2_{noise,DN}$ against the difference between $\bar{S}_{DN}$ and $\bar{S}_{SO}$ gives the system gain G (slope) and the variance of the readout noise $\sigma^2_{r,DN}$ (intercept).

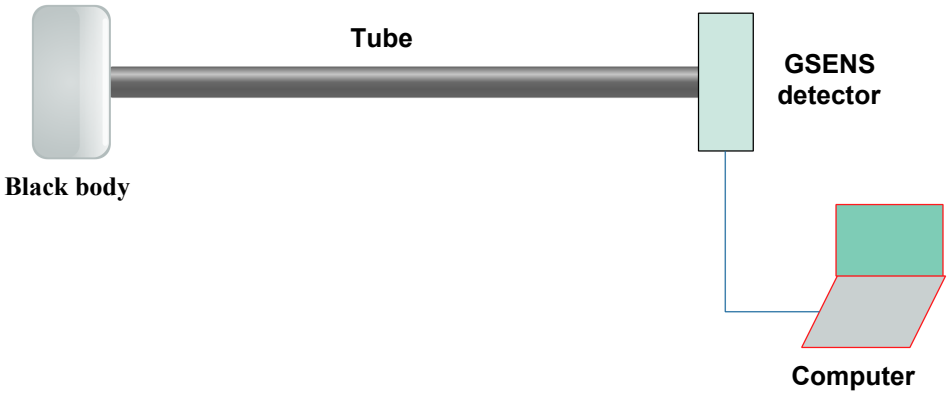

Figure 3.4: Experimental setup for the measurement of photon transfer.

The experimental setup for photon transfer measurement is illustrated in Figure 3.4. The signal source is provided by a black body, and the input signal can be tuned by changing the temperature of the black body. A long tube is applied here as a baffle and

defines the incident solid angle. A bandpass filter is inserted in front of the detector to limit the incoming spectrum. Finally, a computer is used to control the detector and to record data. For each black-body temperature, 20 frames were recorded, and then the mean value and standard deviation of those images were calculated for further analysis.

For each pixel and each black body temperature, the signal mean and signal variance were determined. Then the median values of signal means and signal variances were calculated to represent the signal mean and signal variance at this black body temperature. The signal variance as a function of signal mean is presented in Figure 3.5(a), which indicates that the average system gain of detector is 1.3 counts/e^- and the readout noise is 8 counts similar to the result in dark current measurement. Using the estimated system gain, the readout noise can be converted to 6.2 e^-, which is more than three times larger than the value in the manufacturing specification. As shown in Figure 3.5(b), the distribution of the estimated system gain was also obtained using the linear regression analysis. Although the system gain should be positive, some negative gains appear in the estimation, which may be caused by the hot pixels and defect pixels.

According to Planck's law, the spectral radiance can be calculated. Combining the transmittance of the bandpass filter $T_f(\lambda)$ and the system etendue E, the input signal $I(T)$ as a function of black body temperature T can be estimated using the relation

$$I(T) = \frac{Q_E G t_{int} E}{U_e} \int_{-\infty}^{+\infty} \frac{2hc^2}{\lambda^5} \frac{1}{\exp\left(\frac{hc}{\lambda k_B T}\right) - 1} T_f(\lambda)\, d\lambda, \tag{3.10}$$

where Q_E represents the quantum efficiency of detector, G represents the system gain of detector, t_{int} represents the exposure time of detector, U_e represents the energy of one electron and its value is 1.602×10^{-19} J, c is the speed of light, h is Planck's constant and k_B is Boltzmann's constant.

The measured signal as a function of estimated signal is shown in Figure 3.6, and the measured signal information is provided from the median of all pixels and the values at three different pixels. The estimated system gain G =1.3 counts/e^- is applied to calculate the estimated signal. The fitting result with the slopes approximated to 1.0 indicates that the estimated values are in good agreement with the measured values and the quantum efficiency from manufacturer agrees with the measurement results. The difference of the intercepts results from the variation of the signal offset, which is indicated in Figure 3.1.

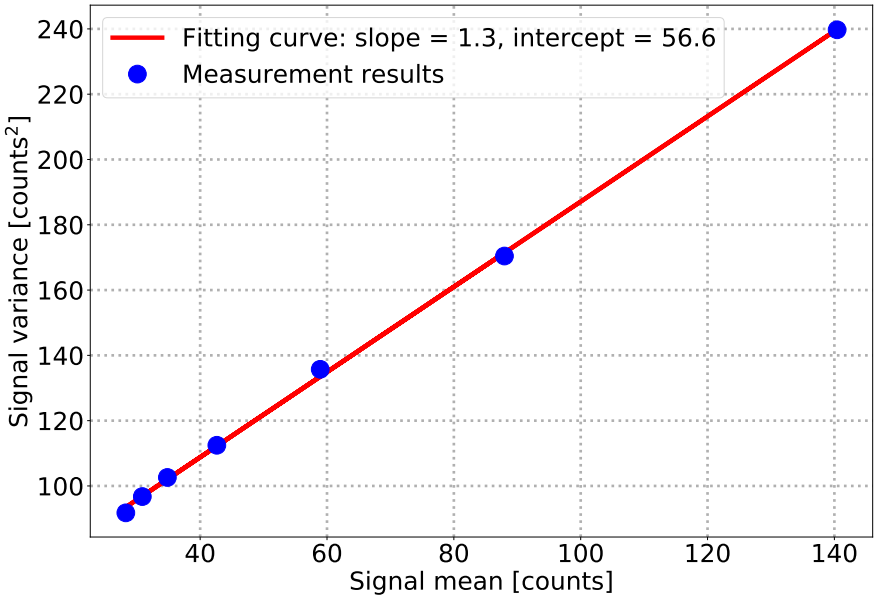

(a) Photon transfer curve

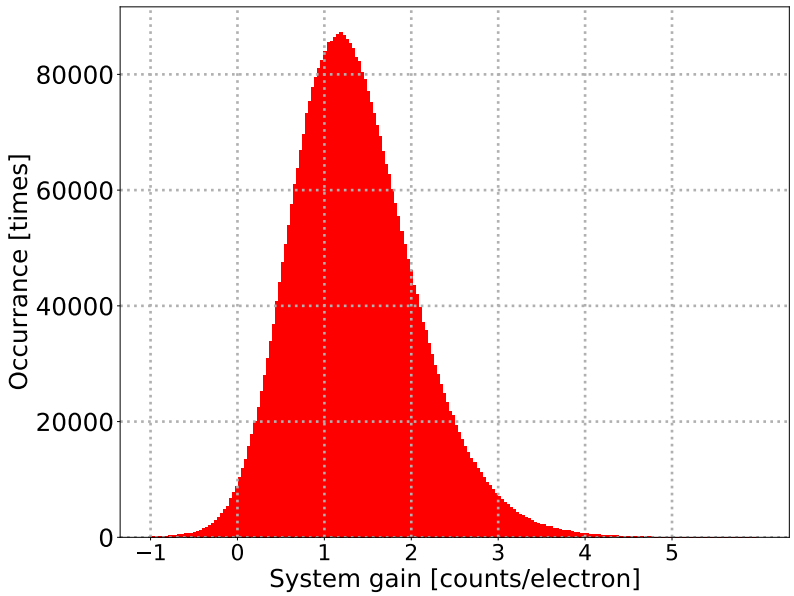

(b) Histogram of the estimated system gain

Figure 3.5: (a) Photon transfer curve and (b) histogram of the estimated system gain. The black body temperatures are from 400°C to 500°C with an interval of 20°C, and one dark current measurement with a same exposure time is also included. Note that the signal offsets are subtracted when calculating the signal mean using the estimated result in Section 3.3.2.

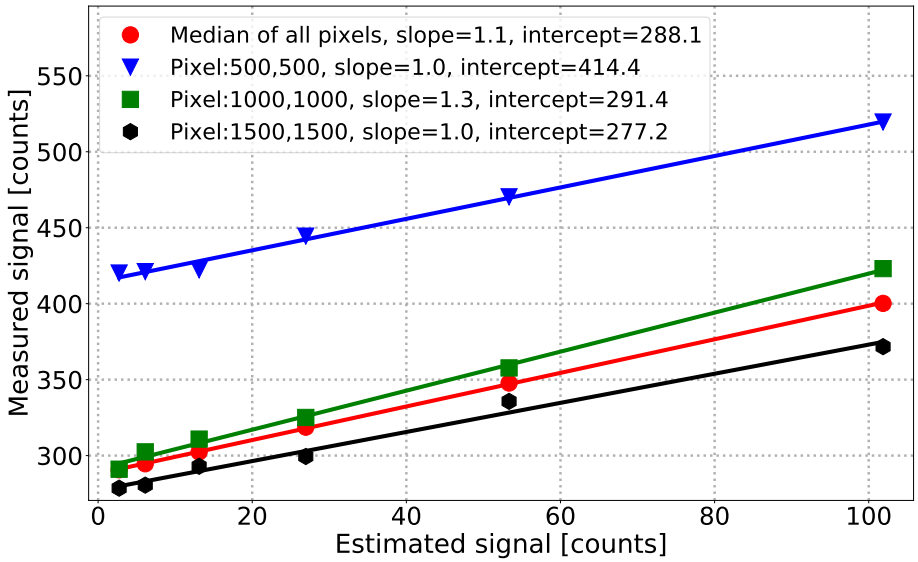

Figure 3.6: Measured signal as a function of estimated signal. The quantum efficiency and transmittance of filter are provided from the manufacturer. Note that black body temperatures from 400°C to 500°C with an interval of 20°C and the average of 20 samples are used for analysis.

3.4 Analysis of Signal to Noise Ratio

In this section, the interferograms obtained from a DASH interferometer are simulated using the established model described in Section 2. According to the estimated signal and the characterization of the detector, the signal noise is added into the interferograms. Based on the simulated interferograms, the SNRs of the instrument operating at different dates are investigated using Equation 3.8.

As discussed in Section 1.3, the atmospheric emission varies with the solar activity and seasonal change. Here, we choose the two years of 2009 and 2014 when the lowest solar activity and the strongest solar activity appear in a recent solar cycle, and observations are simulated for Wuppertal (51.26°N, 7.15°E). Since the intensity of airglow emission reaches a peak in summer and has a minimum in winter, interferograms simulated for Jun 21 and Dec 22 with the local solar time at midnight are discussed. Combining the atmospheric model and Equation 3.2, detected signals were calculated. Then the dark current, shot noise and readout noise were added to the simulated interferograms. The parameters of the interferometer and the detector used in simulation are shown in Table 3.2. The ratio of the background spectra is determined by atmospheric spectra and the feature of the bandpass filter. Transmittances of the filter, beamsplitter, diffraction grating and other optics are considered, and the overall effect is represented

Table 3.2: Parameters of interferometer and detector used in simulation

Parameters of interferometer	Description
Littrow angle	16.4950°
Groove density of grating	900 mm^{-1}
Incident wavelength	630.0304 nm
Full field of view	9°
Temperature of atomic oxygen in thermosphere	1000 K
Optical path difference at center $2\Delta d_0$	32 mm
Visibility	1.0
Background spectrum ratio	0.492
Transmittance of optics	0.315
Parameters of detector	**Description**
Pixel number	2048×2048
Pixel size	$11\ \mu m \times 11\ \mu m$
Readout noise	7.2 counts
Dark current	0.52 e^-/s/pixel
System gain	1.3 counts/e^-
Quantum efficiency	0.92
Exposure time	5 mins

by the transmittance of optics in Table 3.2. The parameters of the detector are obtained from the result in Section 3.3.

The simulated interferograms are presented in Figure 3.7 and Figure 3.9, and their corresponding SNRs are plotted in Figure 3.8 and Figure 3.10. In order to improve the instrument SNR, an average of several rows signals is used for the retrieval routine. Figure 3.7 and Figure 3.8 are the results using the average of 300 rows signals, and the results using the average of 1000 rows signals are shown in Figure 3.9 and Figure 3.10. As shown in these figures, envelopes of the interferograms and SNRs are estimated by the sum of the amplitude and direct current (DC) bias. The elevation angle of the instrument is 45° in these simulations. In the same year, the SNRs on Jun 21 are almost three times of the SNRs on Dec 22 because of the stronger emission intensity in summer. In the year with strong solar activity (2014), the SNRs become higher compared to the SNRs in the year of 2009. With the decrease of the fringe contrast, the SNR declines, which means that the visibility of interferogram affects the system SNR. Comparing the

results in Figure 3.8 and Figure 3.10, it shows that using the average of more rows of signals can improve the instrument SNR. During winter measurements even in the year with strong solar activities, the average of more lines of signals or an extension of the exposure time must to be used to improve the instrument responsivity and accuracy.

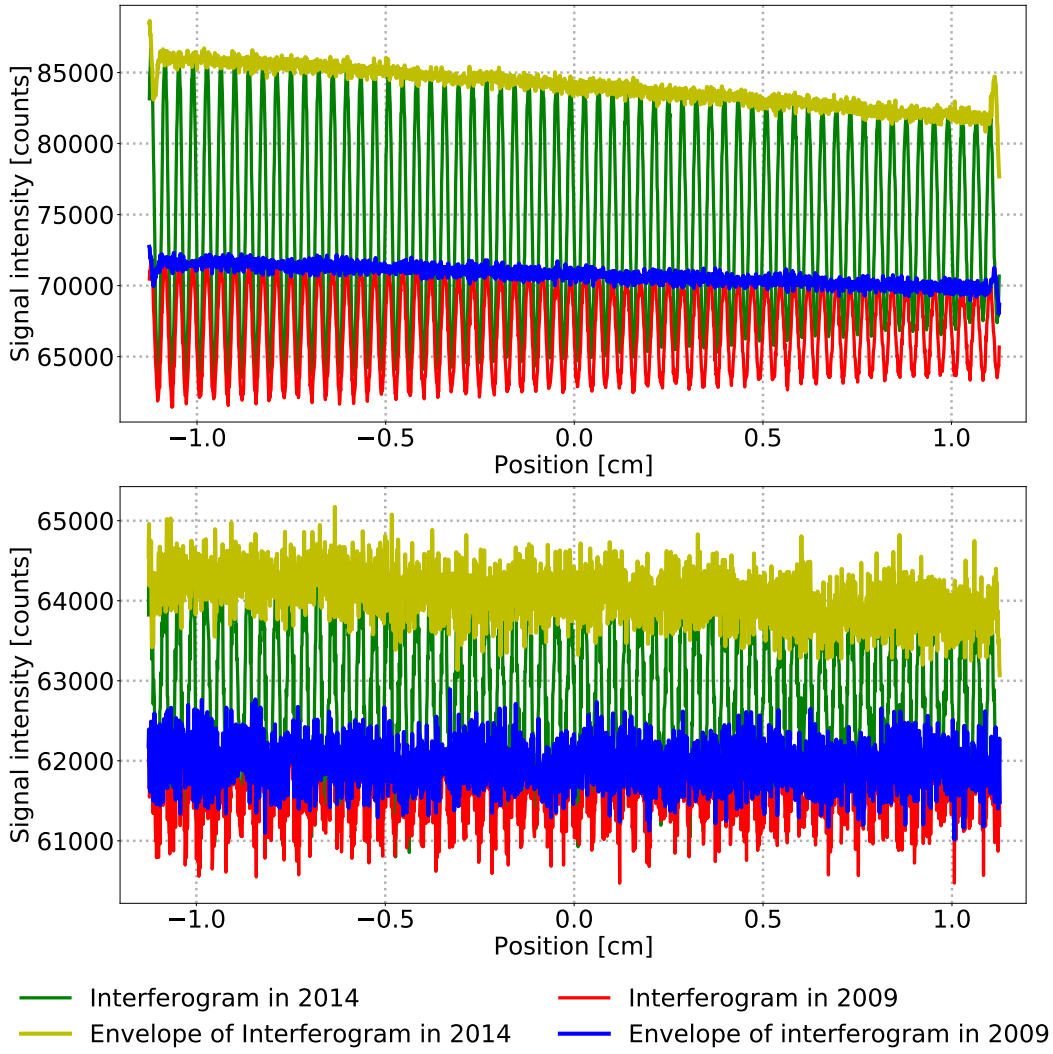

Figure 3.7: Simulated interferograms using the average of 300 rows signals. Upper panel: Interferograms simulated for the date of Jun 21 and their corresponding envelopes. Bottom panel: Interferograms simulated for the date of Dec 22 and their corresponding envelopes.

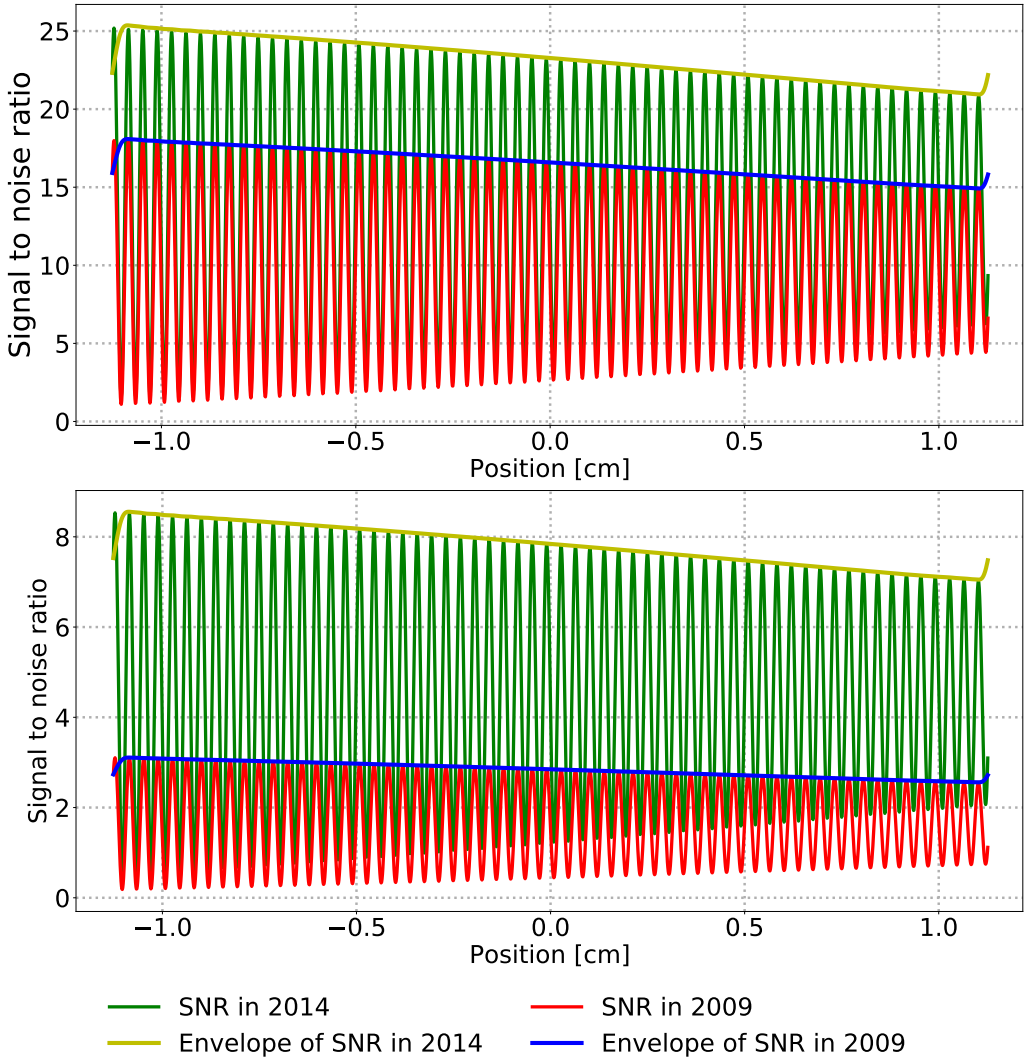

Figure 3.8: SNRs of the interferograms in Figure 3.7. Upper panel: SNRs of the interferograms simulated for the date of Jun 21 and their corresponding envelopes. Bottom panel: SNRs of the interferograms simulated for the date of Dec 22 and their corresponding envelopes.

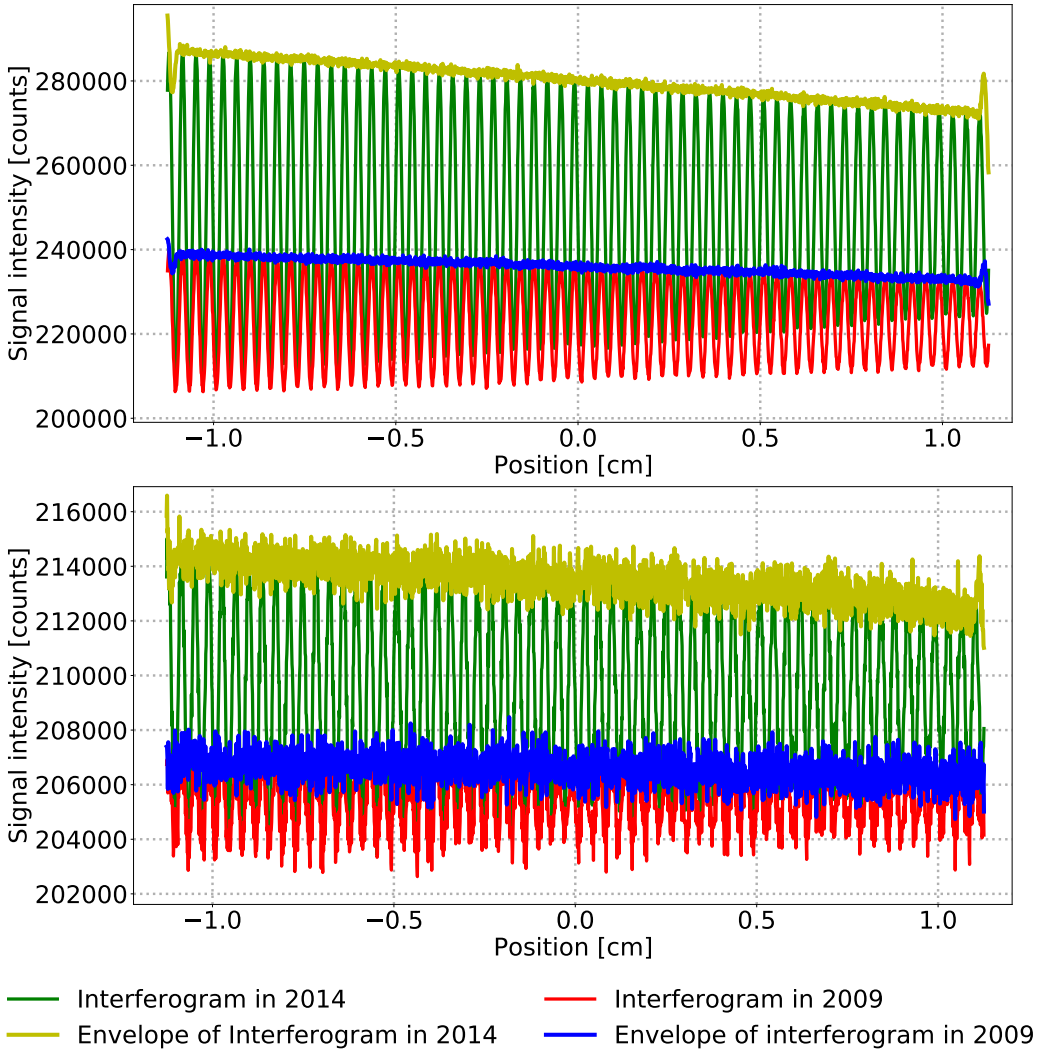

Figure 3.9: Simulated interferograms using the average of 1000 rows signals. Upper panel: Interferograms simulated for the date of Jun 21 and their corresponding envelopes. Bottom panel: Interferograms simulated for the date of Dec 22 and their corresponding envelopes.

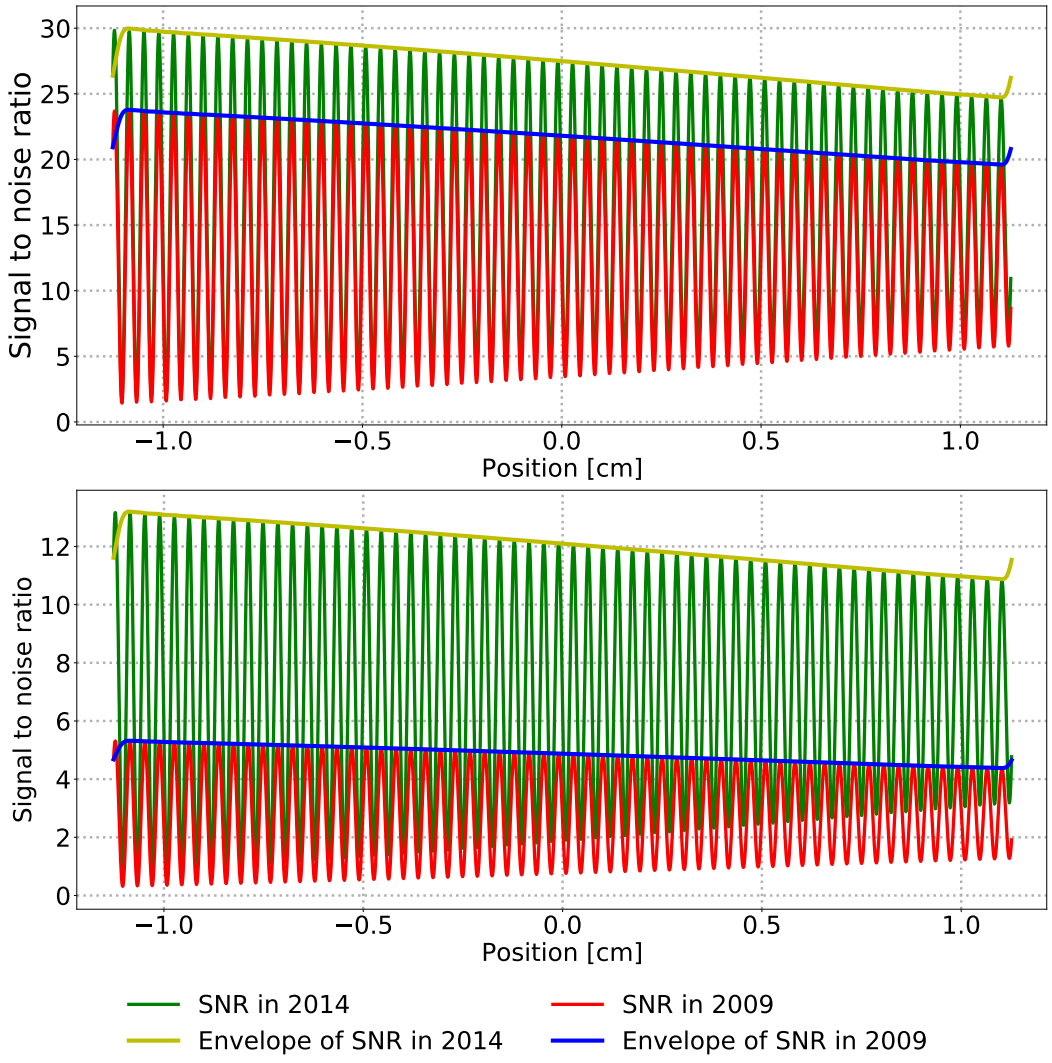

Figure 3.10: SNRs of the interferograms in Figure 3.9. Upper panel: SNRs of the interferograms simulated for the date of Jun 21 and their corresponding envelopes. Bottom panel: SNRs of the interferograms simulated for the date of Dec 22 and their corresponding envelopes.

Chapter 4

Instrument Design

A DASH instrument consists of an interferometer and a camera optics, which images the fringe pattern from the localization plane onto the detector. This chapter discusses the optical designs of a thermally stable DASH interferometer with field-widening prisms and a double-telecentric imaging system. As important parameters of a DASH interferomter, the Littrow wavelength, optical offset, materials and dimensions of components are optimized to achieve thermal compensation and field widening. In order to relay the fringe pattern with high fringe contrasts, a double-telecentric system is selected to realize the high-image-quality and low-distortion imaging process. The thermal analysis and tolerance analysis are also presented in this chapter. The visibility of fringe pattern determines the ability of interferometer to detect periodic signal in the presence of noise. Using ray-tracing software, interferograms obtained from the designed configuration are simulated and the corresponding visibilities are also analyzed. In addition, an instrument performance model is established using the tolerance analysis results, and measurement uncertainties of the instrument during different seasons are also studied in this chapter.

4.1 DASH Interferometer Design

A monolithic DASH interferometer has an advantage over the separate design, especially in the stray light management. A monolithic interferometer can be built to be highly compact and rugged, which is required for the space application. The following discussion of the DASH interferometer is based on a monolithic design.

4.1.1 Components

A monolithic interferometer generally consists of an nonpolarizing cube beamsplitter with a 50% split ratio, two field-widening prisms, two reflective diffraction gratings and spacers which are used to connect the field-widening prism with the beamsplitter and the grating. In order to simplify the assembly, the exit plane of the field-widening prism is designed to be parallel to the incidence plane of the grating. Accordingly, the spacers bonding the field-widening prisms and the gratings are parallel prisms, which are also called parallel spacers. As discussed in Section 2.1, the diffraction gratings, producing two tilted wavefronts, are the crucial elements in a DASH instrument. The resolving power of the system depends on the grating groove density and effective area. Gratings with 900 grooves/mm are chosen here, which have a high diffraction efficiency at the targeted wavelength and satisfy the resolution requirement. More details of the gratings are described in Appendix B.1. In general, there are two strategies to achieve the asymmetric arm. One is to use different field-widening prisms on two arms, another one is to use an asymmetric beamsplitter as shown in Figure 4.4. For cost consideration, the second design is chosen for the DASH interferometer presented in this dissertation.

4.1.2 Choice of Littrow Wavelength

In a DASH system, the Littrow wavelength of the grating is an important parameter, which determines the spatial frequency of the fringes. A reasonable spatial frequency setting is necessary to obtain the precise wind velocity. The spatial frequency is limited by the Nyquist frequency, which is determined by the detector pixel size. Even fringes can be resolved by the certain-pixel-size detector, the spatial frequency still can not be too high. A high spatial frequency makes the samping rate very low in one period, which causes the phase of the fringe is sensitive to the thermal change or system vibration. On the other hand, it is also not a good choice if the spatial frequency is too low. The low spatial frequency increases the risk of aliasing with the DC bias and low frequency components induced by the non-uniformity of light field distribution. The limited pixel number constrains the minimum spatial frequency. In general, some dozens of samplings in one completed signal period is a reasonable setting. As discussed in Section 2.6, thermal drifts have to be tracked using an artificial line during measurements. A combination of a neon lamp and a bandpass filter provides a stable-frequency illumination at a wavelength of 630.479 nm, which can be used to track thermal drifts. The spectrum of the neon lamp is presented in Appendix B.2. For the consideration to isolate the spectra of the airglow emission and calibration source, the difference of the fringe number should be larger than 20. Accordingly, the Littrow wavelength range can be determined given a detector, a groove density of grating and working wavelengths.

In order to obtain the targeted spectrum and to improve the system SNR, an optical bandpass filter with an FWHM of 2.3 nm is employed in the DASH interferometer. More details on this filter are presented in Appendix B.3. According to Equation 2.1 and Equation 2.2, an indistinguishable aliasing occurs when incident wavenumbers are symmetric about the Littrow wavenumber, although their phases are different. In general, the Littrow wavelength should be located on the edge of the transmission curve of the filter to suppress the indistinguishable aliasing.

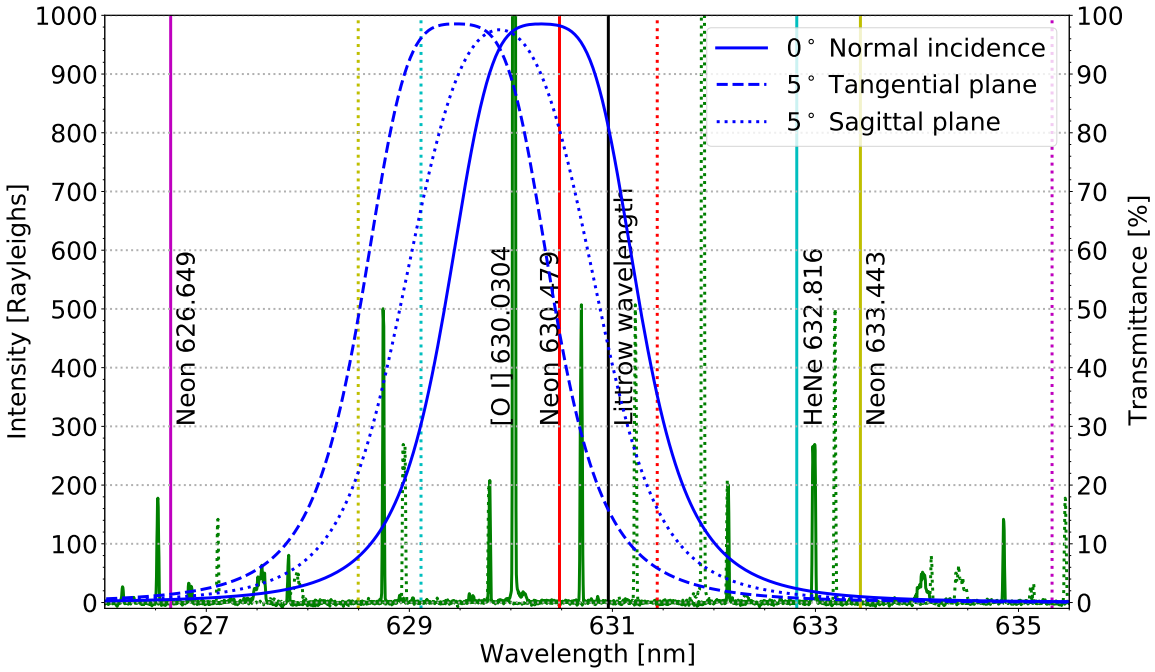

Figure 4.1: Spectra of the observed emissions (green) and transmission curves of the optical bandpass filter (blue). The tangential plane contains both the optical axis and the object point, and the sagittial plane is perpendicular to the tangential plane. The spectrum of the neon lamp close to 630.479 nm and He-Ne laser line are also included here. The black line is the Littrow wavelength and the dashed lines are the aliasing spectra with respect to the Littrow wavelength.

The Littrow wavelength of 630.96 nm is determined in our design and corresponding spatial frequencies are 27.70 per centimeter for the atomic oxygen red line and 14.32 per centimeter for calibration lamp (630.479 nm), respectively. For a 2048×2048 detector with 11-μm pixel size, the fringe number difference is 26.8 for the two incident wavelengths. Note that the magnification of camera optics is 1.0 in this discussion. In order to verify the rationality of this Littrow wavelength, spectra of the observed emissions and the transmission curve of the bandpass filter as functions of wavelength are

plotted in Figure 4.1. The spectrum data are obtained from the Ultraviolet and Visual Echelle Spectrograph (UVES) (*Hanuschik*, 2003). In addition, aliasing spectra, calculated from the symmetries of the original spectrum, are also shown in this figure. Although the Littrow wavelength is not at the edge of the transmission curve, all of the emission lines can be well separated and the aliasing does not happen within the curve of transmission. The combination of the neon lamp and this bandpass filter can achieve the calibration purpose that only one line (630.479 nm) emitted from lamp can pass the filter and there is no aliasing with other existing spectra. Therefore, the Littrow wavelength of 630.96 nm is a scientific choice.

4.1.3 Choice of OPD Offset

As discussed in Appendix A and Section 2.1, the interferogram obtained in a DASH interferometer was modeled and the wind velocity can be retrieved using the phase variation. According to the interferogram expression in Equation 2.1, the phase of interferogram is more sensitive to the wavelength change when its OPD gets larger. On the other hand, the visibility of the fringe pattern, a leading factor to detect periodic wave in the presence of noise, decreases with the increment of OPD due to the contribution of the thermal broadening (the exponential term in Equation 2.1). The contradiction between small and large OPD values shows an optimum OPD offset can be found for accuracy measurements of winds. The difference between the interferograms without and with Doppler shift, as shown in Figure 2.2, also indicates that an optimum OPD offset makes the system most sensitive to the change of interferogram.

Numerical studies have been carried out to determine the OPD offset. Given an OPD offset, the interferogram of the atomic oxygen red line can be produced using Equation 2.1 with a typical temperature (1000 K) broadening. As discussed in Section 3, the noise can be added to the interferogram based on the estimated signal-to-noise ratio, which is calculated from the VER, system etendue, optics transmission and detector characterization. The VER was calculated based on a model developed by Cogger et al, (*Cogger et al.*, 1980; *Link and Cogger*, 1988), which was already presented in Section 1.3. With the 500-row pixel average and a 5-minute exposure time, 10000 Monte Carlo simulations (adding noise) were performed for each OPD. Then estimation errors of the wind speed as functions of different OPD were deduced, which are the mean absolute deviations of all simulations. The observation is simulated for Wuppertal (51.26°N, 7.15°E) on Jun 21, 2014, and the parameters of the detector are from Table 3.2. The zenith observation, as the reference for retrieving the wind velocity, has the smallest signal intensity compared to other direction observations and the brightness difference is also considered in these simulations. The phase comparison between the slant observation and zenith observation was accomplished by the method in Section 2.2. The numerical

result in Figure 4.2 indicates that the minimum wind estimation error can be achieved when the OPD offsets are in the range of 30 mm to 50 mm.

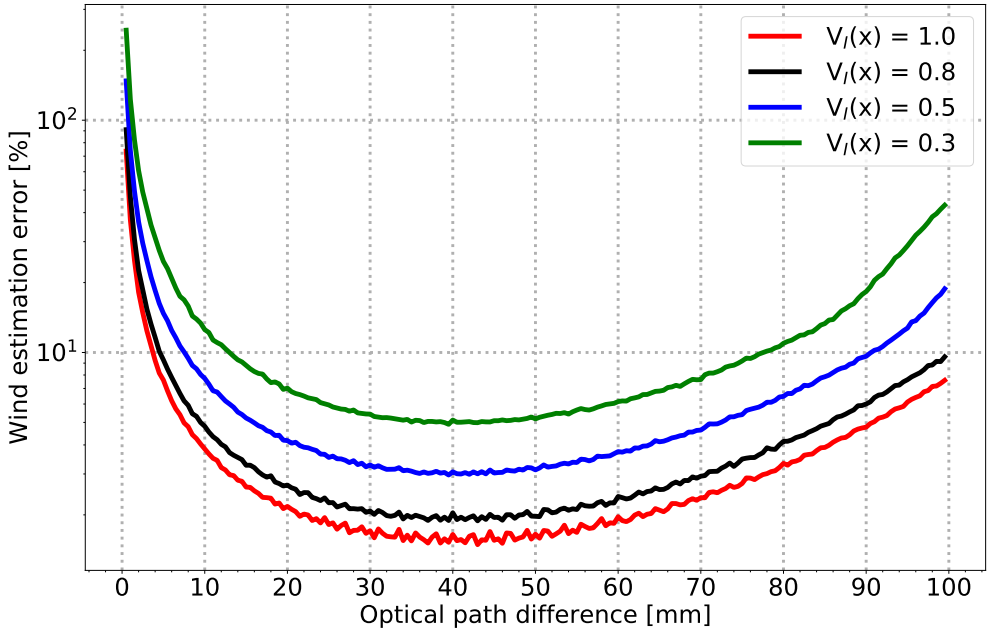

Figure 4.2: Error of wind estimation as a function of the OPD value. The y axis is a logarithmic coordinate.

4.1.4 Thermal Compensation

To resolve the winds within an accuracy of 3 m/s, wavelength shifts smaller than 8 orders of magnitude of the emission wavelength have to be detected and a phase shift of less than 3.2 mrad is required for the 32 mm OPD offset. Therefore, phases of the fringes must be highly stable with respect to ambient temperature, especially for the ground-based instrument which needs relatively long exposure times (usually 3-5 minutes) to collect enough photons. The thermal drift not only introduces an additional phase error but also deteriorates fringes contrasts. The thermal compensation should be taken into account during design.

Choosing the correct combination of glasses and dimensions can achieve thermally stable performance, which has already been employed in Michelson interferometers (*Thuillier and Shepherd*, 1985; *Thuillier and Hersé*, 1991). The phase independence of the surrounding heat requires the derivation of the phase with respect to temperature to

be zero, and the expression can be written according to Equation 2.1

$$\frac{d\varphi(x)}{dT} = 2\pi\left(\frac{df_x}{dT}x + 2\frac{d\Delta d_0}{dT}\sigma\right) = 0, \tag{4.1}$$

with the temperature T and the spatial frequency $f_x = 4\tan\theta\,(\sigma - \sigma_L)$. The angle θ is the Littrow angle of the grating in the DASH interferometer. This equation holds when the two derivative terms $\frac{df_x}{dT}$ and $\frac{d\Delta d_0}{dT}$ are equivalent to zero at the same time.

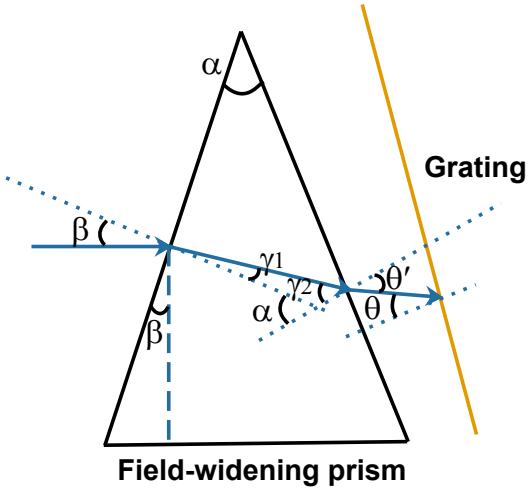

Figure 4.3: Raytrace on a field-widening prism and a reflecting grating at the Littrow angle.

For the $\frac{df_x}{dT}$ term, substituting the grating equation shown in Equation A.1 yields the condition of temperature-independent spatial frequency

$$\begin{aligned}\frac{df_x}{dT} &= \frac{4}{\cos^2\theta}(\sigma - \sigma_L)\frac{d\theta}{dT} + 4\sigma_L\frac{d\theta}{dT} + 4\sigma_L\alpha_{CTE}\tan\theta \\ &\approx 4\sigma_L\frac{d\theta}{dT} + 4\sigma_L\alpha_{CTE}\tan\theta = 0.\end{aligned} \tag{4.2}$$

Here α_{CTE} represents the coefficient of thermal expansion (CTE) of the grating substrate. In general, the incident angle on the grating varies with the refractive index of the field-widening prism as shown in Figure 4.3. Therefore, the derivative of the Littrow angle in Equation 4.2 can be substituted by the product of the derivative of the Littrow angle with respect to the refractive index and the derivative of the refractive index with respect to temperature. Consequently, the condition of the temperature-independent spatial frequency changes to

$$\alpha_{CTE} = -\frac{dn}{dT}\frac{n\sin\alpha}{\tan\theta\cos\theta'\sqrt{n^2-\sin^2\beta}}, \tag{4.3}$$

where n represents the refractive index of the prism. As shown in Figure 4.3, β denotes the incident angle on the first plane of the prism, α denotes the apex angle of the prism, θ' denotes the exit angle on the second plane of the prism and θ denotes the incident angle on the grating. Thus, a suitable material with a negative derivative of the refractive index with respect to temperature employed in the field-widening prism can mitigate the influence from the grating thermal expansion.

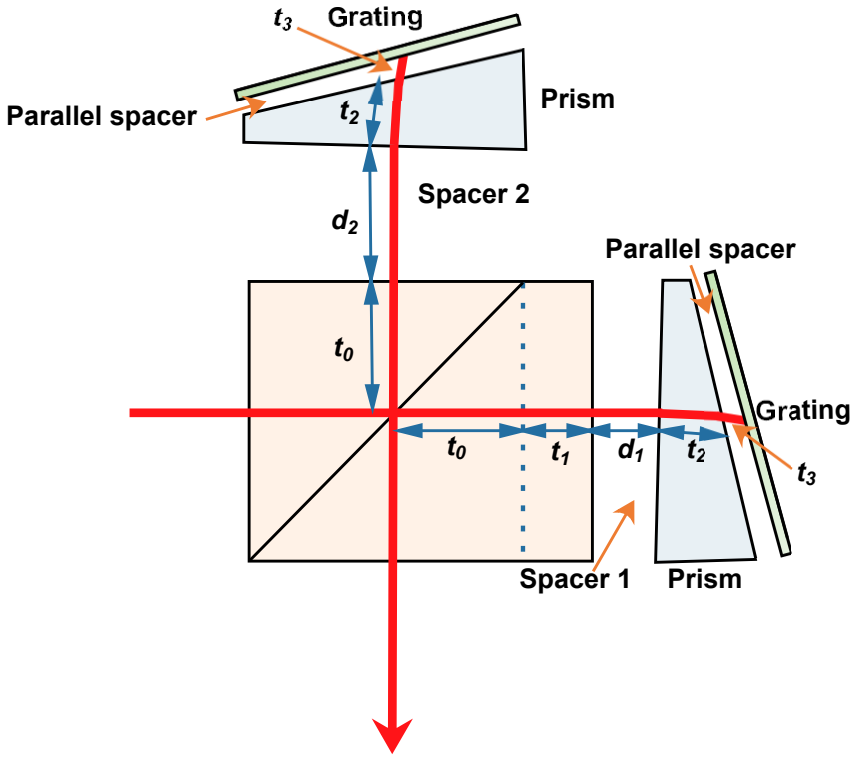

Figure 4.4: Schematic of a thermally compensated field-widening DASH interferometer with an asymmetric beamsplitter.

$\frac{d\Delta d_0}{dT} = 0$ makes the additional OPD of interferometer independent of ambient temperature at a given wavelength. As shown in Figure 4.4, the difference of the beamsplitter and spacers on two arms provides the OPD and the extended distance Δd_0 can be calculated by

$$\Delta d_0 = n_1 t_1 + d_1 - d_2, \tag{4.4}$$

with the beamsplitter refractive index n_1, asymmetric thickness t_1, spacer 1 thickness d_1 and spacer 2 thickness d_2. For a monolithic DASH, the beamsplitter, prisms and gratings are contacted with the spacers made of optical glasses, so that the thermal expansion of the spacers also affects the OPD. Consequently, the temperature-independent OPD offset condition can be expressed as

$$\frac{d\Delta d_0}{dT} = \frac{dn_1}{dT}t_1 + n_1 C_1 t_1 + C_2 d_1 - C_3 d_2 = 0, \tag{4.5}$$

where $C_{1,2,3}$ are the CTEs of the beamsplitter, spacer 1 and spacer 2, respectively. The temperature dependence of the refractive index is discussed in Appendix B.4. The derivative of the refractive index with respect to temperature can be determined using the relation in Appendix B.4. The OPD offset is provided by the difference between the two arms. The thicknesses and materials of the components are selected to achieve the temperature-stable OPD offset. The light beam traverses the beamsplitter and field-widening prisms, so that the corresponding thicknesses and refractive indexes impact Δd_0. Accordingly, the temperature derivatives of refractive index and the CTEs of the beamsplitter and field-widening prisms affect $\frac{d\Delta d_0}{dT}$. The thicknesses of the spacer 1, spacer 2 and parallel spacer affect the OPD offset, and the CTEs have impact on the temperature stability of OPD offset.

4.1.5 Field Widening

Section A.4 indicates that the field of view is limited by the resolving power R and extended distance Δd in a DASH system. According to Equation A.22, the spatial frequency and the OPD offset decrease with the increase of field of view, which results in the deterioration of fringe contrast. The interference visibility, a sinc function of field of view, is presented in Figure 4.5. With the increase of field of view, the visibility declines, and its value decreases dramatically when the field of view is larger than 0.15°. Therefore, it is necessary to apply the field-widening technique to improve system throughput.

According to the discussion in Appendix A.4, the fringe intensity in a DASH system with a field-of-view solid angle Ω at the position x can be expressed as

$$\begin{aligned} I(x) = \int_{-\infty}^{+\infty} \int_{0}^{\Omega_m} B(\sigma) \Bigg\{ 1 + \cos \Bigg[2\pi \Bigg(4 \tan\theta \left(\sigma - \sigma_L - \frac{\Omega\sigma}{2\pi} \right) x \\ + 2\Delta d_0(\omega)\,\sigma \Bigg) \Bigg] \Bigg\} d\Omega d\sigma, \end{aligned} \tag{4.6}$$

where Ω_m is the maximum solid angle, $B(\sigma)$ is the input spectral intensity and ω is

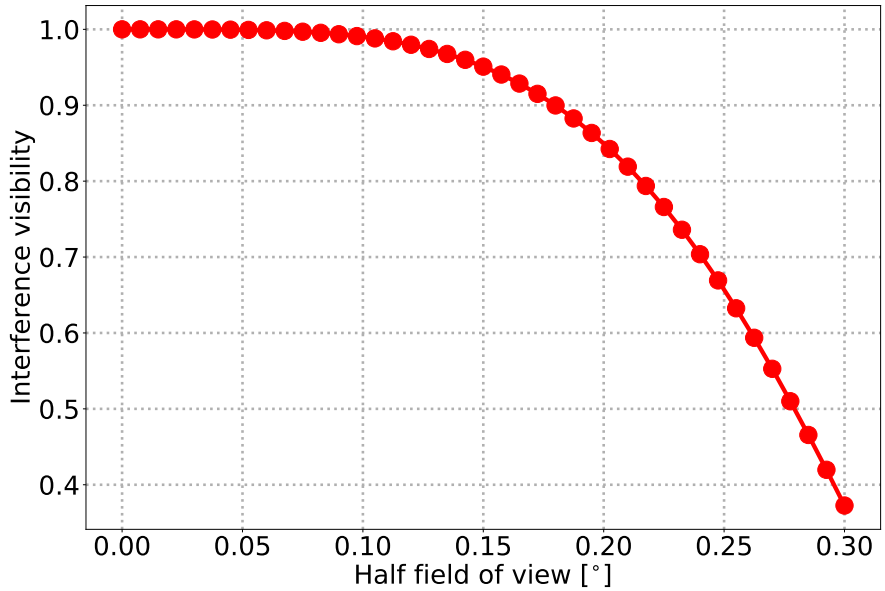

Figure 4.5: Interference visibility as a function of half field of view. Note that x_{max} = 11.264 mm in calculation, which is the half of the detector size.

the incident angle on the spacer 1 or spacer 2. The spatial frequency and optical offset change with the off-axis angle, which limits the field of view and degrades the contrast of interferogram.

The field-widening technique, already employed in a Michelson inteferometer, SHI and DASH interferometer (*Bouchareine and Connes*, 1963; *Harlander et al.*, 1994, 2010), can solve this problem by inserting prisms between the beamsplitter and grating on the both arms, which greatly improve the ability to receive radiation from a relatively large solid angle. The basic principle of field widening is that the additional prism with a certain apex angle can compensate the OPD differences arising from the different rays with different incident angles.

The extended distance Δd_0 in Equation 4.6, as a function of the incident angle ω, can be written as

$$\begin{aligned}\Delta d_0(\omega) &= n_1 t_1 \cos\left(\omega'\right) + d_1 \cos(\omega) - d_2 \cos(\omega) \\ &= n_1 t_1 \sqrt{1 - \frac{\sin^2\omega}{n_1^2}} + d_1 \cos(\omega) - d_2 \cos(\omega) \\ &= n_1 t_1 + d_1 - d_2 - \frac{\sin^2\omega}{2}\left(\frac{t_1}{n_1} + d_1 - d_2\right) - 0\left(\sin^4\omega\right) + \cdots,\end{aligned} \tag{4.7}$$

In order to eliminate the contribution from the angle ω, the second order term should be set to zero, yielding

$$\frac{t_1}{n_1} + d_1 - d_2 = 0, \tag{4.8}$$

which means a suitable combination of material and dimension is required for the beamsplitter and spacers in a field-widening design. From a geometric optics point of view, the images of the gratings on the two arms are coincident when viewed from the exit pupil as Equation 4.8 requires.

The presence of $\frac{\Omega\sigma}{2\pi}$ in Equation 4.6 indicates that the spatial frequency of the fringes varies with the field of view. *Harlander* (1991) inserted prisms in an SHI configuration to achieve field widening, which also works here to eliminate the term $\frac{\Omega\sigma}{2\pi}$. The field-widening prisms are placed between the beamsplitter and gratings so that the gratings seem to be normal to the optical axis when viewed from the exit pupil. According to Harlander's analysis, the field widening can be realized when the minimum deviation in the field-widening prism occurs with an incident angle η (*Harlander*, 1991), and they have the relation

$$2\left(n^2 - 1\right)\tan\eta = n^2 \tan\theta, \tag{4.9}$$

where n is the refraction index of the prism and θ is the Littrow angle of the grating. Then the apex angle α can also be determined according to the minimum-deviation condition of the prism

$$n \sin\frac{\alpha}{2} = \sin\eta. \tag{4.10}$$

Equation 4.9 and Equation 4.10 were deduced from the assumption of minimum-deviation ray, which can not represent the general scenario. In our design where the exit plane of field-widening prism is parallel to the incidence plane of the grating, the minimum-deviation ray is not the Littrow configuration, which is different from the assumption in the analysis of *Harlander* (1991). In Harlander's discussion, the phase expression includes two quadratic angular terms (angles β and ϕ defined in Figure A.2), but Equation 4.9 only eliminates one quadratic angular term (*Harlander*, 1991). Moreover, the dispersion effect was ignored in this analysis. It is necessary to discuss a general situation, and an optimization can be an alternative.

As shown in Figure 4.6, the rays traverse the interferometer, and a fringe localization plane is found at the position between the beamsplitter and the field-widening prism

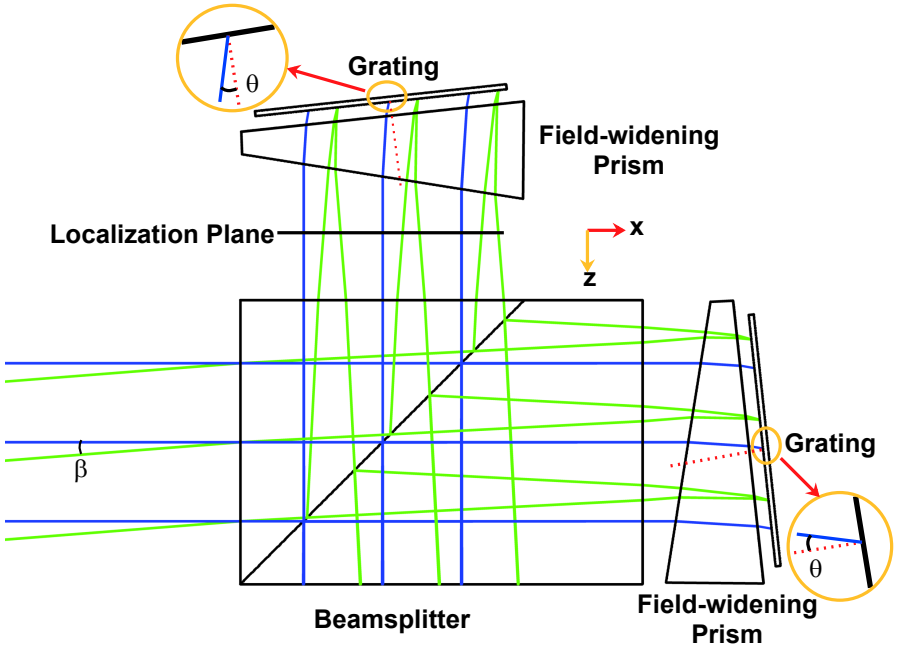

Figure 4.6: Definitions of the angles and the coordinate in a field-widening DASH interferometer. The angle β is the incident angle in the dispersion plane (x-z plane) and the angle deviation with respect to the optical axis (blue line). The optical axis traverses the interferometer at the Littrow angle θ. ϕ is the angle between the wave vector and the dispersion plane, which is not shown in this figure.

after retro-reflection on the exit plane of the beamsplitter. The fringe localization is a virtual plane, which needs an additional camera to image this plane onto a detector. Although it is not possible to recorded signal on the localization plane, it is also rational to analyze the fringe intensity on this localization plane during design. As discussed in Chapter 2, the interferogram is the superposition of the fringe patterns produced from all incidence angles. According to the principle of wave superposition, the visibility of the superposed interferogram becomes higher when the fringe patterns contain similar OPD or phase distribution on the localization plane. The optimization strategy here is to discretize the incident rays, and then to minimize the OPD differences of the fringes produced from the discrete rays.

Given a field of view, the cone angle can be segmented into a certain number of small angles with β_i and ϕ_i, and the OPD $\Delta L\,(x, \phi_i, \beta_i)$ at the localization plane x can be traced. Optimizing the prisms' angles and dimensions to minimize the standard deviation of the OPD $\sigma_{\Delta L}$ can achieve the best field-widening performance, which means the rays at the position x have similar OPDs and phases. Angles β, ϕ and system coordinate are defined in Figure 4.6. For the case without field-widening prisms, the OPD can be expressed as

$$\Delta L(x,\phi,\beta) = 4\tan\theta\frac{\Omega}{2\pi}x + \Delta d\left(2-\frac{\Omega}{2\pi}\right), \tag{4.11}$$

where $\Omega = 2\pi(1-\cos\phi\cos\beta)$. The objective function of optimization can be defined by

$$\begin{aligned} \min\ \sigma_{\Delta L} &= \sqrt{\frac{\sum_{i=1}^{n}\left[\Delta L(x,\phi_i,\beta_i) - \Delta\bar{L}(x,\phi,\beta)\right]^2}{n-1}} \\ \Delta L(x,\phi,\beta) &= P_1(x,\phi,\beta) - P_2(x,\phi,\beta), \end{aligned} \tag{4.12}$$

where $P_{1,2}(x,\phi,\beta)$ represent the optical paths from the beamsplitter to the localization plane on arm 1 and arm 2, respectively. The optical path information can be obtained by ray-tracing software. When differences between $P_{1,2}(x,\phi,\beta)$ and $P_{1,2}(x,0,0)$ (on-axis optical path) are minimum on both arms for the discrete rays, a local optimal solution is found for Equation 4.12.

In order to convert this optimization problem to a problem of imaging system design, a paraxial lens is inserted in front of the interferometer, which does not introduce additional wavefront aberrations. As shown in Figure 4.7(a) and Figure 4.7(b), the rays are focused on the gratings of both arms by an image-space telecentric lens. The ray cones have the same angle of incidence and angular distance on the gratings, where the illumination is homogeneous. The size of the aperture and the focal length were chosen so that the maximum incident angle on the beamsplitter is coincident with the actual application. Therefore, powerful commercial ray-tracing software employed in imaging system design can be used here. The value of $P_{1,2}(x,\phi,\beta) - P_{1,2}(x,0,0)$ are traced by the $OPD_{1,2}(h_x,h_y,p_x,p_y)$ with the reference of the chief ray in this imaging system. Note that h_x and h_x denote the field of view and p_x and p_y denote the pupil position of the ray. In general, the $OPD_{1,2}(h_x,h_y,p_x,p_y)$ can be used to evaluate the image quality in an imaging system. Substituting $OPD_{1,2}(h_x,h_y,p_x,p_y)$ into Equation 4.12, the objective function of optimization changes to

$$\begin{aligned} \min\ \sigma_{\Delta L} &= \sqrt{\frac{\sum_{i=1}^{n}\left[\Delta L(x,\phi_i,\beta_i) - \Delta\bar{L}(x,\phi,\beta)\right]^2}{n-1}} \\ \Delta L(x,\phi,\beta) &= OPD_1(h_x,h_y,p_x,p_y) - OPD_2(h_x,h_y,p_x,p_y) + 2\Delta d_0, \end{aligned} \tag{4.13}$$

where $2\Delta d_0 = P_1(x,0,0) - P_2(x,0,0)$, which is the extended value on arm one. Therefore, optimizing the positions, angles and dimensions of all interferometer elements to minimize the OPD difference $OPD_1(h_x,h_y,p_x,p_y) - OPD_2(h_x,h_y,p_x,p_y)$ in the system

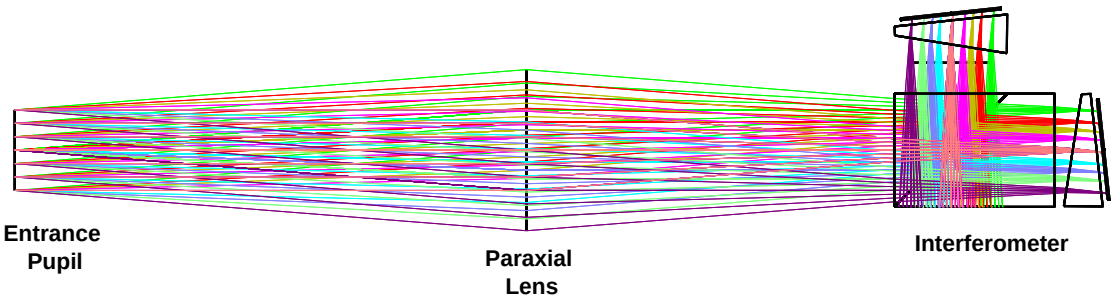

(a) A paraxial lens and a field-widening DASH interferometer

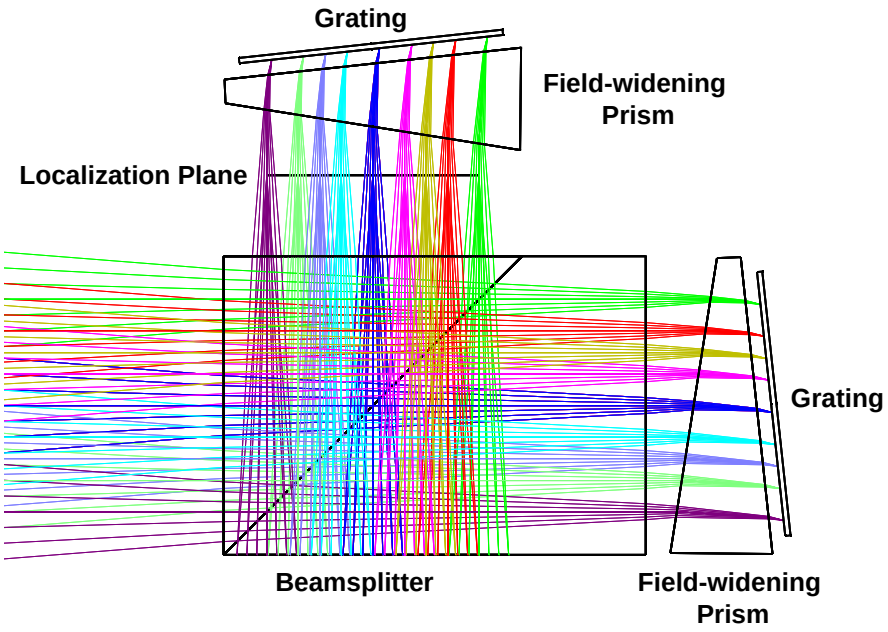

(b) Field-widening interferometer

Figure 4.7: (a) Configuration of a paraxial lens and a field-widening DASH interferometer and (b) the detailed view of the field-widening interferometer. The entrance pupil is located at the front focal plane of the paraxial lens, so that an image-space telcentric lens is used to focus the rays onto the diffraction grating.

of Figure 4.7(a) can achieve the best field-widening performance. The start point of the interferometer can be determined using Equation 4.8, Equation 4.9 and Equation 4.10. The value of $\sigma_{\Delta L}$ can be used to describe the OPD differences between different rays, and a smaller $\sigma_{\Delta L}$ means the higher visibility of the fringe pattern. The zero value of $\sigma_{\Delta L}$ corresponds to 100% visibility.

4.1.6 Configuration Optimization

Table 4.1: Specification of Design Interferometer

Full field of view	9°
Beamsplitter	Asymmetric beamsplitter
Material	Schott N-BK7
Beamsplitting coating	50/50 nonpolarizing
Field-widening prisms	Two prisms are identical
Material	Schott N-LAK12
Apex angle	15.114°
Wedged spacers	Holey spacers
Material	Fused silica (Spacer 1), CD H-FK61 (Spacer 2)
Parallel spacers	Holey spacers
Material	Fused silica
Gratings	Plane ruled reflectance gratings
Blank material	Fused silica
Groove density	900 mm^{-1}
Littrow angle	16.4950°
Optical path difference at center $2\Delta d_0$	32 mm
$\frac{d\Delta d_0}{dT}$ [mm/°C]	1.2×10^{-7}
Spatial frequency [cm^{-1}]	27.7(630.0304 nm) and 14.30 (630.479 nm)
Resolving power	57685
Etendue [cm^2sr]	0.156

The thermal compensation theory and field-widening analysis make it possible to optimize the interferometer parameters. A damped least squares algorithm, minimizing the OPD differences under constraints of Equation 4.3, Equation 4.5 and Equation 4.8, yields an interferometer design shown in Table 4.1. The collocation of the asymmetric beamsplitter, the spacers and the identical field-widening prisms provides the 32 mm OPD offset and also maintains the coincidence of two grating images. The spatial frequencies for the atomic oxygen red line emission and calibration line are 32.7 cm^{-1} and 14.3 cm^{-1}, respectively. The resolving power of 57685 corresponds to the spectral resolution of 0.011 nm at the wavelength of 630.0 nm, which means that interferograms produced from the atmospheric emission line and calibration line can be well separated in the spectral domain. With the resolving power, the limited field of view is 0.4° calculated from Equation A.25. The full field of view is improved to 9° after field widening,

so that the throughput is increased by a factor of 22.5. Due to the negative value of $\frac{dn}{dT}$ at the working wavelength, N-LAK12 glass is selected for the field-widening prisms to stabilize the spatial frequency. Spacer 1 has a smaller thermal expansion coefficient and a thinner dimension, while spacer 2 has a higher thermal expansion coefficient and a thicker dimension. These different expansions on the two arms compensate the OPD variation with the parameter $\frac{d\Delta d_0}{dT}$ of 1.2×10^{-7} mm/°C, which corresponds to 1.2 mrad uncertainty per °C. In recent monolithic DASH interferometers, the spacers were fabricated as hollow frames to connect the beamsplitter, the field-widening prisms and the gratings on the one hand and not to block beam transmission on the other hand (*Harlander et al.*, 2010; *Harding et al.*, 2017). Here two separate prisms are applied to replace the frame, which reduces the mechanical deformation caused by the differential thermal expansion between different materials. In addition, a series of through holes are drilled on the prisms of spacers to further relieve the strain. Note that all of the parameters in Table 4.1 refer to an environment of 25 °C and 1013 hPa and the dispersion effect is also considered.

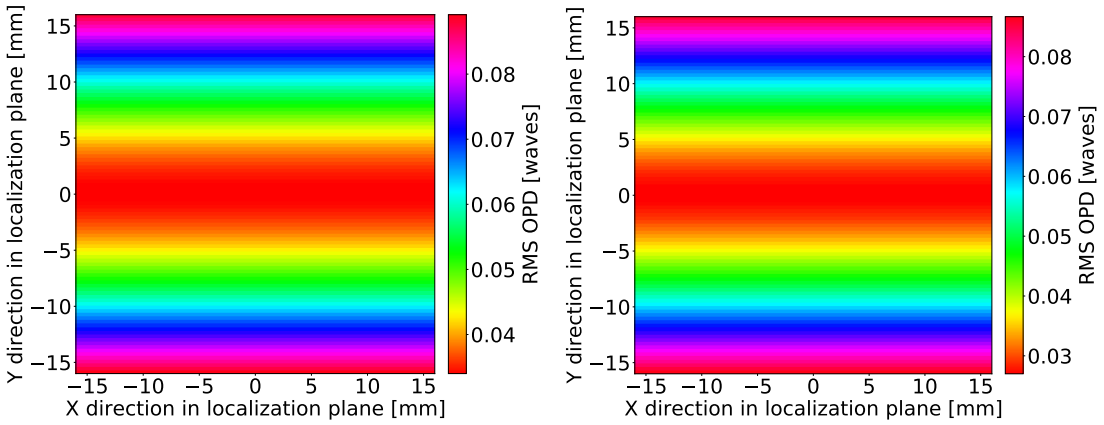

(a) RMS OPD on arm one

(b) RMS OPD on arm two

Figure 4.8: RMS OPD of the interferometer on arm one and arm two. Note that the sampling here is 100×100 points.

To verify the field-widening performance, the OPDs are traced by ray-tracing software based on the system of Figure 4.7(a). The root mean squares (RMS) of the OPD on both arms are presented in Figure 4.8(a) and Figure 4.8(b). The minimum RMS OPD and maximum RMS OPD on arm one are 0.034 waves and 0.089 waves, respectively. And the corresponding numbers on arm two are 0.027 waves and 0.087 waves. Because the OPDs on both arms are minute, the values of the OPD difference $(OPD_1(h_x,h_y,p_x,p_y) - OPD_2(h_x,h_y,p_x,p_y))$ are also minute. In addition, the OPD differences are also directly calculated using the traced OPDs, which are plotted in Figure

4.9. The OPD differences are less than 0.125 waves across the transverse pupil and sagittal pupil for the field of 0° and the chromatic aberration are negligible. The OPD differences for other field of views can be found in Appendix B.5. All in all, the minute OPD differences between two arms are realized in this design, which means the field-widening performance is great and an interferogram with high contrasts can be obtained using this interferometer.

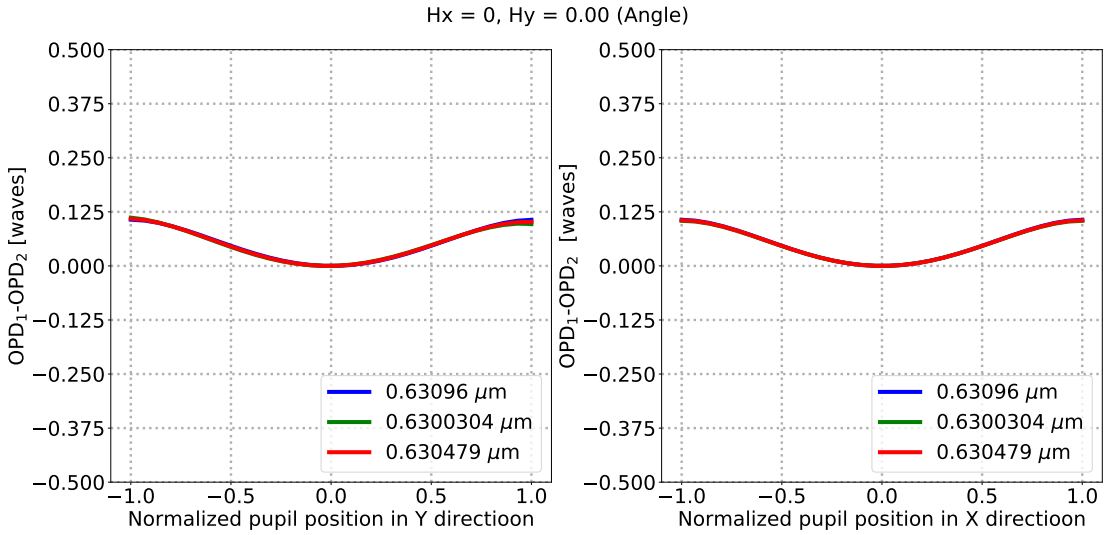

Figure 4.9: Tracing result of the OPD difference on the transverse plane (left) and sagittal plane (right) with the parameters in Table 4.1.

4.2 Camera Optics

After traversing the interferometer, a virtual image of the grating is produced on the fringe localization plane which is perpendicular to the optical axis. Therefore, it is necessary to use camera optics to image the fringe pattern onto the detector. Since the geometrical image of the grating is also located in the fringe localization plane, the recorded image on the detector is the superposition of the Fizeau fringe pattern and the grating image. In this section, the camera optics suited to relay the fringe pattern is designed and analyzed.

4.2.1 Optical Design

The camera optics may introduce an additional OPD at the image plane caused by the potential aberration, which deteriorates the visibility of the obtained interferogram.

Thus, the image quality of the camera is a significant consideration. There is no additional lens in front of the interferometer, hence the radiation from the atmosphere illuminates the grating directly. In order to relay the homogeneous illumination on the gratings, a object-space telecentric imaging system is required. On the other hand, an image-space telecentric configuration reduces the sensitivity of the position of image plane. Accordingly, a double-telecentric camera is proposed to relay the fringe pattern. Compared with conventional lenses, double-telecentric lenses show a huge advantages. A double-telecentric camera performs well with a relatively loose position accuracy, and it tends to have a low distortion.

For a low-cost consideration, we prefer to use off-shelf lenses to design the camera. It is possible to design a double-telecentric system with commercial lenses, because the chromatic aberration can be ignored due to the implementation of a narrow bandpass filter. We started with the paraxial ray tracing for the first-order design, and the determined first-order design was then used to analyze the third-order aberration. The paraxial analysis and third-order aberration optimization are described in Appendix B.6. The initial system obtained from the optimization of third-order aberrations is then served as a start point for further optimization using optical design software.

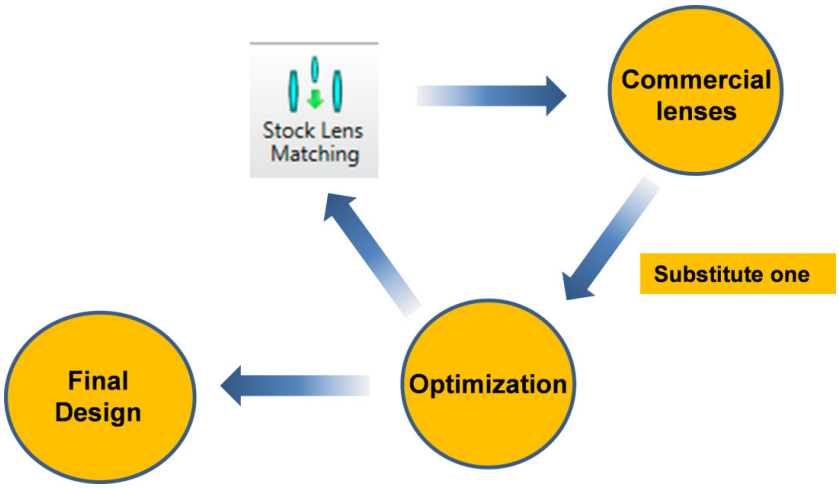

Figure 4.10: Strategy of the lens substitution.

Here, we used ZEMAX, capable of searching the most similar lens in stock (*ZEMAX LLC.*, 2020), to optimize the system and then to substitute the lenses with the commercial components. The strategy of the lens substitution is explained in Figure 4.10. After the optimization, some off-shelf lenses were found using the stock lens matching. The lens whose parameters are closest to the lens found was replaced by the commercial lens, and then the optimization and lens matching were implemented again. Those processes needed to be iterated again and again until all of the lenses were replaced by

off-shelf lenses.

4.2.2 Camera Configuration

As described above, a double-telecentric system using off-shelf lenses was obtained, which is illustrated in Figure 4.11. This camera is composed of five lenses including three spherical singlet lenses, a doublet lens and an aspheric lens. Temperature controls for the interferometer and detector are required, so that two optical windows with high surface flatness were inserted in the object space and image space. The position of aperture is chosen, so that its entrance pupil and exit pupil are at infinity. The size of aperture limits the field of view, which only allows the rays within the field of view to pass through the system.

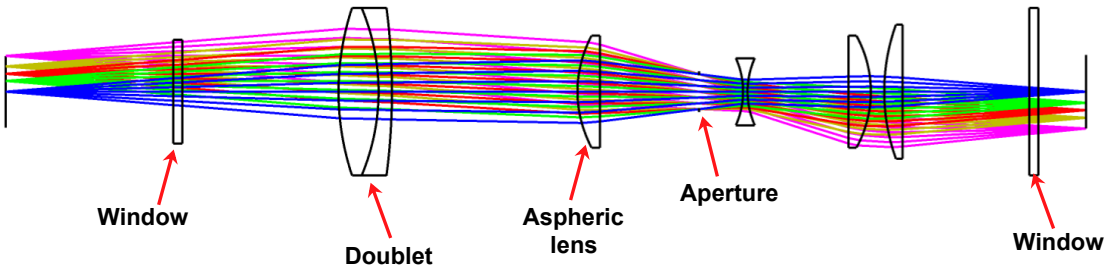

Figure 4.11: Configuration of the double-telecentric camera.

Table 4.2: Specification of the camera

Item	Description
Working wavelength [nm]	630.0 to 631.0
Size of object [mm^2]	$\pi \times 16 \times 16$
Magnification	-1.03
Full field of view	9°
Distance from the object plane to the first lens [mm]	149.1
Distance from the last lens to the image plane [mm]	82.2
Total length (from the object plane to image plane) [mm]	484.1

Table 4.2 presents the specification of this camera. The working wavelength are from 630.0 nm to 631.0 nm, which covers the wavelengths of the atomic oxygen red

line and calibration source. In order to maintain the spatial frequency designed in the interferometer, the magnification is designed to approximately -1.0. The field of view and the object size fit the requirement to relay the fringe pattern produced from the interferometer. In addition, it provides enough spaces for the interferometer on the object side and the detector on the image side.

4.2.3 Imaging Performance

In this section, the imaging performance of the design camera is characterized using ray-tracing software. Modulation transfer function (MTF) of an optical system specifies the response to a periodic pattern passing through the lens system, which is an important parameter to evaluate the imaging quality. The MTF of the design camera at the image plane is shown in Figure 4.12, and the MTFs almost approach the diffraction limit (black line) especially at the low spatial frequency. For the two working spatial frequencies (2.77 mm^{-1} and 1.43 mm^{-1}), the MTF values are almost equivalent to the diffraction limit, which means there is almost no deterioration for the fringes after passing through this camera.

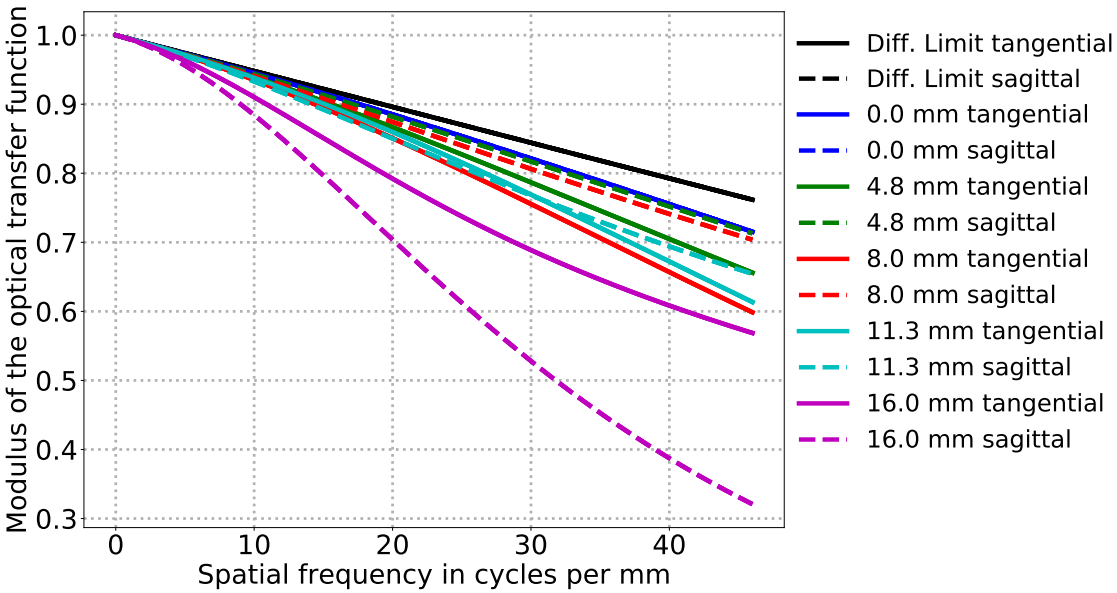

Figure 4.12: Modulation transfer function at the image plane.

Wavefront error is another important evaluation criterion, which directly affects the visibility of the interferogram. As shown in Figure 4.13, the RMS OPD of the camera is in the range from 0.0495 waves to 0.172 waves and the most values are less than 0.1 waves. In addition, OPDs as a function of the pupil position are also plotted in Figure

4.14. For the rays with the different field of views and different pupil positions, the OPDs are almost less than 0.5 waves. After passing through this camera, the change of the OPD distribution is small compared to the original distribution on the localization plane. Therefore, this designed camera is competent to relay the fringe pattern.

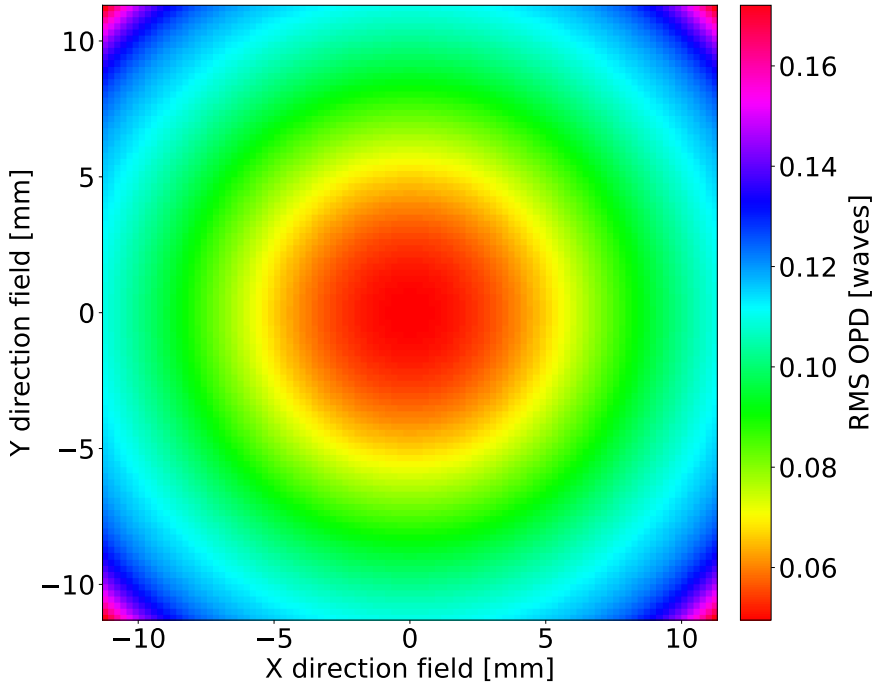

Figure 4.13: RMS OPD of the camera with the sampling of 100×100 points.

Optical lens distortion, a form of optical aberration, describes a non-linear projection from the object to the image. Low distortion is also required for this camera because the existing distortion may change the spatial frequency and broaden the spectrum. In general, the distortion of the imaging system can be described by a distortion in percent, which is defined by

$$Distortion = 100 \times \frac{r_d - r_u}{r_u}, \tag{4.14}$$

where r_d and r_u denote the distorted and undistorted radius in respect of the optical center (*ZEMAX LLC.*, 2020; *Liu*, 2019). In order to analyze the distortion in the double-telecentric camera, the undistorted grid points and distorted grid points are displayed in Figure 4.15. The positions of the distorted points (image points) and undistorted points (object points) are almost coincident except the sporadic edge points. The maximum distortion of the camera is estimated based on Equation 4.14 and its value is -0.5899% at the wavelength of 630.0 nm, which means the camera distortion is negligible.

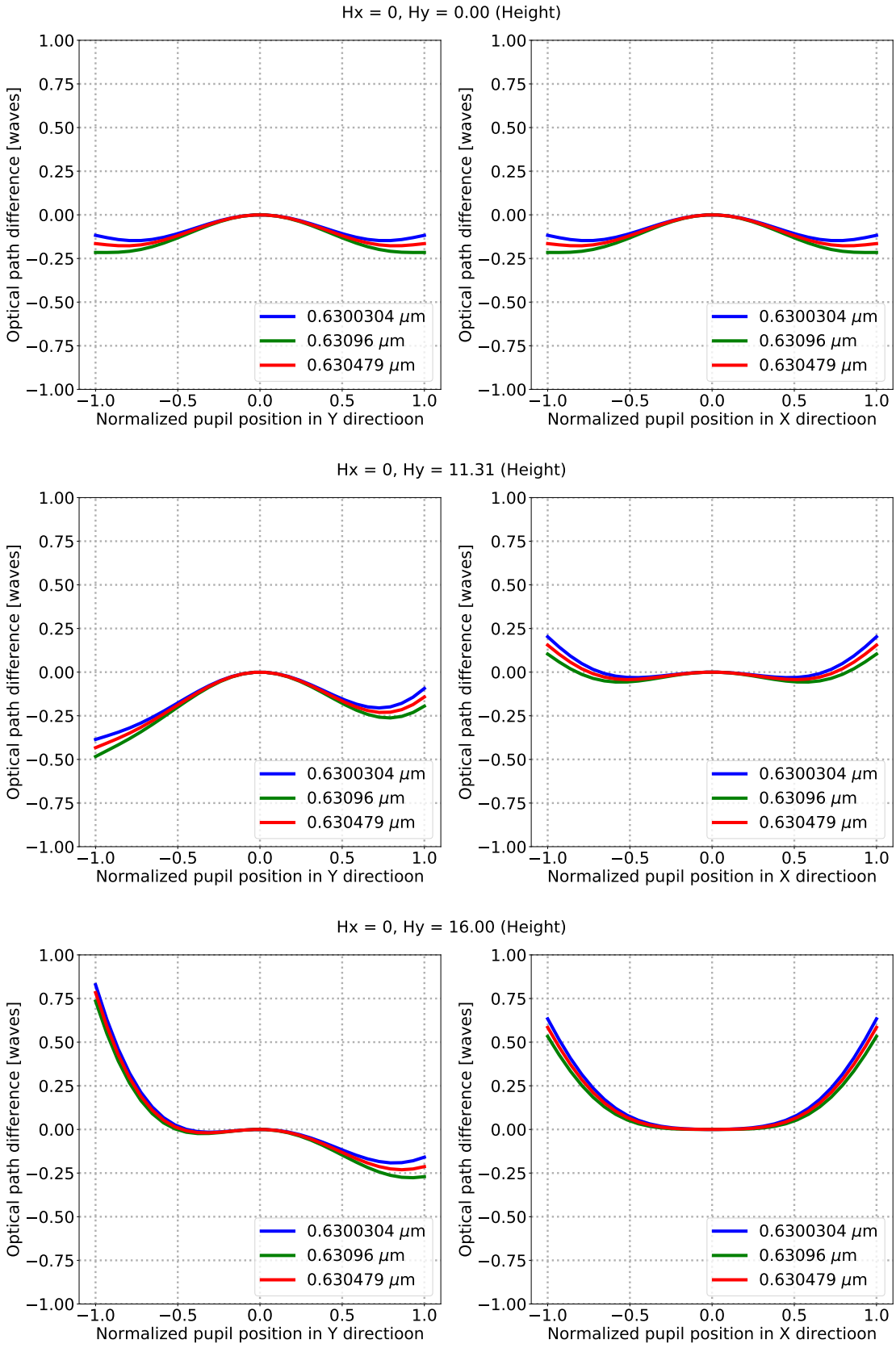

Figure 4.14: OPDs as a function of the pupil position in tangential plane (left) and sagittal plane (right).

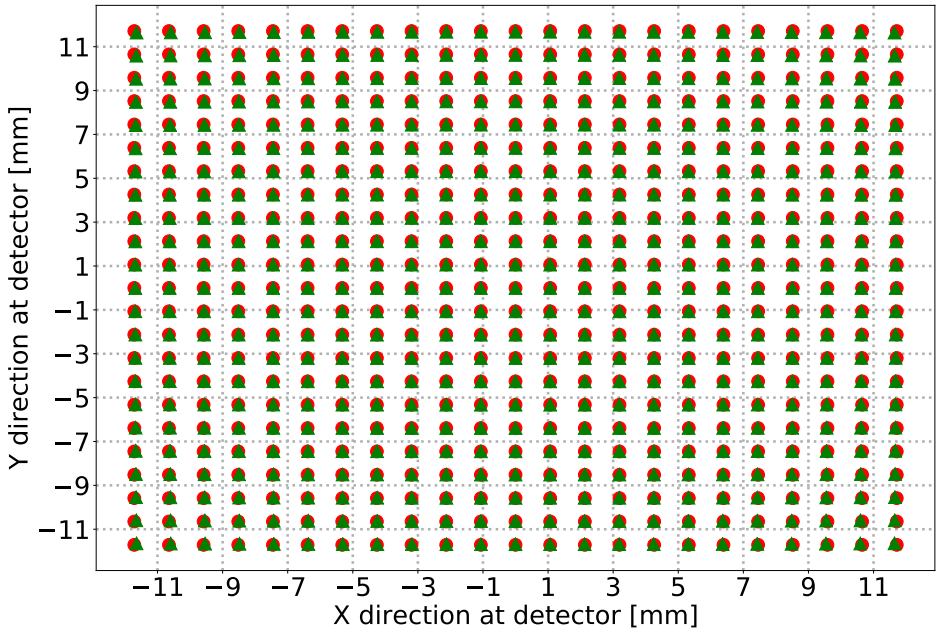

Figure 4.15: Comparison between the undistorted grid points and distorted grid points. Red circles represent undistorted points, green triangles represent distorted points. The positions of the grid points are obtained from the ray-tracing simulation and the number of the grid points is 23×23.

4.2.4 Thermal Stability

As discussed in Section 4.1.4, the thermal stability of the system is a crucial factor to determine the phase change caused by a Doppler shift. Though the temperature in the interferometer is well stabilized using a proportional-integral-derivative (PID) controller, the temperature in the camera is not. It is necessary to discuss the thermal stability of this double-telecentric camera, and the imaging performance during different temperatures can be analyzed by ray-tracing software using different-temperature settings. In this section, the performances of the designed camera at temperatures from 15 °C to 25 °C are analyzed.

RMS OPDs and maximum distortions as functions of ambient temperature are shown in Figure 4.16. The minimum RMS OPD increases with the increase of the temperature, but the maximum RMS OPD decreases with the increase of the temperature. The changes of the maximum RMS OPD and minimum RMS OPD are 0.071 waves and -0.061 waves when the temperature changes from 15 °C to 25 °C. The maximum distortion also varies with the temperature but the variation is only 0.0019% when the temperature increases from 15 °C to 25 °C. Camera MTFs at temperatures from 15 °C

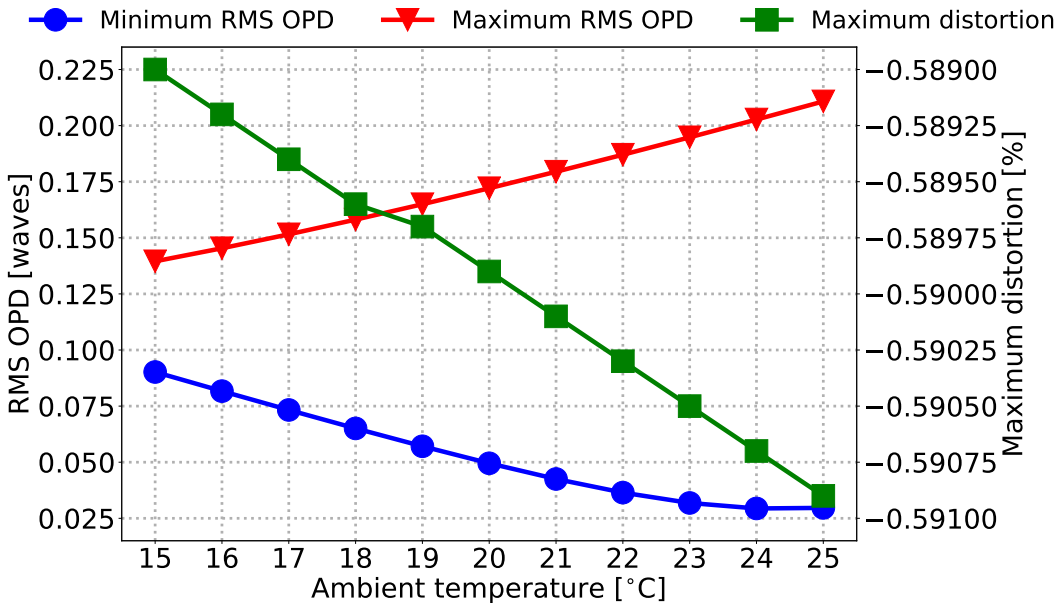

Figure 4.16: RMS OPDs and maximum distortions as functions of ambient temperature.

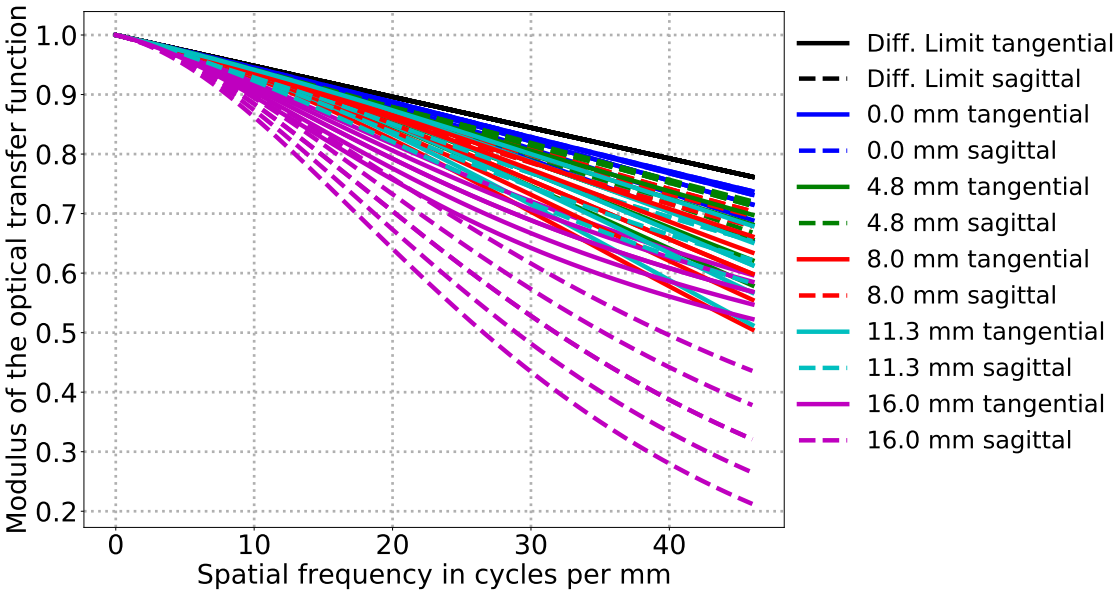

Figure 4.17: Superposition of the camera MTFs during the temperatures from 15 °C to 25 °C.

to 25 °C were also calculated, and the superposition result of these MTFs is presented in Figure 4.17. The MTFs vary with the temperature, but the variations are acceptable. When the spatial frequencies are less than 5 mm^{-1}, the performance of camera during this temperature range almost reaches the diffraction limit. Consequently, this camera can perform stably in the temperature range from 15 °C to 25 °C.

4.3 Interferogram Analysis

The configuration of a DASH instrument is shown in Figure 4.18, which combines the designed interferometer and double-telecentric lenses. After going through the interferometer, a fringe pattern is produced and then imaged onto a detector by the double-telencetric lenses. The interferograms generated in this setup can be simulated using the optical path information of different field of views, which can be obtained by ray-tracing software. In this section, the predicted interferogram is simulated and its corresponding features are also analyzed.

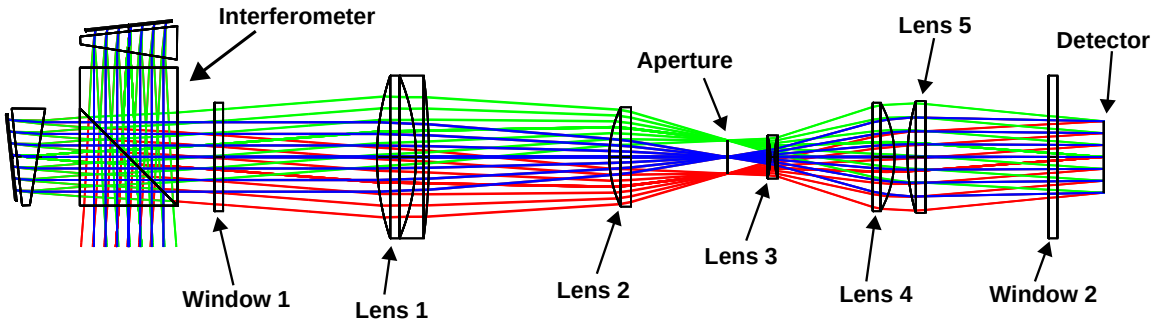

Figure 4.18: Configuration of a DASH instrument including the interferometer and the exit optics.

The half field of view of 4.5° cone angle was divided into 1888 small angles in the simulation. For each small angle, an interferogram can be calculated based on the tracing optical paths. The final interferogram is the superposition result of the 1888 interferograms. Since the detector consists of 2048 × 2048 pixels, 4194304 rays were traced for each interferogram. As shown in Figure 4.19(a) and Figure 4.19(b), the fringe images without and with thermal broadening were simulated. 1000-K thermal broadening was added in Figure 4.19(b) using Equation A.16. Since the spatial difference of the fringes in y direction is negligible, the interferograms at the center of the fringe images are plotted in Figure 4.20(a). Owing to the fact that the modulated part and DC bias can be isolated in the spectral domain, the visibility can be estimated using Equation A.17. The visibilities of the interferograms in Figure 4.20(a) are presented in Figure 4.20(b).

The visibilities of the interferogram without thermal broadening are mostly larger than 0.80 and the values in the middle are larger than 0.97. When thermal broadening is considered, the visibilities decline with the increase of OPD but are mostly larger than 0.65. The high visibilities in the simulated interferograms indicate that the design system is capable of receiving radiation from a relatively large solid angle with high fringe contrasts.

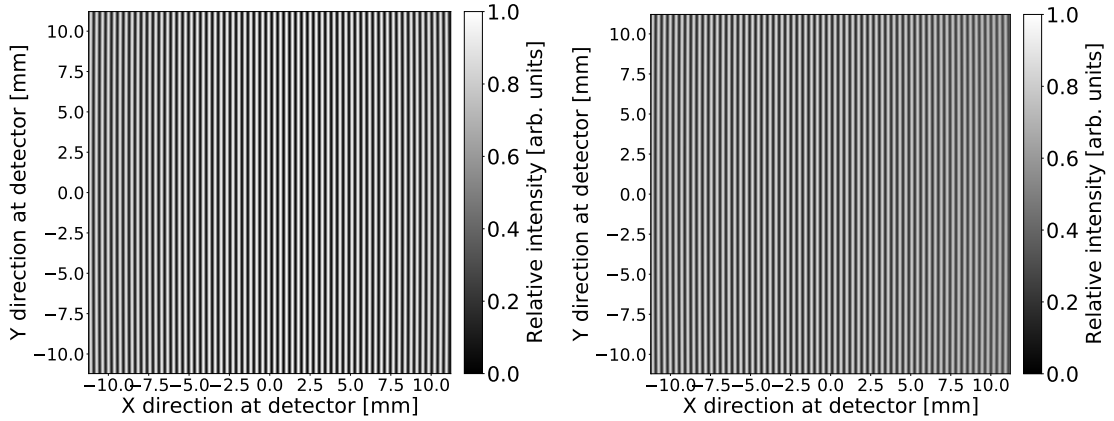

(a) Interferogram withou thermal broadening

(b) Interferogram with 1000 K broadening

Figure 4.19: Simulated interferograms with and without thermal broadening.

4.4 Instrument Performance Model

Section 4.1 and Section 4.2 give the designed interferometer and camera optics, and the estimated interferogram is analyzed in Section 4.3. The alignment tolerance and manufacturing tolerance make the system deviate from the ideal performance, which is required to be considered during design phase. In this section, the tolerance analysis is performed using the defined merit function and the final system performance is modeled.

4.4.1 Tolerance Analysis

Tolerances in the DASH interferometer change the system Littrow angle and degrade the field-widening and thermal-compensation performances. Tolerances from camera optics deteriorate the imaging quality, which therefore results in the reduction of the fringe contrast. Based on Monte Carlo analysis, the tolerances from the interferometer

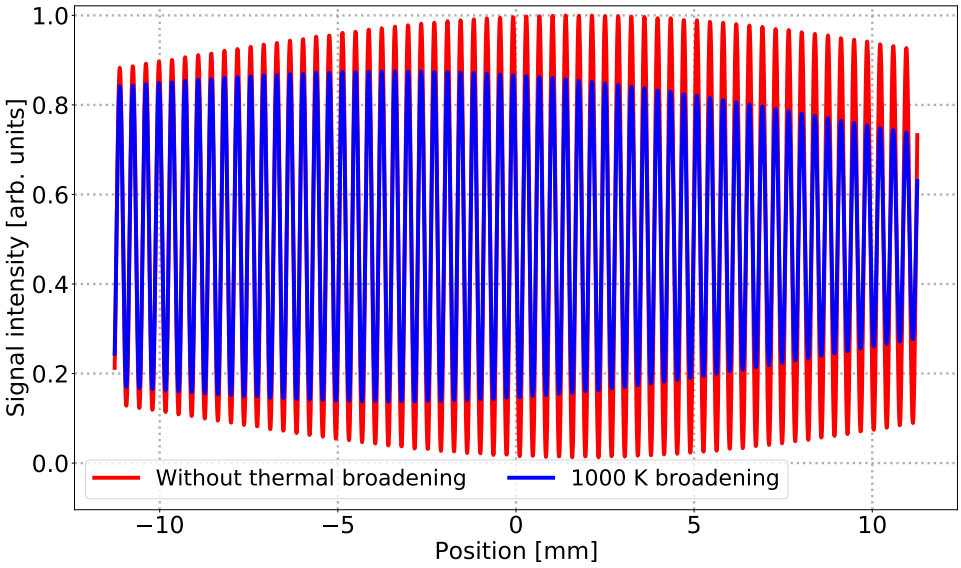

(a) Interferograms at the center of the fringe images

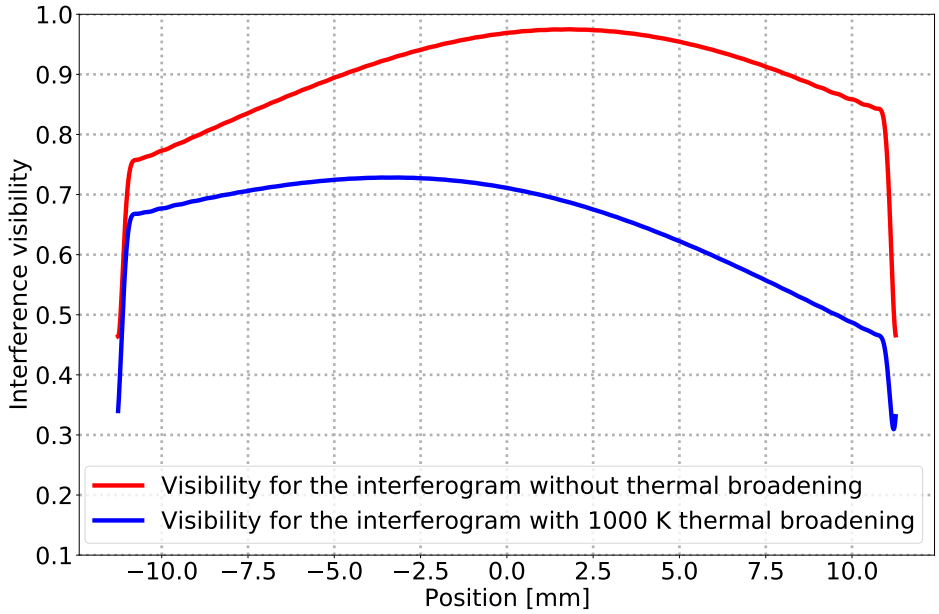

(b) Visbilities of the interferograms

Figure 4.20: Top panel: (a) Interferograms at the center of the fringe images in Figure 4.19(a) and Figure 4.19(b). Lower panel: (b) Visibility distribution of the interferograms plotted in the upper panel. Note that the visibilities decline on the edge results from the endpoint discontinuity artifacts and the estimations in this region are not correct.

and camera optics are analyzed simultaneously, and the tolerances of the interferometer and camera optics are summarized in Table 4.3. In order to ensure the field widening and thermal compensation, the strict angular tolerances ($\pm$30 arcsec) and dimensional tolerances ($\pm$0.02 mm) are required for the beamsplitter, field-widening prisms and spacers. For other off-shelf components, the tolerances are provided from the companies. The tolerances of spacing, tilt and decenter are the typical values for optical assemblies.

Table 4.3: Tolerances of interferometer and camera optics

Interferometer	
Dimension	$\pm$0.02 mm
Angle	$\pm$30 arcsec
Apex angle of field-widening prism	$\pm$15 arcsec
Groove density of gratings	$\pm$0.5 lines/mm
Surface quality	20-40
Surface flatness	λ/10
Surface flatness of grating	λ/4
Refractive Index	$\pm 5.0\times10^{-4}$
Abbe number	$\pm$0.5%
Camera optics	
Lens thickness	$\pm$0.1 mm or $\pm$0.15 mm
Spacing	$\pm$0.2 mm
Radius of curvature	1% of radius or $\pm$0.5 mm
Surface tilt	$\pm$1 arcmin
Element tilt	$\pm$3 arcmin
Element decenter	$\pm$0.02 mm
Surface irregularity	λ/4
Refractive Index	$\pm 5.0\times10^{-4}$
Abbe number	$\pm$0.5%

Owing to the tolerance difference on the two arms, the Littrow angles on the two arms will be different. In order to mitigate the difference, the first compensator, rotation of the interferometer, is defined. As shown in Figure 4.18, the distance between interferometer and window 1 and the distance between lens 5 and window 2 can be adjusted during alignment. Therefore, the two distances are the additional compensators during tolerance analysis. Since the glue thickness of about 10 μm between the parallel spacer and the grating can also be adjusted, the corresponding individual compensator

on each arm is introduced, which sightly adjusts the incident angle and position of the grating. After adding the tolerance for each component, the compensators are optimized to maintain the high visibility of the interferogram. Equation 4.13 is used for the criterion of the optimization and the Littrow angles are also constrained. Note that the tolerance of each component follows a normal distribution and only the angle tolerances on the dispersion plane of the grating are considered in this analysis.

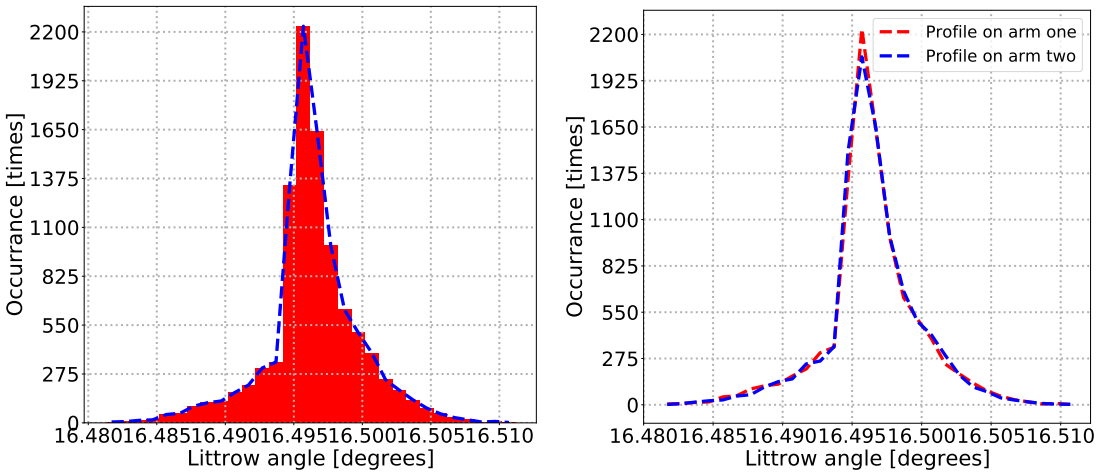

(a) Histogram of Littrow angle on arm one

(b) Comparison of the histogram profiles

Figure 4.21: Distribution of the Littrow angles on two arms.

10000 Monte Carlo simulations were performed, and the corresponding Littrow angles on arm one and arm two were obtained. In order to compare the distribution of the Littrow angles, the histogram of Littrow angle on arm one and the comparison of the two histogram profiles are presented in Figure 4.21(a) and Figure 4.21(b), respectively. The Littrow angle has same distribution on arm one and arm two, and most of the Littrow angles are in the range from 16.495° to 16.50°. According to the value of the merit function, the configurations with the highest visibility and lowest visibility were obtained, and the corresponding interferograms considering 1000 K broadening were also simulated using the ray-tracing information. The simulated interferograms at the center of the detector are plotted in Figure 4.22(a). Owing to the difference of the Littrow angle, the spatial frequencies of the interferograms are different. The corresponding visibilities are also estimated in Figure 4.22(b). Compared with the visibility in Figure 4.20(b), the visibilities decrease especially for the interferogram with the lowest fringe contrast, but the decline of the visibility is still in an acceptable range.

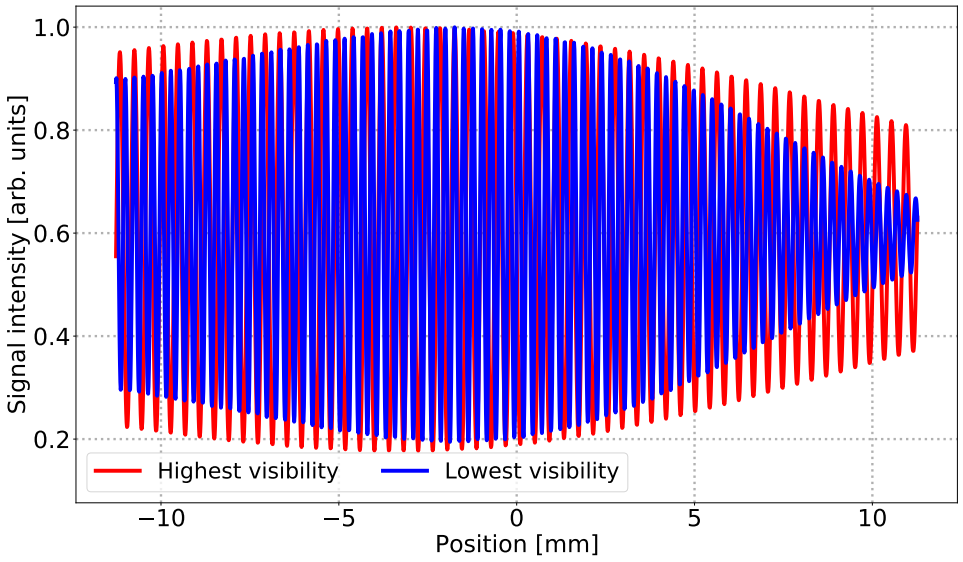

(a) Interferograms with the highest visibility and lowest visibility

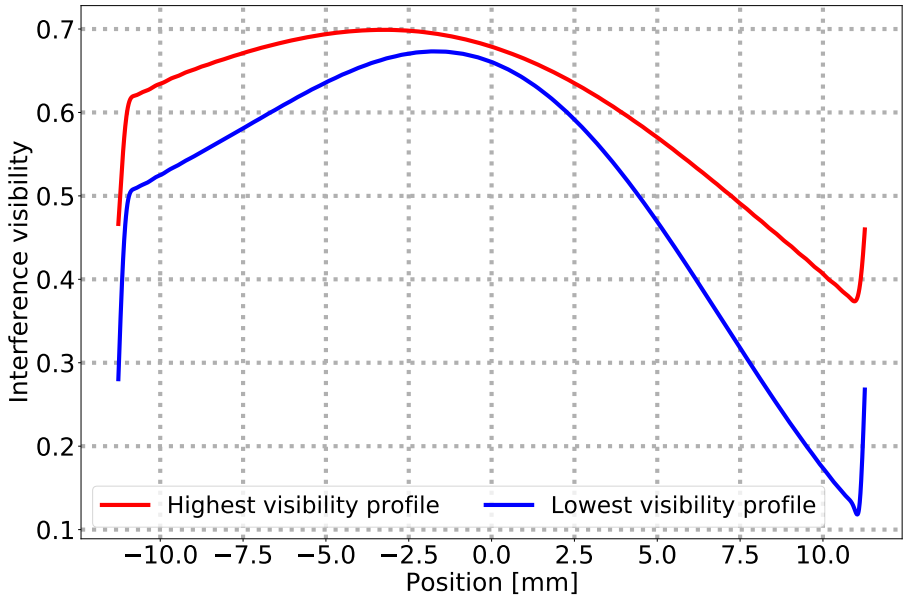

(b) Visibility of the interferograms with the highest visibility and lowest visibility

Figure 4.22: Top panel: (a) Interferograms with the highest visibility and lowest visibility. Lower panel: (b) Visibility profiles including the highest visibility and lowest visibility. Note that the visibilitity decline on the edge results from the endpoint discontinuity artifacts and the estimations in this region are not correct.

4.4.2 Instrument Uncertainty

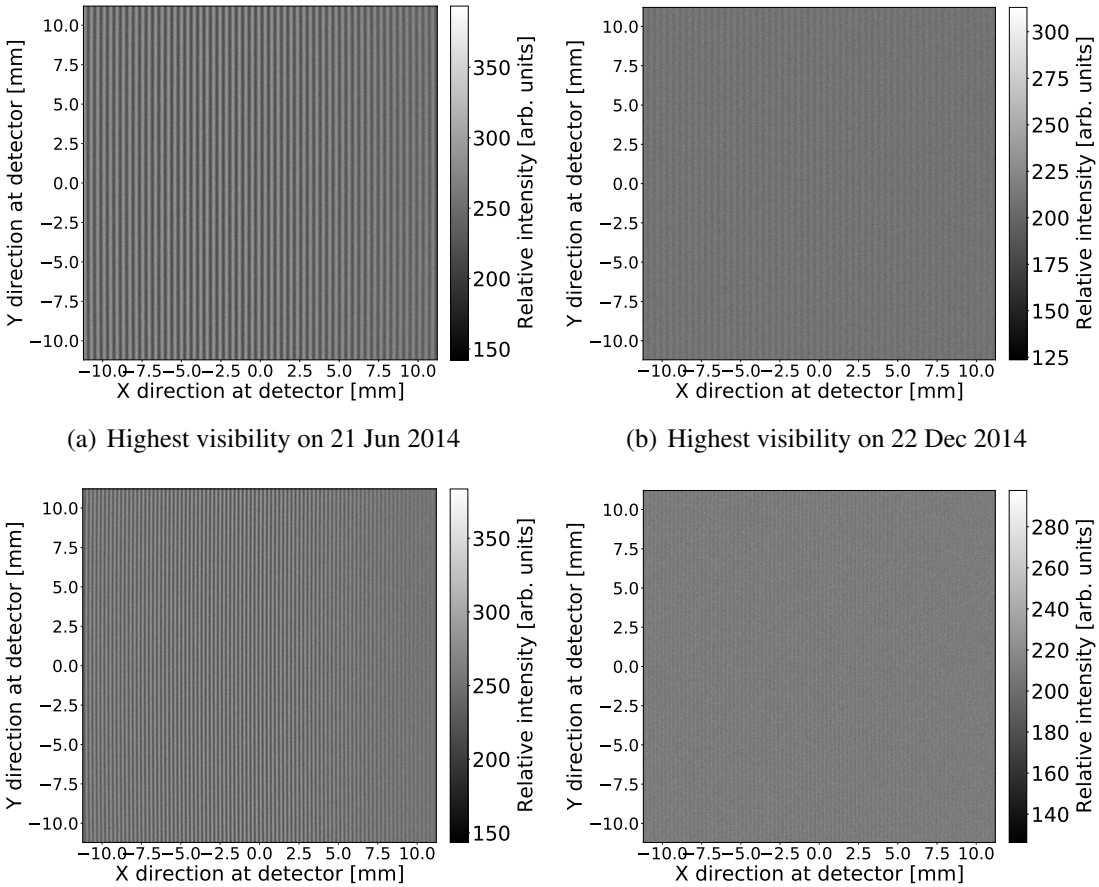

(a) Highest visibility on 21 Jun 2014

(b) Highest visibility on 22 Dec 2014

(c) Lowest visibility on 21 Jun 2014

(d) Lowest visibility on 22 Dec 2014

Figure 4.23: Upper plots: (a, b) Simulated fringe images using the configuration with the highest visibility on 21 Jun 2014 and 22 Dec 2014. Lower plots: (c, d) Simulated fringe images using the configuration with the lowest visibility on 21 Jun 2014 and 22 Dec 2014. Note that we assume the observations are carried out at Wuppertal (51.26°N, 7.15°E) and the elevation angle of instrument is 45 °

The configurations with the highest visibility and lowest visibility are obtained from the tolerance analysis. Based on the obtained configurations, the instrument performance can be predicted and the retrieval uncertainty can also be estimated. As discussed in Section 3.4, the SNR varies with the observation date and the solar activity also affects the signal intensity. Using the two configurations, fringe images from the observation on 21 Jun 2014 and 22 Dec 2014 with the local solar time at midnight are simulated

and shown in Figure 4.23. The exposure time is 5 minutes for each measurement and the parameters of detector shown in Table 3.2 are applied in this simulation. Since the intensity of airglow emission decreases during winter, the fringe contrast of the interferogram simulated for December degrades seriously and the SNR declines simultaneously. Compared with the configuration of the highest visibility, the worse fringe contrast and worst SNR appear in the interferograms obtained from the configuration of the lowest visibility. Consequently, a system which can produce an interferogram with higher visibilities has a stronger ability to resist the effect from noise.

The number of photons collected by the instrument is limited, which results in the low SNR in the fringe image obtained. Taking an example of the fringe image in Figure 4.23(b), a slice interferogram at the center of the fringe image is shown in Figure 4.24(a). Owing to the predominant noise, the signal is submerged in the noise and the profile of the interferogram almost disappears. Calculating the average of 1600 rows interferograms in the central region of the fringe image, the average interferogram is plotted in Figure 4.24(b). Comparing the interferograms in Figure 4.24(a) and Figure 4.24(b), the SNR improves dramatically in the average interferogram and the profile of the interferogram is visible in Figure 4.24(b). Therefore, a binning process calculating the average value of several rows of inteferograms is necessary for the wind retrieval.

To further investigate the effects of the solar activity and the interference visibility, a series of interferograms with Doppler shifts are produced using ray-tracing software, and the corresponding noise are added into the interferograms according to the observation date and detector performance. As discussed in Section 1.2, wind velocities from 20 m/s to 120 m/s in the thermosphere are reasonable, so that Doppler velocities from 20 m/s to 120 m/s are considered in the interferograms. Since 2009 and 2014 are the years with the lowest solar activity and the strongest solar activity in a recent solar cycle, measurements in summer and winter of these years are studied here. Owing to the randomness of noise, 1000 Monte Carlo simulations were performed for each estimation, and then the relative errors and absolute errors were calculated using the average results of all simulations. The averages of 1600 rows interferograms were employed in retrieval routines, and the instrument uncertainties of the two configurations are estimated in Figure 4.25. For the configuration of the highest visibility, the worst retrieval error appears on the 22 Dec 2009 when the signal intensity is lowest and the measurement accuracy only achieves around 25 m/s. However, the accuracy in the summer measurements is dramatically increased to the value less than 3 m/s. On the other hand, the measurement using the configuration of the lowest visibility also performs best in the summer of 2014 and worst in the winter of 2009. But the highest accuracy is around 5 m/s and the lowest accuracy is around 35 m/s because of the deterioration of fringe contrast. Therefore, it is necessary to increase the exposure time to improve the measurement accuracy especially in the winter of the year with the lowest solar activity.

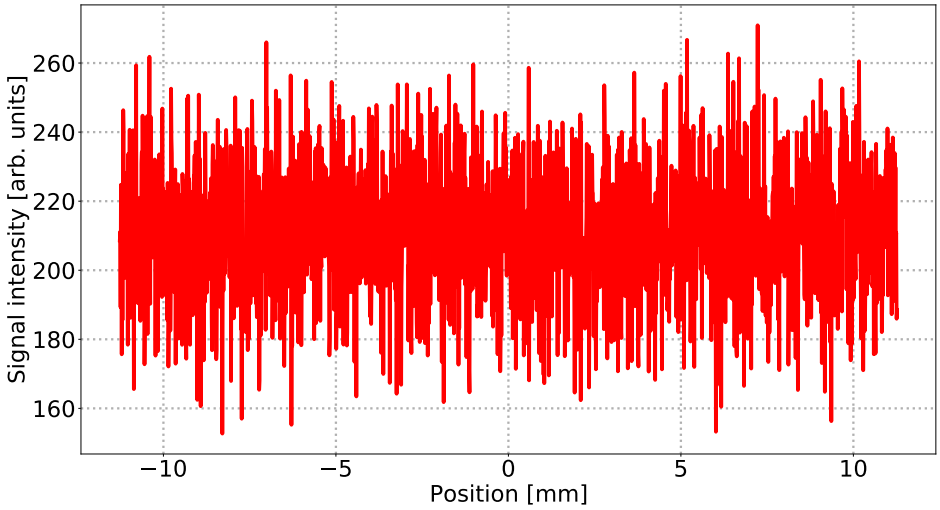

(a) Slice inteferogram at the center of the fringe image

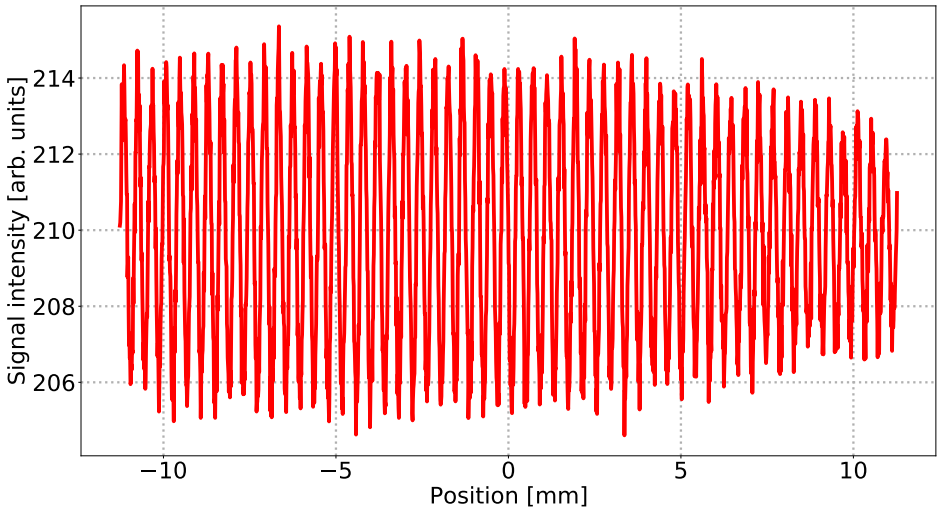

(b) Average of the 1600 rows interferograms

Figure 4.24: Top panel: (a) Slice interferogram at the center of the fringe image shown in Figure 4.23(b). Lower panel: (b) Average of the 1600 rows inteferograms in the central region of the fringe image shown in Figure 4.23(b).

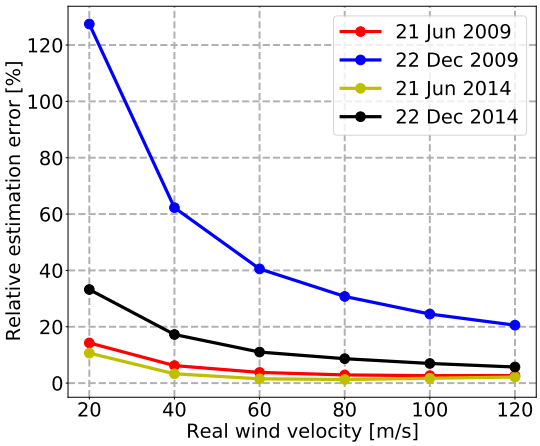

(a) Relative errors using the best configuration

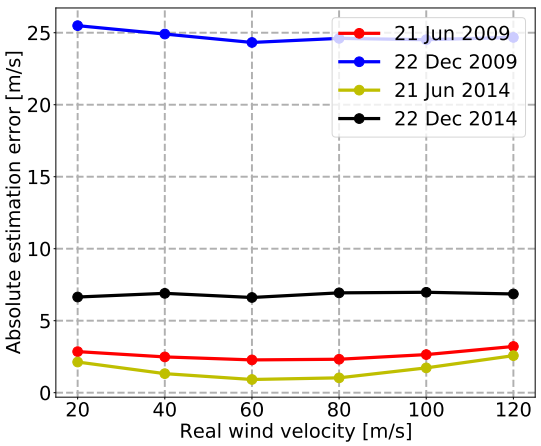

(b) Absolute errors using the best configuration

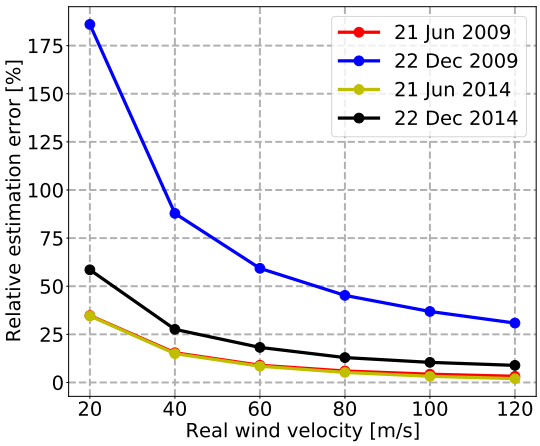

(c) Relative errors using the worst configuration

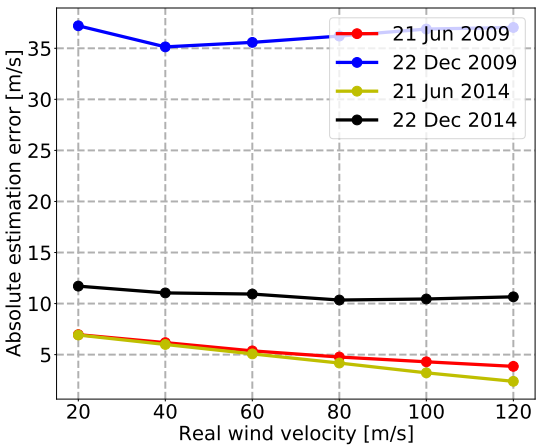

(d) Absolute erros using the worst configuration

Figure 4.25: Upper plots: (a, b) Relative and absolute estimation errors using the configuration of the highest visibility. Lower plots: (c, d) Relative and absolute estimation errors using the configuration of the lowest visibility. Note that the average of 1600 rows interferograms for each fringe image and the exposure time of 5 minutes are employed in the retrieval.

Chapter 5

Instrument Development

With the instrument design and the simulation provided in Chapter 4, our attention will turn to a development of a DASH instrument. A model to analyze the angle tolerance and alignment error is established, and this model helps us to develop a best assembly strategy and provides a theoretical basis to correct the interferogram. A setup which enables us to monitor the fringe contrast and spatial frequency in real time is developed to assemble a monolithic DASH interferometer in laboratory. With the designed double-telecentric system, properties of the interferometer are characterized from the aspects of the fringe visibility and Littrow angle. Before the wind velocity retrieval, a series of corrections must be performed for the raw interferograms. The spike signal, defect pixels, dark current and signal offset are determined by the performance of the detector, and those effects can be removed using the corresponding corrections. Similar to an SHI instrument, the flat-field correction and phase-distortion correction are also applied in a DASH system. The phase-distortion correction can eliminate the effects caused by the misalignment and optical defects. Thermally stable spatial frequency and optical phase are required to observe the thermospheric wind. Based on experimental measurements and the model study, the thermal performance of this interferometer is also investigated. To validate the capability of instrument to measure wind, laboratory Doppler measurements and instrument field tests are also discussed in this chapter.

5.1 Angle Tolerance and Alignment Error

Tolerances from manufacturing and alignment are inevitable, which makes the generated stripes deviate from the ideal fringe pattern. In section 4.4.1, influences of the tolerances on the interferogram visibility and spatial frequency are discussed. Some small angular errors distort the interferogram but do not affect the visibility of the inter-

ferogram seriously. In this section, interferograms with those small angle tolerances and alignment errors are modeled. With this model, an optimum alignment strategy can be devised. Owing to the fact that the fringe pattern is determined by the OPD between two arms in a DASH system, the outcome to analyze the change on one arm is equivalent to the outcome to analyze the relative change between both arms. Assuming that one arm is fixed, the angle tolerances and alignment errors on another arm are modeled in the following.

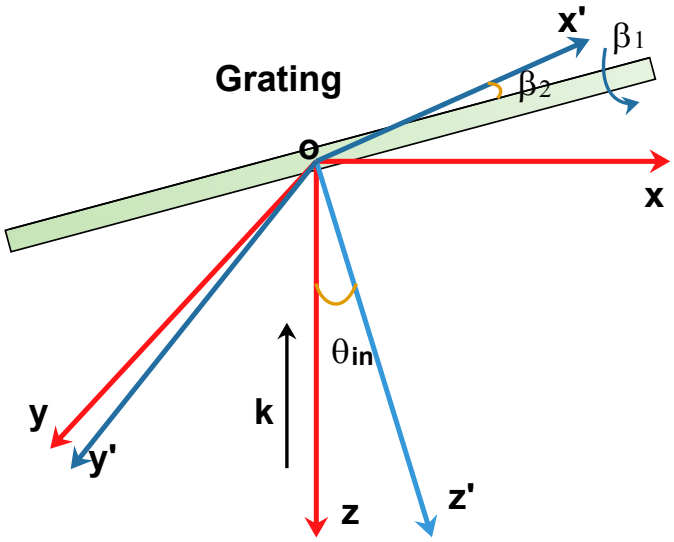

Figure 5.1: Coordinate systems of the grating. The groove of the grating is along the y axis, but it changes to be along the y' axis after introducing the angle deviation β_2.

On one arm, a coordinate xyz is established with the origin on the grating, as shown in Figure 5.1. The line oz' is the normal of the grating, and a wave vector is incident on the grating at an angle θ_{in}. Accordingly, the spatial frequency of the interferogram f_x produced by the grating dispersion can be expressed as

$$f_x = 4 \tan \theta_{in} (\sigma - \sigma_L), \tag{5.1}$$

with the incident wavenumber σ and the Littrow wavenumber σ_L. This deduction is based on the assumption that the incident wave vector is along optical axis and the field widening performs well, which means that the spatial frequencies of the interferograms produced from different incident angles are coincident within the cone angle of field of view. Consequently, the tolerance in angle θ_{in} affects the spatial frequency of the interferogram. As shown in Figure 5.1, if there is a small rotation angle β_1 about the direction perpendicular to the groove of the grating, an additional wavefront tilt in y direction is created consequently. This tilt introduces a spatial modulation in y direction and the corresponding spatial frequency f_y is

$$f_y = 2\beta_1\sigma. \tag{5.2}$$

As illustrated in Figure 5.1, another angle deviation is β_2, which is produced by rotating the grating about its plane normal z'. This angle also can be considered as the angle between the grooves of the two gratings when viewed from the exit pupil. The modeling of this effect on interferogram is studied in Appendix C.1. According to the conclusion in Appendix C.1, this small angle β_2 does not change the component of the wave vector in x direction but introduces an additional wave vector in y direction with the value $-\beta_2\frac{m\lambda}{d}$, which is related to the groove spacing of the grating d and the diffraction order m. Therefore, a spatial modulation in y direction is produced

$$f_y = \beta_2\frac{m}{d}. \tag{5.3}$$

This f_y is a function of the diffraction order rather than the wavenumber, which means that the interferograms along y direction can not be resolved except they are produced from different-order diffraction. Combining Equation 5.1, Equation 5.2 and Equation 5.3, the fringe pattern is recast as

$$\begin{aligned} I(x,y) \propto 1 + V(x,y)\cos\{2\pi[&2\tan\theta_1(\sigma-\sigma_{L1})x \\ &+2\tan\theta_2(\sigma-\sigma_{L2})x + \left(2\beta_1\sigma+\beta_2\frac{m}{d}\right)y + 2\Delta d\sigma + \Theta(x,y)\Big]\Big\}, \end{aligned} \tag{5.4}$$

where $V(x,y)$ represents the interference visibility, θ_1 and θ_2 are the Littrow angles on arm 1 and arm 2, σ_{L1} and σ_{L2} are the corresponding Littrow wavenumbers, $\Theta(x,y)$ represents the local phase induced by optical defects.

If the Littrow angles on both arms are difference, the interferogram with a spatial frequency of zero value can not be found. Using different monochromatic sources, the monitoring of the zero-spatial-frequency interferogram confirms the equivalent of two Littrow angles on both arms during assembly. Both of the angle deviations β_1 and β_2 produce the spatial modulation in y direction, which is different from the modulation produced by the grating dispersion. The spatial frequency in y direction caused by β_1 is not heterodyned but the low spectrum resolution still exists in its interferogram. On the other hand, the interferogram along y direction caused by the dislocation of the two gratings loses the spectral resolution, but it can resolve the interferograms produced from the different-order diffraction. Since the angle tolerances from the three degrees of freedom of the grating distort the interferogram, it is necessary to precisely adjust those angles during interferometer assembly.

5.2 Monolithic DASH Interferometer Assembly

Compared with the mechanical mounts, a monolithic interferometer is robust and less massive. The monolithic configuration is achieved by the connecting spacers made of optical glasses, which bridge the separate components. Owing to the features of strong bond, fast cure and excellent light transmission, Norland UV curing optical adhesive is selected to cement the individual elements. To prevent the glue flowing into the grating groove, a base plate made of fused silica is applied here. At first, the grating and parallel spacers were bonded into this base plate. Then the interferometer assembly was implemented by bonding the spacers to the beamsplitter, the field-widening prisms to the spacers, and the parallel spacers to the field-widening prisms step by step.

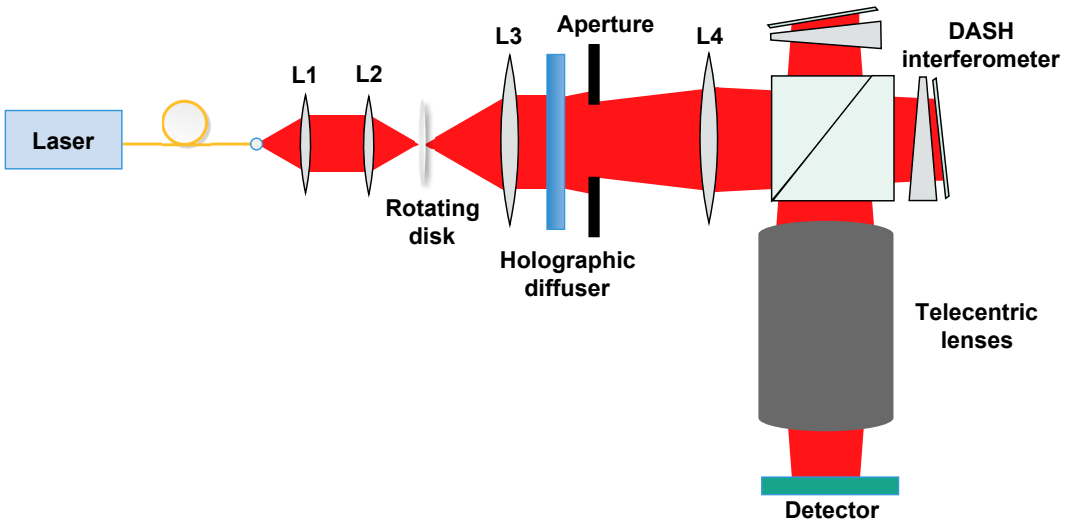

Figure 5.2: Schematic of the setup to monitor the fringe contrast and spatial frequency during final assembly. Note that L denotes lens and the designed double-telecentric lenses are applied in the camera optics.

As discussed in Section 5.1, small angle deviations distort the fringe pattern, which requires an accurate alignment during the bonding between the parallel spacers and the field-widening prism. As shown in Figure 5.2, a setup to monitor the fringe contrast and spatial frequency was constructed, which allows aligning the interferometer in real time before UV curing. The monochromatic light provided from a tunable laser is focused onto a rotating disk, which is used to suppress laser speckle. After passing through lens L3, the collimated light is diffused by a holographic diffuser, which produces a relatively homogeneous radiation. The radiation is focused onto the grating by lens L4, and an aperture is located at the front focal plane of lens L4, so that a telecentric illumination on the grating is achieved. The diameter of the aperture is chosen to realize 4.5° cone angle illumination on the gratings. The designed double-telecentric system

is implemented to relay the fringe pattern to the detector. A jig enables us to tip, tilt and rotate the gratings to avoid the angle deviation in θ_{in}, β_1 and β_2 as discussed in Section 5.1. The jig and fixture on one arm are presented in Figure 5.3. Note that we chose a small detector with 5.04 μm pixel size to record the fringe pattern instead of the detector employed in the designed DASH instrument. As shown in Figure 5.4(a) and Figure 5.4(b), interferograms before UV curing and after UV curing were recorded. Comparing the interferograms, the orientation changed after the glue hardened, which resulted from the shrinkage of the glue and the fixture instability. Finally, a monolithic DASH interferometer was built in the laboratory and the photograph of the built DASH is shown in Figure 5.5.

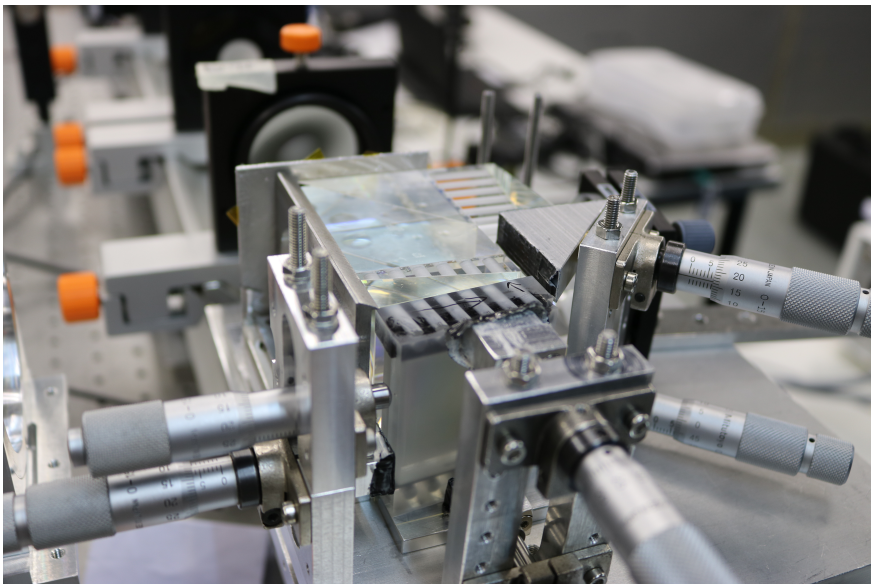

Figure 5.3: Photograph of the jig and fixture on one arm.

5.3 Property Characterization

5.3.1 Experimental Setup

To characterize the performance of the interferometer, a breadboard system was constructed as illustrated in Figure 5.6. After passing through the rotating disk, the narrow linewidth laser was focused into the sphere by lens L4, which then generates a uniform distribution on the output port of the integrating sphere by multiple scatterings. A baffle was inserted between the integrating sphere and the interferometer to eliminate the stray light, so that the uniform radiation within the desired field of view (4.5° half cone angle)

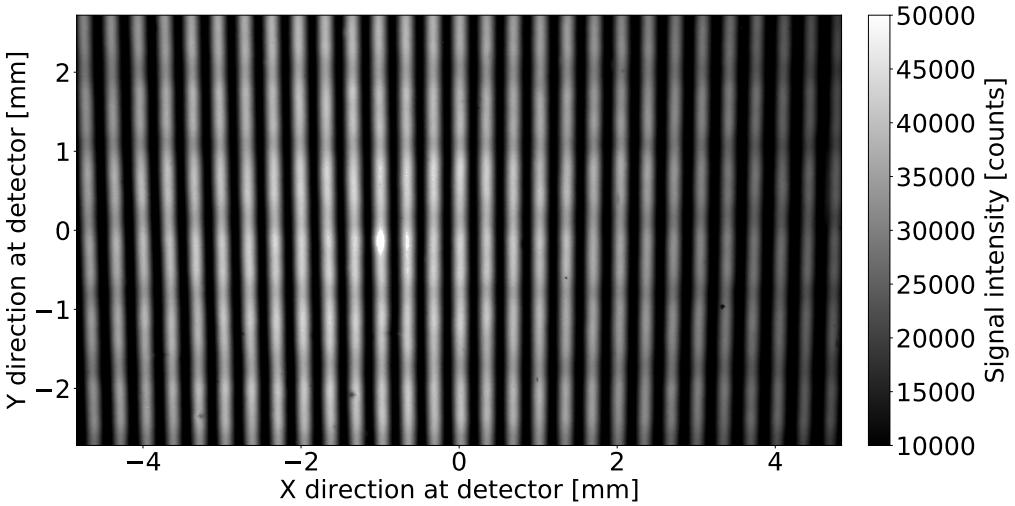

(a) Interferogram befor UV curing

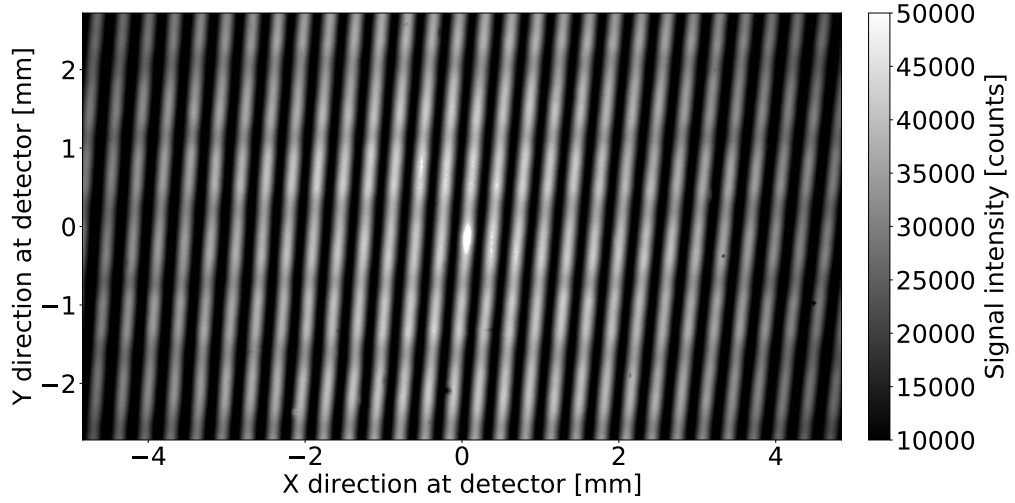

(b) Interferogram after UV curing

Figure 5.4: Interferograms before and after UV curing.

illuminates the interferometer. The position of the baffle is chosen to match the size of the entrance pupil, and details of the baffle are described in Appendix C.2. Owing to the low distortion and stable performance, the designed telecentric lenses are applied to image the fringes from the localization plane onto the array detector. Note that the role of the rotating disk is to suppress laser speckle because the emergence of speckles can deteriorate the fringe pattern.

Figure 5.5: Monolithic DASH interferometer. Each spacer, including spacer 1, spacer 2 and parallel spacers, consists of two identical prisms with several through holes.

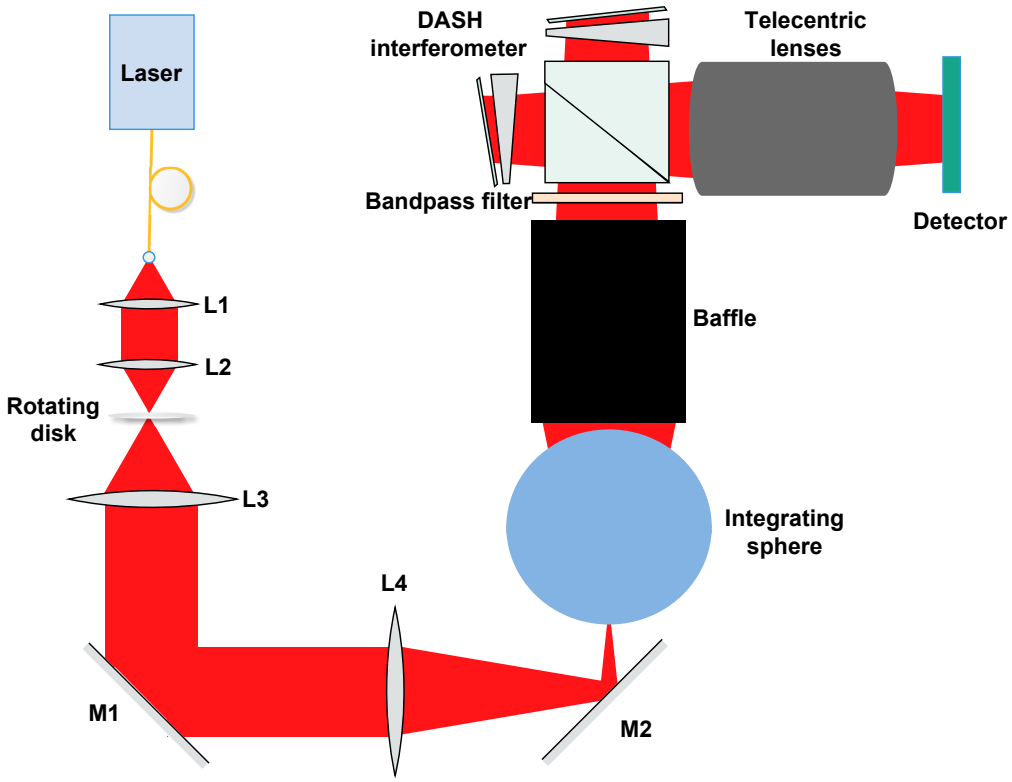

Figure 5.6: Schematic of the laboratory test setup. Different monochromatic homogeneous illumination is obtained by a combination of tunable laser and integrating sphere. L denotes lenses, and M denotes mirrors.

5.3.2 Interference Visibility

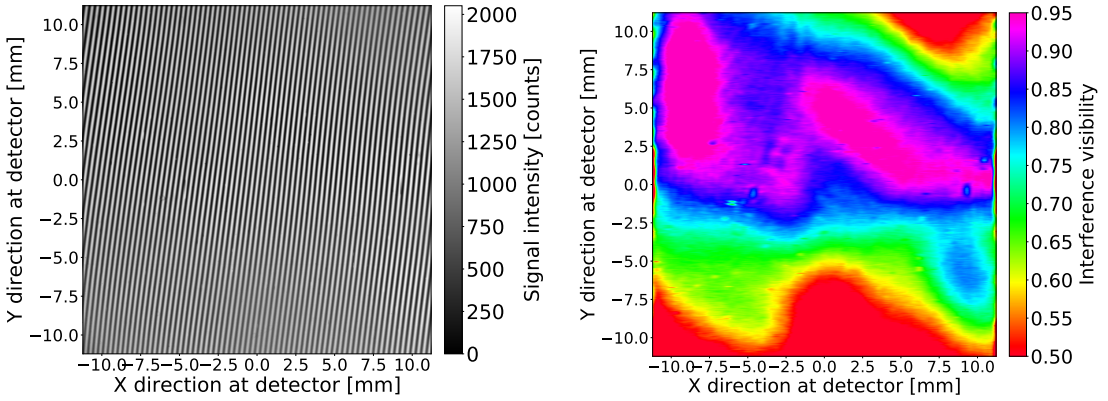

(a) Measured interferogram

(b) Visbility of the obtained interferogram

Figure 5.7: (a) Measured fringe image at a wavelength of 630.03 nm when the 4.5-degree half cone angle radiation illuminates the interferometer and (b) the corresponding visibility of the obtained interferogram.

Based on the setup illustrated in Figure 5.6, a fringe image was recorded when the interferometer viewed the output port of the integrating sphere. The fringe image is shown in Figure 5.7(a) and its corresponding visibilities are presented in Figure 5.7(b). The interference visibility was estimated by the ratio of the signal amplitude to the signal DC bias. The signal-modulated portion can be isolated using a suitable window function and backward transformation in the spectral domain (*Englert et al.*, 2007). Then the signal amplitude can be calculated from the modulus of the isolated signal. Implementing the inverse Fourier transform for the isolated DC component in the spectral domain also yields the signal DC bias. As shown in Figure 5.7(b), the fringe contrasts are higher than 0.7 except the bottom area and the visibility higher than 0.9 is realized in some areas. In addition, an interferogram at the center of Figure 5.7(a) is plotted in Figure 5.8(a) and its visibility as a function of position is estimated in Figure 5.8(b). The estimated envelope is the sum of signal amplitude and signal DC bias. The good evaluation of the interferogram envelope in Figure 5.8(a) verifies the accurate determinations of the signal amplitude and the signal DC bias. Figure 5.8(b) indicates that all of the visibilities are larger than 0.8 in general and the maximum value achieves 0.94 when 9° field-of-view illumination is applied. The serious declines appear on both sides of the envelope and the visibility, which is related to the endpoint-discontinuity artifacts. The estimations of envelope and visibility are not correct in this region. Compared to the design visibilities (general value: larger than 0.8, highest value: 0.97) in Figure 4.20(b), the visibilities slightly decrease. Therefore, the field widening preforms well in this in-

terferometer and the interferogram with high fringe contrasts can be obtained using this interferometer.

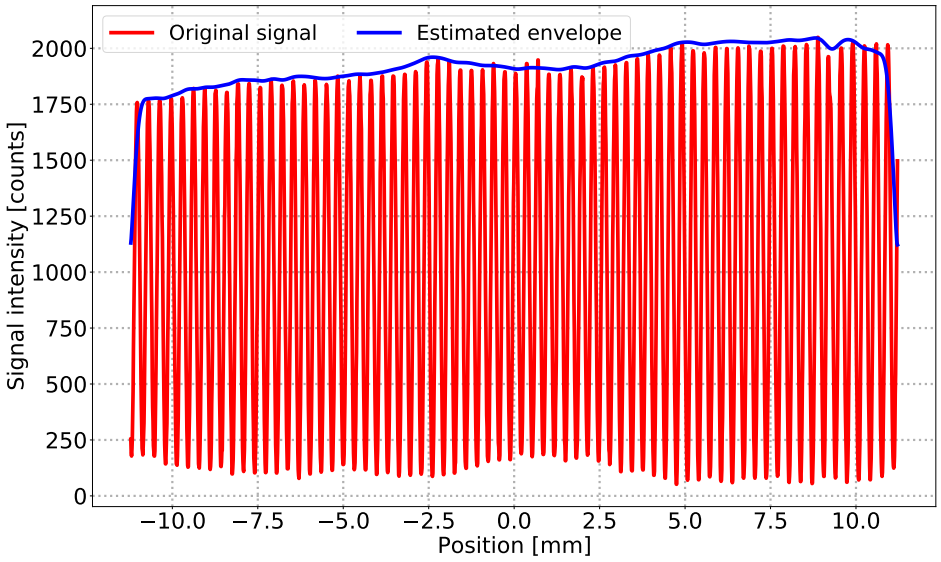

(a) Interferogram at the center of the fringe image

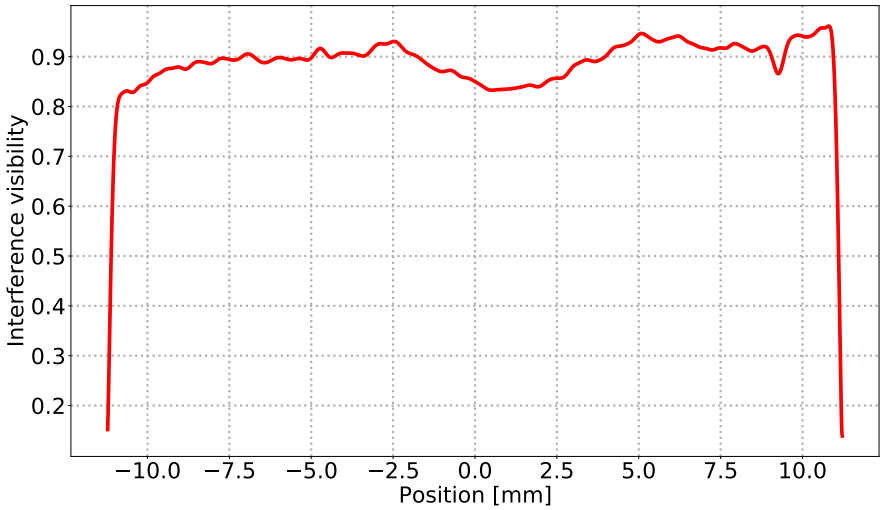

(b) Visbility of the slice interferogram

Figure 5.8: Upper panel: (a) Slice interferogram at the center of the fringe image in Figure 5.7(a) and the corresponding envelope. Lower panel: (b) Visibility distribution of the slice interferogram plotted in the upper panel.

5.3.3 Littrow Angle

The Littrow angle determining the interferogram spatial frequency was characterized based on the setup of Figure 5.6 using a tunable laser. Two methods, phase analysis and spectrum analysis, are discussed to determine the spatial frequency. The phase of an interferogram can be determined by calculating the arctangent value of the ratio of the imaginary part and real part of the modulated component using Equation 2.13. Then the spatial frequency can be considered as the quotient of the rate of phase change with position and 2π. For the spectrum analysis, the corresponding spatial frequency of the spectrum peak corresponds to the interferogram spatial frequency. In order to compare the Littrow angles and Littrow wavelengths in different regions, the detector was divided into 3 sub-regions from the bottom to the top. For each sub-region or whole detector, a two-dimensional Fourier transform was applied to the fringe image to produce a two-dimensional spectrum, which was then averaged to obtain a one-dimensional spectrum. Note that both the phase analysis and the spectrum analysis are based on the one-dimensional spectrum obtained. During the spectrum analysis, zero padding by a factor of 100 is added for each row of the interferogram before the Fourier transform. Fitting a linear function to the measured points yields the relation between the spatial frequency and the input wavenumber shown in Figure 5.9(a) and Figure 5.9(b). The results calculated from two methods are in good agreement with 99.999% consistency.

As shown in Figure 5.9(b), the retrieved Littrow angles using the averages of the whole detector, rows 45-694, rows 695-1344 and rows 1345-1994 are 16.49363°, 16.49362°, 16.49380° and 16.49460°, respectively. Obviously, the vertical variation exists especially in the top region, and the Littrow angle becomes larger in the region closer to the top, which may be caused by the asymmetry of the beamsplitter, field-widening prism and diffraction grating. The variation of the Littrow angle causes the variation of the spatial frequency, which deteriorates the visibility of the interferogram obtained from the average of several rows interferograms. In general, the average of several rows interferograms is used for the wind retrieval. But the small variation of Littrow angle can be corrected in the phase-distortion correction discussed in Section 5.4.4. This variation does not affect the Doppler wind measurement.

5.4 Interferogram Correction

The spike signal, defect pixels, dark current and other instrument effects may impact the fringe phase, which is the basis to retrieve the wind velocity in a DASH instrument. Before going through the retrieval routine, a series of corrections must be performed for the raw interferograms. The following study provides the details on the interferogram corrections, and the step-by-step corrections should be performed in sequence.

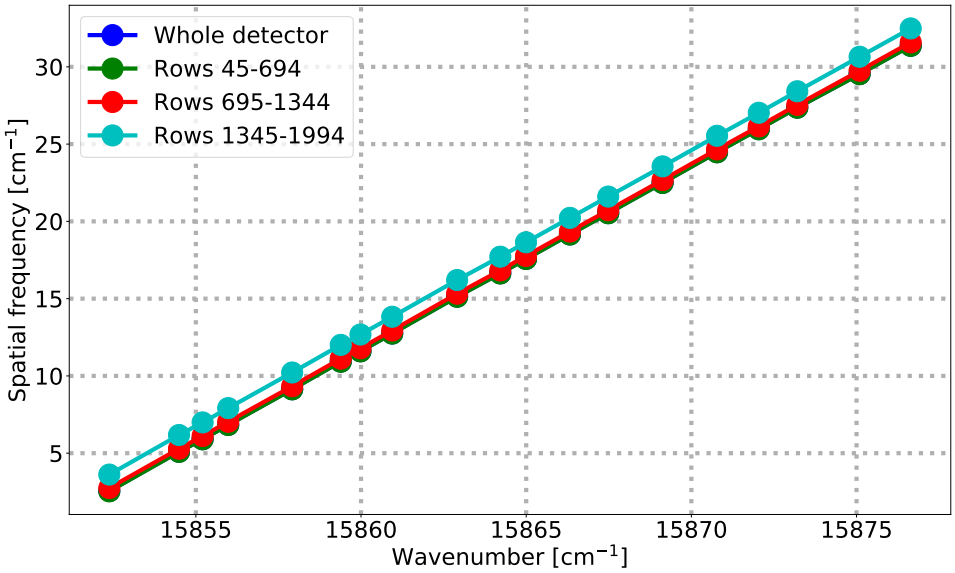

(a) Phase analysis

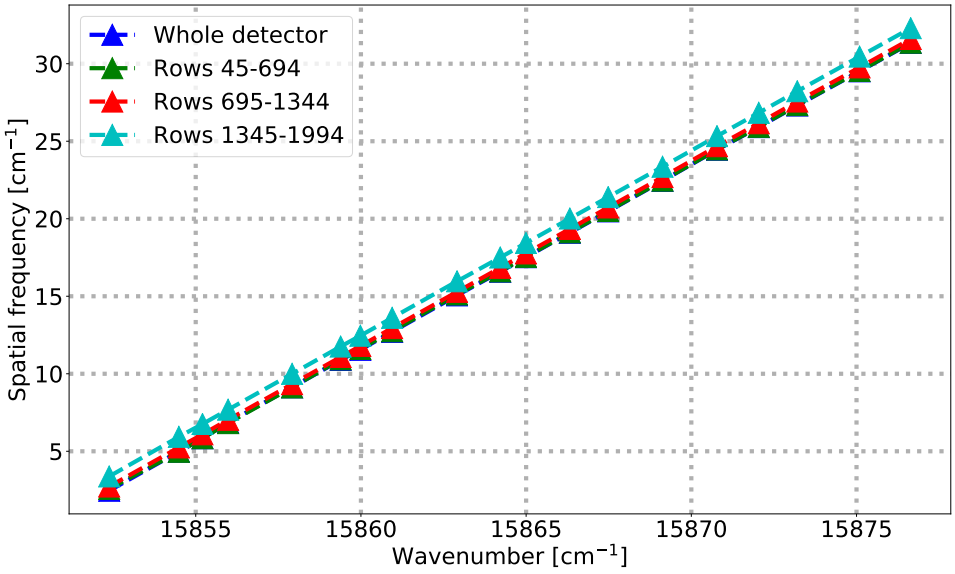

(b) Spectrum analysis

Figure 5.9: Interferogram spatial frequency as a function of the emission wavenumber. All of the wavenumbers are given with respect to air. Blue circles (phase analysis) and blue triangles (spectrum analysis) are covered by green circles and green triangles because of the almost consistent Littrow angles.

5.4.1 Spike and Defect Removal

The presence of hot pixels and defect pixels causes a local discontinuity in the fringe pattern. The pixels with zero-signal intensity or close to zero value can be considered as defect pixels. The signal of the ground-based instrument is the sum of the airglow emission at all altitudes, so that the signal obtained on the detector varies slowly with position. Owing to this fact, the signal spikes can be identified. After the signal spikes and defect pixels are identified, the signals of the pixels are replaced by the mean of the adjacent pixels. In order to further eliminate those effects, a median filtering for the interferograms with a suitable window can also be considered.

5.4.2 Dark Current and Signal Offset Correction

A CMOS sensor is implemented to record the signal and the performance of this detector is characterized in Section 3. The dark current and signal offset are always accompanied by the fringe image detection. Due to the low emission intensity and longer exposure times, the dark current is predominant in the signal recorded on the detector, which seriously degrades the interfrogram visibility. The fixed pattern of detector produces a signal offset at each pixel, which also affects the fringe contrast. With the same exposure time and detector temperature, a dark image can be taken by closing the entrance aperture of instrument. For the interferogram obtained, the dark current and offset correction can be accomplished by subtracting this dark image. With an illumination of the neon lamp and a 3-minutes exposure time, interferograms were recorded and the interferograms with and without the dark current and signal offset are presented in Figure 5.10(a) and Figure 5.10(b). Comparing the interferograms, the fringe contrast increases greatly after subtracting the dark current and signal offset. Since there is no cooling for the detector, massive dark current and consequent noise exist in the interferograms especially in the bottom region shown in Figure 5.10(a). The readout electronic of the CMOS sensor is placed behind the bottom region of the detector, and the consequent heat increases the dark current in this region.

5.4.3 Flat-field Correction

Flat-field technique is developed to eliminate the pixel-to-pixel variations in an SHI instrument (*Englert and Harlander*, 2006). The discussion of flat-fields in DASH interferometry was presented by *Marr et al.* (2012). They pointed out that the flat field has a significant effect on the fringe phase calculation, but the effect on the phase difference between two fringes, the key to derive the wind velocity, remains small (*Marr et al.*, 2012). Although the uncertainty in wind velocity retrieval caused by the uncorrected

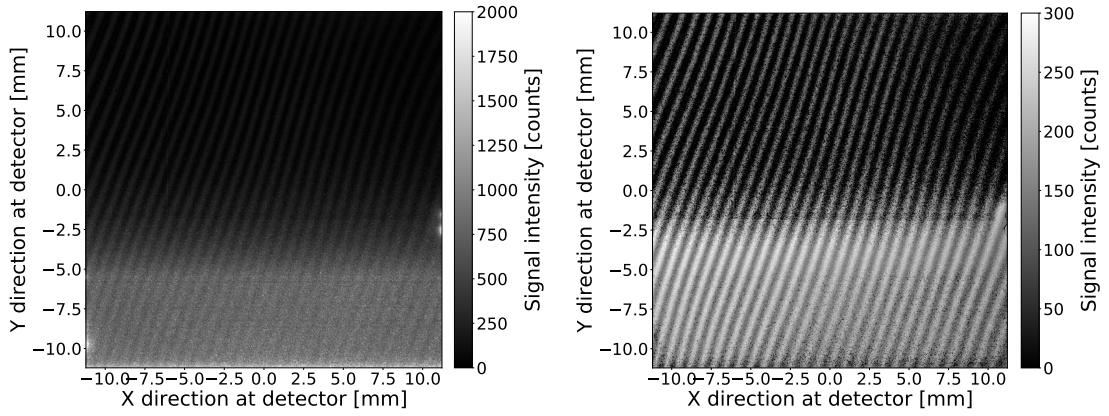

(a) With the dark current and signal offset (b) Without the dark current and signal offset

Figure 5.10: Interferograms with and without the dark current and signal offset at a wavelength of 630.479 nm. Note that the illumination is provided by a combination of a neon lamp and an optical bandpass filter.

flat field is small, it is also suggested to correct the flat field before the derivation of the phase change.

In a non-ideal DASH instrument, the monochromatic interferogram as a function of position can be written as

$$I(x,y) = \int_0^\infty B(f)\,R(x,y)\left[t_{one}^2(x,y) + t_{two}^2(x,y)\right]df + \int_0^\infty 2B(f)\,R(x,y)\,t_{one}(x,y)\,t_{two}(x,y)\,\varepsilon(f,x,y)\cos\left[2\pi fx + \Phi(f,x,y) + \Theta(f,x,y)\right]df, \tag{5.5}$$

where f is the spatial frequency of the fringe, $B(f)$ is the spectral density, $R(x,y)$ is the detector responsivity at the position x and y, $\varepsilon(f,x,y)$ is the modulation efficiency for the spatial frequency f, $t_{one}(x,y)$ and $t_{two}(x,y)$ are the amplitude transmission functions when the radiation passes through the interferometer arm one and arm two, respectively (*Englert and Harlander*, 2006). The term $\Phi(f,x,y)$ is the phase offset, which results from the asymmetric optical path on the two arms. The term $\Theta(f,x,y)$ is introduced to describe the phase distortion cased by optical defects or image distortion and this term does not affect the flat field. The purpose of the flat-field correction is to eliminate the effects from the terms $R(x,y)$, $t_{one}(x,y)$ and $t_{two}(x,y)$. Note that the Equation 5.5 is based on the assumption that the optical transmittances and the detector responses are identical within the wavelengths of the bandpass filter.

In general, there are three different approaches to realize a flat-field correction including a balanced arm approach, unbalanced arm approach and phase-shift approach (*Englert and Harlander*, 2006). *Marr et al.* (2012) discussed the flat field in a DASH system using the temperature variation to shift the phase. The phase-shift approach is based on the derived phase to correct the flat field, which is contradictory to the fact that the flat field affects the calculation of fringe phase. Here we adopted an unbalanced arm approach to correct the flat field, and the unbalanced arm is a feature of a DASH interferometer. The unbalanced arm approach is based on the recorded intensity distribution when one arm is blocked. When arm two is blocked, the signal intensity at position of x and y can be expressed as

$$I_{one}(x,y) = \int_0^\infty B(f)\, R(x,y)\, t_{one}^2(x,y)\, df = K_1 R(x,y)\, t_{one}^2(x,y)\,, \tag{5.6}$$

with a scalar K_1, which is determined by the spectral density. Similarly, the signal intensity $I_{two}(x,y)$ yields when arm one is blocked

$$I_{two}(x,y) = \int_0^\infty B(f)\, R(x,y)\, t_{two}^2(x,y)\, df = K_1 R(x,y)\, t_{two}^2(x,y)\,. \tag{5.7}$$

Using Equation 5.5, Equation 5.6 and Equation 5.7, the quotient of $I(x,y)$ and the sum of $I_{one}(x,y)$ and $I_{two}(x,y)$ can be calculated by

$$\begin{aligned}\frac{I(x,y)}{I_{one}(x,y)+I_{two}(x,y)} =& K_2 + \frac{1}{K_1}\int_0^\infty 2B(f)\,\varepsilon(f,x,y)\,\frac{t_{one}(x,y)\,t_{two}(x,y)}{t_{one}^2(x,y)+t_{two}^2(x,y)} \\ & \cos\left[2\pi f x + \Phi(f,x,y) + \Theta(f,x,y)\right] df,\end{aligned} \tag{5.8}$$

with a scalar K_2, which is approximated to the average of Equation 5.8 over all pixels. In addition, the ratio of $t_{one}(x,y)\,t_{two}(x,y)$ and $t_{one}^2(x,y)+t_{two}^2(x,y)$ can be determined by

$$\frac{t_{one}(x,y)\,t_{two}(x,y)}{t_{one}^2(x,y)+t_{two}^2(x,y)} = \frac{\sqrt{I_{one}(x,y)\,I_{two}(x,y)}}{I_{one}(x,y)+I_{two}(x,y)}. \tag{5.9}$$

After subtracting the scalar K_2, the modulated part of Equation 5.8 remains. Then using the relation of Equation 5.9, the flat field is corrected and the corrected interferogram yields

$$I_C(x,y) = \frac{1}{K_1}\int_0^\infty 2B(f)\,\varepsilon(f,x,y)\cos\left[2\pi f x + \Phi(f,x,y) + \Theta(f,x,y)\right] df. \tag{5.10}$$

Since the spacers consist of two separate prisms, a black plate can be inserted between the beamsplitter and the field-widening prism to block the light transmission on this arm. Based on the setup of Figure 5.6, the signal distributions of arm one and arm two were recorded when arm two and arm one were blocked respectively. The recorded signal distributions are shown in Figure 5.11(a) and Figure 5.11(b). The interference disappeared when one arm was blocked, which is confirmed by the vanishing of the fringe in the signal distributions.

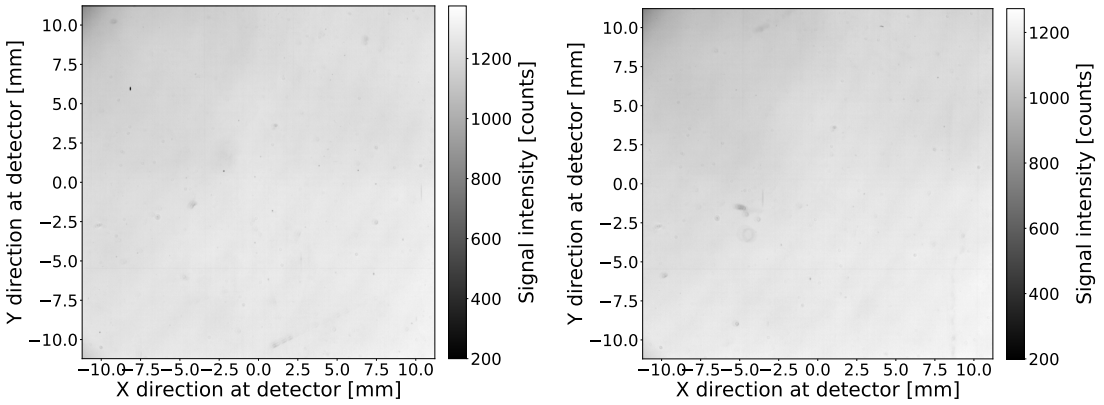

(a) Signal distribution when arm two was blocked (b) Signal distribution when arm one was blocked

Figure 5.11: Signal distribution when arm two or arm one were blocked

The flat field was corrected using the recorded results and the corrected interferogram are presented in Figure 5.12(a) and Figure 5.12(b). Compared with the original interferogram in Figure 5.7(a), the modulated parts are reserved and the fluctuations of the envelope become weakened. The slight wobbles of envelope in the corrected interferogram result from the variation of $\varepsilon(f,x,y)$. Notice that the illumination was provided by a laser, so that the thermal broadening can be neglected here.

5.4.4 Phase-distortion Correction

As discussed in Section 5.1, the misalignment of a DASH interferometer may produce a y-direction modulation with $f_y = 2\beta_1\sigma + \beta_2\frac{m}{d}$, and this modulation is related to the angle tolerances β_1 and β_2. The stripe tilt in Figure 5.7(a) indicates that the y-direction spatial frequency exists, which destroys the binning process calculating the average value of several rows of inteferograms. The binning process is a crucial step to improve system SNR, which is required for the ground-based thermospheric wind measurement. As described in Section 5.3.3, the variation of spatial frequency along the direction of grating groove appears in the interferogram, which also affects the binning process.

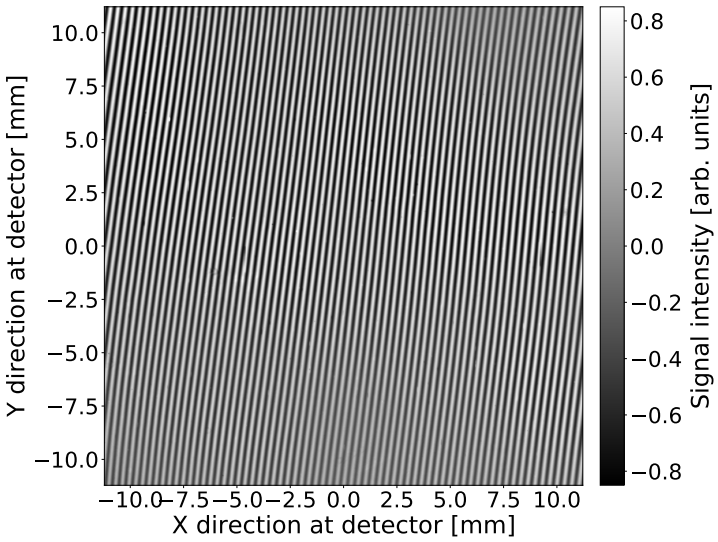

(a) Interferogram after flat-field correction

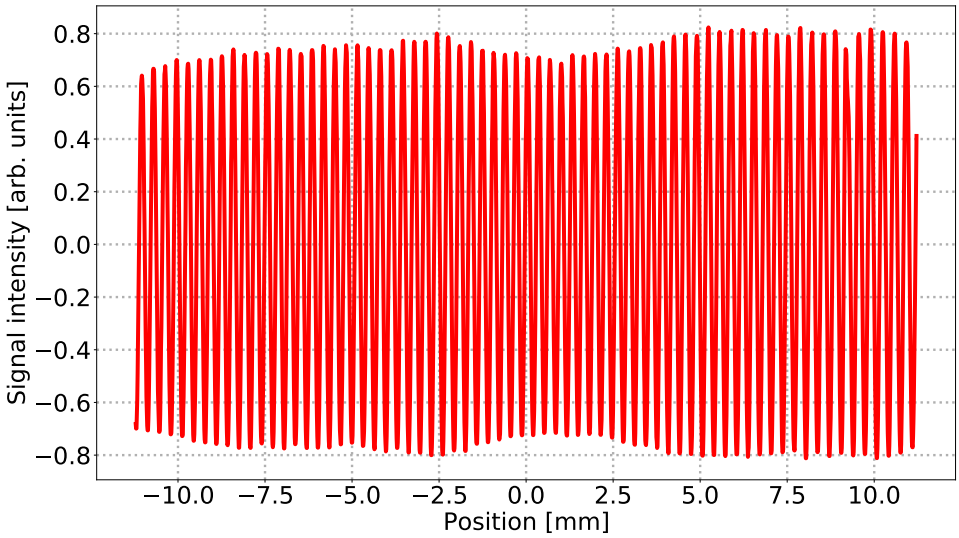

(b) Slice interferogram at the center of the corrected interferogram

Figure 5.12: (a) Interferogram after flat-field correction and (b) its slice interferogram at the center.

Moreover, the optical defects distort the interferogram, which causes an additional error. The phase-distortion correction is a general method to correct the interferogram obtained from an SHI instrument (*Englert et al.*, 2004). This technique can also eliminate the unwanted y-direction modulation, variation of spatial frequency and effect from the optical defects in a DASH interferometer.

According to Equation 5.4, the interferogram phase $\varphi(x,y)$ can be written as

$$\varphi(x,y) = 2\pi\left[4\tan\theta(\sigma-\sigma_L)x + \left(2\beta_1\sigma + \beta_2\frac{m}{d}\right)y + 2\Delta d\sigma + \Theta(x,y)\right]. \tag{5.11}$$

Here the Littrow angles on arm one and arm two are same because the zero-spatial frequency exists after assembly. The y-direction modulation and optical defects make the interferogram deviate from the ideal fringe pattern, so that the term from the y-direction modulation and optical defects can be considered as the phase distortion. Given a monochromatic interferogram, the phase information can be determined using the method described in Section 2.4. Using the Littrow angle and Littrow wavenumber obtained in Section 5.3.3, the phase distortion can be characterized by

$$2\pi\left[\left(2\beta_1\sigma + \beta_2\frac{m}{d}\right)y + \Theta(x,y)\right] = \varphi(x,y) - 2\pi(f_x x + 2\Delta d\sigma), \tag{5.12}$$

where $f_x = 4\tan\theta(\sigma-\sigma_L)$. In order to correct the phase distortion, a matrix $M(x,y)$ is defined by

$$M(x,y) = \exp\left\{-i2\pi\left[\left(2\beta_1\sigma + \beta_2\frac{m}{d}\right)y + \Theta(x,y)\right]\right\}. \tag{5.13}$$

Then the modulated part of an interferogram multiplied by the corrected matrix yields the corrected interferogram. As described in Section 2.4, the modulated part of an interferogram can be obtained by using a suitable window function and backward transformation in the spectral domain. Accordingly, the corrected interferogram can be expressed as

$$\begin{aligned} I(x,y) &= M(x,y)V(x,y)\exp[i\varphi(x,y)] \\ &= V(x,y)\exp\{i2\pi[4\tan\theta(\sigma-\sigma_L)x + 2\Delta d\sigma]\}, \end{aligned} \tag{5.14}$$

where $V(x,y)$ is the interference visibility. Note that the optical dispersion effect is not considered in this discussion. The narrow optical bandpass filter is employed in the DASH system, so that the wavelength-dependent optical defects can be neglected. Because the angle tolerance β_1 is extremely small, the y-direction modulations within the wavelength range of bandpass filter can be regarded as a consistent value. Therefore, ignoring the optical dispersion effect is a reasonable approximation.

With the monitoring of the wavelength, an interferogram produced by a laser illumination using the setup of Figure 5.6 was recorded. The spatial frequency of the interferogram was calculated according to the Littrow angle, Littrow wavelength and the wavelength of the input laser. Using the phase information and the spatial frequency of the obtained interferogram, the phase distortion was characterized based on Equa-

tion 5.12 and Equation 5.13. Using the obtained phase-distortion matrix, the corrected fringe image after flat-field correction and phase-distortion correction is shown in Figure 5.13. Compared with the original image in Figure 5.7(a), the tilts and distortions of the stripes have been corrected. The remaining distortion on the edges results from the endpoint-discontinuity artifacts, which may cause an additional error during Fourier transformation. The edge region must be excluded from the further retrieval process. Only modulated parts are reserved after the corrections, hence the relative intensity changes compared with the initial signal intensity.

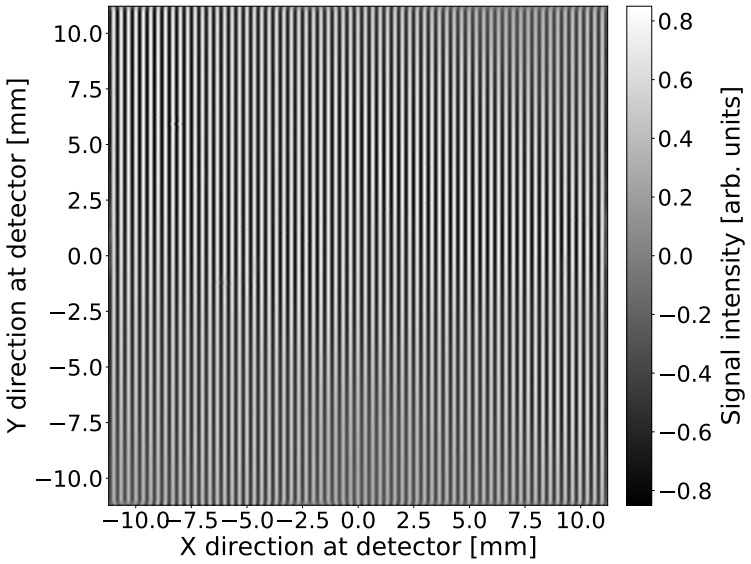

Figure 5.13: Corrected fringe image after flat-field correction and phase-distortion correction.

Owing to the fact that an identical spatial frequency f_x is employed in Equation 5.12 to calculate the phase-distortion matrix for the whole detector, the variation of spatial frequency can be corrected after the phase-distortion correction, which is validated in Figure 5.14. For the interferograms before the phase-distortion correction, the spatial frequency increases with the gain of the row number. After the phase-distortion correction, the spatial frequencies of the different-row interferograms are identical and they are equal to the value of f_x used in the previous determination of the matrix $M(x,y)$.

In order to inspect the wavelength dependency of the phase distortion, a fringe image at a wavelength of 630.48 nm was recorded as shown in Figure 5.15(a), and its corresponding fringe image after flat-field correction and phase-distortion correction is also plotted in Figure 5.15(b). An identical corrected matrix is applied in the both corrections for the interferograms of 630.03 nm and 630.48 nm. The corrected results indicate that the wavelength dependency of the phase distortion can be neglected within

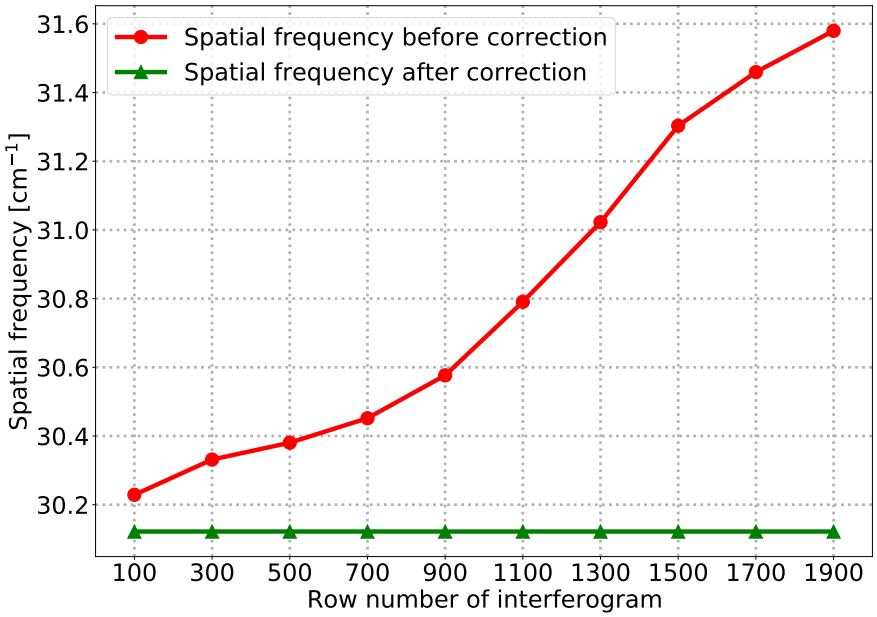

Figure 5.14: Spatial frequencies of the interferograms before and after phase-distortion correction as functions of row number of interferogram.

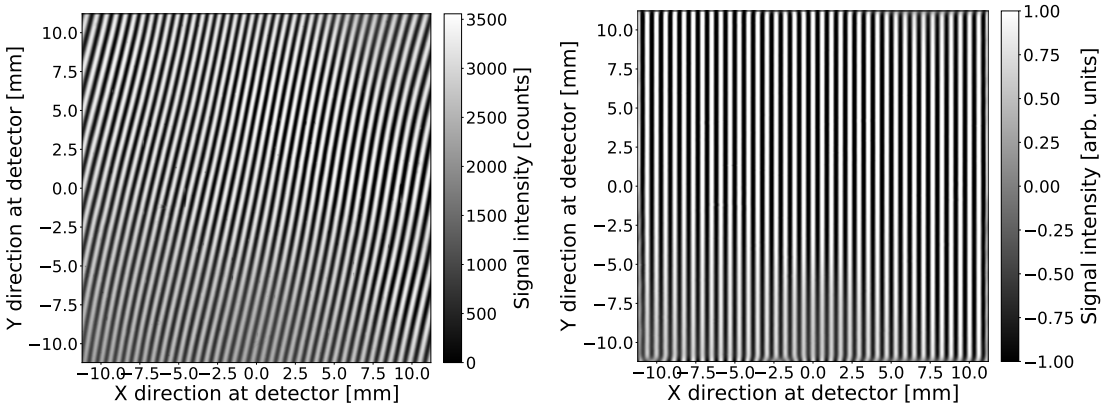

(a) Measured fringe image

(b) Corrected fringe image

Figure 5.15: (a) Measured fringe image at a wavelength of 630.48 nm when the 4.5-degree half cone angle radiation illuminates the interferometer and (b) its corresponding fringe image after the flat-field correction and phase-distortion correction.

the bandpass wavelengths. The phase distortions in the interferograms produced from the airglow emission and the calibration lamp can be corrected using an identical correction matrix. When calculating the phase change, the same correction matrix must

be used for the both interferograms, which ensures that there is no extra phase change incurred during corrections.

5.5 Thermal Performance

A thermally stable monolithic DASH interferometer was designed and built in the laboratory. The accurate wind measurement requires that the fringe phase obtained from this interferometer is insensitive to the change of ambient temperature. In this DASH interferometer, a thermally-induced phase drift of less than 3.2 mrad is required to achieve 3 m/s accuracy. To evaluate the thermal performance, the sensitivities of the spatial frequency and the optical phase offset are characterized based on laboratory tests and a model study in this section.

A similar system as shown in Figure 5.6 was built for the thermal performance test. Instead of laser light, a frequency-stable neon lamp was utilized here. The interferometer was glued to two plates made of stainless steel, then it was contained in an aluminium housing where the temperature was stabilized under a PID (proportional-integral-derivative) controller with an accuracy better than 0.1 °C. Details of the temperature control in the interferometer are discussed in Appendix C.3. The ambient temperature was also controlled using an air condition with a temperature of 20 °C. The measurements were performed from 22 °C to 30 °C with an interval of 1 °C. When a thermal equilibrium was established in the housing, 10 frames of the interferograms for each temperature were recorded with an exposure time of 30 seconds. Then the mean value of the 10 frames, equivalent to the typical exposure time in ground-based nightglow observation, was calculated for further analysis. For each interferogram, the flat-field correction and the phase-distortion correction using identical phase-distortion parameters were implemented. The 500-row signal near the center of the fringe image was then averaged to derive the phase change. The phase change can be directly retrieved using the Fourier transform algorithm described in Section 2.4. Based on the determined phases, a linear function $\Delta\varphi(x)$ was fitted and the fitting result shows the change of spatial frequency (slope divided by 2π) and phase offset (intercept) due to the temperature variation.

As discussed in *Marr et al.* (2013), a predictive model using ray-tracing software and a finite element analysis can be built. The model can adjust the parameters including the refractive index, the grating groove density and the dimensions of the elements according to the respective ambient temperature. Note that all of the dimensions and angles are provided with the manufacturer's inspection data and the material data are based on the glass catalogs (*SCHOTT Advance Optics*, 2019; *CDGM GLASS CO.,LTD*, 2018). The mechanical deformations resulting from the differential expansion between

Table 5.1: Properties of the materials used in FEM analysis

	Density [kg/m^3]	CTE [$\times 10^{-5}$ /°C]	Young's modulus [$\times 10^{10}$ Pa]	Poisson's ratio
Aluminum	2700	2.31	7.0	0.35
Stainless steel	7900	1.65	20	0.27
Fussed silica	2203	0.051	7.3	0.17
H-FK61	3700	1.31	7.007	0.3
N-LAK12	4100	0.76	8.7	0.288
N-BK7	2510	0.71	8.2	0.206
Adhesive	1700	27.5	0.0025	0.48

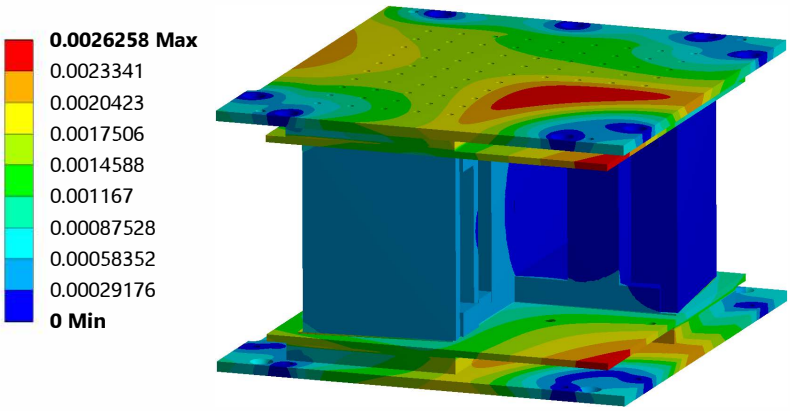

Figure 5.16: Deformation of the interferometer when the temperature changes from 25° to 26°. The FEM analysis includes 3059857 nodes and 1400125 elements with the fixed constraints on the screw holes. Note that the top and bottom plates are the covers of the interferometer housing and the unit of the legend is millimeter.

two different materials were characterized by a finite element model (FEM) analysis. Table 5.1 gives the relevant properties of the materials used in the FEM analysis. A linear static stress model considering the monolithic interferometer, the covers and the 5-mm adhesive layers between the interferometer and the covers was established and the deformation (relative position change) result is shown in Figure 5.16. After adding the deformation into every element, the new angles were calculated by fitting the updated plane. On arm one, the distortions on the angle between field-widening prism and beamsplitter and the angle between field-widening prism and grating are -1.466$\times 10^{-6}$

rad/°C and 4.111 $\times 10^{-7}$ rad/°C, respectively. The corresponding distortions on arm two are -1.119$\times 10^{-6}$ rad/°C and 7.623$\times 10^{-7}$ rad/°C. Updating the angles in the ray-tracing model, the Littrow angle and the optical OPD offset at different temperatures were tracked. The spatial frequency and the phase offset were therefore also monitored in this predictive model. Note that the thickness difference of the adhesive between two arms is used to compensate the image difference of two gratings, which is considered in the model study.

Figure 5.17(a) and Figure 5.17(b) show how the spatial frequency and the phase offset change in the measurements and the model study when the temperature changes. As the temperature increases, the spatial frequencies increase linearly at 0.0154 cm^{-1}/°C in the measurements and 0.0313 cm^{-1}/°C in the model study, respectively. Similarly, the phase offsets change at linear rates of 0.469 rad/°C in the measurements and 0.330 rad/°C in the model study, respectively. The thermal drift of the spatial frequency agrees with the model value within a factor of two, and the thermal drift of the phase offset agrees with the model value within 29.6%. The air pressure may change during the measurements, but we did not consider this effect in the model study. In addition, the parameters of uncertainty and alignment tolerances cause the measurements and the model to differ further.

Compared with other DASH interferometers with a phase drift of 1.25 rad/°C (*Harlander et al.*, 2010) and 4.29 rad/°C (*Marr et al.*, 2013), a more stable DASH interferometer has been realized. However, the temperature response (0.469 rad/°C) is still higher than the design value (1.2 mrad/°C) due to the manufacturing and alignment tolerances. The temperature control and calibration thermal tracking are also necessary during wind measurement for this interferometer. An UV curing adhesive was used to glue the separate optical components, and the thermal coefficient of the adhesive is an order of magnitude larger than the thermal expansion coefficient of H-FK61 (*Norland Products*, 2020). In order to compensate the incoincidence of the two grating images caused by the manufacturing and alignment tolerances, the difference of the adhesive thickness between two arms is inevitable during final gluing. Table 5.2 analyzes the change of the thermal sensitivity of the phase offset occurred from the thickness deviation. Assuming that there are individual 0.1 mm thickness deviations on the beamsplitter, field-widening prism, spacer 1, spacer 2 and parallel spacer, the corresponding compensated thickness of the adhesive and the change rate of the phase offset are calculated using Equation 4.8 and Equation 4.5, respectively. The light beam traverses the beamsplitter and field-widening prism, so that the change rates of phase offset are related to the derivative of the refractive index with respect to temperature and the CTEs of the glasses. For the spacer 1, spacer 2 and parallel spacer, the compensated thickness are equal to the thickness deviations. Owing to the same optical glasses used in the spacer 1 and parallel spacer, their change rates are consistent. The thickness deviations of 0.1 mm bring in thermal instabilities of the phase offset from 0.119 rad/°C to 0.219

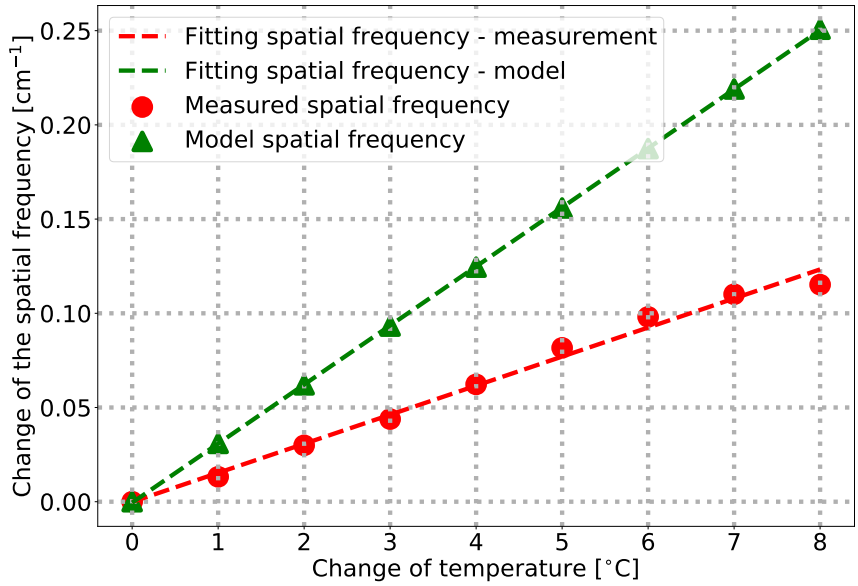

(a) Change of the spatial frequency

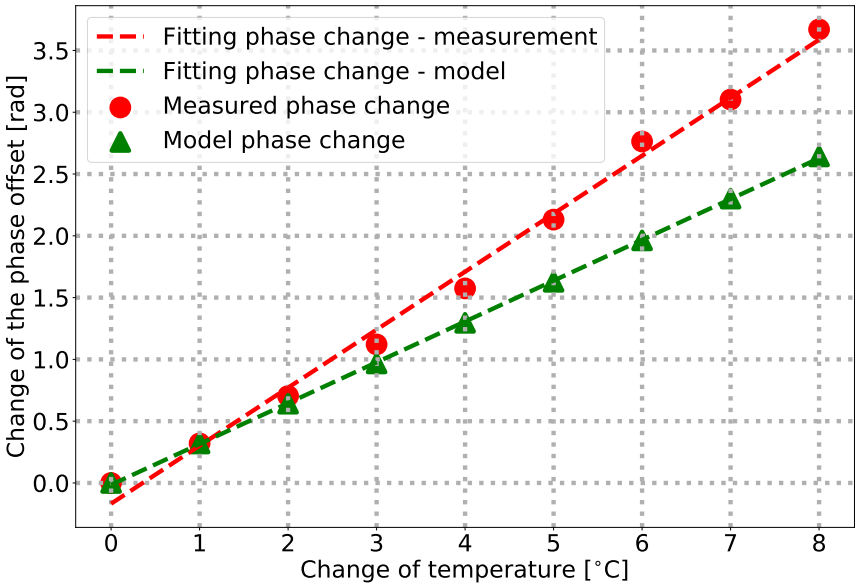

(b) Change of the phase offset

Figure 5.17: (a) Change of the spatial frequency and (b) change of the phase offset when the temperature is varied from 22 °C to 30 °C. Red circles represent measurements, green triangles represent model results. Dashed lines represent fitting results to theses data.

rad/°C. Therefore, the variation of the adhesive thickness on two arms seriously deteriorates the expected thermal compensation. In order to achieve better thermal stability, a more thermally stable adhesive and a more precise alignment are suggested during the interferometer assembly.

Table 5.2: Change of the thermal sensitivity of phase offset occurred from the thickness deviation

	Thickness deviation [mm]	Compensated thickness of adhesive [mm]	Change rate of phase offset [rad/°C]
Beamsplitter	0.100	0.066	0.131
Field-widening prism	0.100	0.060	0.119
Spacer 1	0.100	0.100	0.219
Spacer 2	0.100	0.100	0.206
Parallel spacer	0.100	0.100	0.219

5.6 Laboratory Doppler Measurements

A critical work in the development of the instrument is to validate its capability to measure wind velocities. Laboratory measurements of a Doppler-shifted emission line can be used to assess the instrument performance. *Dötzer* (2019) developed a Doppler-shift generator which produces different Doppler shifts by varying the rotation speed of a retro-reflecting wheel. The Doppler-shift generator was used in our laboratory Doppler measurements. With the known Doppler velocities, a series of measurements were taken using our DASH instrument and a comparison between the measured Doppler velocities and expected Doppler velocities was also performed.

A schematic of the setup is shown in Figure 5.18. A frequency-stable HeNe laser provides the light source at a wavelength of 632.991 nm. The frequency stability of the laser achieves ± 2 MHz, which corresponds to ± 1.3 m/s uncertainty. An optical isolator is inserted in front of the laser to prevent the influence of the back reflected light. After passing the isolator, the laser is focused into the Doppler wheel by lenses L1 and L2. Mirror M1 reflects the Doppler-shift light from the Doppler wheel and lens L3 focuses light into the rotating disk to suppress laser speckle. The light beam enters the interferometer and produces a fringe pattern on the detector after passing through the collimating lens L4 and beamsplitter. A combination of a neon lamp and a bandpass filter provides the calibration light source which is used to track thermal changes of

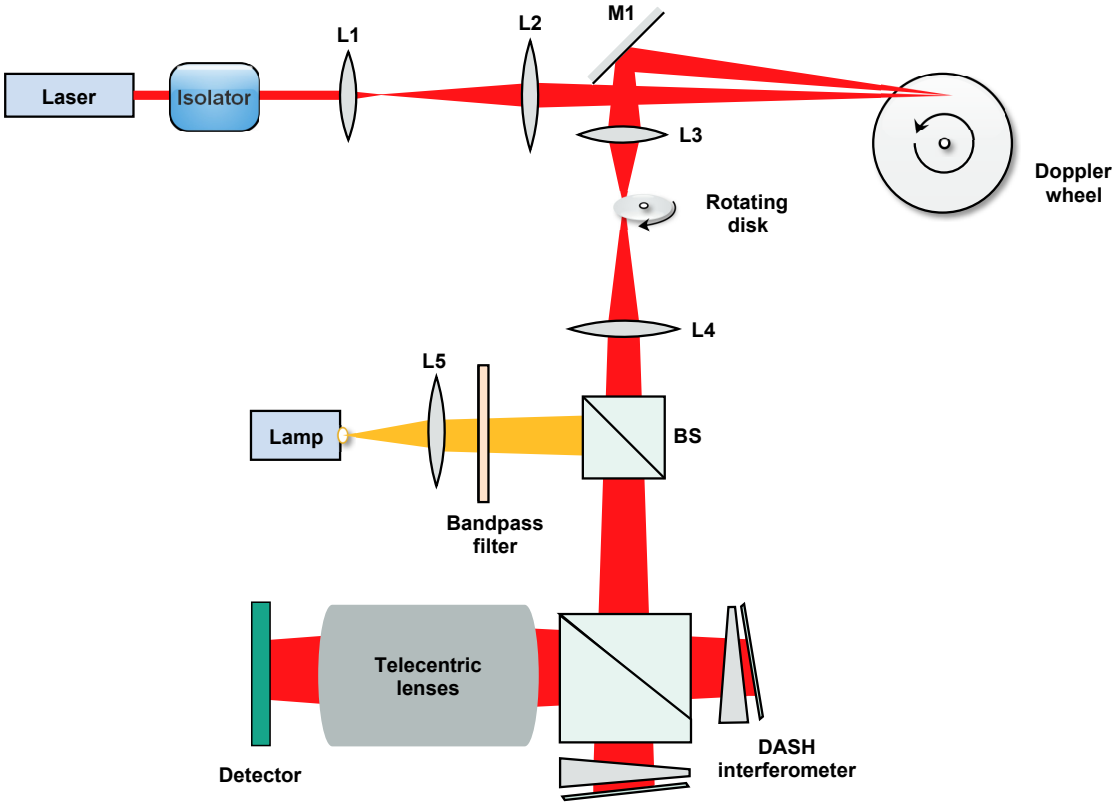

Figure 5.18: Setup of the laboratory Doppler measurements.

the DASH instrument. The calibration light is collimated by lens L5 and reflected into interferometer by the beamsplitter.

The motor of the Doppler wheel is precisely controlled by a Vedder electronic speed controller (VESC) (*VESC project*, 2020). The input electrical revolutions per minute (ERPM) of the motor is monitored and the mechanical revolutions per minute (RPM) of the motor is equal to the ERPM divided by the number of polar pairs of the motor. Therefore, the rotation frequency of the Doppler wheel is monitored. Figure 5.19 presents the schematic of the Doppler-shift generator. A light beam is incident on the point A, then it is reflected back by the microspheres on the wheel. As shown in Figure 5.19, the angle between the incident ray and the rotation plane is α_i and the angle between the reflective ray and the rotation plane is α_r. Owing to the microspheres featuring a retroreflector (*Dötzer*, 2019), angles α_i and α_r are almost identical. A Doppler shift is imposed on the reflective ray and the corresponding Doppler velocity v_D can be expressed as

$$v_D = v_t \left(\cos \alpha_i + \cos \alpha_r\right), \tag{5.15}$$

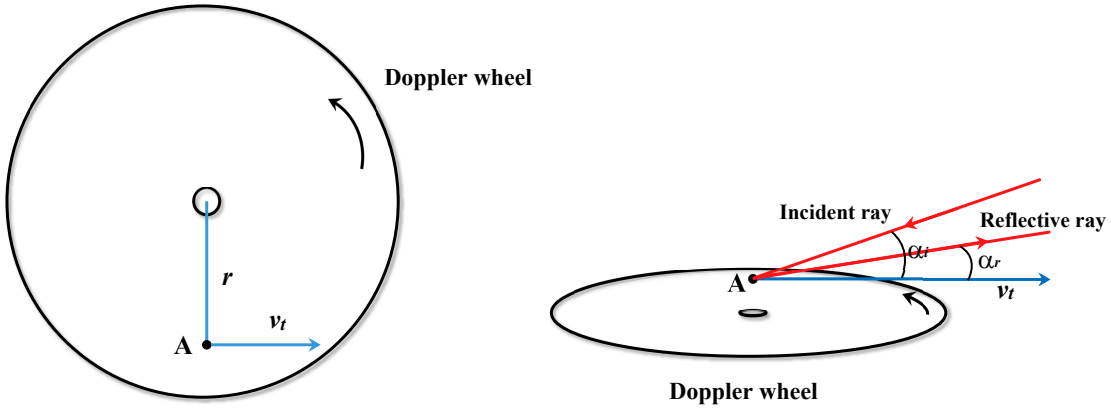

(a) Top view of Doppler wheel (b) Side view of Doppler wheel

Figure 5.19: Schematic of the Doppler-shift generator.

with the tangential velocity of the rotation wheel v_t (*Nichols et al.*, 1985). The tangential velocity is related to the rotation frequency f_r and the radius of rotation r, thus the tangential velocity v_t yields

$$v_t = 2\pi f_r r. \tag{5.16}$$

With different rotation speeds of the Doppler wheel, a series of measurements were taken using the setup of Figure 5.18. For each rotation speed, seven separate interferograms were recorded and the interval is 750 RPM during measurements. The radius of rotation, angles α_i and α_r were measured after the measurements, and then those numbers are employed in calculating the expected Doppler velocities using Equation 5.15 and Equation 5.16. Before the retrieval of the Doppler velocity, the interferograms were processed with the spike and defect removal, dark current and signal offset correction and phase-distortion correction. After the corrections, averages of the 600 rows inteferograms in the central region were used to retrieve the Doppler velocities. The phase shifts of the interferograms produced by neon lamp were used to calibrate the thermal drifts using Equation 2.21. Using the dimensions measured by the manufacturer and Equation 2.3, an effective OPD was determined and this value was used in the retrieval routine.

Using the separate interferograms, seven Doppler velocities were retrieved for each rotation frequency, and the mean value of these seven velocities is regarded as the retrieved velocity for this rotation frequency. The retrieved Doppler velocities and expected Doppler velocities as functions of the rotation frequency of the Doppler wheel are presented in Figure 5.20, which indicates that the retrieved Doppler velocities agree well with the expected Doppler velocities. Comparing the retrieved Doppler velocities

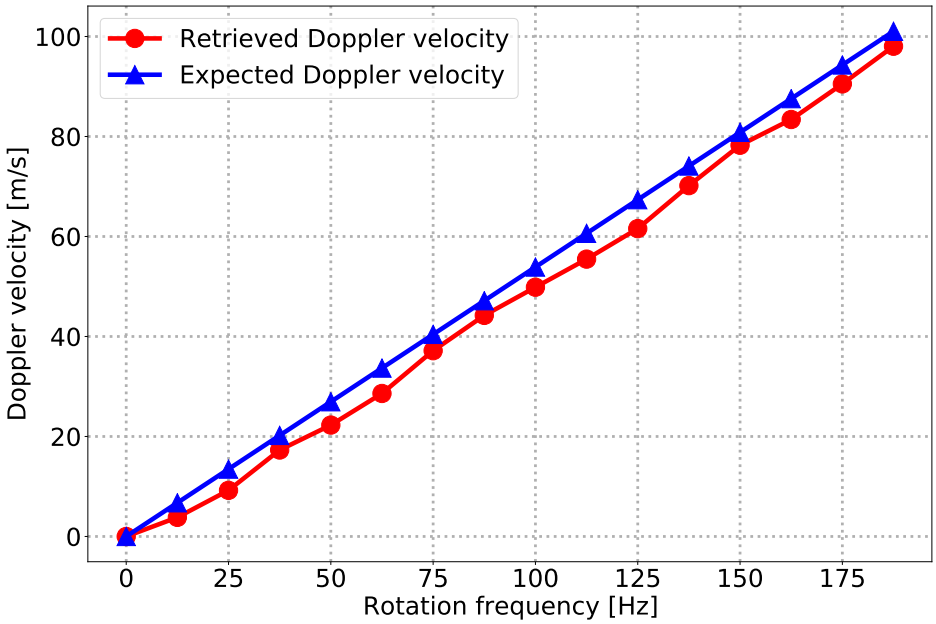

Figure 5.20: Retrieved Doppler velocities and expected Doppler velocities as functions of the rotation frequency of the Doppler wheel. The measured factor of proportionality (0.54 m/(s·Hz)) is employed here.

and expected Doppler velocities, the deviations of the Doppler velocities are calculated and they are presented in Figure 5.21. With the increase of the rotation frequency, the deviation fluctuates between -2.58 m/s and -5.78 m/s and the mean absolute deviation is 3.90 m/s. The error bars in Figure 5.21 represent twice the standard deviation of the seven Doppler velocities retrieved from seven independent interferograms. Except the zero-rotation frequency, all of the retrieved Doppler velocities are smaller than the expected Doppler velocities as shown in Figure 5.20. There are two possible causes for the underestimation of the Doppler velocities. One is an overestimation of the effective OPD used in the retrieval. The deviation of OPD caused by manufacturing and assembly tolerances is in the order of 0.1 mm, which corresponds to 0.3m/s estimation error of the Doppler velocities. Compared to the real estimation deviations, the contribution of the overestimation of the effective OPD can be neglected. Another possibility is that the deviations of the measured radius r, angles α_i and α_r increase the factor of proportionality between the rotation frequency of the Doppler wheel and the Doppler velocity, which is the predominant cause of the negative biases of the retrieved Doppler velocities. A meter was used to measure the radius r, angles α_i and α_r when the Doppler wheel was at rest. Owing to the diffraction and defocusing of light, there was a laser spot with a finite radius on the wheel, which inevitably caused the estimation deviation of the factor of proportionality.

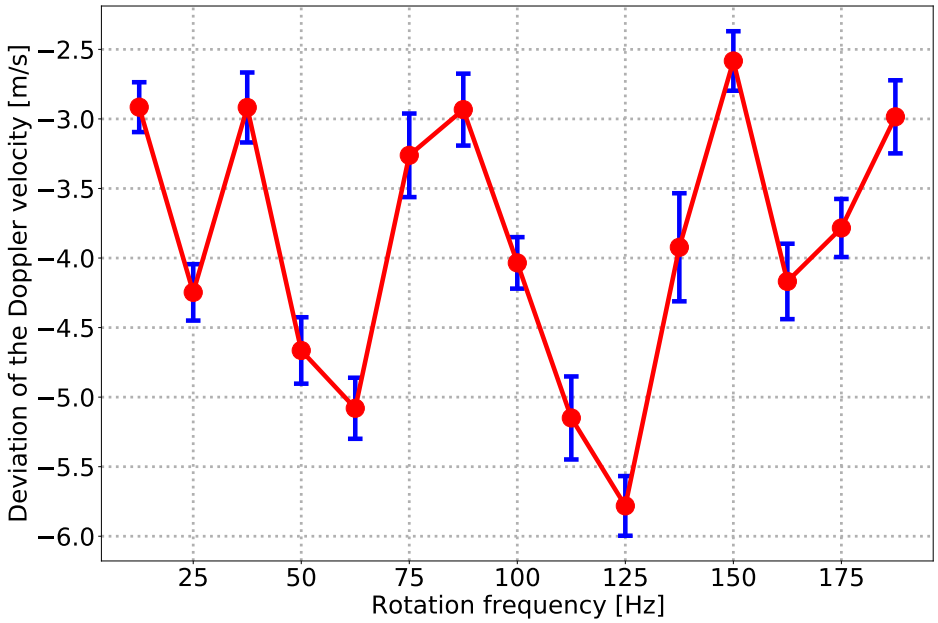

Figure 5.21: Deviation of the retrieved Doppler velocity as a function of the rotation frequency of the Doppler wheel. The measured factor of proportionality (0.54 m/(s·Hz)) is employed here.

Using the results in Figure 5.20, a zero-intercept linear regression of the retrieved Doppler velocity gives the factor of proportionality of 0.51 m/(s·Hz) instead of the measured value of 0.54 m/(s·Hz). Updating the factor of the proportionality, the expected Doppler velocities were calculated again. Comparisons between the retrieved velocities and the expected velocities are presented in Figure 5.22, and the corresponding retrieval deviations are presented in Figure 5.23. Compared to the results in Figure 5.21, the deviation varies between -3.49 m/s and 2.66 m/s and the mean absolute deviation is reduced to 1.82 m/s. The frequency drift of the laser ($\pm$2 MHz) results in a measurement uncertainty of $\pm$1.3 m/s, and the uncertainty of the rotation speed of the Doppler wheel ($\pm$100 ERPM) produces a velocity uncertainty of $\pm$0.42 m/s. Moreover, the noise of the signal also produces a retrieval uncertainty of the order of 0.1 m/s. Therefore, the measurement deviation of 1.82 m/s is reasonable and the Doppler measurements validate the ability of the DASH instrument to measure wind speed.

5.7 Instrument Field Tests

Owing to the low intensity of the oxygen red-line nightglow emission, a long-exposure observation is necessary, which requires a compact and stable system. To verify its

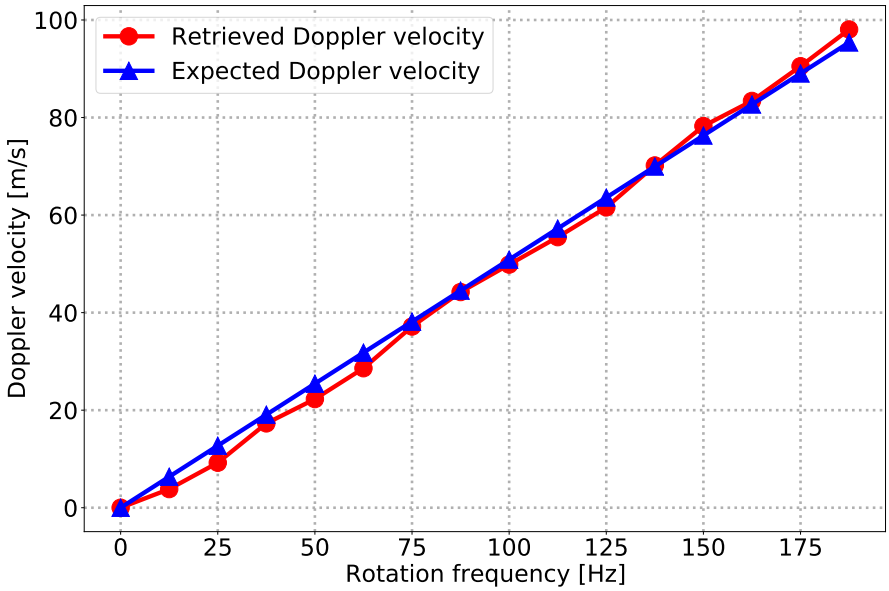

Figure 5.22: Retrieved Doppler velocities and expected Doppler velocities as functions of the rotation frequency of the Doppler wheel. The fitting factor of proportionality (0.51 m/(s·Hz)) is employed here.

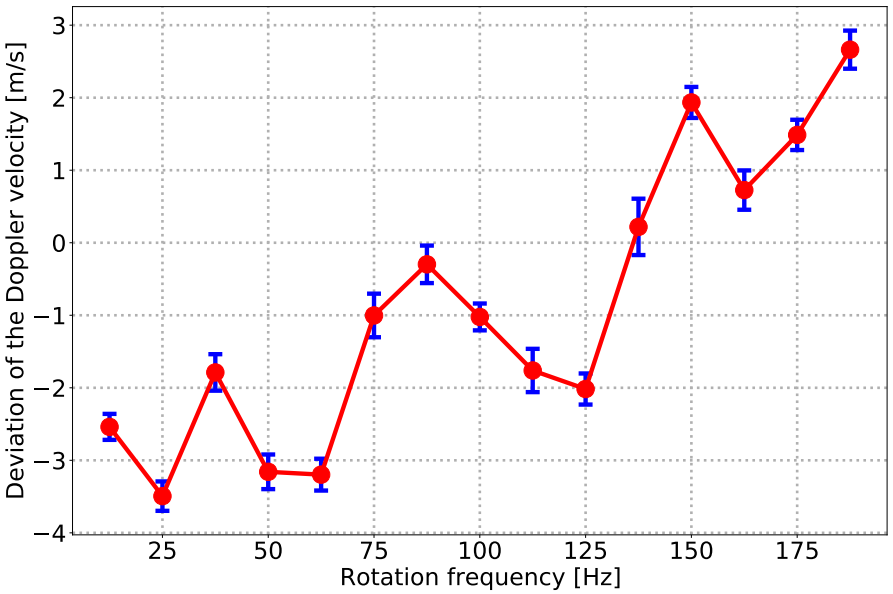

Figure 5.23: Deviation of the retrieved Doppler velocity as a function of the rotation frequency of the Doppler wheel. The fitting factor of proportionality (0.51 m/(s·Hz)) is employed here.

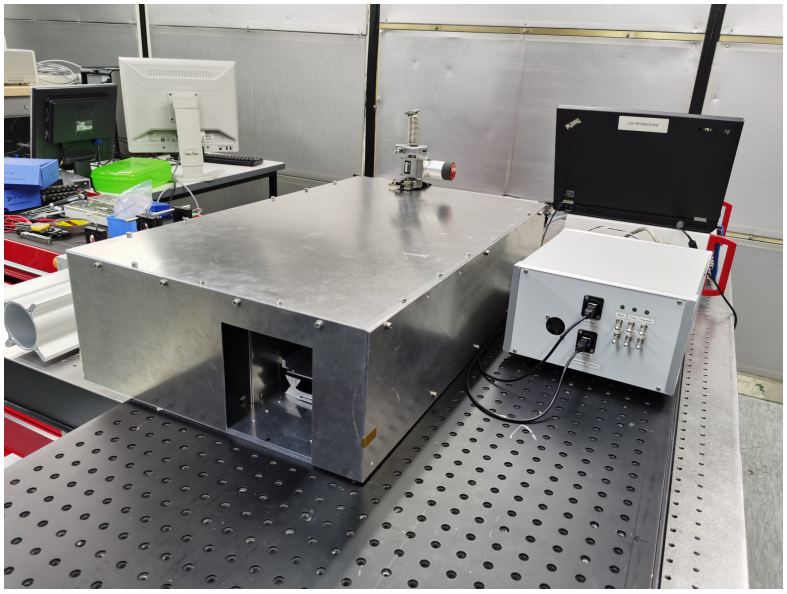

(a) Photograph of the prototype of the instrument

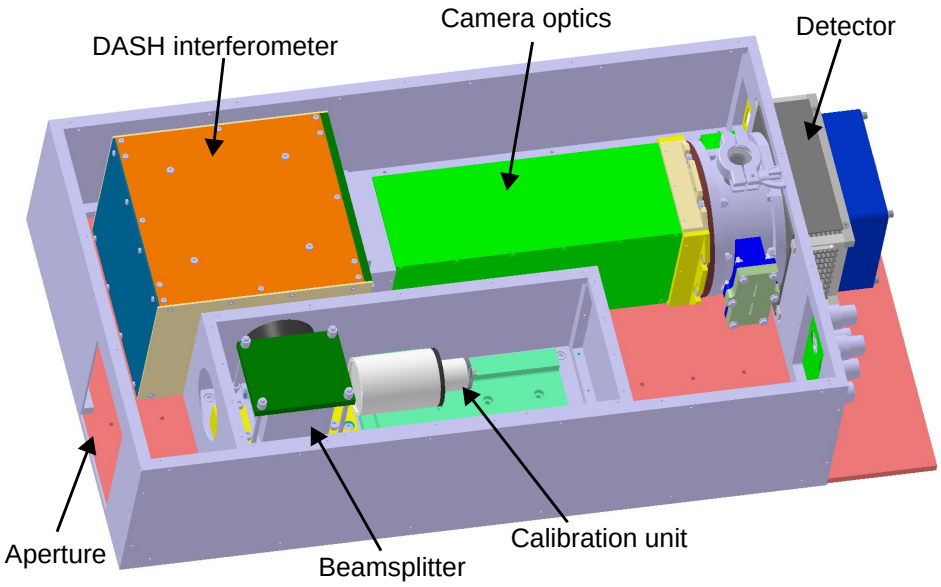

(b) System layout of the instrument

Figure 5.24: (a) Prototype of the instrument and (b) the system layout.

ability to observe the weak nightglow emission, a prototype of the instrument was built and filed tests were performed using this prototype. In this section, the results of the field tests are discussed.

The prototype of the instrument and the system layout are shown in Figure 5.24. The DASH interferometer is contained in a closed housing where the temperature is controlled using PID controllers with an accuracy of ± 0.1 °C. In order to suppress the dark current, a Dewar is used to contain the detector which is cooled by a fan and several thermoelectric coolers (TEC). The collimated neon-line radiation is diffused by a holographic diffuser. After twice reflections on the beamsplitter, the diffused radiation, as a calibration signal, illuminates the DASH interferometer. The bandpass filter described in Appendix B.3 is mounted between the beamspiltter and the interferometer. With an exposure time of 5 minutes, an interferogram produced from the calibration line was recorded and it is presented in Figure 5.25(a). The detector was cooled to -25 °C, but the generated dark current was still high. As shown in the white region of Figure 5.25(a), the signal intensities are saturated because of the extremely high dark current in this region. Covering the entrance aperture and using the same configuration of the detector, a dark image was recorded as shown in Figure 5.25(b). This dark image characterizes the dark current and the signal offset, which can be used for the dark current and signal offset correction in the following field tests.

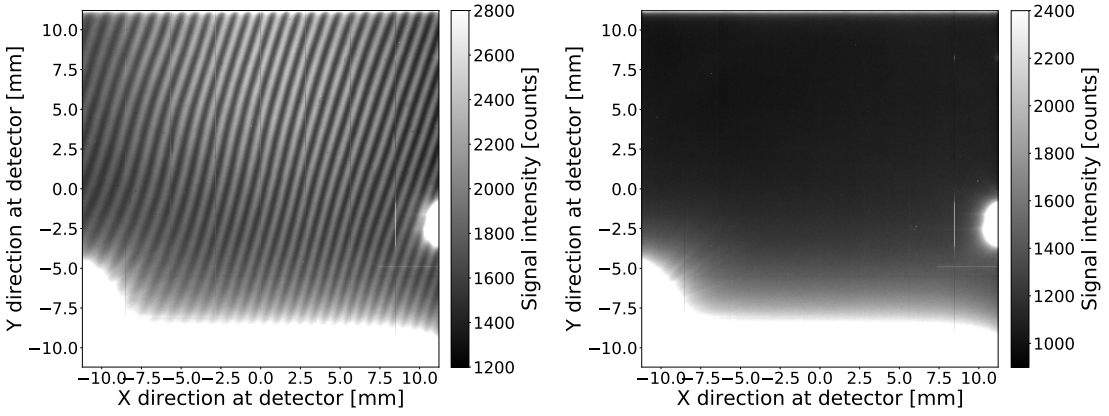

(a) Recorded fringe image

(b) Dark current distribution

Figure 5.25: (a) Measured fringe image produced from the neon-line radiation and (b) dark image when the detector is cooled to -25 °C and the exposure time is 5 minutes. In both images, the spikes and defect pixels have been corrected.

The field tests were performed on the night of September 22, 2020 at Wuppertal (51.26 °N, 7.15 °E). The detector was cooled to -25 °C and the exposure time is 5 minutes for each frame. The intensity of the neon-line radiation is much higher than the

intensity of the nightglow emission. It is quiet difficult to further decrease the intensity of the calibration signal using the current configuration. Therefore, the simultaneous illumination of the calibration line was not employed in these field tests. In order to suppress the stray light, a baffle was mounted on the front of the instrument aperture. Figure 5.26(a) shows a fringe image taken at around 20:31 CET (Central European Time) using an elevation angle of 50°. Owing to the predominant dark current and the extremely weak nightglow emission, the visibility of the fringe pattern is pretty low. Subtracting the dark image shown in Figure 5.25(b), the corrected fringe image is shown in Figure 5.26(b). Notice that the shot noise produced from the dark current can not be corrected in this subtraction, so that the visibility of the interferogram in Figure 5.26(b) remains low. The saturated signal intensities appear in the same region of Figure 5.25(b) and Figure 5.26(a), which results in the zero-value intensity in the black region of Figure 5.26(b).

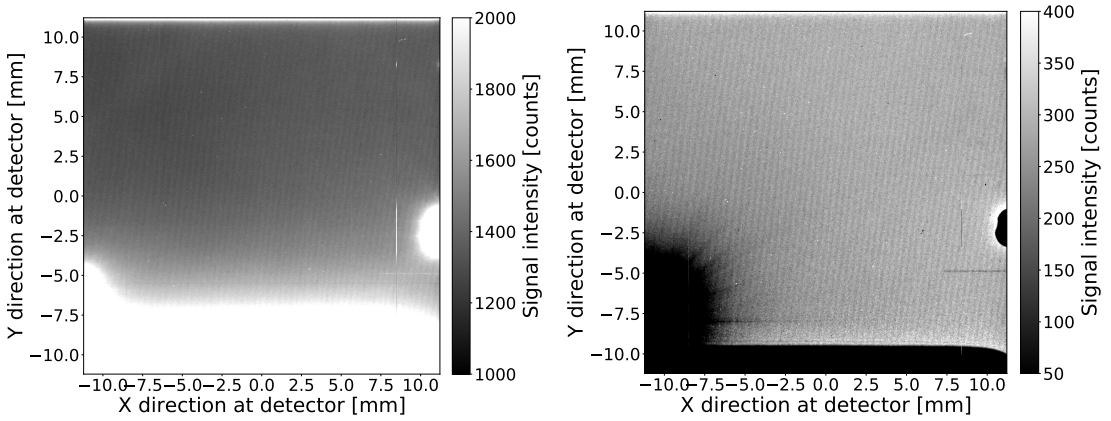

(a) With the dark current

(b) Without the dark current

Figure 5.26: (a) Measured fringe image produced from the oxygen red-line nightglow emission and (b) its corresponding fringe image after subtracting the dark image. In both images, the spikes and defect pixels have been corrected.

Two-dimensional Fourier transform is performed for the obtained fringe image, yielding an amplitude spectrum as shown in Figure 5.27. Zooming in on the region marked by a red rectangle, detailed spectra in the central region is obtained and placed in the upper right corner of this image. As shown in Figure 5.27, the targeted spectra produced from the nightglow emission is circled. A two-dimensional window function can be used to filter the targeted spectrum, and then the modulated parts of the interferogram can be obtained by implementing inverse Fourier transform for the filtered spectrum. Figure 5.28(a) shows the restored fringe image after the spectral filtering in the spectral domain, which indicates that not only the modulated parts of the interferogram remain but also the tremendous noise are removed. Except the saturated regions, the

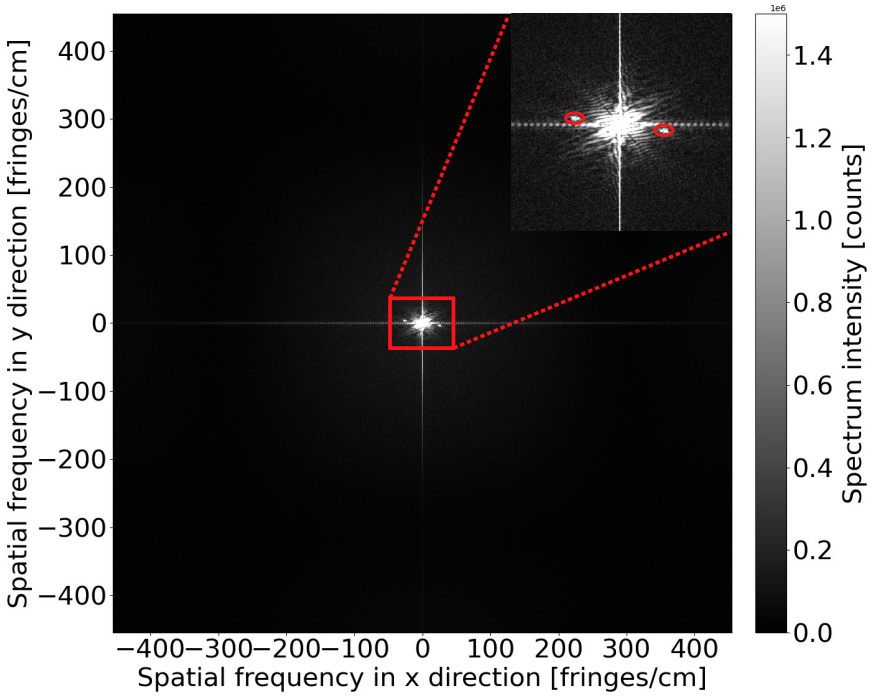

Figure 5.27: Two-dimensional amplitude spectrum of the interferogram in Figure 5.26(b).

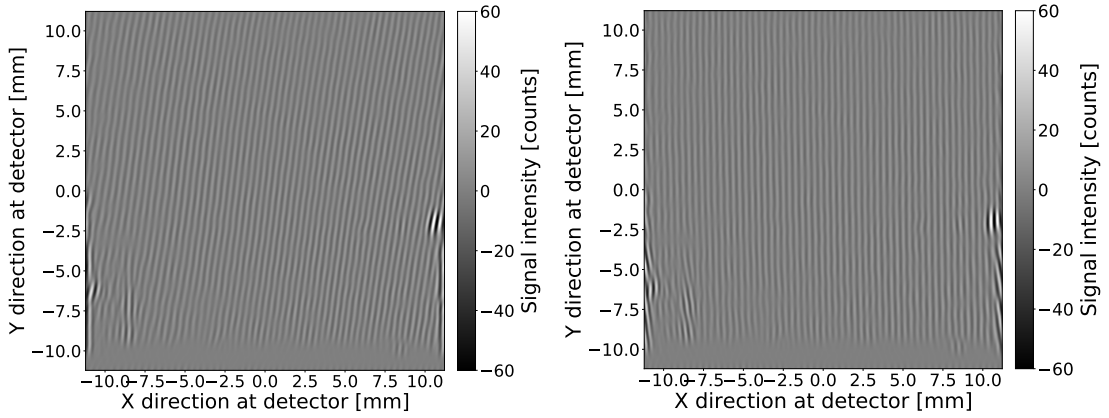

(a) Restored fringe image

(b) Corrected fringe image

Figure 5.28: (a) Restored fringe image after the spectral filtering in the spectral domain and (b) corrected fringe image after the phase-distortion correction. A two-dimensional Hamming window with a width of 40 pixels is selected here to extract the targeted spectrum.

restored fringes are almost same to the fringes taken in the laboratory shown in Figure 5.12(a). Using the phase-distortion matrix obtained in Section 5.4.4, the fringe image of Figure 5.28(a) can be further corrected and the corrected fringe image is presented in Figure 5.28(b). In order to improve the SNR, an average of rows 500-2000 in the corrected fringe image is calculated and the obtained interferogram is plotted in Figure 5.29(a). The thermal-broadening effect can be observed in the interferogram. As seen in Figure 5.28(b), the fringe contrast shows a negative correlation with the x position, which is opposed to the result in Section 4.3. This contradiction results from the opposite x-axis directions in the definition and rotating the detector 180 degrees about the optical axis can solve this contradiction. Using the algorithm described in Section 2.4, the phase of the interferogram can be determined. As shown in Figure 5.29(b), the unwrapped phase also shows a negative correlation with the x position.

The Solar Cycle 24/25 minimum was predicted to occur in 2020 (*Upton and Hathaway*, 2018), which means that the intensity of the nightglow is relatively low on these observations. The prototype instrument successfully recorded the fringe image viewing the oxygen red-line nightglow. Based on the obtained interferogram, the corresponding phase information, the key to retrieve the wind velocity, was determined. Although the wind velocity was not derived, these field tests prove that this DASH instrument has the ability to observe the oxygen red-line nightglow and the phase information also can be obtained. With multi-directional observations and a suitable calibration source, this DASH instrument can be used to measure thermospheric winds from the ground.

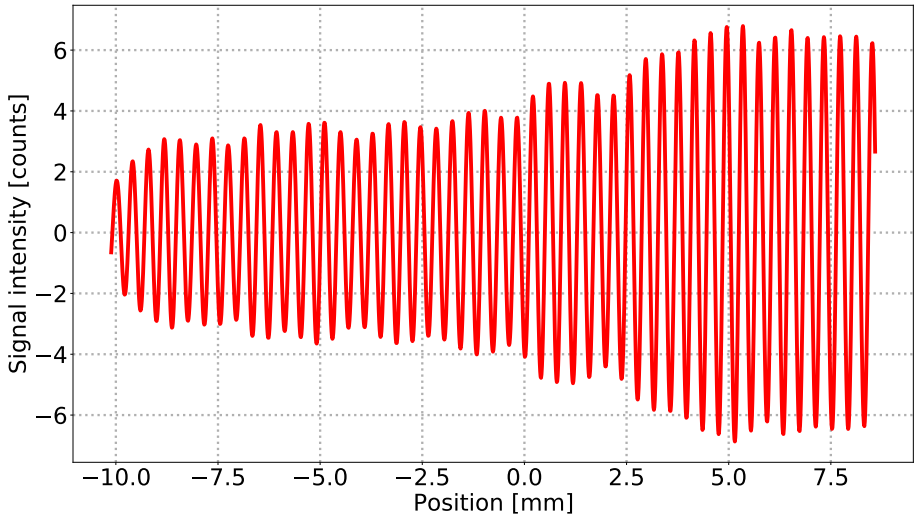

(a) Interferogram using the average of rows 500-2000

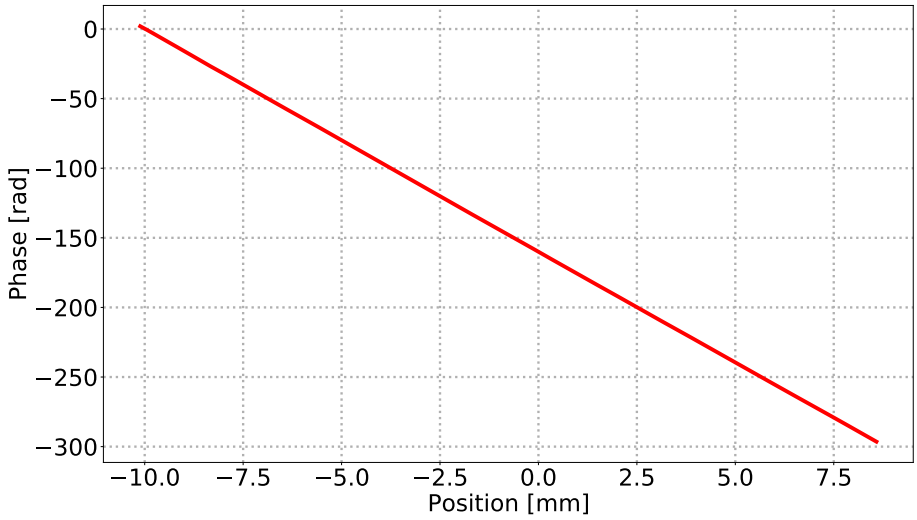

(b) Phase of the interferogram

Figure 5.29: (a) Interferogram using the average of rows 500-2000 and (b) its corresponding phase distribution. Note that the phase of the interferogram is unwrapped.

Chapter 6

Summary and outlook

6.1 Summary

Neutral winds in Earth's upper atmosphere affect the ionospheric variability. In order to understand the dynamics and energetics in this region, there is an increasing desire to obtain the neutral winds in the middle and upper atmosphere. Owing to the limitation of detection techniques, the observed wind data in this region still remain sparse. Global network observation of thermospheric winds is an effective method to obtain the thermospheric wind data. As a potential candidate to observe the neutral winds in Earth's upper atmosphere from the ground, an optical instrument based on a thermally stable monolithic DASH interferometer was developed.

The detection principle of DASH interferometer was discussed from the aspects of DASH instrument concept, derivation of wind velocities and associated algorithms. The interferogram produced from a DASH instrument was modeled. A extended value Δd on one arm makes the phase sensitive to the wavenumber change, which makes the Doppler shift of the emission line detectable. Thermal broadening of the emission line degrades the fringe visibility with the increase of OPD, so that the fringe visibility can be used to derive the Doppler temperature. An algorithm based on a Fourier transform was developed to derive the wind velocity, which bypasses the phase unwrapping process. Numerical studies show that using a Hanning or Hamming window with a suitable width to isolate the targeted spectrum yields a more precise result during the retrieval compared to the application of a rectangle window.

With the knowledge of spectral radiance values of the airglow emissions and instrument parameters, the signal detected in a DASH instrument was estimated. A CMOS image sensor is employed in the DASH system, and a series of tests was performed to characterize the performance of this detector. The results from the dark current meas-

urement and photon-transfer measurement are almost coincident with the parameters provided by the manufacturer. Combining the test results of the detector, interferograms were simulated for the summers and winters of the years 2009 and 2014 and the corresponding signal-to-noise ratios were also analyzed. From the analysis results, we confirm that it is necessary to use more lines of the signal to average or to increase the exposure time to improve the instrument responsivity and accuracy during winter measurements.

A thermally insensitive monolithic DASH interferometer with field-widening prisms was designed. Two emission lines including airglow emission and calibration line were considered when determining the Littrow wavelength. An optimum OPD offset was chosen to mitigate the contradiction between increasing phase sensitivity and visibility decline. Optimizing the material, dimensions and angles of each component, the thermal compensation and field widening were realized. A camera optics consisting of five commercial lenses was designed to relay the fringe pattern with a high imaging quality and a low distortion. The ray-tracing results show that this camera optics can perform stably within a temperature range of 10 °C. To validate the performance of the designed configuration, interferograms were simulated using ray-tracing software. The visibilities of the interferograms were further calculated to evaluate the performance of the designed system. Tolerances from the interferometer and the camera were analyzed simultaneously, and two configurations with the best visibility and worst visibility were obtained from 10000 Monte Carlo simulations. Using the two configurations, instrument measurement uncertainties for different measurement situations were discussed. With a 5-minute exposure time, the wind accuracy achieves 5 m/s during summer. Owing to the low airglow emission, the accuracy decreases to 35 m/s during winter.

A DASH instrument based on a monolithic interferometer was developed in the laboratory. With the support of a setup which allows monitoring the fringe contrast and spatial frequency in real time, a thermally stable monolithic DASH interferometer with a large etendue was built. The field of view test shows that the high contrast of the fringes is maintained when the field of view reaches 9 °C. The effects from spike signals, defect pixels, dark current and signal offset can be removed according to the performance of detector. The flat-field correction and phase-distortion correction are suggested to be applied for the interferograms before the wind velocity retrieval. The effects caused by the misalignment and optical defects can be eliminated by the phase-distortion correction. Temperature dependences of the phase offset and the spatial frequency were determined with thermal sensitivities of 0.469 rad/°C and 0.0154 cm^{-1}/°C, respectively. Temperature control for the interferometer and calibration thermal tracking are required during wind measurement. The Doppler measurements using the Doppler wheel validate the capability of instrument to measure wind speed with a mean uncertainty of 1.82 m/s. Instrument field tests successfully obtained the interferogram produced from the oxygen red-line nightglow and its corresponding phase information. The laboratory perform-

ance and field tests indicate that this DASH instrument meets the requirement to observe the thermospheric wind from the ground.

6.2 Outlook

An optical instrument based on a DASH technique was demonstrated in the laboratory, which shows the ability to observe the Doppler shift of the atomic oxygen airglow at a wavelength of 630.0 nm. The focus of future work will shift to develop a compact and rugged DASH instrument suited for field measurements, which is capable of viewing multiple fields of view. Using a suitable calibration source, field measurements of thermospheric winds will be carried out with this DASH sensor in the future. To further validate this technique, it is suggested to perform ground-based measurements simultaneously with a well established Fabry-Perot interferometer and then to compare the obtained results.

Although the tilt of the interferogram can be corrected by a phase-distortion correction, the unwanted tilt of the interferogram appeared after UV curing, which resulted from the shrinkage of glue and the fixture instability. A more stable alignment system, providing six-axis precision control over the orientation of grating, is expected in the future. The thermally induced image shift introduces an additional error during measurement. Periodic notches on the top of grating, achieving sub-pixel accuracy, can be used to track the image shift (*Englert et al.*, 2010b, 2017a). The notches can be inscribed in the gratings of the next-version interferometer, or other methods to track the image shift can be investigated in the future. Owing to the loss of spatial resolution, the starlight illuminates the whole detector, which increases the background noise. In the next version, a telescope in front of the interferometer should be considered. The temperature response of the DASH interferometer as built in laboratory is still higher than the design value, and the calibration lamp is still necessary during measurement. A more thermally stable adhesive and a more precise alignment are suggested to realize a thermally insensitive performance, so that the calibration line will not be necessary in the future.

Owing to the features of high throughput and no moving parts, DASH technique is particularly suited to a space application of the limb observation. Compared with the ground-based measurement, the signal enhances seriously because of the long limb path and the temporal resolution also increases greatly. The possibility to employ a DASH instrument in a space mission will be studied in the future.

Appendix A

Interferogram Modeling

A.1 Grating Equation

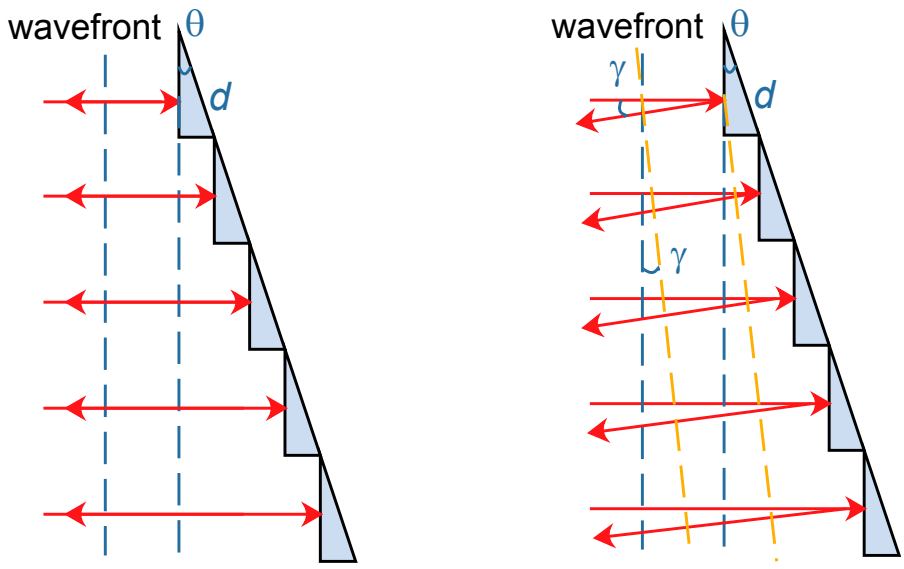

(a) Littrow wavelength (b) Wavelength near to Littrow wavelength

Figure A.1: Wavefront propagation after going through grating at the Littrow wavelength and a wavelength near to Littrow wavelenght.

Similar to an SHI, the dispersion element determines the primary properties in a DASH interferometer. The grating equation describing the beam transmission on the

grating is given by

$$d\left(\sin\theta_{in}+\sin\theta_{out}\right)=m\lambda, \tag{A.1}$$

where d is the groove spacing of the grating, θ_{in} and θ_{out} are the incident angle and exit angle on the grating, m is the order of diffraction and λ is the wavelength of light beam. Therefore, the wavefront maintains when the wavelength is equal to the Littrow wavelength of the grating, as shown in Figure A.1(a). When the wavelength diverges the Littrow wavelength in Figure A.1(b), the wavefront tilts with an angle γ. Note that the Littrow configuration for a optical grating is a special ray when the incident angle and the diffraction angle are identical.

A.2 General Framework

In a DASH interferometer, the introduction of gratings on two arms produces two crossed wavefronts, and the interference result of two wavefronts is the intensity distribution on the detector. Therefore, the key to model the interferogram is to model the wavefronts. The wavefronts can be characterized by complex amplitudes E_1 and E_2 using wave vectors $\vec{k_1}$ and $\vec{k_2}$ (*Born and Wolf*, 2013), which can be expressed as

$$\begin{aligned} E_1 =& A\exp\left[i\left(\vec{k_1}\cdot\vec{r}+\varphi_{01}\right)\right] \\ E_2 =& A\exp\left[i\left(\vec{k_2}\cdot\vec{r}+\varphi_{02}\right)\right], \end{aligned} \tag{A.2}$$

where A is the amplitude; φ_{01} and φ_{02} represent the phase offsets of E_1 and E_2, respectively.

As illustrated in Figure A.2, a general wave vector $\vec{k}$ passes through a DASH interferometer with incoming angles β and ϕ, which are the angle between the wave vector and the optical axis of the interferometer and the angle between the wave vector and the dispersion plane. The wave vector is divided into two parts by a beamsplitter, and then they are reflected from Grating 1 and Grating 2 at angles γ_1 and γ_2. The Grating $2'$ is the image of Grating 2 on arm one, and the distance between Grating 1 and Grating $2'$ is Δd. A coordinate system xyz with the origin on Grating 1 is defined in this figure. The y axis, not shown in the figure, is along the groove of the gratings, and the z axis is along the optical axis. The wave vector $\vec{k_i}$ can be described in this coordinate as

$$\begin{aligned} k_{x1,2} =& k\cos\phi_{1,2}\sin\gamma_{1,2} \\ k_{y1,2} =& k\sin\phi_{1,2} \\ k_{z1,2} =& k\cos\phi_{1,2}\cos\gamma_{1,2}, \end{aligned} \tag{A.3}$$

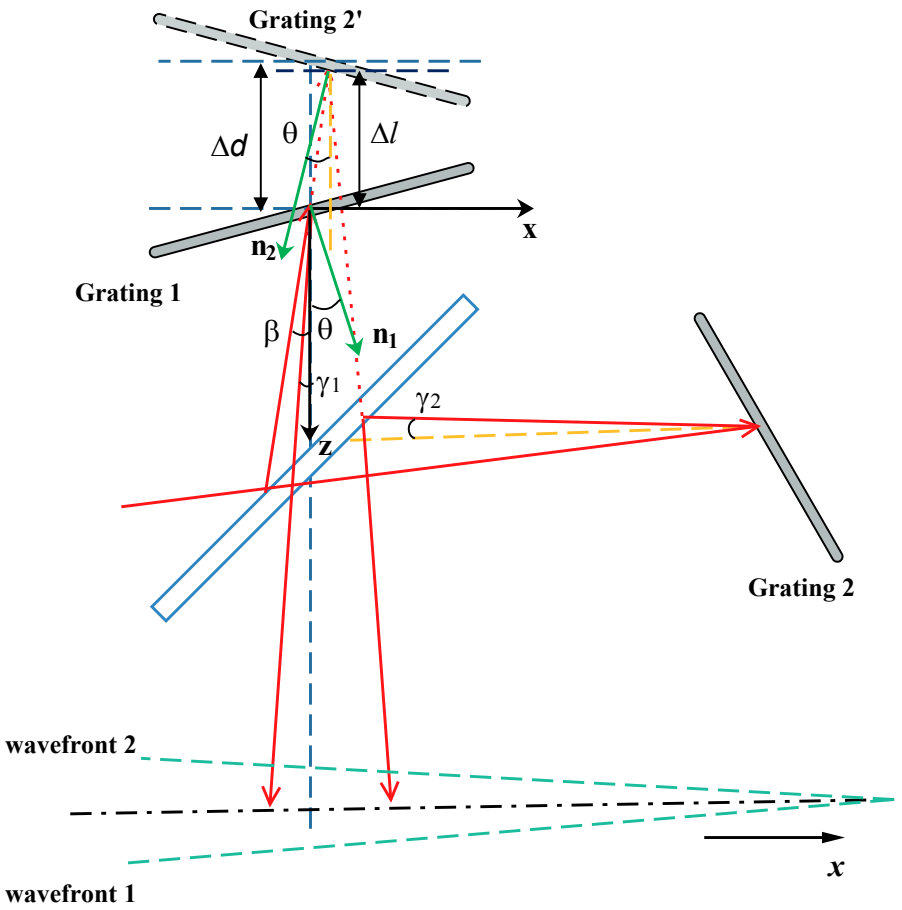

Figure A.2: Sketch of a DASH interferometer. Note that γ_1 and γ_2 are almost equal to zero in reality, but they are exaggerated here for better understanding. n_1 and n_2) represent the normals of Grating 1 and Grating 2′, and θ is the angle between the normal and optical axis.

where $k = \dfrac{2\pi}{\lambda}$ is the length of the wave vector; ϕ_1 and ϕ_2 are outgoing angles between the wave vector and $x-z$ plane on arm one and arm two. Using $\phi_1 = \phi_2 = -\phi$, the relation between phase offsets φ_{01} and φ_{02} can expressed as

$$\varphi_{02} = \varphi_{01} + k\cos\phi\Delta l\tan\beta\left(\sin\beta - \sin\gamma_2\right) + k\cos\phi\Delta l\left(\cos\beta + \cos\gamma_2\right). \tag{A.4}$$

Δl denotes the distance in z direction between the two points of incidence on Grating 1 and Grating $2'$ as shown in Figure A.2. Owing to the angle β, Δl is different from Δd. When angle $\beta \to 0$, $\Delta l \approx \Delta d$. Substituting this relation, Equation A.3 and Equation A.4 into Equation A.2 and calculating the interference distribution gives

$$\begin{aligned} I = \frac{I_0}{2}\{1 + \cos[&k\cos\phi\left(\sin\gamma_2 - \sin\gamma_1\right)x + k\cos\phi\left(\cos\gamma_2 - \cos\gamma_1\right)z \\ &+ k\cos\phi\Delta d\left(1+\cos\gamma_2\right)]\}. \end{aligned} \tag{A.5}$$

We assume the transmittance of the beamsplitter is 50% and the initial intensity of beam is I_0. The position of y does not affect the fringe pattern, and only when $x = 0, z = 0$, the phase is independent upon the incident angle. So that the fringe localization plane is located on the plane $z = 0$.

A.3 On-axis analysis

When a wave vector enters the DASH interferometer along the optical axis, $\beta = 0$ and $\phi = 0$. In this case, the angles of γ_1 and γ_2 can be determined by the grating equation, and their relations are

$$\begin{aligned} &2d\sin\theta = m\lambda_L \\ &d\left[\sin\theta + \sin\left(\theta \mp \gamma_{1,2}\right)\right] = m\lambda, \end{aligned} \tag{A.6}$$

where θ is the angle between the grating normal (n_1 or n_2) and z axis, which is the Littrow angle for the wavelength of λ_L. Dividing the lower formula by the upper formula and taking the approximation of $\cos\gamma_{1,2} = 1$, Equation A.6 reduces to

$$\sin\gamma_{1,2} = \mp\left(\frac{\sigma_L}{\sigma} - 1\right)2\tan\theta, \tag{A.7}$$

where σ_L and σ are the Littrow wavenumber and the wavenumber, respectively. Their

relations with their corresponding wavelengths are $\sigma_L = 1/\lambda_L$ and $\sigma = 1/\lambda$. Substituting this result and Equation A.7 into Equation A.5 gives

$$I(x) = \frac{I_0}{2}\left\{1 + \cos\left[2\pi\left(4\tan\theta\left(\sigma_L - \sigma\right)x + 2\sigma\Delta d\right)\right]\right\}. \tag{A.8}$$

Because the existence of camera optics in a DASH configuration, the fringe image on the detector is a conjugate image of localization plane. Accordingly, the intensity distribution on the detector changes to

$$I(x) = \frac{I_0}{2}\left\{1 + \cos\left[2\pi\left(4\tan\theta\left(\sigma - \sigma_L\right)x + 2\sigma\Delta d\right)\right]\right\}. \tag{A.9}$$

Consequently, an interferogram with a spatial frequency of $f_x = 4\tan\theta\left(\sigma - \sigma_L\right)$ is produced on the detector.

Spectral broadening is a common phenomenon for an emission line, but Equation A.9 does not consider this effect. A spectral line shape is defined to describe the spectral broadening (*Hollas*, 2004), which is also useful here. With a spectral line shape $B(\sigma)$, the intensity distribution can be expressed as

$$I(x) = \frac{I_0}{2}\int_{-\infty}^{+\infty} B(\sigma)\left\{1 + \cos\left[2\pi\left(4\tan\theta\left(\sigma - \sigma_L\right)x + 2\sigma\Delta d\right)\right]\right\} d\sigma. \tag{A.10}$$

In the thermosphere, the thermal broadening is predominant for the emission line and its spectral line shape can be regard as a Gaussian function, which is related to the temperature of atomic oxygen. The thermal broadening can be written as

$$\begin{aligned} B(\sigma) &= \frac{1}{\sqrt{2\pi}P_D}\exp\left[\frac{-\left(\sigma - \sigma_0\right)^2}{2P_D^2}\right] \\ P_D &= \sigma_0\sqrt{\frac{k_B T}{mc^2}}, \end{aligned} \tag{A.11}$$

where σ_0 is the central wavenumber of the emission line, k_B denotes the Boltzmannn constant, T gives the kinetic temperature, m represents the mass of the emitting matter and c is the velocity of light. Meanwhile, the effect of optical dispersion is pronounced owing to the spectral broadening when analyzing the interferogram in a DASH system. Considering this optical dispersion effect, Δd is a function of σ rather than a constant value. Similar to a Michelson interferometer (*Thuillier and Hersé*, 1991; *Thuillier et al.*, 1998; *Lathuillère et al.*, 2002), an effective OPD D is defined by

$$D = 2\Delta d_0 - \lambda_0 \left[2\frac{\partial(\Delta d)}{\partial \lambda} \right], \tag{A.12}$$

where Δd_0 is the extended value ($\Delta d(\sigma_0)$) at the central wavelength of the emission line, λ_0 is the central wavelength of the emission line, and $\frac{\partial \Delta d}{\partial \lambda} = \frac{\partial \Delta d}{\partial n}\frac{\partial n}{\partial \lambda}$, which describes the optical dispersion of the utilized glass. Consequently, the expression of $\sigma\Delta d$ is given when a first-order approximation of the dispersion is applied

$$\begin{aligned}
\sigma\Delta d &= \sigma\left[\Delta d_0 + (\lambda - \lambda_0)\frac{\partial(\Delta d)}{\partial \lambda}\right] \\
&= (\sigma - \sigma_0 + \sigma_0)\left[\Delta d_0 - \lambda_0\frac{\partial(\Delta d)}{\partial \lambda}\right] + \lambda\sigma\frac{\partial(\Delta d)}{\partial \lambda} \\
&= (\sigma - \sigma_0)\frac{D}{2} + \sigma_0\Delta d_0 + (-\lambda_0\sigma_0 + \lambda\sigma)\frac{\partial(\Delta d)}{\partial \lambda} \\
&= (\sigma - \sigma_0)\frac{D}{2} + \sigma_0\Delta d_0.
\end{aligned} \tag{A.13}$$

For simplicity, a new parameter has been defined.

$$L = D + 4\tan\theta x \tag{A.14}$$

Substituting Equation A.11, Equation A.13 and Equation A.14 into Equation A.10 yields

$$\begin{aligned}
I(x) = \frac{I_0/2}{\sqrt{2\pi}P_D}\int_{-\infty}^{\infty}\exp\left[\frac{-(\sigma-\sigma_0)^2}{2P_D^2}\right]\{1+\cos[2\pi(L(\sigma-\sigma_L) \\
+D(\sigma_L-\sigma_0)+2\sigma_0\Delta d_0)]\}\,d\sigma.
\end{aligned} \tag{A.15}$$

Integrating Equation A.15 from negative infinity to positive infinity gives the radiation distribution on x plane.

$$\begin{aligned}
I(x) &= \frac{I_0}{2}\left\{1+\cos[2\pi((L-D)(\sigma_0-\sigma_L)+2\sigma_0\Delta d_0)]\exp -2\pi^2P_D^2L^2\right\} \\
&= \frac{I_0}{2}\left\{1+\cos[2\pi(4\tan\theta(\sigma_0-\sigma_L)x+2\sigma_0\Delta d_0)]\exp -2\pi^2P_D^2L^2\right\}.
\end{aligned} \tag{A.16}$$

The exponential term in this equation, determined by P_D and L, results in a decrease in the fringe amplitude with the increment of L, which also explains that the spectral

broadening is the source of the decline of the fringe contrast. Given an interference pattern, the fringe contrast can be characterized by a function of interference visibility (*Born and Wolf*, 2013), and the interference visibility is defined by

$$V(\sigma,x)=\frac{I_{max}(\sigma,x)-I_{min}(\sigma,x)}{I_{max}(\sigma,x)+I_{min}(\sigma,x)}=\frac{I_{amp}(\sigma,x)}{I_{DC}(\sigma,x)}, \tag{A.17}$$

where I_{max} is the signal intensity when the phase is a multiple of 2π, I_{min} is signal intensity when the phase is an odd multiple of π , I_{amp} is the signal amplitude of fringe at position x and I_{DC} is the signal direct current (DC) bias of fringe at position x.

A.4 Off-axis Analysis

In order to improve system sensitivity, an illumination with a solid angle is employed in a DASH instrument, which allows more radiation to go through the system. Therefore, it is necessary to analyze the fringe pattern with the off-axis illumination. With incoming angles β and ϕ as illustrated in Figure A.2, Equation A.6 changes

$$\begin{aligned} &2d\sin\theta = m\lambda_L \\ &d\cos\phi\left[\sin(\theta\mp\beta)+\sin(\theta\mp\gamma_{1,2})\right]=m\lambda\,. \end{aligned} \tag{A.18}$$

Similarly, dividing the lower formula by the upper formula in Equation A.18 gives

$$\tan\theta\cos\phi\cos\beta\mp\cos\phi\sin\beta+\tan\theta\cos\phi\cos\gamma_{1,2}\mp\cos\phi\sin\gamma_{1,2}=\frac{2\tan\theta\sigma_L}{\sigma}. \tag{A.19}$$

Using the geometric relationships, the solid angle $\Omega = 2\pi(1-\cos\phi\cos\beta)$ and $\cos\phi\cos\beta \approx \cos\phi\cos\gamma_{1,2}$ when $\beta \to 0$. Accordingly, the modification of Equation A.19 can be written as

$$\mp\cos\phi\sin\gamma_{1,2}=\frac{2\tan\theta\sigma_L}{\sigma}-2\tan\theta\left(1-\frac{\Omega}{2\pi}\right)\mp\cos\phi\sin\beta. \tag{A.20}$$

Substituting $\Omega = 2\pi(1-\cos\phi\cos\beta)$, $x=-x$ and Equation A.20 into Equation A.5, the intensity $I(x)$ with the a solid angle Ω on the localization plane can be expressed as

$$I(x) = \int_{-\infty}^{\infty} \int_{0}^{\Omega_m} B(\sigma)\, d\sigma \left\{ 1 + \cos \left[2\pi \left(4 \tan\theta \left(\sigma - \sigma_L - \frac{\Omega\sigma}{2\pi} \right) x \right. \right. \right. \\ \left. \left. \left. + \sigma \Delta d \left(2 - \frac{\Omega}{2\pi} \right) \right) \right] \right\} d\Omega. \tag{A.21}$$

The spatial frequency and the OPD offset are dependent on the field of view of the instrument due to the terms of $\frac{\Omega\sigma}{2\pi}$ and $\frac{\Omega}{2\pi}$. Integrating this equation from 0 to the maximum solid angle Ω_m yields

$$I(x) = \Omega_m \int_{-\infty}^{\infty} B(\sigma)\, d\sigma \left\{ 1 + \operatorname{sinc} \left(\frac{4 \tan\theta \sigma x + \sigma \Delta d}{2} \Omega_m \right) \right. \\ \left. \cos \left[2\pi \left(4 \tan\theta \left(\sigma - \sigma_L - \frac{\Omega_m \sigma}{4\pi} \right) x + \sigma \Delta d \left(2 - \frac{\Omega_m}{4\pi} \right) \right) \right] \right\}. \tag{A.22}$$

The factor Ω_m indicates the gain of the received energy with the increase of field of view. On the other hand, the sinc function in this equation explains the deterioration of the interference visibility. In general, the allowed solid angle is limited, which is determined by the maximum fringe amplitude at the largest OPD position (*Brault, J. W.*, 1985). Neglecting the effect of $B(\sigma)$, the fringe amplitude at x_{max} can be expressed as

$$I_{amp}(x_{max}) = \frac{2}{(4 \tan\theta \sigma x_{max} + \sigma \Delta d)\, \Omega_m} \sin \left(\frac{4 \tan\theta \sigma x_{max} + \sigma \Delta d}{2} \Omega_m \right). \tag{A.23}$$

When the maximum $I_{amp}(x_{max})$ is achieved, $\Omega_m = \pi / (4 \tan\theta \sigma x_{max} + \sigma \Delta d)$, which is the limited solid angle. According to the Rayleigh criterion, the resolution limit of the system can be regarded as the wavenumber interval when the difference of the fringe number at x_{max} is 1/2 for the two wavenumber (*Harlander*, 1991; *Born and Wolf*, 2013). Thus, the resolving power of the system is given by

$$R = 8 x_{max} \sigma \tan\theta = 4 W \sigma \sin\theta, \tag{A.24}$$

where W is the illuminated width of the grating. Same to the SHI instrument, the resolving power of a DASH instrument is determined by the dispersive elements, which achieves their theoretical resolving power (*Harlander*, 1991). Using this result, the limited solid angle changes to

$$\Omega_m = \frac{2\pi}{R + 2\sigma \Delta d}. \tag{A.25}$$

Owing to the existence of the extended OPD, the limitation on the field of view is more serious compared with an SHI system. Therefore, the field of view should be widened

in a more practical DASH configuration.

The field widening technique was firstly introduced in a Michelson interferometer (*Bouchareine and Connes*, 1963), and then this technique was extended to an SHI system (*Harlander*, 1991). The basic theory of field widening is to reduce the OPD differences between the on-axis rays and off-axis rays by inserting prisms between the beamsplitter and the gratings, so that the effects from Ω in Equation A.21 can be eliminated. An instrument visibility function $V_I(\sigma,x)$ is defined, which is used to describe the field-widening result of the fringe pattern. Thus, the intensity distribution in a field-widening DASH system can be expressed as

$$I(x) = \frac{I_0}{2}\int_{-\infty}^{+\infty} B(\sigma)\left\{1+V_I(\sigma,x)\cos\left[2\pi\left(4\tan\theta\left(\sigma-\sigma_L\right)x+2\sigma\Delta d\right)\right]\right\}d\sigma, \quad \text{(A.26)}$$

which is the modification of Equation A.10. Consequently, the fringe pattern in a conventional DASH system, as shown in Figure 2.1, yields

$$I(x) = \frac{I_0}{2}\left\{1+V_I(\sigma_0,x)\cos\left[2\pi\left(fx+2\sigma_0\Delta d_0\right)\right]\exp-2\pi^2P_D^2L^2\right\}, \quad \text{(A.27)}$$

with $f = 4\tan\theta\left(\sigma_0-\sigma_L\right)$. Note that $V_I(\sigma,x)$ is different from the visibility $V(\sigma,x)$ defined in Equation A.17. $V_I(\sigma,x)$ is the internal feature of an instrument, while $V(\sigma,x)$ includes all of the effects which may affect the interference visibility.

Appendix B

Instrument Design

B.1 Diffraction Grating

Due to the high efficiency, plane ruled reflection gratings are selected in the DASH interferometer, the specification of the grating is shown in Table B.1. The gratings were replicated from a master grating, which is a general technique to produce a great number of gratings with high performance. This grating was designed for the blaze wavelength of 550 nm, which means the maximum efficiency is achieved when the light at a wavelength of 550 nm is diffracted with the incident angle of 14.3°. Accordingly, the grating equation changes for a blazed grating

$$2d \sin \theta_b = m\lambda_b, \tag{B.1}$$

where d represents the groove spacing, m denotes the diffraction order, θ_b and λ_b are the blaze angle and blaze wavelength, respectively. Although the blaze wavelength is different from our targeted wavelength (630.03 nm), the diffraction efficiency is still larger than 70% at 630.03 nm as shown in Figure B.1. In order to suppress the thermal expansion effect, fused silica is chosen as the blank material because of its low thermal expansion coefficient.

The diffraction efficiency is a parameter to describe the energy transmission in the diffraction process. In general, the efficiency can be classified into the absolute diffraction efficiency and the relative diffraction efficiency. The absolute diffraction efficiency is the quotient of the intensity of diffracted light and the intensity of incident light. The reflectance on the grating plane is also considered in the relative diffraction efficiency, which can be calculated by dividing the absolute efficiency by the reflectance. As a function of incident wavelength, the diffraction efficiency of the grating is shown in

Table B.1: Diffraction grating specification

Item	Description
Grating type	Plane ruled reflection grating
Groove density [grooves/mm]	900
Spectral order	m = 1
Normal blaze wavelength [nm]	550
Normal blaze angle	14.3°
Blank dimensions [mm]	$40 \times 40 \times 10$
Ruled area [mm]	36×36
Blank material	Fused silica
Dimension tolerance [mm]	$\pm$ 0.1
Groove density tolerance [grooves/mm]	$\pm$ 0.5
Coating	Aluminum
Polarization	Unpolarized

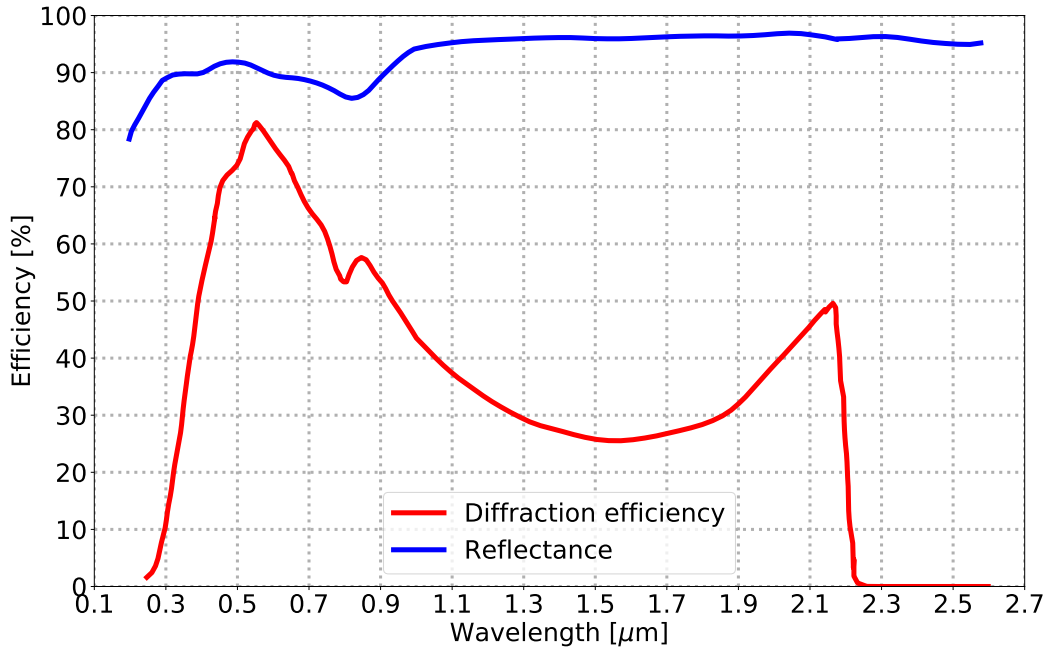

Figure B.1: Grating diffraction efficiency as a function of wavelength. An unpolarized light was used in the efficiency measurement.

Figure B.1. An aluminum optical coating was employed in the grating plane, and the reflectance on the grating plane is also presented in Figure B.1. The efficiency curve below is a relative efficiency, which is measured by the manufacture (*Rochesterson*, 2020).

B.2 Spectrum of Neon Lamp

Multiple emission lines can be resolved simultaneously in a DASH system, so that a reference line can be used to track thermal changes to the instrument. NE-1 neon calibration light source, provided by Ocean Optics, produces a series of neon lines from 540-754 nm. The relative intensities of the emission lines are shown in Figure B.2, which are provided from the manufacturer (*Ocean Optics*, 2018). In order to close to the wavelength of atomic oxygen red line emission, a line at 630.479 nm is selected as the reference line, which is also in the passband of the optical filter. Therefore, the combination of a neon lamp and a narrow bandpass filter, providing the emission line closed to 630.03 nm, is employed in a DASH instrument to track the thermal drift.

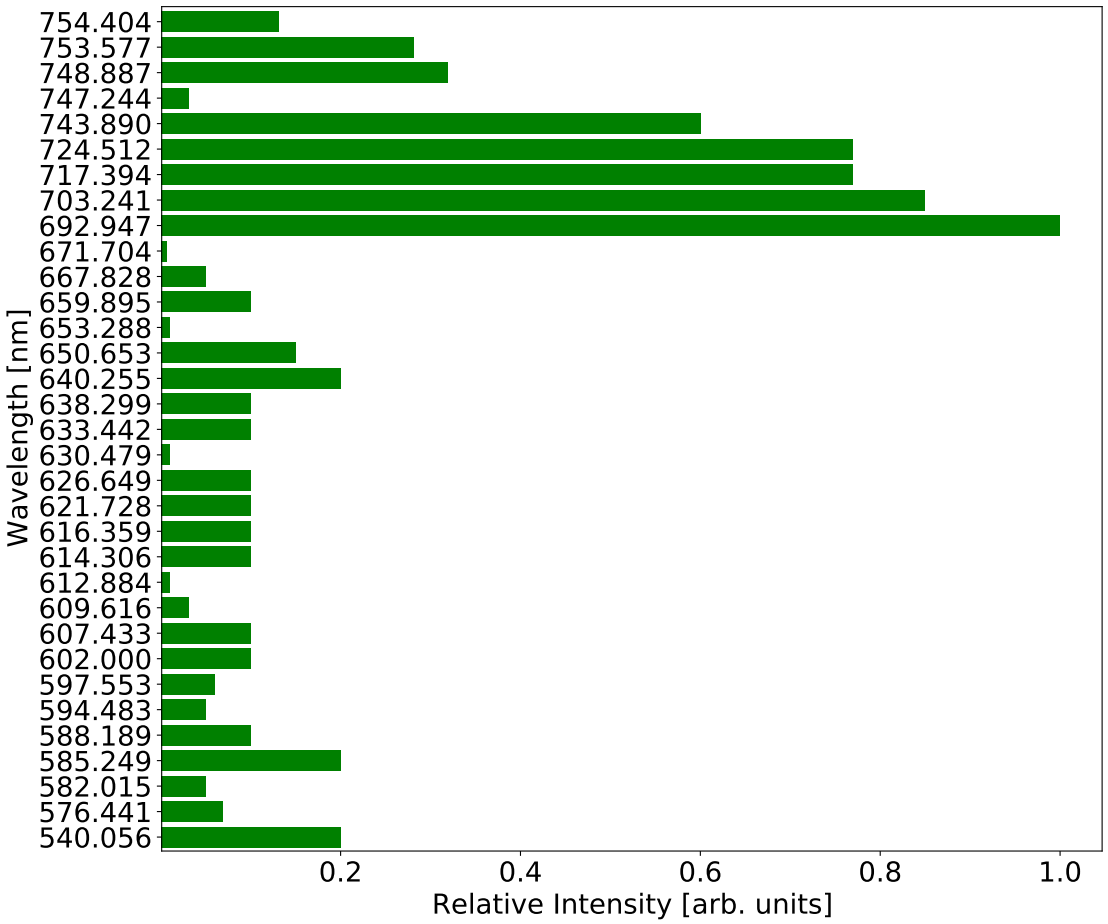

Figure B.2: Relative intensities of emission lines emitted by a neon lamp.

B.3 Bandpass Filter

The optical bandpass filter is used to isolated the targeted spectrum. The specification of the filter is shown in Table B.2. Note that the center wavelength (CWL) is the wavelength at the center of the passband and the full width at half maximum (FWHM) is the bandwidth at 50% of the maximum transmission. The transmittance curve is also presented in Figure B.3. Obviously, there is a blueshift for the transmittance curve due to the change of the incident angle. When the incident planes are different, blueshifts of the transmittance are also different, and it prefers to have a larger shift in the tangential plane. In a half cone angle of 5°, the blueshift is acceptable and the transmittance at around 630.0 nm is always larger than 90%.

Table B.2: Bandpass filter specification

Item	Description
Angle of incidence	0°, collimated
Center wavelength(CWL)	630.3 nm, nominal
Full width at half maximum (FWHM)	< 2.3 nm
Transmission	> 90% peak @630.3 nm
Blocking	> OD 4 average @300-616 nm + 645-1200 nm
Diameter	49.95 mm $\pm$ 0.05, ring mounted
Ring thickness	3.5 mm $\pm$ 0.1 mm
Substrate Thickness	2.0 mm
Substrate	NBK-7
Coating type	Hard coating

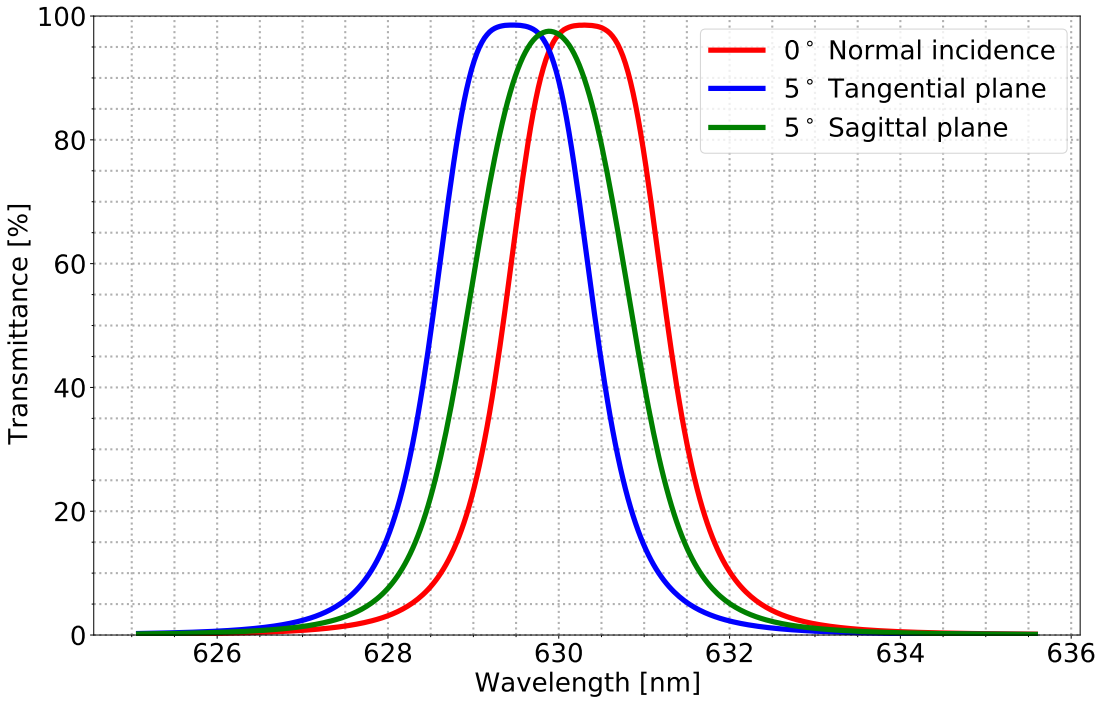

Figure B.3: Optical bandpass filter transmittance as a function of wavelength.

B.4 Temperature Dependence of the Refractive Index

The refractive index of optical glass changes with temperature and wavelength. The refractive index of glass relative to vacuum can be described by a Sellmeiler-Type formula, which is a function of wavelength from the near infrared through the visible to the near UV region (*SCHOTT Advance Optics*, 2016). The derivative of the absolute refractive index with respect to temperature can be expressed as

$$\frac{dn_{abs}(\lambda, T_0)}{dT} = \frac{n^2(\lambda, T_0) - 1}{2n(\lambda, T_0)} \left(D_0 + 2D_1\Delta T + 3D_2\Delta T^2 + \frac{E_0 + 2E_1\Delta T}{\lambda^2 - \lambda_{TK}^2} \right), \tag{B.2}$$

where T_0 is the reference temperature (20 °C), T represents the temperature in °C, ΔT represents the temperature difference versus T_0, λ represents the wavelength in a vacuum (in μm), coefficients D_O, D_1, D_2, E_0, E_1 and λ_{TK} are determined by fitting the experimentally data (*SCHOTT Advance Optics*, 2016). Using relation of Equation B.2, the change of the absolute refractive index $\Delta n_{abs}(\lambda, T)$ with the temperature difference $T - T_0$ can be derived

$$\Delta n_{abs}(\lambda, T) = \frac{n^2(\lambda, T_0) - 1}{2n(\lambda, T_0)} \left(D_0\Delta T + 2D_1\Delta T^2 + 3D_2\Delta T^3 + \frac{E_0\Delta T + 2E_1\Delta T^2}{\lambda^2 - \lambda_{TK}^2} \right). \tag{B.3}$$

Accordingly, the absolute refractive index $n_{abs}(\lambda, T)$ yields

$$n_{abs}(\lambda, T) = n_{abs}(\lambda, T_0) + \Delta n_{abs}(\lambda, T). \tag{B.4}$$

The refractive index of glass relative to air at the a temperature T and a pressure p is called relative refractive index $n_{rel}(\lambda, T, p)$, which can be calculated by

$$n_{rel}(\lambda, T, p) = \frac{n_{abs}(\lambda, T)}{n_{air}(\lambda, T, p)}, \tag{B.5}$$

with the the refractive index of air $n_{air}(\lambda, T, p)$. Consequently, the derivative of the relative refractive index with respect to temperature can be obtained by

$$\frac{dn_{rel}(\lambda, T, p)}{dT} = \frac{\frac{dn_{abs}(\lambda, T)}{dT} - n_{rel}(\lambda, T, p)\frac{dn_{air}(\lambda, T, p)}{dT}}{n_{air}(\lambda, T, p)}. \tag{B.6}$$

The refractive index of air $n_{air}(\lambda, T, p)$ can be calculated with a good accuracy by

$$n_{air}(\lambda, T, p) = 1 + \frac{n_{air}(\lambda, 15, p_0) - 1}{1 + 3.4785 \times 10^{-3} \times (T - 15)} \frac{p}{p_0}, \tag{B.7}$$

where p_0 is normal pressure with the value of 0.101325×10^6 Pa (*SCHOTT Advance Optics*, 2016). The refractive index of air at a temperature 15 °C and a pressure p_0 can be obtained using the following approximation

$$n_{air}(\lambda, 15, p_0) = 1 + \left[6432.8 + \frac{2949810\lambda^2}{146\lambda^2 - 1} + \frac{25540\lambda^2}{41\lambda^2 - 1}\right] \times 10^{-8}. \tag{B.8}$$

The value of $\frac{dn_{air}(\lambda, T, p)}{dT}$ can also be calculated with a good accuracy by

$$\frac{dn_{air}(\lambda, T, p)}{dT} = -0.00367 \frac{n_{air}(\lambda, T, p) - 1}{1 + 0.00367T}. \tag{B.9}$$

B.5 OPD Difference in a DASH Interferometer

In a field-widening DASH interferometer, the OPD difference, an important parameter to evaluate the field-widening performance, can be obtained by tracing the OPD on the both arms separately using ray-tracing software. The tracing results of the optimized interferometer are presented in Figure B.4, Figure B.5 and Figure B.6.

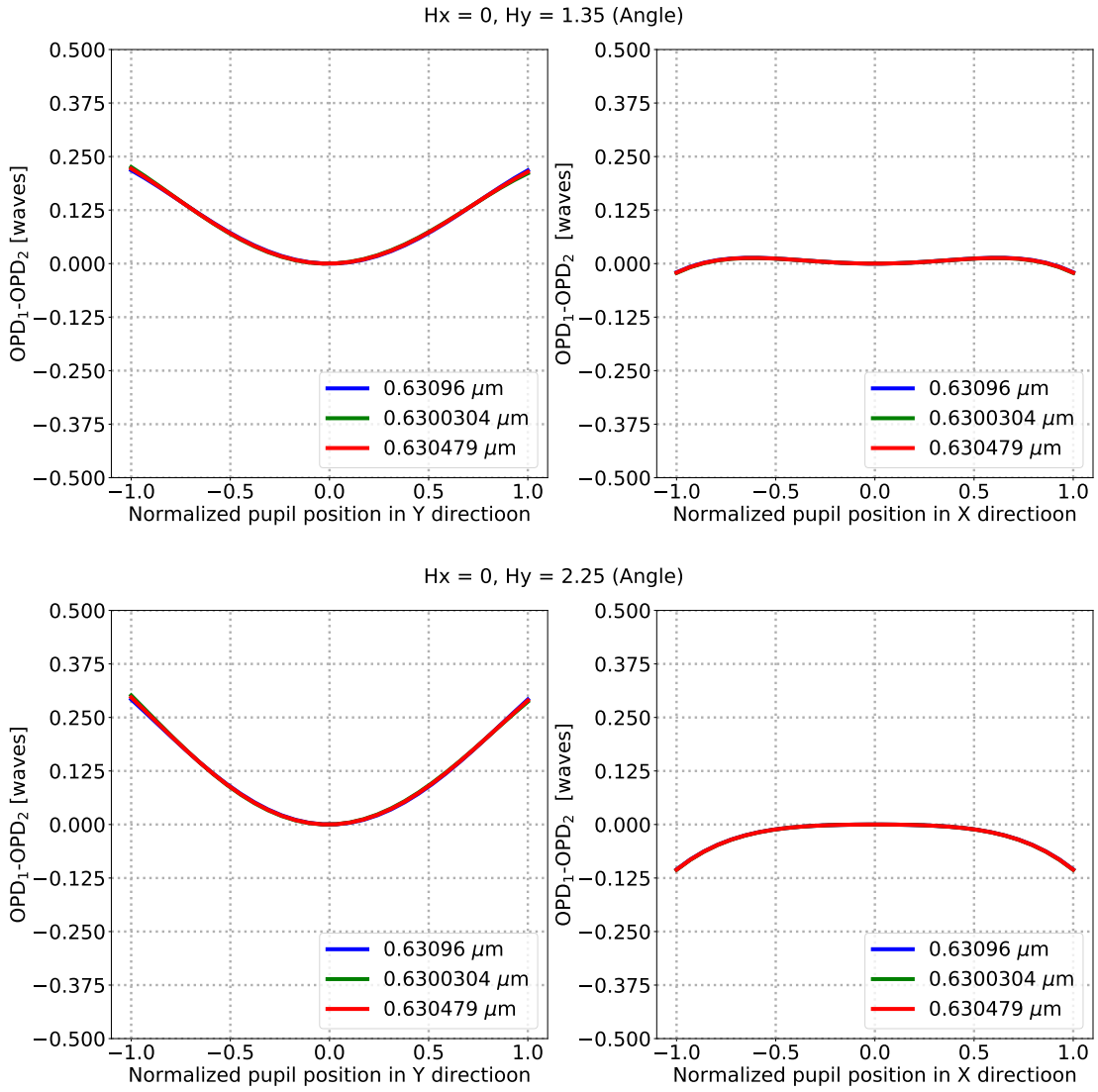

Figure B.4: Tracing result of the OPD difference on the transverse plane (left) and sagittal plane (right) for the fields of 1.35° and 2.25°.

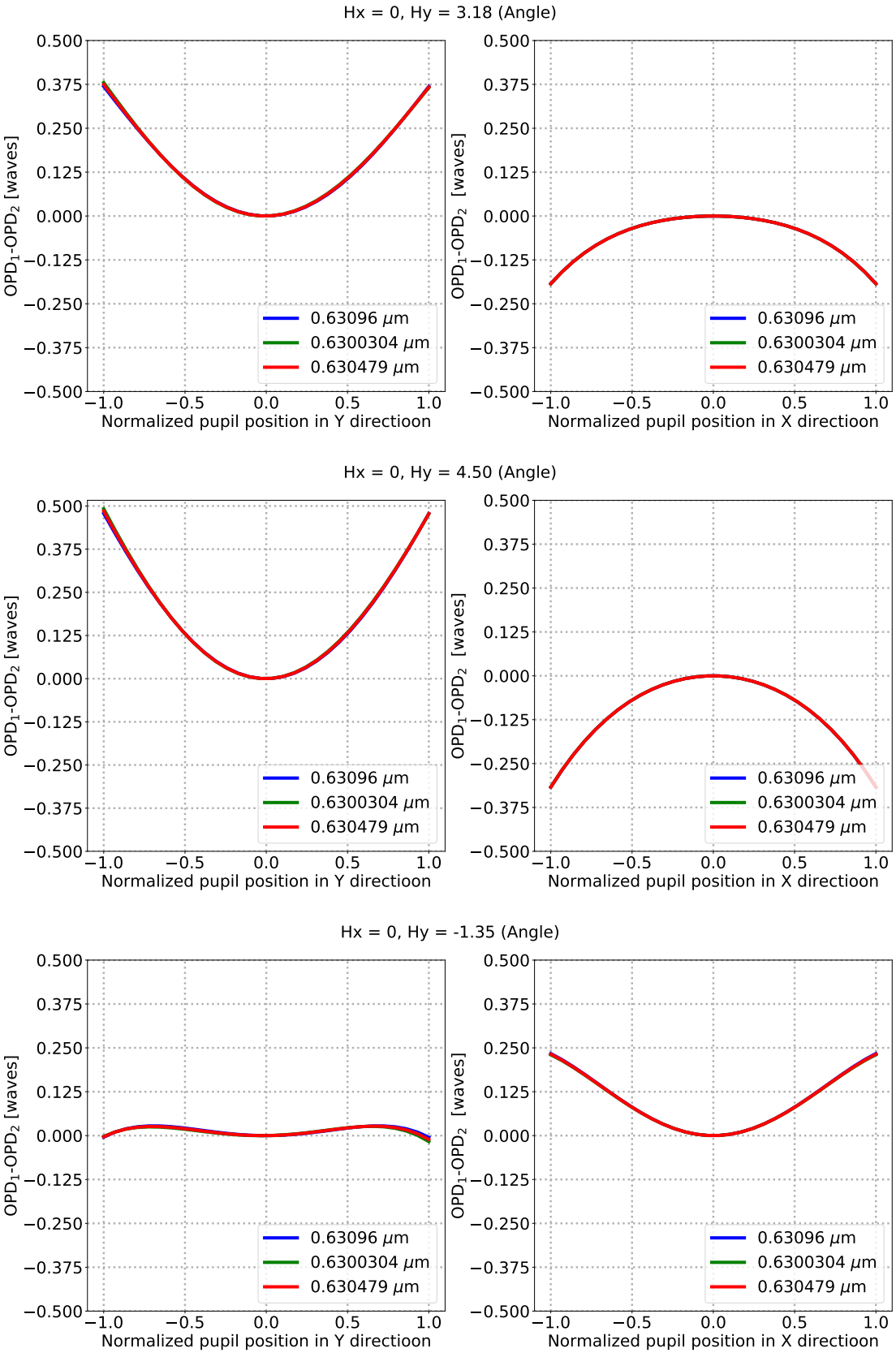

Figure B.5: Tracing result of the OPD difference on the transverse plane (left) and sagittal plane (right) for the fields of 3.18°, 4.5° and -1.35°.

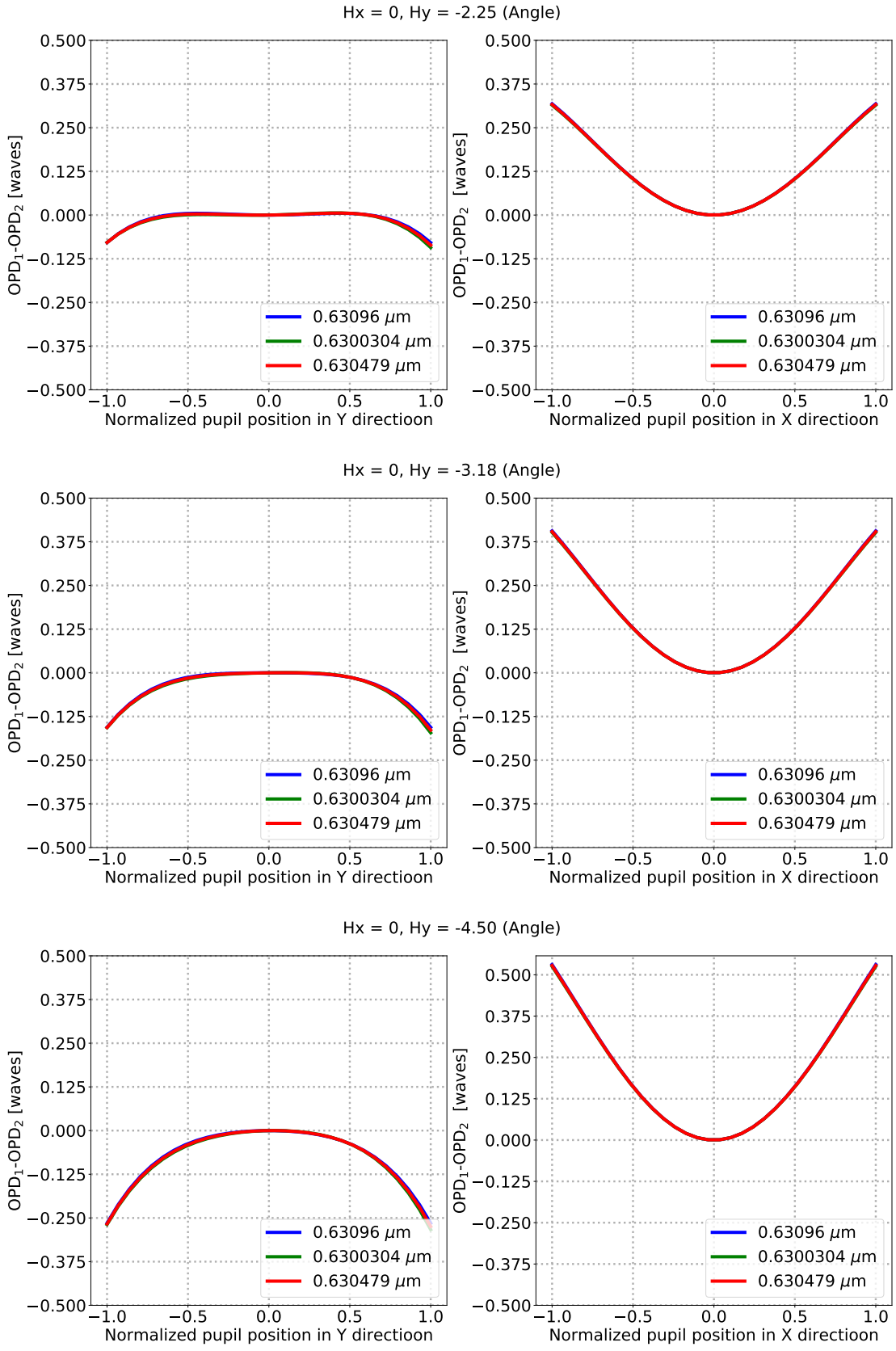

Figure B.6: Tracing result of the OPD difference on the transverse plane (left) and sagittal plane (right) for the field of -2.25°, -3.18° and -4.5°.

B.6 Paraxial Optics and Third-order Aberrations

The paraxial analysis and third-order aberration calculation are important steps in optical design. Firstly, an optical system is designed using paraxial ray tracing or the first-order calculation. Assuming all of lenses are thin lenses, the paraxial ray tracing in a system comprised of k lenses can be expressed as

$$\begin{aligned} &\frac{1}{l_i'} - \frac{1}{l_i} = \frac{1}{f_i'} = \varphi_i \\ &l_i = l_{i-1} - d_{i-1} \\ &\prod_{i=1}^{k} \frac{l_i'}{l_i} = m \\ &i = 1, 2 \cdots k, \end{aligned} \tag{B.10}$$

where l_i denotes the object distance from the ith lens, l_i' denotes the image distance from the ith lens, f_i' denotes the focal length of the ith lens, φ_i denotes the optical power of the ith lens, d_i denotes the distance between the ith lens and the $(i+1)$th lens and m denotes the magnification of this system (*Smith*, 2000). In order to correct the field curvature in a optical system, a zero value of the Petzval sum is also required (*Smith*, 2000),

$$\sum_{i=1}^{k} \frac{1}{f_i'} = 0. \tag{B.11}$$

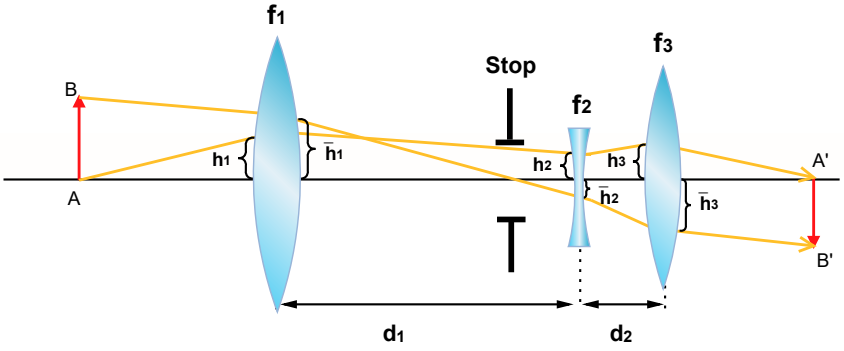

Figure B.7: Definition of the paraxial marginal ray and principle ray.

Combining Equation B.10, Equation B.11 and the dimension consideration, the first-order design was determined, which was then used to analyze the third-order aberration. The paraxial marginal ray and the paraxial principle ray are two auxiliary rays in calculating the third-order aberration. Using three lenses system as a example, the definition of auxiliary rays are presented in Figure B.7. From a on-axis point A, the ray goes

through the edge of the stop and reaches the image point A', which is the paraxial marginal ray. The paraxial principle ray is the ray which starts the off-axis point B, traverses the center of the stop and reaches the point B'. The incidence heights of the marginal ray and the principle ray at the lenses can be traced using Equation B.10, and the heights at the ith lens are defined by h_i and $\bar{h}_i$, respectively.

The third-order aberration can be described by Seidel sums, which consist of the spherical aberration (S_{I}), coma (S_{II}), astigmatism (S_{III}), field curvature (S_{IV}) and distortion (S_{V}) (*Smith*, 2000; *Laikin*, 2001). Using the first-order design and the paraxial-ray result, Seidel sums are given

$$
\begin{aligned}
S_{\mathrm{I}} &= \sum_{i=1}^{k} h_i^4 \varphi_i^3 \bar{M}_i + 2\sum_{i=1}^{k} h_i^4 \varphi_i^3 Y_i \bar{N}_i + 1.06\sum_{i=1}^{k} h_i^4 \varphi_i^3 Y_i^2, \\
S_{\mathrm{II}} &= \sum_{i=1}^{k} h_i^3 \bar{h}_i \varphi_i^3 \bar{M}_i + \sum_{i=1}^{k} h_i^2 \varphi_i^2 \left(2h_i \bar{h}_i \varphi_i Y_i + 1\right) \bar{N}_i \\
&\quad + \sum_{i=1}^{k} h_i^2 \varphi_i^2 Y_i \left(1.06 h_i \bar{h}_i \varphi_i Y_i + 1.31\right), \\
S_{\mathrm{III}} &= \sum_{i=1}^{k} h_i^2 \bar{h}_i^2 \varphi_i^3 \bar{M}_i + 2\sum_{i=1}^{k} h_i \bar{h}_i \varphi_i^2 \left(h_i \bar{h}_i \varphi_i Y_i + 1\right) \bar{N}_i \\
&\quad + \sum_{i=1}^{k} h_i \bar{h}_i \varphi_i^2 Y_i \left(1.06 h_i \bar{h}_i \varphi_i Y_i + 2.62\right) + \sum_{i=1}^{k} \varphi_i, \\
S_{\mathrm{IV}} &= 0.62 \sum_{i=1}^{k} \varphi_i, \\
S_{\mathrm{V}} &= \sum_{i=1}^{k} h_i \bar{h}_i^3 \varphi_i^3 \bar{M}_i + \sum_{i=1}^{k} \bar{h}_i^2 \varphi_i^2 \left(2h_i \bar{h}_i \varphi_i Y_i + 3\right) \bar{N}_i \\
&\quad + \sum_{i=1}^{k} \bar{h}_i^2 \varphi_i^2 Y_i \left(1.06 h_i \bar{h}_i \varphi_i Y_i + 3.93\right) + 3.62 \sum_{i=1}^{k} \frac{\bar{h}_i}{h_i} \varphi_i,
\end{aligned}
\tag{B.12}
$$

where Y_i is the conjugate parameter of the ith lens, $\bar{M}_i$ and $\bar{N}_i$ are the parameters associated with the refractive index and the radii of curvature of the ith lens (*Mikš*, 2002). The conjugate parameter Y can be calculated by

$$
Y = \frac{l' + l}{l' - l} = -1 - \frac{2}{l\varphi}. \tag{B.13}
$$

In order to correct the aberrations, equations of $S_{\mathrm{I,II,III,IV,V}} = 0$ are yielded. Solving

those equations using a least-squares method gives the $\bar{M}$ and $\bar{N}$ for individual lens. The refractive index n and the radii of curvature r and r' were deduced using the following formulas (*Mikš*, 2002):

$$\begin{aligned} n &= \frac{\sqrt{\bar{M} - 0.86\bar{N}^2}}{\sqrt{\bar{M} - 0.86\bar{N}^2} - 0.5} \\ \bar{N} &= 0.5 \left[\frac{n+1}{n(n-1)} X \right] \\ r &= \frac{2(n-1)}{\varphi(X+1)} \\ r' &= \frac{2(n-1)}{\varphi(X-1)}. \end{aligned} \tag{B.14}$$

Notice that the refractive index should be in the range of $1.43 < n < 2$, otherwise the simple lens needs to be replaced by a doublet or triplet lens. Accordingly, an imaging system with the optimization of third-order aberrations is obtained.

Appendix C

Instrument Development

C.1 Dislocation of the gratings

In a DASH interferometer, dislocation of the gratings breaks the coincidence of the grating images on two arms, which introduces an angle β_2 as shown in Figure 5.1. In this section, the effect of dislocation of the gratings on the interfergram is studied.

As shown in Figure 5.1, a wave vector is incident on the grating at an angle θ_{in}, and this wave vector can be expressed in coordinate xyz as

$$\vec{k} = \begin{pmatrix} 0 \\ 0 \\ k \end{pmatrix}. \tag{C.1}$$

Angle β_2 can be produced by rotating the grating about it plane normal z'. In order to model this effect, another coordinate $x'y'z'$ is established as presented in Figure 5.1. The coordinate $x'y'z'$ can be obtained by rotating the coordinate xyz by an angle θ_{in} about y axis and then rotating the coordinate by an angle β_2 about z axis again. Thus, the transformation matrix between the two coordinates is given by

$$M = R_z \cdot R_y = \begin{pmatrix} \cos\beta_2\cos\theta_{in} & \sin\beta_2 & -\cos\beta_2\sin\theta_{in} \\ -\sin\beta_2\cos\theta_{in} & \cos\beta_2 & \sin\beta_2\cos\theta_{in} \\ \sin\theta_{in} & 0 & \cos\theta_{in} \end{pmatrix}. \tag{C.2}$$

With the transformation matrix M, the incident wave vector in coordinate $x'y'z'$ can

be modified by

$$\vec{k'} = M \cdot \vec{k} = \begin{pmatrix} -\cos\beta_2 \sin\theta_{in} k \\ \sin\beta_2 \sin\theta_{in} k \\ \cos\theta_{in} k \end{pmatrix}. \tag{C.3}$$

The wave vector propagation in the dispersion plane ($x'oz'$ plane) can be described by the grating equation, as shown in Equation A.1. Using the wave vector in coordinate $x'y'z'$, the grating equation changes to

$$\begin{aligned} & d\cos\phi\left(\sin\theta'_{in} + \sin\theta'_{out}\right) = m\lambda \\ & \theta'_{in} = \arctan\left(\cos\beta_2 \tan\theta_{in}\right) \\ & \cos\phi = \sqrt{\cos^2\beta_2 \sin^2\theta_{in} + \cos^2\theta_{in}} \end{aligned}, \tag{C.4}$$

where d denotes the groove spacing of the grating, ϕ denotes the angle between the wave vector and the dispersion plane, θ'_{in} and θ'_{out} are the incident angle and exit angle in the dispersion plane, m represents the diffraction order and λ represents the wavelength of the incident wave vector. The wave propagation in the $y'oz'$ is a reflection process, which just changes the direction of wave vector in this plane. Therefore, the exit wave vector $\vec{k'}_{exit}$ can be determined by

$$\vec{k'}_{exit} = \begin{pmatrix} -\sin\theta'_{out}\cos\phi k \\ -\sin\beta_2 \sin\theta_{in} k \\ \cos\theta'_{out}\cos\phi k \end{pmatrix}. \tag{C.5}$$

Using the transformation matrix, the exit wave vector in coordinate xyz can be calculated by

$$\vec{k}_{exit} = M^{-1}\vec{k'}_{exit}. \tag{C.6}$$

When $\beta_2 \to 0$, $\theta'_{in} \approx \theta_{in}$, $\phi \approx 0$ and the exit wave vector can be expressed as

$$\vec{k}_{exit} = \begin{pmatrix} \sin\left(\theta_{in} - \theta'_{out}\right) k \\ -\beta_2 \dfrac{m\lambda}{d} k \\ \sin\theta_{in}\sin\theta'_{out} k + \cos\theta_{in}\cos\theta'_{out} k \end{pmatrix}. \tag{C.7}$$

With $\beta_2 = 0$ and $\theta_{in} = -\theta_{in}$, the wave vector on another arm can be also determined using similar method. The small angle β_2 does not change the component of wave vector in x direction but introduces an additional wave vector in y direction with the

value $-\beta_2 \frac{m\lambda}{d}$, which produces a spatial modulation in y direction

$$f_y = \beta_2 \frac{m}{d}. \tag{C.8}$$

This f_y is a function of the diffraction order rather than the wavenumber, which means that interferograms along y direction can not be resolved except that they are produced from different-order diffraction.

C.2 Baffle System

Baffles are generally used to block light from sources outside of the field of view of the system. A baffle with the half field of view of 4.5° is described in this section. A systematic layout of the baffle is presented in Figure C.1. In order to block all of the first-order stray light, six vanes are introduced here. The vane apertures, spacing and bevel angles are determined by the construction lines (red dashed lines in Figure C.1), so that the first-order stray light can not go through the system (*Lee et al.*, 2000; *Fest*, 2013). Scatterings from the edges of vanes are also considered in design. In the front section of the baffle, the bevels are on the object side of the vanes. In the deeper section, the bevels are on the opposite side to prevent the direct radiation reaching the beveled edge.

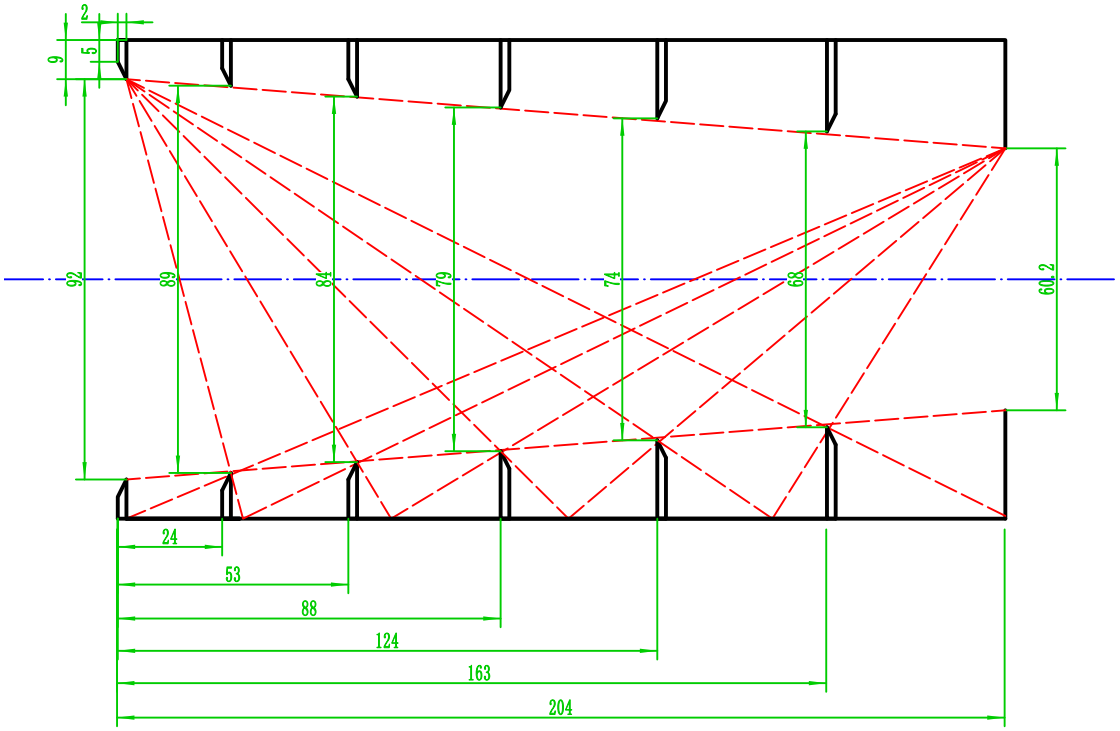

Figure C.1: A systematic layout of the baffle and construction lines (red dashed lines) to determine the vane apertures, spacing and bevel angles.

C.3 DASH Housing and Temperature Control Unit

An interferometer housing was designed and built for the monolithic DASH interferometer. As shown in Figure C.2, a window and a optical filter are included in this housing, which reduces the thermal interaction between the housing and the outside environment. The DASH interferometer was glued into the housing under the monitoring of the interferogram using the setup described in Section 5.2. For thermal insulation, the housing was covered with 5 cm thick foam boards, which is shown in Figure C.3.

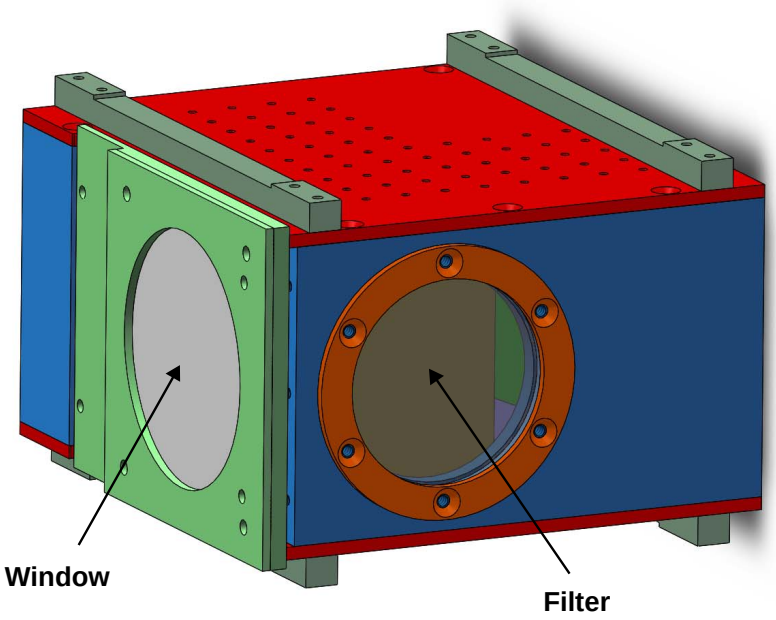

Figure C.2: DASH interferometer housing

Except the passive insulation, an active temperature control is also employed. Two Kapton heaters attached on the top and bottom of the aluminum housing in combination with temperature sensors mounted on the inside of the housing stabilizes the temperature of interferometer using a PID controller. Since the heaters are implemented to control the temperature, the stabilized temperature of housing must be higher than the ambient temperature. The temperature sensor is hung in the air, so that the air temperature in the inside of the housing is stabilized. In order to verify the performance of the temperature control unit, experimental tests were performed in laboratory and the results are presented in Figure C.4. The environment temperature is around 22 °C, and our purpose is to stabilize the temperature at 25 °C. After about 4 hours, a thermal stabilization was realized and the temperature was well maintained after achieving the

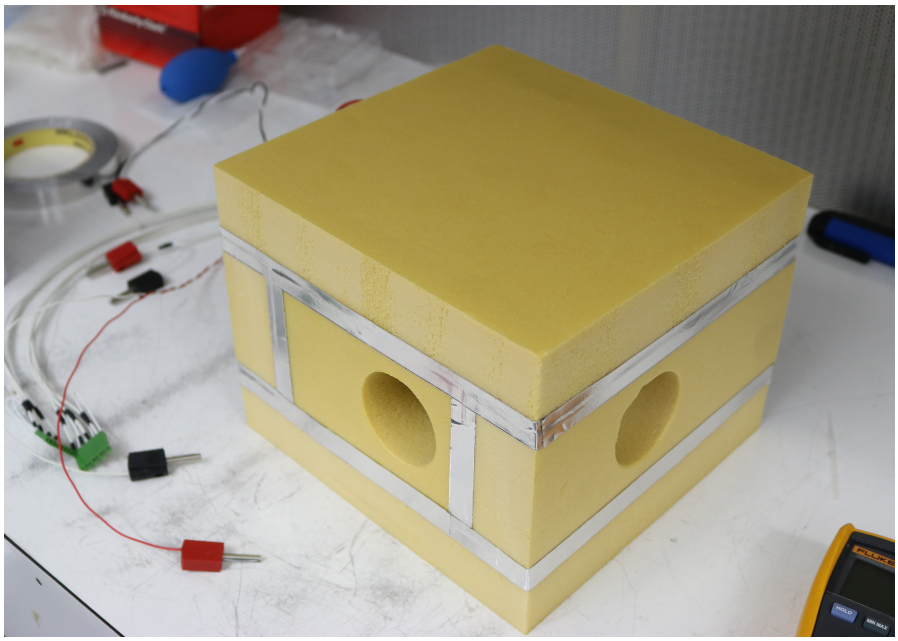

Figure C.3: Housing of a DASH interferometer covered with foam boards.

stabilization. Although it needs a long time to achieve the stabilization because of the lack of cooling function of this control unit, the temperature can be stabilized within $\pm$ 0.02 °C.

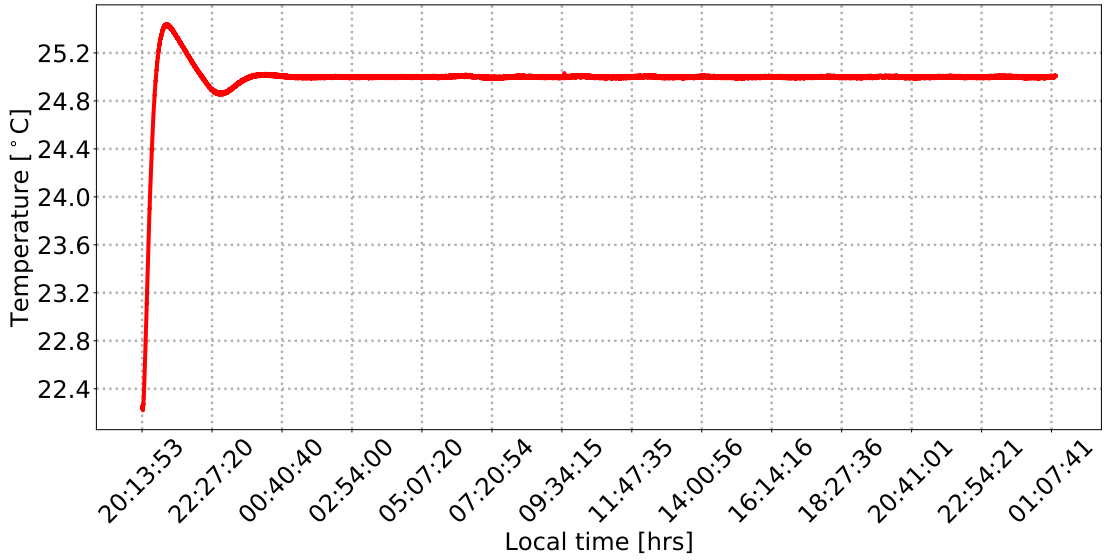

(a) Temperature stabilized process

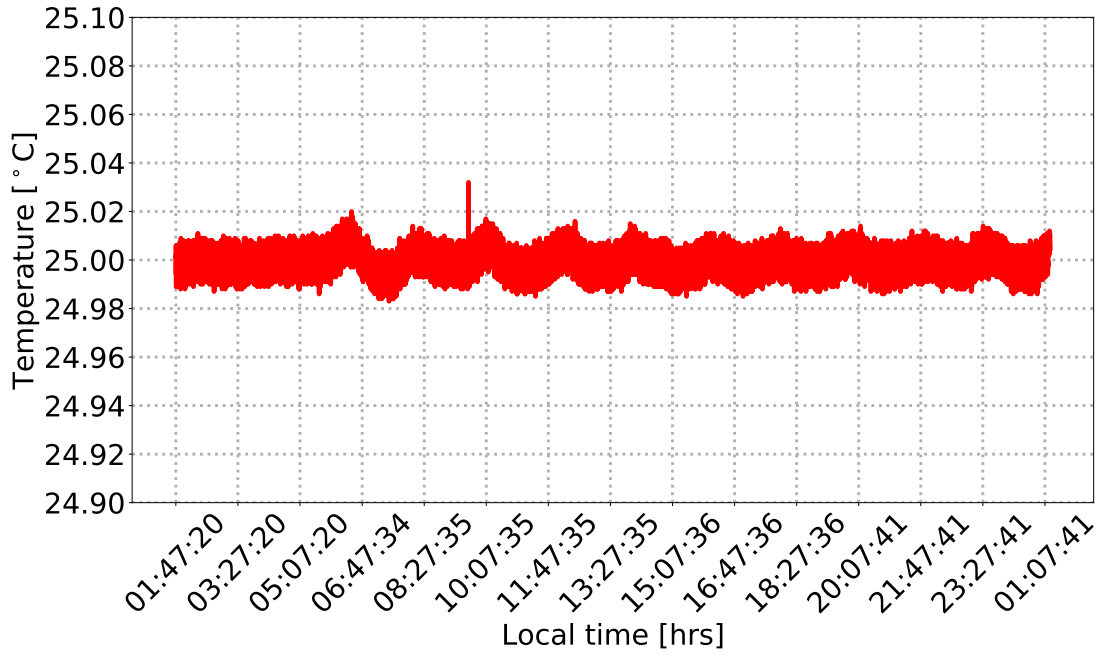

(b) Temperature variation after thermal stabilization is achieved

Figure C.4: (a) Temperature stabilized process and (b) the temperature variation after the thermal stabilization is established in a DASH interferometer.

Acknowledgements

This dissertation would not have been completed without the active support and encouragement of many people. I would like to thank all of the people who contributed to my dissertation.

First of all, I would like to express my deep gratitude to my doctoral supervisor Prof. Dr. Martin Riese for the opportunity to participate in this project and work at IEK-7, Forschungszentrum Jülich. I am also deeply appreciative of Prof. Dr. Ralf Koppmann, who has provided me the opportunity to study at Bergische Universität Wuppertal. I have benefited much from their invaluable guidance and continuous support throughout my Ph.D study.

I would like to thank my academic supervisor Dr. Martin Kaufmann for his patient supervision, continuous encouragement and helpful advice. He has constantly helped me throughout my entire Ph.D study. His knowledge of atmospheric physic, combined with his rich experience in remote-sensing instrument, and his open-minded approach contributed much to the completion of my project. I am also really grateful to Dr. Yajun Zhu, who has brought me into a new topic and given me lots of constructive suggestions and profound advices on my work. The discussion with him were also valued.

Many thanks goes to Peter Knieling and Dr. Heinz Rongen for their continued support on the electronics and detector. I thank Friedhelm Olschewski for sharing his expertise and providing continuous support on the mechanics. The experimental support from Florian Dötzer of Friedrich-Alexander Universität Erlangen-Nürnberg is greatly appreciated. I also thank Dr. Klaus Mantel of Max-Planck-Institute for the Science of Light for his suggestions and comments on the optics.

I would also like to thank Dr. Jilin Liu, Dr. Qiuyu Chen, Qiucheng Gong, Ivona Prusina, Oliver Wroblowski, Dr. Rui Song, Dr. Michael Deiml and other colleagues at IEK-7 and Bergische Universität Wuppertal for the good moment we worked together.

Outside of the work, I am grateful to my parents, family and friends for their encouragement and support. Finally, I would like to thank my girlfriend, her love, encouragement and support made this all possible.

Acronyms

CCD	Coupled Charge Device.
CET	Central European Time.
CLIO	Circle-to-Line Interferometer Optic.
CMOS	Complementary Metal-Oxide-Semiconductor.
CTE	Coefficient of thermal expansion.
CWL	Center Wavelength.
DASH	Doppler Asymmetric Spatial Heterodyne.
DC	Direct Current.
ERPM	Electrical Revolutions Per Minute.
EUV	Extreme Ultraviolet.
FEM	Finite Element Model.
FPI	Fabry-Perot Interferometer.
FPN	Fixed Pattern Noise.
FTS	Fourier Transform Spectrometer.
FWHM	Full Width at Half Maximum.
HDR	High Dynamic Range.
HRDI	High Resolution Doppler imager.
HWM	Horizontal Wind Model.
ICON	Ionospheric Conection.
IRI2012	International Reference Ionosphere 2012.

IRISHI	Infrared Imaging Spatial Heterodyne Interferometer.
MICADO	Michelson Interferometer for Coordinated Auroral Doppler Observations.
MIGHTI	Michelson Interferometer for Global High-resolution Thermospheric Imaging.
MLT	Mesosphere and Lower Thermosphere.
MTF	Modulation Transfer Function.
NRLMSISE-00	Naval Research Laboratory Mass Spectrometer Incoherent Scatter Radar 2000.
NSPWII	Novel Static Polarization Wind Imaging Interferometer.
OPD	Optical Path Difference.
PID	Proportional Integral Derivative.
PTC	Photon Transfer Curve.
REDDI	Redline DASH Demonstration Instrument.
RMS	Root Mean Square.
RPM	Revolutions Per Minute.
SHI	Spatial Heterodyne Interferometer.
SHIMMER	Spatial Heterodyne Imager for Mesospheric Radicals.
SHOW	Spatial Heterodyne Observations of Water.
SISAM	Spectromètre Interférentiel à Sélection par L'amplitude de Modulation.
SNR	Signal-to-noise Ratio.
STD	Standard Dynamic Range.
STPSat-1	Space Test Program Satellite-1.
TEC	Thermoelectric Cooler.

TIDI	TIMED Doppler Interferometer.
TIMED	Thermosphere Ionosphere Mesosphere Energetics and Dynamics Satellite.
UARS	Upper Atmosphere Research Satellite.
UV	Ultraviolet.
UVES	Ultraviolet and Visual Echelle Spectrograph.
VER	Volume Emission Rate.
VESC	Vedder Electronic Speed Controller.
WAMDII	Wide Angle Michelson Doppler Imaging Interferometer.
WINDII	Wind Imaging Interferometer.
WINTERS	WINd and TemperaturE by Remote Sensing.

List of Symbols

$A(f,x)$	Amplitude of Interferogram.
$A_{^1D}$	Transition Coefficient of $O(^1D_2 - ^3P_2)$ and $O(^1D_2 - ^3P_1)$.
A_{6300}	Einstein Transition Probability of $O(^1D_2 - ^3P_2)$.
A_{6364}	Einstein Transition Probability of $O(^1D_2 - ^3P_1)$.
α	Apex Angle of Prism.
α_1	Rate Coefficient of the Dissociative Recombination of O_2^+ in the Atmosphere (R2 in Table 1.1).
α_{CTE}	Coefficient of Thermal Expansion of Grating Substrate.
α_i	Angle between the Incident Ray and the Rotation Plane.
α_r	Angle between the Reflective Ray and the Rotation Plane.
$B(f)$	Spectral Density.
$B(\sigma)$	Input Spectral Intensity.
β	Incident Angle in the Dispersion Plane.
β_1	Rotation Angle about the Direction Perpendicular to the Groove of Grating.
$\beta_{^1D}$	Production Efficiency of $O(^1D)$ in the Dissociative Recombination of O_2^+ in the Atmosphere (R2 in Table 1.1).
β_2	Angle between the Grooves of the Two Gratings.
c	Speed of Light.

$C_{1,2,3}$	CTEs of the Beamsplitter, Spacer 1 and Spacer 2.
$\circledast$	Convolution Operator.
d	Groove Spacing of Grating.
D	Effective Optical Path Difference.
d_1	Thickness of Spacer 1.
d_2	Thickness of Spacer 2.
Δd	Extended Distance on One Arm.
Δd_0	Extended Distance at the Central Wavelength of Emission Line.
δd_{cal}	Thermally Induced OPD-offset Variation at the Wavenumber of σ_{cal}.
$\Delta d_{E,cal}$	Wavenumbers of Red Line Emission and Calibration Line.
$\delta d'_E$	Thermally Induced OPD-offset Variation at the Wavenumber of σ'_E.
$\Delta L(x, \phi_i, \beta_i)$	OPD at the Localization Plane x.
$\Delta\varphi(x)$	Phase Change.
Δx	Thermally Induced Image Shift.
E	Etendue of Instrument.
E_1	Complex Amplitude on Arm 1.
E_2	Complex Amplitude on Arm 2.
$\varepsilon(l)$	Volume Emission Rate at Position l.
η	Incident Angle on the Field-widening Prism When Minimum Deviation Occurs.
f	Spatial Frequency.
f_r	Rotation Frequency of the Rotation Wheel.
f_x	Spatial Frequency in x Direction.
f_y	Spatial Frequency in y Direction.
G	System Gain.
γ	Angle of Wavefront Tilt.

h	Plank's Constant.
h_x	Field of View in x Direction.
h_x	Field of View in y Direction.
I_0	Intensity of the Input Radiation.
$\Im\left[I_f(x)\right]$	Imaginary Part of the Modulated Portion of Interferogram.
$\Re\left[I_f(x)\right]$	Real Part of the Modulated Portion of Interferogram.
$I(x)$	Intensity of interferogram at position x.
k_1	Rate Coefficient of the Reaction between O^+ and O_2 in the Atmosphere (R1 in Table 1.1).
K_1	Scalar Quantity.
K_2	Scalar Quantity.
k_3	Rate Coefficient of the Reaction between $O(^1D)$ and N_2 in the Atmosphere (R3 in Table 1.1).
k_4	Rate Coefficient of the Reaction between $O(^1D)$ and O_2 in the Atmosphere (R4 in Table 1.1).
k_5	Rate Coefficient of the Reaction between $O(^1D)$ and e in the Atmosphere (R5 in Table 1.1).
k_B	Boltzmann's Constant.
L	Describe a Descrease of Fringe Contrast, $L = D + 4\tan\theta x$.
L_γ	Spectral Radiance.
λ	Wavelength.
λ_0	Central Wavelength of Emission Line.
m	Diffraction Order.
$M(x,y)$	Phase Distortion Matrix.
n	Refractive Index.
N	Pixel Number of Detector.
$\bar{n}_{e_d}$	Dark Current.

n_{e_γ}	Photoelectrons.
n_x	Pixel Index in x Direction.
NA	Numerical Aperture.
ω	Incident Angle on the Spacer 1 or Spacer 2.
Ω	Solid Angle.
$OPD_{1,2}(h_x, h_y, p_x, p_y)$	OPD with the Reference of Chief Ray.
$P_{1,2}(x, \phi, \beta)$	Optical Paths from the Beamsplitter to the Localization Plane on Arm 1 and Arm 2.
P_D	Doppler-broadening Parameter.
p_x	Pupil Position in x Direction.
p_y	Pupil Position in y Direction.
ϕ	Angle between Incoming Wavevector and the Dispersion Plane.
$\Phi(f, x)$	Phase Offset.
Φ_γ	Photon Flux.
Q_E	Quantum Efficiency.
r	Radius of Rotation.
R	Resolving Power.
r_b	Ratio of the Background Spectrum to the Targeted Emission Line.
r_d	Distorted Radius in Respect of the Optical Center.
r_u	Undistorted Radius in Respect of the Optical Center.
$R(x, y)$	Spectral Density.
s	Line of Sight.
S	Crossing Area.
$\bar{S}_{DN}$	Mean Signal in Units of counts.
s_p	Pixel Size.
$\bar{S}_{SO}$	Signal Offset in Units of counts.

σ	Wavenumber.
σ_0	Central Wavenumber of the Emission Line.
$\sigma_{\Delta L}$	Standard Deviation of ΔL.
$\sigma_{E,cal}$	Wavenumbers of Red Line Emission and Calibration Line.
σ_L	Littrow Wavenumber of Grating.
σ^2_{noise}	Variance of Detector Noise.
$\sigma^2_{noise,DN}$	Variance of Signal Noise in Units of counts^2.
σ^2_r	Variance of Readout Noise.
$\sigma_{r,DN}$	Readout Noise in Units of counts.
σ^2_s	Variance of Shot Noise.
σ_{s,e^-}	Shot Noise in Units of e^-.
σ_v	Wavenumber with a Doppler Shift of v.
t_1	Asymmetric Thickness.
T_a	Transmittance of the Atmosphere.
T_e	Temperature of Electron.
$t(f)$	Window Function.
T_f	Transmittance of the Filter.
T_i	Temperature of Ion.
t_{int}	Exposure Time of Detector.
T_n	Temperature of Neutral.
T_o	Transmittance of the Optics.
$t_{one}(x,y)$	Amplitude Transmission Function on Arm one.
$t_{two}(x,y)$	Amplitude Transmission Function on Arm two.
$T(x)$	Inverse Fourier Transform of $t(f)$.
θ	Littrow Angle of Grating.
$\Theta(x,y)$	Local Phase Induced by Optical Defects.
θ_{in}	Incident Angle on the Grating.
θ_{out}	Exit Angle on the Grating.
θ'	Exit Angle on the Second Plane of Prism.
U_e	Energy of One Electron.

V_{6300}	Volume Emission Rate of Oxygen Red Line.
v_D	Doppler Velocity.
$V_I(\sigma, x)$	Instrument Visibility Function.
v_t	Tangential Velocity of the Rotation Wheel.
$V(\sigma, x)$	Interferogram Visibility.
$V(x, y)$	Interfernce Visibility.
$\varepsilon(f, x, y)$	Modulation Efficiency for the Spatial Frequecny f.
$\varphi(f, x)$	Phase of Interferogram.
$\vec{v}$	Horizontal Wind Velocity.
$\vec{v}_{east}$	Horizontal Wind Velocity in the East Direction.
$\vec{k}$	Wave Vector.
$\vec{v}_{north}$	Horizontal Wind Velocity in the East Direction.
W	Illuminated Width.
x	Position in x Axis.
ζ	Incline Angle.

List of Figures

List of Tables

Bibliography

Armstrong, E. B. (1955), The observation of line profiles in the airglow and aurora with a photoelectric Fabry-Perot interferometer, p. 366.

Armstrong, E. B. (1959), The temperature in the atmospheric region emitting the night-glow OI 5577 line and in regions above faint auroral arcs, *Journal of Atmospheric and Terrestrial Physics*, *13*(3), 205–216, doi:10.1016/0021-9169(59)90114-X.

Armstrong, S. J. (2008), *Fabry-Perot Data Analysis and Simulation for the REN-OIR Observatories*, University of Illinois at Urbana-Champaign, google-Books-ID: b4b6PgAACAAJ.

Bilitza, D., D. Altadill, Y. Zhang, C. Mertens, V. Truhlik, P. Richards, L.-A. McKinnell, and B. Reinisch (2014), The International Reference Ionosphere 2012 - a model of international collaboration, *Journal of Space Weather and Space Climate*, *4*, A07, doi:10.1051/swsc/2014004.

Born, M., and E. Wolf (2013), *Principles of Optics: Electromagnetic Theory of Propagation, Interference and Diffraction of Light*, Elsevier.

Bouchareine, P., and P. Connes (1963), Interferometer with compensated field for Fourier transform spectroscopy, *J. Phy*, *24*(2), 134–138.

Brault, J. W. (1985), Fourier Transform Spectroscopy, *High Resolution in Astronomy, Fifteenth Advanced Course of the Swiss Society of Astronomy and Astrophysics*, (3-61).

Burnside, R. G., and C. A. Tepley (1989), Optical observations of thermospheric neutral winds at Arecibo between 1980 and 1987, *Journal of Geophysical Research: Space Physics*, *94*(A3), 2711–2716, doi:10.1029/JA094iA03p02711.

CDGM GLASS CO.,LTD (2018), OPTICAL GLASS DATABASE.

Cogger, L., J. Walker, J. Meriwether, and R. Burnside (1980), F region airglow: Are ground-based observations consistent with recent satellite results?, *Journal of Geophysical Research*, *85*(A6), 3013, doi:10.1029/JA085iA06p03013.

Connes, P. (1958), Spectromètre interférentiel à sélection par l'amplitude de modulation, *Journal de Physique et le Radium*, *19*(3), 215–222, doi:10.1051/jphysrad:01958001903021500.

Doornbos, E., J. van den IJssel, H. Luhr, M. Forster, and G. Koppenwallner (2010), Neutral Density and Crosswind Determination from Arbitrarily Oriented Multiaxis Accelerometers on Satellites, *Journal of Spacecraft and Rockets*, *47*(4), 580–589, doi:10.2514/1.48114.

Dötzer, F. (2019), Calibration of a Doppler asymmetric spatial heterodyne interferometer for atmospheric wind measurements, Ph.D. thesis, University of Erlangen-Nuremberg.

Drob, D. P., J. T. Emmert, G. Crowley, J. M. Picone, G. G. Shepherd, W. Skinner, P. Hays, R. J. Niciejewski, M. Larsen, C. Y. She, J. W. Meriwether, G. Hernandez, M. J. Jarvis, D. P. Sipler, C. A. Tepley, M. S. O'Brien, J. R. Bowman, Q. Wu, Y. Murayama, S. Kawamura, I. M. Reid, and R. A. Vincent (2008), An empirical model of the Earth's horizontal wind fields: HWM07, *Journal of Geophysical Research: Space Physics*, *113*(A12), doi:10.1029/2008JA013668.

Drob, D. P., J. T. Emmert, J. W. Meriwether, J. J. Makela, E. Doornbos, M. Conde, G. Hernandez, J. Noto, K. A. Zawdie, S. E. McDonald, J. D. Huba, and J. H. Klenzing (2015), An update to the Horizontal Wind Model (HWM): The quiet time thermosphere, *Earth and Space Science*, *2*(7), 301–319, doi:10.1002/2014EA000089.

Dupont, F., F. Grandmont, B. Solheim, A. Bourassa, D. Degenstein, N. Lloyd, and R. Cooney (2015), Spatial Heterodyne Spectrometer for Observation of Water for a Balloon Flight: Overview of the Instrument & Preliminary Flight Data Results, in *Fourier Transform Spectroscopy and Hyperspectral Imaging and Sounding of the Environment*, p. FW4A.5, OSA, Lake Arrowhead, California, doi:10.1364/FTS.2015.FW4A.5.

Emmert, J. T., M. L. Faivre, G. Hernandez, M. J. Jarvis, J. W. Meriwether, R. J. Niciejewski, D. P. Sipler, and C. A. Tepley (2006), Climatologies of nighttime upper thermospheric winds measured by ground-based Fabry-Perot interferometers during geomagnetically quiet conditions: 1. Local time, latitudinal, seasonal, and solar cycle dependence, *Journal of Geophysical Research: Space Physics*, *111*(A12), doi:10.1029/2006JA011948.

England, S. L., S. Maus, T. J. Immel, and S. B. Mende (2006), Longitudinal variation of the E-region electric fields caused by atmospheric tides, *Geophysical Research Letters*, *33*(21), doi:10.1029/2006GL027465.

England, S. L., T. J. Immel, E. Sagawa, S. B. Henderson, M. E. Hagan, S. B. Mende, H. U. Frey, C. M. Swenson, and L. J. Paxton (2018), Effect of atmospheric tides on the morphology of the quiet time, postsunset equatorial ionospheric anomaly, *Journal of Geophysical Research: Space Physics*, doi:10.1029/2006JA011795@10.1002/(ISSN)2169-9402.TIMED1.

Englert, C. R., and J. M. Harlander (2006), Flatfielding in spatial heterodyne spectroscopy, *Applied Optics*, *45*(19), 4583, doi:10.1364/AO.45.004583.

Englert, C. R., J. M. Harlander, J. G. Cardon, and F. L. Roesler (2004), Correction of phase distortion in spatial heterodyne spectroscopy, *Applied Optics*, *43*(36), 6680, doi:10.1364/AO.43.006680.

Englert, C. R., J. M. Harlander, D. D. Babcock, M. H. Stevens, and D. E. Siskind (2006), Doppler asymmetric spatial heterodyne spectroscopy (DASH): an innovative concept for measuring winds in planetary atmospheres, p. 63030T, San Diego, California, USA, doi:10.1117/12.681704.

Englert, C. R., D. D. Babcock, and J. M. Harlander (2007), Doppler asymmetric spatial heterodyne spectroscopy (DASH): concept and experimental demonstration, *Applied Optics*, *46*(29), 7297, doi:10.1364/AO.46.007297.

Englert, C. R., M. H. Stevens, D. E. Siskind, J. M. Harlander, and F. L. Roesler (2010a), Spatial Heterodyne Imager for Mesospheric Radicals on STPSat-1, *Journal of Geophysical Research*, *115*(D20), doi:10.1029/2010JD014398.

Englert, C. R., J. M. Harlander, J. T. Emmert, D. D. Babcock, and F. L. Roesler (2010b), Initial ground-based thermospheric wind measurements using Doppler asymmetric spatial heterodyne spectroscopy (DASH), *Optics Express*, *18*(26), 27,416, doi:10.1364/OE.18.027416.

Englert, C. R., J. M. Harlander, C. M. Brown, J. W. Meriwether, J. J. Makela, M. Castelaz, J. T. Emmert, D. P. Drob, and K. D. Marr (2012), Coincident thermospheric wind measurements using ground-based Doppler Asymmetric Spatial Heterodyne (DASH) and Fabry-Perot Interferometer (FPI) instruments, *Journal of Atmospheric and Solar-Terrestrial Physics*, *86*, 92–98, doi:10.1016/j.jastp.2012.07.002.

Englert, C. R., J. M. Harlander, C. M. Brown, K. D. Marr, I. J. Miller, J. E. Stump, J. Hancock, J. Q. Peterson, J. Kumler, W. H. Morrow, T. A. Mooney, S. Ellis, S. B. Mende, S. E. Harris, M. H. Stevens, J. J. Makela, B. J. Harding, and T. J. Immel (2017a), Michelson Interferometer for Global High-Resolution Thermospheric Imaging (MIGHTI): Instrument Design and Calibration, *Space Science Reviews*, *212*(1-2), 553–584, doi:10.1007/s11214-017-0358-4.

Englert, C. R., C. M. Brown, B. Bach, E. Bach, K. Bach, J. M. Harlander, J. F. Seely, K. D. Marr, and I. Miller (2017b), High-efficiency echelle gratings for mighti, the spatial heterodyne interferometers for the icon mission, *Applied Optics*, *56*(8), 2090–2098.

Fang, T.-W., R. Akmaev, T. Fuller-Rowell, F. Wu, N. Maruyama, and G. Millward (2013), Longitudinal and day-to-day variability in the ionosphere from lower atmosphere tidal forcing, *Geophysical Research Letters*, *40*(11), 2523–2528, doi: 10.1002/grl.50550.

Fest, E. C. (2013), *Stray light analysis and control*, SPIE Press, Bellingham, Washington.

Gao, H., Y. Tang, D. Hua, L. Qin, and C. Zhu (2011), Modified super-wide-angle Sagnac imaging interferometer based on LCoS for atmospheric wind measurement, *Journal of Quantitative Spectroscopy and Radiative Transfer*, *112*(2), 268–276, doi:10.1016/j.jqsrt.2010.06.008.

Gault, W. A., G. G. Shepherd, W. E. Ward, C. H. Hersom, Y. J. Rochon, and B. H. Solheim (1994), On-orbit performance of the WINDII instrument on the Upper Atmosphere Research Satellite (UARS), in *Optical Spectroscopic Techniques and Instrumentation for Atmospheric and Space Research*, vol. 2266, pp. 307–310, International Society for Optics and Photonics, doi:10.1117/12.187567.

Gault, W. A., S. I. Sargoytchev, and G. G. Shepherd (1996), Divided-mirror scanning technique for a small Michelson interferometer, in *Optical Spectroscopic Techniques and Instrumentation for Atmospheric and Space Research II*, vol. 2830, pp. 15–18, International Society for Optics and Photonics, doi:10.1117/12.256111.

Gentry, B. M., H. Chen, and S. X. Li (2000), Wind measurements with 355-nm molecular Doppler lidar, *Optics Letters*, *25*(17), 1231–1233, doi:10.1364/OL.25.001231.

Gpixel Inc. (2017), GSENSE400BSI Datasheet.

Hagan, M. E., A. Maute, R. G. Roble, A. D. Richmond, T. J. Immel, and S. L. England (2007), Connections between deep tropical clouds and the Earth's ionosphere, *Geophysical Research Letters*, *34*(20), doi:10.1029/2007GL030142.

Hanuschik, R. W. (2003), A flux-calibrated, high-resolution atlas of optical sky emission from UVES, *Astronomy & Astrophysics*, *407*(3), 1157–1164, doi:10.1051/0004-6361:20030885.

Harding, B. J., J. J. Makela, C. R. Englert, K. D. Marr, J. M. Harlander, S. L. England, and T. J. Immel (2017), The MIGHTI Wind Retrieval Algorithm: Description and Verification, *Space Science Reviews*, *212*(1-2), 585–600, doi:10.1007/s11214-017-0359-3.

Hargreaves, J. K. (1992), *The Solar-Terrestrial Environment: An Introduction to Geospace - the Science of the Terrestrial Upper Atmosphere, Ionosphere, and Magnetosphere*, Cambridge University Press, google-Books-ID: HmqOicm_YXUC.

Harlander, J., Reynolds, J, R, and Roesler, L, F (1992), spatial heterodyne spectroscope for the epiration of diffuse internation emmintion line at far-ultraviolet wavelength, *THE ASTROPHYSICAL JOURNAL*, *396*, 730–740.

Harlander, J. M. (1991), Spatial Heterodyne Spectroscopy: Interferometric Performance at any Wavelength Without Scanning, Ph.D. thesis, The University of Wisconsin - Madison.

Harlander, J. M., and F. L. Roesler (1990), Spatial heterodyne spectroscopy: a novel interferometric technique for ground-based and space astronomy, in *Instrumentation in Astronomy VII*, vol. 1235, pp. 622–633, International Society for Optics and Photonics, doi:10.1117/12.19125.

Harlander, J. M., F. L. Roesler, R. J. Reynolds, K. P. Jaehnig, and W. T. S. Iii (1993), Differential field-widened spatial heterodyne spectrometer for investigations at high spectral resolution of the diffuse far-ultraviolet 1548-A emission line from the interstellar medium, in *EUV, X-Ray, and Gamma-Ray Instrumentation for Astronomy IV*, vol. 2006, pp. 139–148, International Society for Optics and Photonics, doi:10.1117/12.162827.

Harlander, J. M., H. Tran, F. L. Roesler, K. P. Jaehnig, S. M. Seo, W. T. S. Iii, and R. J. Reynolds (1994), Field-widened spatial heterodyne spectroscopy: correcting for optical defects and new vacuum ultraviolet performance tests, in *EUV, X-Ray, and Gamma-Ray Instrumentation for Astronomy V*, vol. 2280, pp. 310–319, International Society for Optics and Photonics, doi:10.1117/12.186821.

Harlander, J. M., H. Tran, F. L. Roesler, K. P. Jaehnig, S. Watchorn, W. T. S. Iii, and R. J. Reynolds (1995), Sounding rocket payload designed for investigations of the distribution and dynamics of the hot component of the interstellar medium using a field-widened spatial heterodyne spectrometer, in *EUV, X-Ray, and Gamma-Ray Instrumentation for Astronomy VI*, vol. 2518, pp. 132–140, International Society for Optics and Photonics, doi:10.1117/12.218372.

Harlander, J. M., F. L. Roesler, J. G. Cardon, C. R. Englert, and R. R. Conway (2002), SHIMMER: a spatial heterodyne spectrometer for remote sensing of Earth's middle atmosphere, p. 10.

Harlander, J. M., F. L. Roesler, C. R. Englert, J. G. Cardon, R. R. Conway, C. M. Brown, and J. Wimperis (2003), Robust monolithic ultraviolet interferometer for the SHIMMER instrument on STPSat-1, *Applied Optics*, *42*(15), 2829, doi:10.1364/AO.42.002829.

Harlander, J. M., C. R. Englert, D. D. Babcock, and F. L. Roesler (2010), Design and laboratory tests of a Doppler Asymmetric Spatial Heterodyne (DASH) interferometer for upper atmospheric wind and temperature observations, *Optics Express*, *18*(25), 26,430, doi:10.1364/OE.18.026430.

Harlander, J. M., C. R. Englert, C. M. Brown, K. D. Marr, I. J. Miller, V. Zastera, B. W. Bach, and S. B. Mende (2017), Michelson Interferometer for Global High-Resolution Thermospheric Imaging (MIGHTI): Monolithic Interferometer Design and Test, *Space Science Reviews*, *212*(1-2), 601–613, doi:10.1007/s11214-017-0374-4.

Hays, P. B., and HRDI Science Team (1992), Remote sensing of mesospheric winds with the high-resolution doppler imager, *Planetary and Space Science*, *40*(12), 1599–1606, doi:10.1016/0032-0633(92)90119-9.

Hays, P. B., V. J. Abreu, M. E. Dobbs, D. A. Gell, H. J. Grassl, and W. R. Skinner (1993), The high-resolution doppler imager on the Upper Atmosphere Research Satellite, *Journal of Geophysical Research*, *98*(D6), 10,713, doi:10.1029/93JD00409.

Hedin, A. E., N. W. Spencer, and T. L. Killeen (1988), Empirical global model of upper thermosphere winds based on Atmosphere and Dynamics Explorer satellite data, *Journal of Geophysical Research: Space Physics*, *93*(A9), 9959–9978, doi:10.1029/JA093iA09p09959.

Hedin, A. E., M. J. Buonsanto, M. Codrescu, M.-L. Duboin, C. G. Fesen, M. E. Hagan, K. L. Miller, and D. P. Sipler (1994), Solar activity variations in midlatitude thermospheric meridional winds, *Journal of Geophysical Research: Space Physics*, *99*(A9), 17,601–17,608, doi:10.1029/94JA01134.

Hedin, A. E., E. L. Fleming, A. H. Manson, F. J. Schmidlin, S. K. Avery, R. R. Clark, S. J. Franke, G. J. Fraser, T. Tsuda, F. Vial, and R. A. Vincent (1996), Empirical wind model for the upper, middle and lower atmosphere, *Journal of Atmospheric and Terrestrial Physics*, *58*(13), 1421–1447, doi:10.1016/0021-9169(95)00122-0.

Hedlund, P. R. (2010), USING A BISTATIC FABRY-PEROT INTERFEROMETER SYSTEM TO IMPROVE THE ESTIMATION OF THERMOSPHERIC WINDS, Ph.D. thesis.

Hernandez, G. (1988), *Fabry-Perot Interferometers*, Cambridge University Press, google-Books-ID: og7uKhM01K8C.

Hersom, C., and G. Shepherd (1995), Characterization of the wind imaging interferometer, *Applied optics*, *34*(16), 2871–2879.

Hilliard, R. L., and G. G. Shepherd (1966), Wide-Angle Michelson Interferometer for Measuring Doppler Line Widths*, *Journal of the Optical Society of America*, *56*(3), 362, doi:10.1364/JOSA.56.000362.

Hines, C. O., G. W. Adams, J. W. Brosnahan, F. T. Djuth, M. P. Sulzer, C. A. Tepley, and J. S. Van Baelen (1993), Multi-instrument observations of mesospheric motions over Arecibo: comparisons and interpretations, *Journal of Atmospheric and Terrestrial Physics*, *55*(3), 241–287, doi:10.1016/0021-9169(93)90069-B.

Hollas, J. M. (2004), *Modern Spectroscopy*, John Wiley & Sons, google-Books-ID: lVyXQZkcKKkC.

Hunten, D. M., F. E. Roach, and J. W. Ci-Iamberlain (1956), A photometric nnit lot the airglow and aurora, *Journal of Atmospheric and terrestrial Physics*, *8*, 345–346.

Immel, T. J. (2018), The Ionospheric Connection Explorer: Mission Design and Goals, *AGU Fall Meeting Abstracts*, *21*.

Immel, T. J., E. Sagawa, S. L. England, S. B. Henderson, M. E. Hagan, S. B. Mende, H. U. Frey, C. M. Swenson, and L. J. Paxton (2006), Control of equatorial ionospheric morphology by atmospheric tides, *Geophysical Research Letters*, *33*(15), doi:10.1029/2006GL026161.

Immel, T. J., S. L. England, X. Zhang, J. M. Forbes, and R. DeMajistre (2009), Upward propagating tidal effects across the E- and F-regions of the ionosphere, *Earth, Planets and Space*, *61*(4), 505–512, doi:10.1186/BF03353167.

Janesick, J. R., K. P. Klaasen, and T. Elliott (1987), Charge-Coupled-Device Charge-Collection Efficiency And The Photon-Transfer Technique, *Optical Engineering*, *26*(10), doi:10.1117/12.7974183.

Jiang, G., J. Xu, W. Yuan, B. Ning, W. Wan, and L. Hu (2012), A comparison of mesospheric winds measured by FPI and meteor radar located at 40N, *Science China Technological Sciences*, *55*(5), 1245–1250, doi:10.1007/s11431-012-4773-1.

Kaufmann, M., F. Olschewski, K. Mantel, B. Solheim, G. Shepherd, M. Deiml, J. Liu, R. Song, Q. Chen, O. Wroblowski, D. Wei, Y. Zhu, F. Wagner, F. Loosen, D. Froehlich, T. Neubert, H. Rongen, P. Knieling, P. Toumpas, J. Shan, G. Tang, R. Koppmann, and M. Riese (2018), A highly miniaturized satellite payload based on a spatial heterodyne spectrometer for atmospheric temperature measurements in the mesosphere and lower thermosphere, *Atmospheric Measurement Techniques*, *11*(7), 3861–3870, doi:10.5194/amt-11-3861-2018.

Kelley, M. C. (2009), *The Earth's Ionosphere: Plasma Physics and Electrodynamics*, Academic Press, google-Books-ID: 3GlWQnjBQNgC.

Kelly, M. A., J. M. Comberiate, E. S. Miller, and L. J. Paxton (2014), Progress toward forecasting of space weather effects on UHF SATCOM after Operation Anaconda, *Space Weather*, *12*(10), 601–611, doi:10.1002/2014SW001081.

Killeen, T. L., B. C. Kennedy, P. B. Hays, D. A. Symanow, and D. H. Ceckowski (1983), Image plane detector for the Dynamics Explorer Fabry-Perot interferometer, *Applied Optics*, *22*(22), 3503, doi:10.1364/AO.22.003503.

Killeen, T. L., W. R. Skinner, R. M. Johnson, C. J. Edmonson, Q. Wu, R. J. Niciejewski, H. J. Grassl, D. A. Gell, P. E. Hansen, J. D. Harvey, and J. F. Kafkalidis (1999), TIMED Doppler interferometer (TIDI), in *Optical Spectroscopic Techniques and Instrumentation for Atmospheric and Space Research III*, vol. 3756, pp. 289–301, International Society for Optics and Photonics, doi:10.1117/12.366383.

Killeen, T. L., Q. Wu, S. C. Solomon, D. A. Ortland, W. R. Skinner, R. J. Niciejewski, and D. A. Gell (2006), TIMED Doppler Interferometer: Overview and recent results, *Journal of Geophysical Research: Space Physics*, *111*(A10), doi:10.1029/2005JA011484.

Koppmann, R. (2017), *Lecture notes in Introduction to atmospheric physics*, University of Wuppertal.

Laikin, M. (2001), *Lens design*, no. 27 in Optical engineering, 3rd ed., rev. and expanded ed., Marcel Dekker, New York.

Langille, J., D. Letros, D. Zawada, A. Bourassa, D. Degenstein, and B. Solheim (2018), Spatial Heterodyne Observations of Water (SHOW) vapour in the upper troposphere and lower stratosphere from a high altitude aircraft: Modelling and sensitivity analysis, *Journal of Quantitative Spectroscopy and Radiative Transfer*, *209*, 137–149, doi:10.1016/j.jqsrt.2018.01.026.

Langille, J. A., B. Solheim, A. Bourassa, D. Degenstein, S. Brown, and G. G. Shepherd (2017), Measurement of water vapor using an imaging field-widened spatial heterodyne spectrometer, *Applied Optics*, *56*(15), 4297–4308, doi:10.1364/AO.56.004297.

Lathuillère, C., W. A. Gault, B. Lamballais, Y. J. Rochon, and B. H. Solheim (2002), Doppler temperatures from O(^{1}D) airglow in the daytime thermosphere as observed by the Wind Imaging Interferometer (WINDII) on the UARS satellite, *Annales Geophysicae*, *20*(2), 203–212.

Lee, Y. S., Y. H. Kim, Y. Yi, and J. Kim (2000), A baffle design for an airglow photometer onboard the korea sounding rocket-iii, *Journal of Korean Astronomical Society*, *33*, 165–172.

Lin, Y., G. Shepherd, B. Solheim, M. Shepherd, S. Brown, J. Harlander, and J. Whiteway (2005), Introduction to Spatial Heterodyne Observations of Water (SHOW) Project and its Instrument Development, p. 8.

Link, R., and L. L. Cogger (1988), A reexamination of the O I 6300-Å nightglow, *Journal of Geophysical Research*, *93*(A9), 9883, doi:10.1029/JA093iA09p09883.

Liu, J. (2019), Study on a miniaturized satellite payload for atmospheric temperature measurements, Wissenschaftliche Abschlussarbeiten Dissertation, University of Wuppertal, doi:https://doi.org/10.25926/hm6f-nf38.

Liu, J., D. Wei, Y. Zhu, M. Kaufmann, F. Olschewski, K. Mantel, J. Xu, and M. Riese (2018), Effective wind and temperature retrieval from Doppler asymmetric spatial heterodyne spectrometer interferograms, *Applied Optics*, *57*(30), 8829, doi:10.1364/AO.57.008829.

Makela, J. J., J. W. Meriwether, J. P. Lima, E. S. Miller, and S. J. Armstrong (2009), The Remote Equatorial Nighttime Observatory of Ionospheric Regions Project and the International Heliospherical Year, *Earth, Moon, and Planets*, *104*(1), 211–226, doi:10.1007/s11038-008-9289-0.

Marr, K. D., C. R. Englert, and J. M. Harlander (2012), Flat-fields in DASH interferometry, *Optics Express*, *20*(9), 9535, doi:10.1364/OE.20.009535.

Marr, K. D., C. R. Englert, J. M. Harlander, and K. W. Miller (2013), Thermal sensitivity of DASH interferometers: the role of thermal effects during the calibration of an Echelle DASH interferometer, *Applied Optics*, *52*(33), 8082, doi:10.1364/AO.52.008082.

Meriwether, J. W. (2006), Studies of thermospheric dynamics with a Fabry-Perot interferometer network: A review, *Journal of Atmospheric and Solar-Terrestrial Physics*, *68*(13), 1576–1589, doi:10.1016/j.jastp.2005.11.014.

Mikš, A. (2002), Modification of the formulas for third-order aberration coefficients, *JOSA A*, *19*(9), 1867–1871, doi:10.1364/JOSAA.19.001867.

Milligan, S., J. W. Howard, B. E. Laubscher, B. W. Smith, R. R. Berggren, and J. M. Harlander (1999), Optical design of an imaging spatial heterodyne infrared spectrometer, in *Infrared Technology and Applications XXV*, vol. 3698, pp. 869–881, International Society for Optics and Photonics, doi:10.1117/12.354491.

Nichols, T., D. Harrison, and S. Alpert (1985), Simple laboratory demonstration of the Doppler shift of laser light, *American Journal of Physics*, *53*(7), 657–660.

Norland Products (2020), Norland Optical Adhesive 61.

Oberheide, J., Q. Wu, T. L. Killeen, M. E. Hagan, and R. G. Roble (2006), Diurnal nonmigrating tides from TIMED Doppler Interferometer wind data: Monthly climatologies and seasonal variations, *Journal of Geophysical Research: Space Physics*, *111*(A10), doi:10.1029/2005JA011491.

Ocean Optics (2018), NE-1 Neon Calibration Light Source Installation and Operation Instructions.

Picone, J. M., A. E. Hedin, D. P. Drob, and A. C. Aikin (2002), NRLMSISE-00 empirical model of the atmosphere: Statistical comparisons and scientific issues, *Journal of Geophysical Research: Space Physics*, *107*(A12), SIA 15–1–SIA 15–16, doi:10.1029/2002JA009430.

Rees, M. H., and N. H. Rees (1989), *Physics and Chemistry of the Upper Atmosphere*, Cambridge University Press, google-Books-ID: AwFlTrgY55MC.

Reitebuch, O., C. Lemmerz, E. Nagel, U. Paffrath, Y. Durand, M. Endemann, F. Fabre, and M. Chaloupy (2009), The Airborne Demonstrator for the Direct-Detection Doppler Wind Lidar ALADIN on ADM-Aeolus. Part I: Instrument Design and Comparison to Satellite Instrument, *Journal of Atmospheric and Oceanic Technology*, *26*(12), 2501–2515, doi:10.1175/2009JTECHA1309.1.

Rider, K., T. Immel, E. Taylor, and W. Craig (2015), ICON: Where earth's weather meets space weather, in *2015 IEEE Aerospace Conference*, pp. 1–10, doi:10.1109/AERO.2015.7119120, iSSN: 1095-323X.

Roble, R. G. (2000), On the Feasibility of Developing a Global Atmospheric Model Extending from the Ground to the Exosphere, in *Atmospheric Science Across the Stratopause*, pp. 53–67, American Geophysical Union (AGU), doi:10.1029/GM123p0053.

Rochesterson (2020), Richardson Gratings - Specification Sheet.

Roesler, F. L., and J. M. Harlander (1990), Spatial heterodyne spectroscopy: interferometric performance at any wavelength without scanning, in *Optical Spectroscopic Instrumentation and Techniques for the 1990s: Applications in Astronomy, Chemistry, and Physics*, vol. 1318, pp. 234–243, International Society for Optics and Photonics, doi:10.1117/12.22119.

Sagawa, E., T. J. Immel, H. U. Frey, and S. B. Mende (2005), Longitudinal structure of the equatorial anomaly in the nighttime ionosphere observed by IMAGE/-FUV, *Journal of Geophysical Research: Space Physics*, *110*(A11), doi:10.1029/2004JA010848.

Salah, J. E., and J. M. Holt (1974), Midlatitude thermospheric winds from incoherent scatter radar and theory, *Radio Science*, *9*(2), 301–313, doi:10.1029/RS009i002p00301.

SCHOTT Advance Optics (2016), Temperature coefficient of the refractive index.

SCHOTT Advance Optics (2019), Optical Glass - Overview.

Shepherd, G. G. (1996), Application of doppler michelson imaging to upper atmospheric wind measurement: Windii and beyond, *Applied optics*, *35*(16), 2764–2773.

Shepherd, G. G., W. A. Gault, D. W. Miller, Z. Pasturczyk, S. F. Johnston, P. R. Kosteniuk, J. W. Haslett, D. J. W. Kendall, and J. R. Wimperis (1985), WAMDII: wide-angle Michelson Doppler imaging interferometer for Spacelab, *Applied Optics*, *24*(11), 1571, doi:10.1364/AO.24.001571.

Shepherd, G. G., G. Thuillier, W. A. Gault, B. H. Solheim, C. Hersom, J. M. Alunni, J.-F. Brun, S. Brune, P. Charlot, L. L. Cogger, D.-L. Desaulniers, W. F. J. Evans, R. L. Gattinger, F. Girod, D. Harvie, R. H. Hum, D. J. W. Kendall, E. J. Llewellyn, R. P. Lowe, J. Ohrt, F. Pasternak, O. Peillet, I. Powell, Y. Rochon, W. E. Ward, R. H. Wiens, and J. Wimperis (1993), WINDII, the wind imaging interferometer on the Upper Atmosphere Research Satellite, *Journal of Geophysical Research*, *98*(D6), 10,725, doi:10.1029/93JD00227.

Sipler, D., M. Biondi, and M. Zipf (1995), Vertical winds in the midlatitude thermosphere from Fabry-Perot interferometer measurements, *Journal of Atmospheric and Terrestrial Physics*, *57*(6), 621–629.

Sivjee, G. G., T. J. Hallinan, and G. R. Swenson (1980), Fabry-Perot-interferometer imaging system for thermospheric temperature and wind measurements, *Applied Optics*, *19*(13), 2206–2209, doi:10.1364/AO.19.002206.

Smith, B. W., and J. M. Harlander (1999), Imaging spatial heterodyne spectroscopy: theory and practice, in *Infrared Technology and Applications XXV*, vol. 3698, pp. 925–931, International Society for Optics and Photonics, doi:10.1117/12.354497.

Smith, B. W., B. E. Laubscher, B. J. Cooke, P. C. LaDelfe, J. M. Harlander, J. W. Howard, and S. Milligan (1999), IRISHS: the infrared imaging spatial heterodyne spectrometer: a new pushbroom Fourier transform ultraspectral imager with no moving parts, in *Infrared Technology and Applications XXV*, vol. 3698, pp. 501–509, International Society for Optics and Photonics, doi:10.1117/12.354552.

Smith, R. W. (1998), Vertical winds: A tutorial, *Journal of atmospheric and solar-terrestrial physics*, *60*(14), 1425–1434.

Smith, W. J. (2000), *Modern optical engineering: the design of optical systems*, 3rd ed ed., McGraw Hill, New York.

Souprayen, C., A. Garnier, A. Hertzog, A. Hauchecorne, and J. Porteneuve (1999), Rayleigh-Mie Doppler wind lidar for atmospheric measurements. I. Instrumental setup, validation, and first climatological results, *Applied Optics*, *38*(12), 2410–2421, doi:10.1364/AO.38.002410.

Sultan, P. J. (1996), Linear theory and modeling of the Rayleigh-Taylor instability leading to the occurrence of equatorial spread F, *Journal of Geophysical Research: Space Physics*, pp. 26,875–26,891, doi:10.1029/96JA00682@10.1002/(ISSN)2169-9402.MISETA1.

Survey, B. G. (2014), ap Index inquiry form.

Thuillier, G., and M. Hersé (1991), Thermally stable field compensated Michelson interferometer for measurement of temperature and wind of the planetary atmospheres, *Applied Optics*, *30*(10), 1210–1220, doi:10.1364/AO.30.001210.

Thuillier, G., and G. G. Shepherd (1985), Fully compensated Michelson interferometer of fixed-path difference, *Applied Optics*, *24*(11), 1599, doi:10.1364/AO.24.001599.

Thuillier, G., W. Gault, J.-F. Brun, M. Hersé, W. Ward, and C. Hersom (1998), In-flight calibration of the Wind Imaging Interferometer (WINDII) on board the Upper Atmosphere Research Satellite, *Applied Optics*, *37*(8), 1356–1369, doi:10.1364/AO.37.001356.

Titheridge, J. E. (1995), Winds in the ionosphere-A review, *Journal of Atmospheric and Terrestrial Physics*, *57*(14), 1681–1714, doi:10.1016/0021-9169(95)00091-F.

Upton, L. A., and D. H. Hathaway (2018), An updated solar cycle 25 prediction with aft: the modern minimum, *Geophysical Research Letters*, *45*(16), 8091–8095.

VESC project (2020), VESC tool.

Ward, W. E., W. A. Gault, G. G. Shepherd, and N. Rowlands (2001), Waves Michelson Interferometer: a visible/near-IR interferometer for observing middle atmosphere dynamics and constituents, in *Sensors, Systems, and Next-Generation Satellites V*, vol. 4540, pp. 100–111, International Society for Optics and Photonics, doi: 10.1117/12.450652.

Ward, W. E., W. A. Gault, N. Rowlands, S. Wang, G. G. Shepherd, I. C. McDade, J. C. McConnell, D. Michelangeli, and J. Caldwell (2003), Imaging interferometer for satellite observations of wind and temperature on Mars, the Dynamics Atmosphere Mars Observer (DYNAMO), in *Applications of Photonic Technology 5*, vol. 4833, pp. 226–236, International Society for Optics and Photonics, doi:10.1117/12.473823.

Widdel, H.-U. (1987), Vertical movements in the middle atmosphere derived from foil cloud experiments, *Journal of atmospheric and terrestrial physics*, *49*(7-8), 723–741.

Witasse, O., J. Lilensten, C. Lathuillère, and P.-L. Blelly (1999), Modeling the OI 630.0 and 557.7 nm thermospheric dayglow during EISCAT-WINDII coordinated measurements, *Journal of Geophysical Research: Space Physics*, *104*(A11), 24,639–24,655, doi:10.1029/1999JA900260.

Yiyi, H. (2012), Application and simulation of imaging Fabry-Perot interferometers to observe the upper atmosphere, Ph.D. thesis, University of Illinois at Urbana-Champaign.

ZEMAX LLC. (2020), OpticStudio_usermanual.

Zhang, C., Q. Wu, and T. Mu (2011), Influences of pyramid prism deflection on inversion of wind velocity and temperature in a novel static polarization wind imaging interferometer, *Applied Optics*, *50*(32), 6134–6139, doi:10.1364/AO.50.006134.